Universidade de Aveiro Departamento de Engenharia de Materiais e Cerâmica
Ano 2015

ALI
BAGHI ZADEH

Acoplamento da deformação e dos campos magnético e de polarização elétrica em materiais multiferróicos

Coupling of magnetic, strain and electric polarization fields in the structure of multiferroic materials

Universidade de Aveiro
Ano 2015
Departamento de Engenharia de Materiais e Cerâmica

ALI
BAGHI ZADEH

Acoplamento da deformação e dos campos magnético e de polarização elétrica em materiais multiferróicos

Coupling of magnetic, strain and electric polarization fields in the structure of multiferroic material

Tese apresentada à Universidade de Aveiro para cumprimento dos requisitos necessários à obtenção do grau de Doutor em Ciência e Engenharia de Materiais ALI BAGHIZADEH, realizada sob a orientação científica do Doutor Joaquim Manuel Vieira, Professor Catedrático do Departamento de Engenharia de Materiais e Cerâmica da Universidade de Aveiro e co-orientação do Doutor Vitor Brás de Sequeira Amaral Professor Catedrático do Departamento de Física da Universidade de Aveiro.

Apoio financeiro da FCT no âmbito
da Bolsa de Doutoramento:
SRRH/BD/51140/2010

To my wife

o júri

presidente

Professor Doutor Artur da Rosa Pires
Professor Catedrático da Universidade de Aveiro

Professor Doutor Vitor Brás de Sequeira Amaral
Professor Catedrático da Universidade de Aveiro, Co-orientador

Professor Doutor Joaquim Manuel Vieira
Professor Catedrático da Universidade de Aveiro, Orientador

Professor Doutor Pedro Manuel de Melo Bandeira Tavares
Professor Associado da Universidade de Trás-os-Montes e Alto Douro

Professor Doutor Marc-Georg Willinger
Coordenador do Group of Electron Microscopy, Fritz Haber Institute of the Max-Planck-Society, Berlin

Professor Doutor João Pedro Esteves de Araújo
Professor Auxiliar da Faculdade de Ciências da Universidade do Porto

Professor Doutor Bernardo Gonçalves Almeida
Professor Auxiliar da Escola de Ciências da Universidade do Minho

Doutor Manuel Pedro Fernandes Graça
Equiparado a Investigador Auxiliar do I3N da Universidade de Aveiro

acknowledgments

This PhD work which has mainly an experimental focus, demanded participation of many people who either did teach me techniques or software, or with whom I did take parts of the research work. I would like to acknowledge FCT – SESAME program on giving me four years grant to carry out research of my PhD (SRRH/BD/51140/2010), also supporting my staying in Firtz Haber Institute, Berlin for a while in two successive years. I appreciate RNME-UA national network of electron microscopy project (REDE/1509/RME/2005) for access to equipment and extension of the grant for the FCT project. I acknowledge CICECO Institute in Aveiro University for providing me access to many facilities in the Institute and funding of attending workshops or conferences. Also this work was supported by following projects:PTDC/FIS/105416/2008, co-financed by FEDER, QREN reference COMPETE:FCOMP-01-0124-FEDER-010470 and RECI/CTM-CER/0336/2012 co-financed by FEDER, QREN reference COMPETE: FCOMP-01-0124-FEDER-027465 and was developed within the scope of the project CICECO-Aveiro Institute of Materials, POCI-01-0145-FEDER-007679 (FCT Ref. UID /CTM /50011/2013), financed by national funds through the FCT/MEC and when appropriate co-financed by FEDER under the PT2020 Partnership Agreement

Very special thanks to my wife and my family, mostly to my wife for standing all difficulties during PhD work, for her great support and motivation and for her fruitful helps on helping in parts of my PhD work on AFM/PFM analysis and in making the Thesis ready for submission.
Also, especial thank to my Supervisor, Prof. Joaquim Manuel Vieira who have tried kindly to train me and teach materials science, to fill my lack of knowledge in relevant topics, for spending lots of time and energy on progressing our research. I acknowledge deeply my co-supervisor, Prof. Vitor Brás de Sequeira Amaral who is so patient on teaching physical concepts of magnetism, magnetic measurements, frequent discussions and coordinating this PhD research. My special thanks to Porf. Augusto Lopez, Marta Ferro and Bruno Almeida in Electron Microscopy for their training and support, and more often discussions on techniques and results, also to the technicians and secretaries of the Department of Materials and Ceramic Engineering, to my colleagues in Physics Department, technicians and secretaries, particularly my colleagues in the Lab for VSM magnetometers. I am deeply grateful to my colleagues in the group of Prof. Vitor Amaral in Physics Department and SQUID lab, for their helpful training and discussions on the magnetic studies and first-principles calculations, particularly Joao Amaral, Joao Nuno Gonçalves and Nuno Joao Silva. Also thanks to Prof. Manuel Graça for his help on performing dielectric measurements in Physics Department. I would like to acknowledge the collaboration of Dr. Rosario Soares in XRD labs of CICECO, for always being helpful and performing XRD analysis. My heartfelt appreciation to Prof. Marc Willinger for the hospitality in Fritz Haber Institute, Berlin, Germany for few months, for teaching advanced microscopy and techniques of preparing the samples while I was there, and to the members of his department who were always kind and helpful on whatever I was asking. I give my sincere gratitude to Mr. Achim Klein-Hoffmann, the technician for TEM sample preparation in Fritz Haber Institute, who taught me different techniques and details of relevant equipment for the needs of sample preparation. I would like to acknowledge Dr. Daniel Stroppa in INL, Braga for the opportunity to do TEM/STEM experiments using aberration corrected Microscope and initiate new directions in my research. My appreciation to Prof.Rui Silva and Dr.Filipe Oliveira and my colleagues in their laboratories in the Department of Ceramics and Materials Engineering where we shared some facilities and I spent most of my time there. Also I acknowledge Daniel Mota in IFIMUP, Department of Physics, University of Porto.

palavras-chave

multiferróicos, desvio estequiométrico, $LuMnO_3$, acoplamento magneto-dielétrico, defeitos topológicos, microscopia.

resumo

No trabalho de investigação para o doutoramento foi realizado um estudo abrangente dos efeitos do desvio estequiométrico sobre o comportamento magnético e o acoplamento do magnetismo com a polarização elétrica e a rede cristalina do óxido cerâmico multiferróico de rede hexagonal do $LuMn_xO_{3\pm\delta}$ auto-dopado no intervalo de composição ($0.92 \leq x \leq 1.12$). Existe um acoplamento complexo dos diferentes ordenamentos ferróicos. O cancelamento dos momentos magnéticos dos iões Mn no sistema antiferromagnético, a polarização elétrica com topologia específica de vórtice/antivórtice conduziram os investigadores a propor modelos para a física e química subjacentes ao acoplamento magneto-elétrico e magneto-elásticas dos materiais multiferróicos de h- $RMnO_3$. Neste trabalho optou-se pela auto-dopagem das posições R e do Mn da rede cristalina dos cerâmicos h-$LuMn_xO_{3\pm\delta}$ preparados por reacção no estado sólido como caminho para uma compreensão mais completa da transição antiferromagnética, do ferromagnetismo fraco frequentemente observado nas mesmas redes cristalinas e das propriedades dieléctricas e ferroeléctricas associadas a alterações impostas à rede pela auto-dopagem.
Em linha com o propósito traçado para a tese de doutoramento, foram dois os objectivos definidos para o estudo de sinterização no primeiro capítulo sobre resultados experimentais. Primeiro foi feito o estudo de sinterização das amostras com desvio de estequiometria em correspondência com condições do processamento relatadas na bibliografia e conformes com os diagramas de fases do $LuMnO_3$, tendo-se optado por diversas etapas de reacção a temperatura elevada terminando com um último passo a 1300ºC durante 24 horas. Numa segunda parte, explorou-se o efeito do aumento do tempo de recozimento até às 240 horas à mesma temperatura fixa de 1300 ºC para melhorar as propriedades sob estudo da solução sólida. Caracterizaram-se todas as séries para cada tempo de recozimento dos cerâmicos de h-$LuMn_xO_{3\pm\delta}$ na tentativa de construir um referencial que permitisse a comparação das propriedades medidas nas composições com desvio de estequiometria com os resultados de outros estudos da bibliografia. A difracção de raios-X (DRX) e o refinamento de Rietveld dão a evolução dos parâmetros de rede em função de x tendo-se observado uma retracção nos parâmetros de rede com o aumento dos valores de x e identificado em primeira aproximação o limite de estabilidade da solução sólida pela análise dos mesmos parâmetros de rede. As evoluções do tamanho do grão e a da quantidade de fases residuais detectadas foram investigadas por técnicas de TEM, SEM, EDS e EBSD. Foram ainda caracterizadas as dependências do crescimento de grão e da diminuição de teor em fases secundárias em função da composição x e tempo de processo.

A susceptibilidade magnética das amostras e a irreversibilidade magnética são caracterizadas e avaliadas extensivamente no capítulo seguinte da tese. Foram determinadas as dependências da susceptibilidade magnética, da temperatura de Néel da transição antiferromagnética e dos parâmetros principais do comportamento magnético e comparadas com observações feitas em outros multiferróicos. Como ferramenta de alta sensibilidade para detectar vestígios menores da fase magnética hausmannite, sugere-se que as medidas magnéticas podem ser úteis na confirmação dos diagramas de fase dos óxidos $RMnO_3$. São discutidas dificuldades patentes em estudos anteriores sobre as interpretações dadas à anomalia magnética nos óxidos h-$RMnO_3$ abaixo de 43 K sendo esta atribuída à fase Mn_3O_4 com suporte na microscopia eletrónica. No capítulo final da tese é investigado o acoplamento magneto-eléctrico com o ordenamento AFM acoplado às fronteiras de domínio da polarização dielétrica e com a determinação da constante dielétrica complexa em função da frequência e temperatura. Dentro do limite de estabilidade da solução sólida do h-$LuMn_xO_{3\pm\delta}$, o acoplamento magneto-eléctrico em T_N continua a observar-se em todo o intervalo do desvio estequiométrico. Tanto quanto o autor tem conhecimento este estudo representa o primeiro trabalho de investigação sobre acoplamento magneto-eléctrico modificado por auto-dopagem com lacunas nas redes de h-$RMnO_3$.

A observação das redes cristalinas revela distorções à escala atómica criadas pelas variações locais da razão x na composição do $LuMn_xO_{3\pm\delta}$, dependentes das condições de sinterização as quais foram analisadas em detalhe por TEM/STEM, complementado com EDS e espectroscopia EELS por forma a obterem-se informações mais completas sobre relações cruzadas entre distorção, falta de homogeneidade composicional e estrutura eletrónica. Estes resultados encontram-se reunidos e são discutidos num capítulo específico da tese. Foram encontradas interfaces internas nas secções finas TEM dos grãos cristalinos de várias tipologias. São propostas explanações qualitativas para as propriedades magnéticas e ferroelétricas medidas correlacionando-as com as observações feitas à nano-escala nos cerâmicos de $LuMn_xO_{3\pm\delta}$. Os domínios ferroelétricos e defeitos topológicos estão presentes tanto em imagens de TEM como de AFM/PFM. Esta última técnica é utilizada para a caracterização do tamanho, distribuição e comutação de polaridade dos domínios ferroelétricos na escala do mícron em relação com potenciais efeitos da dopagem por lacuna e fazendo a ponte com os estudos TEM sobre a estrutura atómica dos mesmos domínios ferroelétricos. Como suporte ao estudo experimental, foram feitas simulações DFT usando o código Wien2K a fim de interpretar os espectros de EELS da banda K do oxigénio e para obter informação sobre a hibridização dos catiões com o oxigénio. As linhas das bandas $L_{3,2}$ do Mn nos espectros de EELS são utilizadas para estabelecer o estado de oxidação dos iões Mn no interior dos grãos cristalinos. Além disso, a ferroelectricidade induzida por re-hibridização é também avaliada por comparação com a densidade parcial de estados dos orbitais do conjunto de iões da estrutura cristalina e a polarização elétrica é computada e correlacionada com efeitos do desvio estequiométrico.

keywords

Multiferroics, off-stoichiometry, $LuMnO_3$, magneto-dielectric coupling, topological defects, microscopy.

abstract

The comprehensive study on the coupling of magnetism, electrical polarization and the crystalline lattice with the off-stoichiometric effects in self-doped multiferroic hexagonal h-$LuMn_xO_{3\pm\delta}$ ($0.92 \leq x \leq 1.12$) ceramic oxides was carried out for the PhD work. There is a complex coupling of the three ferroic degrees. The cancelation of the magnetic moments of ions in the antiferromagnetic order, electric polarization with specific vortex/antivortex topology and lattice properties have pushed researchers to find out ways to disclose the underlying physics and chemistry of magneto-electric and magneto-elastic couplings of h-$RMnO_3$ multiferroic materials. In this research work, self-doping of Lu-sites or Mn-sites of h-$LuMn_xO_{3\pm\delta}$ ceramics prepared via solid state route was done to pave a way for deeper understanding of the antiferromagnetic transition, the weak ferromagnetism often reported in the same crystalline lattices and the ferroelectric properties coupled to the imposed lattice changes.

Accordingly to the aim of the PhD thesis, the objectives set for the sintering study in the first chapter on experimental results were two. First, study of sintering off-stoichiometric samples within conditions reported in the bibliography and also extracted from the phase diagrams of the $LuMn_xO_{3\pm\delta}$, with a multiple firings ending with a last high temperature step at 1300ºC for 24 hours. Second, explore longer annealing times of up to 240 hours at the fixed temperature of 1300 ºC in a search for improving the properties of the solid solution under study. All series of $LuMn_xO_{3\pm\delta}$ ceramics for each annealing time were characterized to tentatively build a framework enabling comparison of measured properties with results of others available in literature. XRD and Rietveld refinement of data give the evolution the lattice parameters as a function to x. Shrinkage of the lattice parameters with increasing x values was observed, the stability limit of the solid solution being determined by analysis of lattice parameters. The evolution of grain size and presence of secondary phases have been investigated by means of TEM, SEM, EDS and EBSD techniques. The dependencies of grain growth and regression of secondary phases on composition x and time were further characterized.

Magnetic susceptibility of samples and magnetic irreversibility were extensively examined in the present work. The dependency of magnetic susceptibility, Neel ordering transition and important magnetic parameters are determined and compared to observation in other multiferroics in the following chapter of the thesis. As a tool of high sensitivity to detect minor traces of the secondary phase hausmannite, magnetic measurements are suggested for cross-checking of phase diagrams. Difficulty of previous studies on interpreting the magnetic anomaly below 43 K in h-$RMnO_3$ oxides was discussed and assigned to the Mn_3O_4 phase, with supported of the electron microscopy. Magneto-electric coupling where AFM ordering is coupled to dielectric polarization is investigated as a function of x and of

sintering condition via frequency and temperature dependent complex dielectric constant measurements in the final chapter of the thesis. Within the limits of solid solubility, the crystalline lattice of off-stoichiometric ceramics was shown to preserve the magneto-electric coupling at T_N. It represents the first research work on magneto-electric coupling modified by vacancy doping to author's knowledge.

Studied lattices would reveal distortions at the atomic scale imposed by local changes of x dependent on sintering conditions which were widely inspected by using TEM/STEM methods, complemented with EDS and EELS spectroscopy all together to provide comprehensive information on cross coupling of distortions, inhomogeneity and electronic structure assembled and discussed in a specific chapter. Internal interfaces inside crystalline grains were examined. Qualitative explanations of the measured magnetic and ferroelectric properties were established in relation to observed nano-scale features of h-$LuMn_xO_{3\pm\delta}$ ceramics. Ferroelectric domains and topological defects are displayed both in TEM and AFM/PFM images, the later technique being used to look at size, distribution and switching of ferroelectric domains influenced by vacancy doping at the micron scale bridging to complementary TEM studies on the atomic structure of ferroelectric domains. In support to experimental study, DFT simulations using Wien2K code have been carried out in order to interpret the results of EELS spectra of O K-edge and to obtain information on the cation hybridization to oxygen ions. The $L_{3,2}$ edges of Mn is used to access the oxidation state of the Mn ions inside crystalline grains. In addition, re-hybridization driven ferroelectricity is also evaluated by comparing the partial density of states of the orbitals of all ions of the samples, also the polarization was calculated and correlated to the off-stoichiometric effect.

Content

List of Figures

List of Tables

Abbreviations and symbols

Abbreviation	Meaning
AFM	Atomic Force Microscope
AFM	Antiferromagnetic
APB	Anti-phase boundary
APB/FE- DW	Anti-phase boundary/Ferroelectric domain wall
BEC	Born effective moment
BF	Bright Field
CIF	Crystallographic information file
CIP	Cold Isostatic Press
DF	Dark- field
DFT	Density functional theory
DG	Debye-Grüneisen
DM	Dzyalloshinskii-Moryia
DW	Domain wall
EDS	Energy Dispersive Spectroscopy
EBSD	Electron Backscatter Diffraction
EELS	Electron Energy Loss Spectroscopy
FE	Ferroelectric
FM	Ferromagnetic
HAADF	High angle annular dark field detector
H_C	Coercive field
H_{EB}	Magnetic exchange bias
LDA	Local density approximation
LMO	$LuMnO_3$
M	Magnetization
MeFM	Magnetoelectric force microscopy
M_r	Magnetic remanent
PFM	Pizeoresponse force microscopy
RMS	Root mean square
T1max	Neel transition from dielectric measurement
T2max	anomaly in magnetic and dielectric at 69 K

T3max	anomaly around 30 K in dielectric constant
T_{CW}	Curie-Weiss temperature
TEM	Transmission electron microscopy
T_N	Neel transition
SEM	Scanning electron microscopy
SQUID	Superconducting quantum interference device
STEM	Scanning transmission electron microscopy
U	activation energy
VESTA	Visualization for electronic and structural Analysis
VSM	Vibrating sample magnetometer
XRD	X-ray diffraction

Symbol	Meaning
f_H*	hausmanite weight fraction from XRD line intensity ratio
f_H+	hausmanite weight fraction from magnetic measurements
f_m	hausmanite weight fraction from XRD Rietveld refinement
J	Exchange interaction parameter
K_1	P6_3/mcm (193)
K_3	P6_3cm (185)
k_B	Boltzmann constant
Oe	Oersted
Q	Mode amplitude
S_i	Component of spin of Mn^{3+} ions
Å	Angstrom
$\alpha^{\pm}$	phase shift on FE domain walls
$\beta^{\pm}$	phase shift on FE domain walls
$\gamma^{\pm}$	phase shift on FE domain walls
Γ_1	P6_3/mmc (194)
Γ_2	P6_3mc (186)
δ	off-stoichiometric value of oxygen
μ_{eff}	Effective magnetic moment
μ_B	Bohr magneton
ε*	Dielectric constant
ε'	Real part of dielectric constant
ε''	Imaginary part of dielectric constant
τ	Relaxation time
ϕ	Azimuthal angle, orientation of tilting the bipyramids
χ	Magnetic susceptibility
x_r	Effective value of x of main phase from XRD Rietveld refinement

1. Outline

Multiferroic hexagonal $RMnO_3$ manganites (R= Er, Ho, In, Lu, Sc, Tm, Y, Yb) deserve receiving large attention from researchers as these materials permitted new fundamental findings showing coexistence of magnetic interactions, electrical polarization and structural distortion of the crystalline lattices. Coupling of correlated ferroic orders (magnetic, electrical polarization and structural orders) in a material imposes in-deep exploration of physical and chemical properties to figure out the role of each ferroic order behind experimentally measured quantities. To the current state of research, these interactions can appear as a result of cross-coupling of two or even three of the ferroic orders, within a same unit cell or coming out as a collective mechanism extended in a wider scale inside the bulk volume of the material. Difficulty arises here as how to discern the contribution of each coupling contribution to in studied properties. In the hexagonal h-$RMnO_3$ oxides and among them in $LuMnO_3$ with Lu^{3+} ion with the smallest rare-earth ionic radii it is challenging to deduce the role of rare-earth ion, of transition metal ion or oxygen on each ferroic property and their cross-coupling, which will later provide the understanding and feasibility to control those properties and make technological applications in future.

Previous research on off-stoichiometry of oxides like $LaMnO_3$ of perovskite structure paved the way to look for clues on disclosing the underlying physics and chemistry of the h-$RMnO_3$ oxides by introducing rare-earth vacancies or transition metal vacancies in the crystalline lattice. The aim of the PhD work is to assess the effect of transition metal vacancies (Mn vacancy in the present study) or rare-earth vacancies (strictly R-site) on multiferroic properties of h-$RMnO_3$ (for the case of R=Lu) in order to find out the interplaying connection of magnetic moments, electrical polarization and crystalline

structure. Recognizing the presence of coupling effects like magneto-elastic, magneto-electric and structural Anti-phase/FE, acting in separate or together as driving force for the properties, ferroic orders have to be broadly surveyed. The essential connection of any ferroic order to Lu or Mn cations in the $LuMnO_3$ materials will be exposed by tuning the relevant A-site or B-site vacancy to changes induced on the measured physical property. On reviewing related literature of h-$RMnO_3$ (R= Ho-Lu, Y and Sc) reported values for properties like unit cell parameters or magnetic behaviour of nominally stoichiometric samples present significant scatter which hypothetically comes from point defects in their lattices, namely cation vacancies and oxygen vacancies.

This thesis is composed of eight chapters with this introductory outline to the research carried out as thesis work and the final chapter of conclusions and future work. It includes a review of the structure and multiferroic properties of hexagonal $RMnO_3$ phases focused on the $LuMnO_3$ phase as second chapter and a description of the materials, preparation methods, main experimental techniques and equipment for testing and characterization of the samples as third chapter. Self-doping of h-$LuMn_xO_{3\pm\delta}$ ceramics in combination to sintering conditions demand refined characterization of the phases present in the samples of each composition. Analytical techniques such as XRD, EDS-mapping, EBSD and transmission electron microscopy images are used to determine the presence of secondary phases on both sides of composition in vacancy doped lattices. Limitations of each characterizing technique on tracing very minute amounts and minuscule particles of the secondary phases are ascertained.

The option on taking the solid state reaction of mixed oxides as the sample preparation method was taken in order to simplify the number of variables under study, to preserve the high purity of the reactants as bought by avoiding further chemical handling, to assure proper retention of the cation fraction in the synthesized samples and to allow later comparison of results with data in the literature as conventional solid state sintering had been a prevalent technique for preparation of h-$RMnO_3$ oxides. As further discussed in chapter four, the first set of $LuMn_xO_{3\pm\delta}$ samples were sintered by choosing

conditions of high temperature and time holds reported in related literature for the conventional solid state method. Then taking one step forward, efforts were devoted to improve measured properties in relation to increased homogeneity of the materials by focusing on the effect of sintering time, rarely quoted in the publications but which was found referenced in the studies on phase diagrams of h-$RMnO_{3\pm\delta}$ (R= Ho-Lu, Y and Sc) oxides.

The effects of self-doping of the hexagonal $LuMnO_3$ materials on the lattice parameters and microstructural evolution are described in chapter four. Studies of self-doped lattices of perovskite $RMnO_3$ (R= La, …) have shown that the direct effect of doping appears as changes of crystalline lattice constants. They will also be distinguishable in geometrically frustrated structures of h-$RMnO_3$ oxides as titling of MnO_5 polyhedron and buckling of R^{3+} ions will modify coupling of ferroic orders. XRD Rietveld refinement provided the insight into lattice modification imposed by self-doping and as a function of sintering time at constant final temperature. Subsequently, calculating the unit cell parameters like buckling of MnO5 polyhedron revealed the effect of vacancy doping on the properties of these materials. Comparison to doped h-$RMnO_3$ oxides available in literature would help to build up a model to predict or explain measured changes in lattice parameters. Studies on stoichiometric h-$RMnO_3$ (R= Y, Lu) confirm, as expected, that lattice parameters are temperature dependent. Their evolution with temperature bridges the high temperature paraelectric state to room temperature ferroelectricity, and at even lower temperatures to AFM spin ordering with magneto-electric coupling. It had been shown that upon phase transition at high temperature there is an intermediary phase with polar characteristic along c-axis which is the direction of electrical polarization. The stable room temperature phase is actually anti-ferrodistortive, an improper ferroelectric, and would not induce the electrical polarization measured at room temperature and below room temperature.

As for the lattice parameters, the magnetic behaviour, dielectric polarization, magnetic and ferroelectric domain formation of h-$RMnO_3$ materials all exhibit temperature

dependent characteristics. Therefore, it is intention of this research to include in the studies of the concerned properties temperature dependent measurements bound to available facilities. The important feature of vacancy doping of the lattices on modifying the magnetic interaction of Mn^{3+} spins in h-$LuMnO_3$ to which dielectric polarization is coupled below T_N will be considered in chapter five. The extensive evaluation of the magnetic behaviour of off-stoichiometric samples was included to figure out the dependency of basal plane AFM interaction of Mn^{3+} ions and Curie-Weiss temperature (and the associated frustration factor) on the amplitude of stoichiometry shifting and also on extending of sintering time.

Widespread investigation of the structure of off-stoichiometric $LuMn_xO_{3\pm\delta}$ ceramics was considered and implemented by using HRTEM and STEM imaging, completed by EELS and EDS spectroscopies, relevant observations being condensed in the sixth chapter. Linked to all measured quantities and properties, the microstructural analysis of the crystalline domains of a lattice with vacancies (Mn or Lu) will most probably display in-homogeneities and defects of several types creating distortion of the lattice planes. Planar defects or inclusions of secondary phases would duly affect the relevant properties, namely the magnetic behaviour and ferroelectricity. Views of the atomic structure and arrangement of ions in basal plane or along c-axis, representing very exact pictures for the AFM interactions of the Mn^{3+} ions and electrical polarization induced by R^{3+} ion displacement, respectively, became of great interest for the study of h-$RMnO_3$ materials in recent years. Interlocking of the structural anti-phase state and ferroelectric state in these materials attracted high impact research work, and gives space for the interplay of uncompensated spins, electrical polarization and structural distortions. The identification of the function of off-stoichiometric shifts and understanding of the role of Mn^{3+} or Lu^{3+} ions on topological defects was intended to be investigated be means of TEM and PFM microscopy techniques.

Dielectric measurements in chapter seven are complementary tools used to understand the magneto-electric coupling of $LuMn_xO_{3\pm\delta}$ materials under the effect of changing the

Mn/Lu ratio x in the composition of the self-doped samples to bring in evidence of any transition. Magneto-electric coupling has the benefit of not suffering from interferences caused by presence of hausmannite, the secondary phase of Mn, often found as impurity in manganites. Additional information of the interplay of ferroelectricity and off-stoichiometric conditions can be extracted from Piezo Response Force microscopy of the ceramic samples. It was predicted that introducing vacancies in the lattice of $LuMn_xO_{3\pm\delta}$ ceramics would necessarily modify the unit cell in off-stoichiometric compositions, expectedly resulting in different piezo response of A-site and B-site vacancy doped samples. Ferroelectricity is of great importance as it shows itself at room temperature and makes these same materials of interest for memory devices.

To shed light on enhancement or weakening of ferroelectricity in relation to off-stoichiometry of samples the symmetry mode decomposition was done in the same chapter seventh based on hypothetical high temperature phase and comparing the amplitude of room temperature mode and the intermediary ferroelectric mode. First principles calculations give the insight into the energy scheme of these modes versus composition and additionally provided in the fifth chapter some understanding of the change of magnetic moments within framework of a simple model of A-type AFM configuration of Mn spins. EELS spectroscopy of the lattice of crystalline grains combined with first-principles calculations were done to bring the changes in the electronic structure of geometrically frustrated unit cells of h-$LuMn_xO_{3\pm\delta}$ oxides and inquire on the oxidation state of the Mn ions. Both are believed to be of significant importance for the magnetic behaviour and induced ferroelectricity in crystalline lattice. EELS is also a valuable tool in the determination of the oxidation state of the Mn ions in secondary phases as well as in the interfaces.

2. Introduction to multiferroics

The phenomena that lead to coupling of magnetic and dielectric properties, of electric polarization fields, magnetoelectric, magnetocaloric and transport properties in the structure of multiferroic materials are necessarily complex and have created a wide field for interdisciplinary studies at the boundaries between Physics and Materials [1–6]. The coupling of properties aroused enormous interest, namely for better understanding of the multiferroic oxides and in sight of their technological uses in tuneable multifunctional devices operating on the CMR (Colossal Magneto-Resonance) and TMR (Tunnelling Magneto-Resistance) effects or with electrically controllable magnetic barriers [2,4,5]. Magnetic, electronic and lattice interactions lead to cooperative phenomena [7]. The fundamental physics of colossal magnetoresistance, multiferroism and ubiquitous phase separation phenomena and nanoscale inhomogeneities remains challenging [8]. The inner interfaces such as ferroelectric domain walls and hetero-interfaces in such materials also show new properties: electronic states between two insulators, exchange coupling and coupling between ferroelectric and ferromagnetic orders occurring at the interfaces [9–16]. Manganites and other transition metal-based oxides (chromites, nickelites, ferrites) are representative examples of strongly correlated electron oxides, the manganites and ferrites being mostly studied for their multiferroic properties. In the wide field of research work on hexagonal rare-earth manganites that is running at the present time, the $LuMnO_3$ manganite was singled out for the study of coupling of magnetic and ferroelectric behaviour when processed as bulk ceramics firstly because Lu^{3+} is non-magnetic and the study could be focused on the magnetism of Mn ions AFM ordered in trimers and second because the review of literature clearly suggested that accidentally or intentionally created deviations of the cation ratio from unit [17–19] in the chemical composition of $RMnO_3$ materials was the cause of

significant differences of values of the multiferroic properties of the hexagonal manganites reported in literature. The crystalline structure and main properties ascribed to the multiferroic behaviour of the hexagonal manganite of $LuMnO_3$ elected for the present study are characterised in literature review in the following of this introductory chapter.

2-1 Rare-earth hexagonal manganites

There is a great deal of research around rare-earth manganites, $RMnO_3$, (R = La, …, Lu, Y). CMR (Colossal Magneto-Resonance) and TMR (Tunnelling Magneto-Resistance) phenomena were already investigated widely in the perovskite rare-earth manganites like $LaMnO_3$ where the effect of doping showed significant role on changing the mentioned phenomena [20]. There was also interest on oxygen exchange behaviour in relation to structural and chemical changes at high temperatures of some of these oxides with expected applications in fuel cells [21]. Generally, the rare-earth manganites with orthorhombic perovskite structure include rare-earth elements, R^{3+}, of large ionic radius (La, … , Dy) [20,22]. Rare-earth elements with smaller ionic radius (Ho-Lu, Y, Sc) form manganites with hexagonal structure of space group of $P6_3cm$ at ambient pressure. In the hexagonal structure, each Mn^{3+} ion is in five-fold trigonal bipyramidal coordination surrounded by 5 oxygen ions, with two planar sheets of the Mn ions in the unit cell separated by the corrugated plane of R-O ions. High temperature paraelectric ($P6_3/mmc$) to ferroelectric ($P6_3cm$) phase transformation distorts the unit cell of the h-$RMnO_3$ by reducing the symmetry of the unit cell and tripling of the volume the paraelectric unit cell [23]. This structural distortion occurs with Mn^{3+} ions forming trimers with the oxygen ion in the centre. There are hexagonal networks of Mn^{3+} trimers at z = 0 and 1/2, the Mn planes follow the ABABAB stacking sequence of the hexagonal lattices with large separation due to R and O ions in between. R^{3+} ions have coordination number of 7, with

R^{3+} ions making planes of rare-earth ions separating the Mn^{3+} planes in the unit cell [22,24–27].

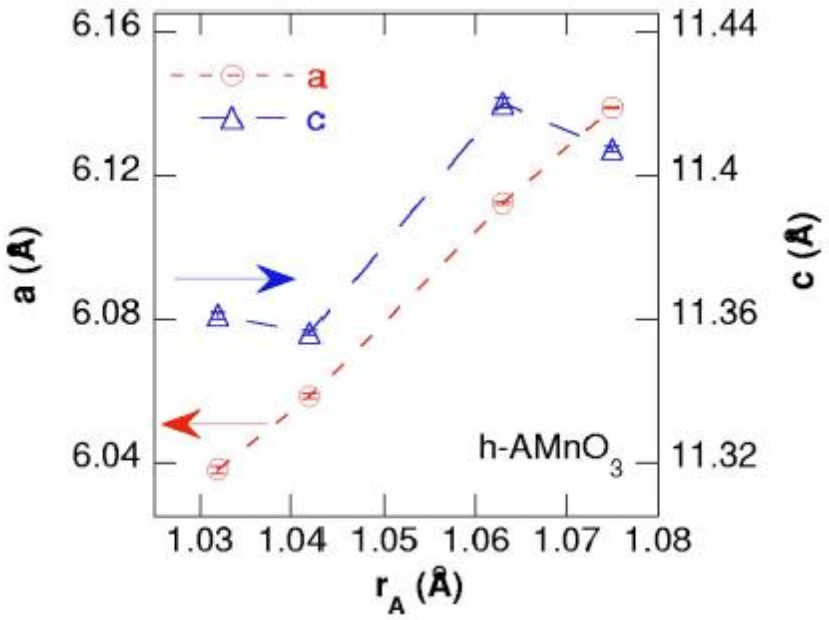

Figure 2-1. Room temperature dependence of lattice parameters of hexagonal $RMnO_3$ on rare-earth ionic radius of Lu, Er, Yb, and Y, from reference [6].

The effect of the ionic radius on the properties of h-$RMnO_3$ oxides either in bulk samples or thin films was investigated (for instance [24,25]). Figure **2-1** shows the dependence of the lattice constants of the crystalline structure of h-$RMnO_3$ (R= Lu, Er, Yb, and Y) on ionic radius of the rare-earth element [25]. Due to this strong dependency of the crystalline lattice cell dimensions on the ionic radius of the rare-earth elements, the formation of the perovskite or hexagonal structures can be qualitatively explained by the value of the Goldschmidt tolerance factor t, the perovskite structure being stable only in the range of values of t 0.855-1.00 [25,28]. The hexagonal structure becomes the stable phase for values of t below the lower threshold in the given range.

Besides differences at the atomic scale in values of the atomic positions and lattice constants being reported for hexagonal $RMnO_3$ compounds, the only crystal structure

found under common preparation conditions (near atmosphere pressure) is the hexagonal $P6_3cm$ crystalline structure with six formula units of $LuMnO_3$ in the unit cell [24,29,30]. Figure **2-2**.a shows the atomic arrangements in the hexagonal $LuMnO_3$ unit cell with the Wyckoff symbol of each atom in the unit cell. The network of Mn trimers in the a-b plane has oxygen ion in the centre of 3 Mn^{3+} ions forming one trimer.

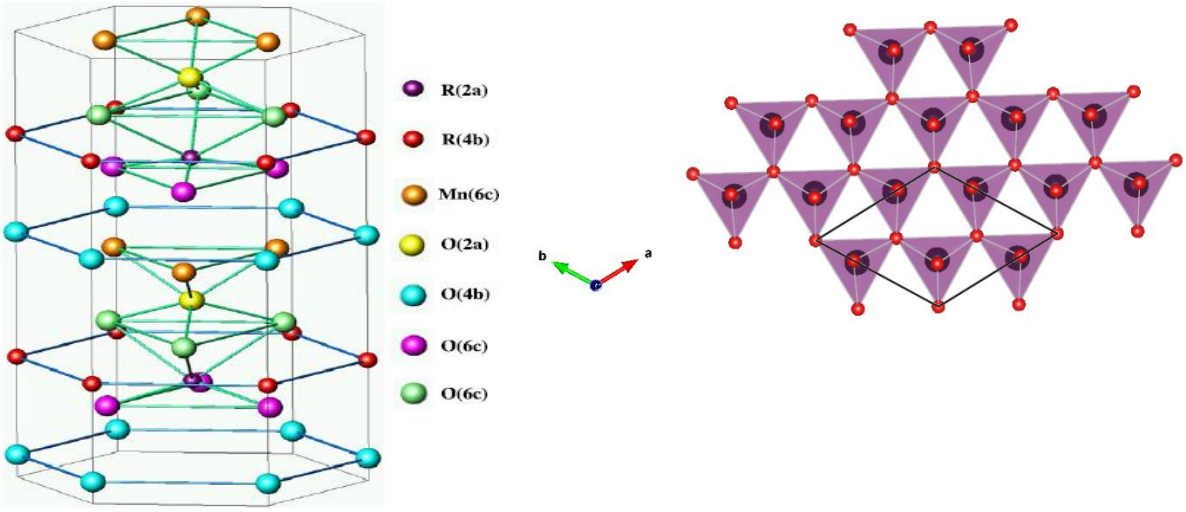

a b

Figure 2-2.(a). Schematic representation of the unit cell in h-$RMnO_3$ with atomic positions and their corresponding Wyckoff positions [26]. (b) A sheet of the Mn ions in a hexagonal structure of $LuMnO_3$ viewed along the c-axis. The red spheres are oxygen ions and the black Mn ions (made using VESTA software).

The space group $P6_3cm$ sets 6 or 8 different magnetic structures in the h-$RMnO_3$ phases depending on the rare-earth elements carrying spin or not [26,27,31]. Taking just the Mn^{3+} ions as possessing free spins (cases of R = Y, Lu), the magnetic interactions are restrained either to the basal plane or between consecutive basal planes. The spin orientation in each plane lies in the xy plane with non-collinear configuration. The spin orientation in the basal plane and between two adjacent planes will define the dominant magnetic structure. Theoretical calculations and experimental observations have proved

the existence of two types of nearest neighbour interactions between Mn^{3+} moments [26,31]. The first interaction takes place in the hexagonal plane with non-collinear spin ordering of Mn^{3+} ions within trimers of the Mn^{3+} ions with oxygen in the centre which in fact is the prevailing 2D antiferromagnetic interaction considering the spin orientation [26,27,31,32]. The spin configuration of the Mn^{3+} ions in basal plane and their AFM interactions in AFM region have been considered to result in geometrically frustrated structures of these oxides [26,31]. The second one is the antiferromagnetic interaction of the Mn^{3+} ions in adjacent planes along c-axis which will result in 3D magnetic ordering. Whereas in-plane magnetic interaction is mediated by the planar oxygen in the basal plane, this last interaction is the super-super-exchange magnetic interaction between Mn ions in adjacent x-y planes and operates via the apical oxygen ions at the apexes of MnO_5 bipyramids.

2-2 Data on crystalline structure of $LuMnO_3$

Clearly dependent on details of sample synthesis routes and methods of measurement of the lattice constants of h-$RMnO_3$ compounds, values of the lattice constants and atomic positions reported in the literature often do not match at all together. For the case of lattice parameters of $LuMnO_3$, the h-$RMnO_3$ compound of this study, Table 2-1 and Table **2-2** give the summary of reported values of lattice constants and the corresponding atomic positions, respectively. Authors assumed that samples in these three studies have the correct stoichiometry of the Lu, Mn and O elements [12-15].

Table 2-1. Lattice parameters of $LuMnO_3$ conventional solid state sintered extracted from the references.

	Ref. [29]	Ref. [30]	Ref. [33]	Ref.[34]
a	6.038	6.1022	6.1005	6.0465
c	11.361	11.4182	11.3598	11.367
space group	$P6_3cm$	$P6_3cm$	$P6_3cm$	$P6_3cm$

Data gathered in Table **2-1** and Table **2-2**. are restrictedly from samples of conventional solid state sintering, the method often used for preparation of $RMnO_3$ oxides [29,30,33,34]. There is an apparent sensitivity of data to preparation conditions and measurement methods, the observed scatter in a-axis and c-axis values amounting to 0.5 % and 0.3 %, respectively. The causes of this scatter in the values of lattice constants have to be found on different scales of the microstructure of the samples and in any chemical non-uniformity of the sintered materials. The lattice parameters in Ref.[30] were determined with crushed powders of the single crystal of $LuMnO_3$, close to reported value of a-constant of Ref.[34] from ceramic samples of the solid state reaction, however, the value of c-constant is significantly different.

Table 2-2. Atomic positions of the present ions in the $LuMnO_3$ from literature [29,30,33].

				Ref. [29]	Ref. [30]	Ref. [33]	Ref. [29]	Ref. [30]	Ref. [33]	Ref. [29]	Ref. [30]	Ref. [33]
Label	Type	multiplicity	Wyckoff symbol	x	x	x	y	y	y	z	z	Z
Lu1	Lu3+	2	a	0	0	0	0	0	0.2760(7)	0.27394(6)	0.270(1)	0
Lu2	Lu3+	4	b	-0.66667	0.3333	0.3333(0=	-0.33333	0.6667	0.66667	0.23038(2)	0.234(2)	0.2323(7)
Mn1	Mn3+	6	c	-.3355(10)	0.355(1)	0.3348(16)	-.3355(10)	0	0	-.00077(13)	0	0
O1	O2-	6	c	-.3070(18)	0.323(6)	0.3039(16)	-.3070(18)	0	0	0.1642(6)	0.161(6)	0.1661(7)
O2	O2-	6	c	-.3614(17)	0.652(6)	0.6402(16)	-.3614(17)	0	0	-.1638(6)	0.326(6)	0.3364(7)
O3	O2-	2	a	0	0	0	0	0	0	-.0285(12)	0.467(5)	0.4736(7)
O4	O2-	4	b	-0.66667	0.3333	0.3333	-0.33333	0.6667	0.66667	0.0190(9)	0.011(4)	0.0220(7)

2-3 Neel ordering transition and Curie-Weiss temperatures

Two characteristic values are used to characterize the magnetic interactions of h-$RMnO_3$ oxides: the Neel temperature (T_N) signals the AFM ordering temperature and the Curie-Weiss temperature (T_{CW}) that determines the extrapolation of the high temperature magnetic susceptibility. The Curie-Weiss temperature of stoichiometric $LuMnO_3$ single crystal is reported as -880K [35], being -760 K [36] for polycrystalline material sintered at 1300°C for 24 h, lower than the value of -520 K [37] found in second study of

polycrystalline $LuMnO_3$ with final heating at 1400 °C for 48 h . The same references gave values of T_N of 86 K for the single crystal $LuMnO_3$, 90 K for polycrystals sintered at 1300 °C after 24 h and 87 K for the polycrystals with final heating at 1400°C for 48 h.

The available data for T_N in the off-stoichiometric ceramics is limited to YMn_xO_3 oxides reported in separate publications for Mn-rich side and Y-rich side of the solid solution [17,19]. In Mn-rich side of YMn_xO_3, T_N changes from 66 K at stoichiometric composition to 72 K for x = 1.1. The trend observed in the absolute values of T_{CW} goes in opposite direction to the increase on T_N, the T_{CW} being -330 K (x = 1) to -530 K (x = 1.1) [19]. Increasing the amount of Mn content to x = 1.15 did not result in further increasing of T_N or decreasing of the T_{CW}. The analogous study of magnetic parameters on the Y-rich side of YMn_xO_3 ceramics showed that the increase of Y content to x = 0.9 reduces the T_N and increases the absolute value of T_{CW} from -448 K for x = 1 to -330 K for x = 0.9 [17]. The values of T_N and T_{CW} of YMn_xO_3 present the same directions for change with x in both studies.

The magnetic interaction of Mn moments in h-$RMnO_3$ oxide can be decomposed to different components, two of the nearest-neighbour AFM interactions and one FM. Since the AFM interaction is dominant in unit cell of the stoichiometric h-$RMnO_3$ oxide it is discussed with more details here. The Hamiltonian for these two AFM interactions can be written in the following forms:

$$\boldsymbol{H_{AFM} = H_{in-plane} + H_{inter-planar}} \quad (2\text{-}1)$$

$$\boldsymbol{H_{in-plane} = \sum_{i,j=1,2,3} J\, S_i \,.S_j + \sum_{i,j=4,5,6} J\, S_i \,.S_j} \quad (2\text{-}2)$$

$$\boldsymbol{H_{inter-planar} = \sum_{i=1,2,3, j=4,5,6} J_Z\, S_i \,.S_j} \quad (2\text{-}3)$$

where J is exchange interaction parameter for the Heisenberg model in basal plane, J_z the exchange interaction between two Mn planes with S_i and S_j the spin operators [26,34,38]. In the above equations, asymmetric in-plane interactions of the Mn^{3+} ions are assumed, otherwise the magnetic contribution in basal plane will be zero. The value of J for two different paths of Mn-O_3-Mn and Mn-O_4-Mn is different; we consider the average value

for J [34]. This magnetic picture is corroborated once one looks at in-plane oxygen ions with different bond lengths to Mn ions in the crystal structure of the h-$RMnO_3$ compounds. According to the parameterization of Harrison [34,39], the magnetic exchange interaction between transition metal ions would depend on the reverse of distance between neighbouring ions as $1/d^{2l+1}$, d shows the importance of bond lengths of Mn-O_{apical} on the strength of any magnetic component in basal plane. However, because of tilting of the MnO_5 bipyramids, and displacement of the Lu ions which was shown affects the Lu-O_{pl} bond lengths, the angles of the Mn-O_{pl}-Mn path would also play a role.

2-5 Magneto-elastic Coupling in $LuMnO_3$ and $YMnO_3$

The changes of crystal lattice parameters of the $RMnO_3$ as a function of temperature, rare-earth ionic radius and of (R,R′) mutual substitutions have been investigated to further understand the interplay of the lattice and physical properties, namely the magnetization and electric polarization [30,33,34,37,40–42]. Of direct relevance for the present research is the temperature dependence of the lattice parameters of $YMnO_3$ and $LuMnO_3$ from room temperature to below T_N, in the region where antiferromagnetic ordering is found. Figure 2-3 gives the variation of cell a-axis, c-axis and cell volume of $YMnO_3$ and $LuMnO_3$ with temperature where a visibly different behaviour of the c-axis of the lattices of the hexagonal manganite of the two non-magnetic rare-earths is observed [37].

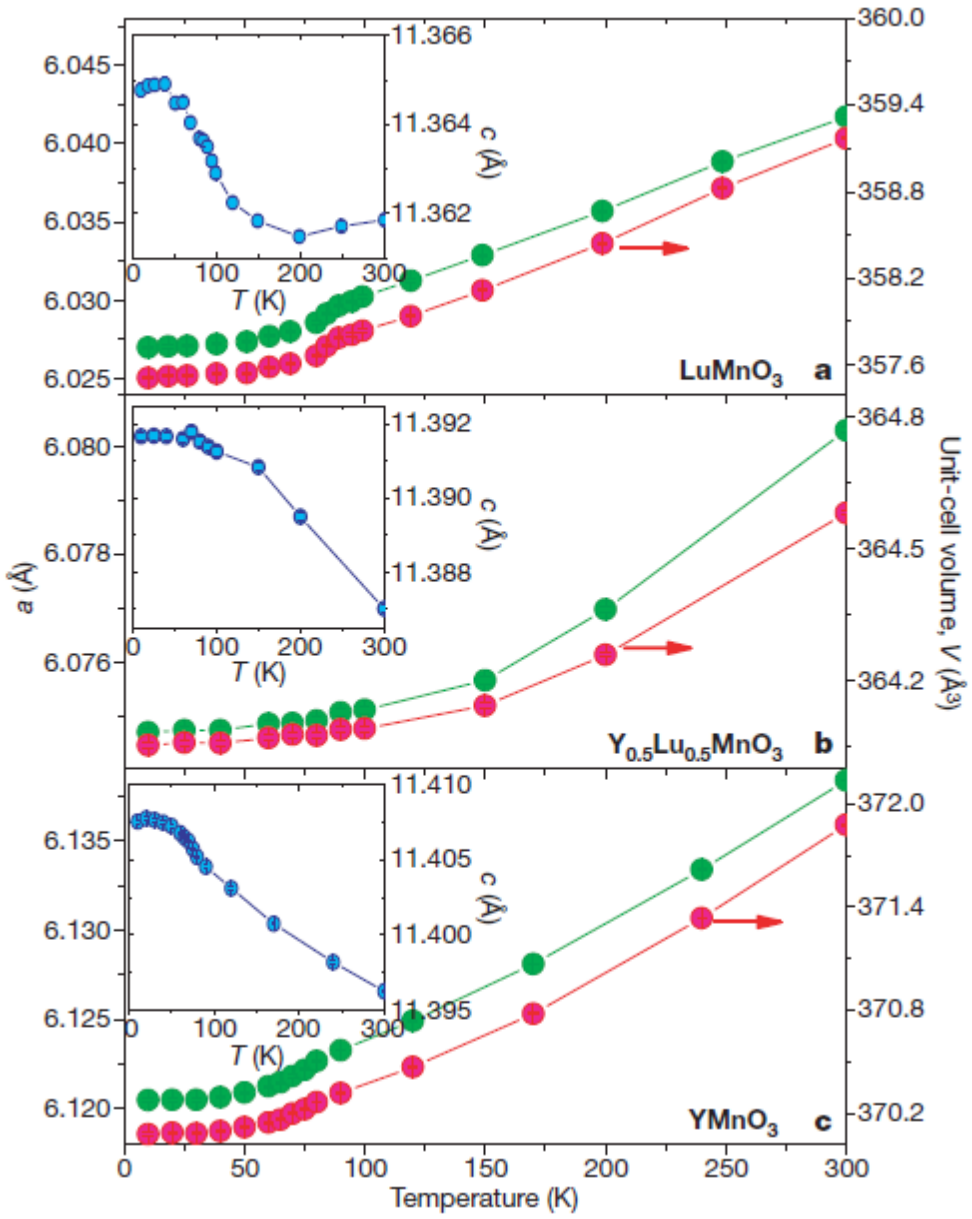

Figure 2-3. Lattice evolution of the $Lu_xY_{1-x}MnO_3$ lattice parameters and cell volume with temperature with the knee at Neel temperature in a-axis constant and cell volume [37].

The displacement of ion positions within the unit cell of these oxides showed up the lattice parameters, Mn position and Mn-O_3 and Mn-O_4 bond lengths of the Mn and planar oxygen ions all correlated to the magnetic ordering transition at T_N. The dependence of cell volume of $YMnO_3$ and $LuMnO_3$ above T_N closely follow the Debye-Grüneisen (DG)

model with four fitting parameters [34]. Below T_N the differences between the experimental values of unit-cell volume and the DG model are mostly due to the evolution of c-axis in the AFM ordered system, the difference of unit-cell volume and the AFM ordered magnetic moment becoming correlated [34]. This study and similar studies published afterwards demonstrated the existence of the coupling of the magnetic properties particularly at magnetic AFM ordering transition to the lattice structure of these oxides [27,30,34,37,43–45]. In $LuMnO_3$ the non-zero magnetic contribution in heat capacity measurement above T_N [34] and FM fluctuations of the Mn^{3+} spins observed in inelastic neutron scattering both extended up to $3T_N$ [45] are also closely correlated to magneto-elastic coupling of Mn^{3+} ions and lattice changes as temperature crosses the Neel ordering transition.

2-5 Topological defects of the interlocking of ferroelectric to anti-phase domain walls

Important feature of the h-$RMnO_3$ materials is their potential for application as ferroelectric materials or to serve as models to novel multiferroics of the same hexagonal lattice that display room temperature multiferroism, as is the case of $LuFeO_3$ [46]. The complex nature of coupling of ferroelectricity and spin ordering in geometrically frustrated magnetic materials is known for mainly two decades [9,35]. There has been notable improvement on the understanding of the magneto-electric coupling phenomenon in these materials [9,35,47]. Extensive research unraveled the underlying physics of the coupling of the structural distortion and electrical polarization and their interaction with ferroelectric domains and domain walls, particularly at room temperature where spin ordering in the h-$RMnO_3$ lattices had vanished [16,48–52]. Experimental works and theoretical modelling showed that combining of structural distortion and electrical polarization results in complex shapes of the ferroelectric domains of h-$RMnO_3$, with specific topology of six-folded vortex structure or the “clover-

leaf" pattern [9,10,16,30,51]. In fact, the vortex pattern is composed of two types of distortions. One is the net electrical polarization induced upon reducing the symmetry of the high temperature, paraelectric phase ($P6_3/mmc$) to lower symmetry, ferroelectric phase ($P6_3cm$). The second distortion comes from tilting of the bipyramids. The angle between Mn-O_{ap} (apical oxygen) is the magnitude of the tilting and the azimuthal angle, ϕ describing the orientation of the tilting [51,53]. Tilting of the bipyramids in the unit cell shifts the Lu ions along c-axis which produces upward (+) and downward (-) polarization in different ferroelectric domains as depicted in Figure 2-4. The arrows are showing the direction of the polarization for two typical domains in the ferroelectric phase. The allowed values for the φ are 0° and 180° ($\alpha^{\pm}$), 240° and 60° ($\beta^{\pm}$), 120° and 300° ($\gamma^{\pm}$) where + or – represents up and down electric polarization. Combination of the symmetry breaking and tilting of the unit cell gives rise to six anti-phase domains. Therefore, in h-$RMnO_3$ compounds, there exists interlocking of the structural translation domain walls, the anti-phase domain walls (APB), and ferroelectric (FE) domain walls, resulting in a/3 or 2a/3 displacements in the basal plane of the unit cell at the walls [54].

Figure 2-4.a shows the $P6_3cm$ crystal structure of $LuMnO_3$ (ferroelectric phase) as projected from the (001) zone axis, (c-axis view), the bipyramids with oxygen in the vertices and Mn in the center forming Mn trimers. There is neat tilting of the bipyramids in Figure 2-4.a. as the apical oxygen is not exactly at top of the Mn ion in the bipyramid. Tilting of the bipyramids in the ferroelectric phase, as quoted, would force rotation of the apical oxygen ions (those ions close to the R ions at top of the bipyramid) at different angles (ϕ), giving rise to the six APB/FE domains in Figure 2-4.b [51]. Current state of research is being continued to understand the reaction of the topological domains to the conditions of preparation of materials, namely heat treatment during sample preparation [15,55,56] or chemistry shift in the composition [57–61]. This matter is of great importance for the potential use of these materials in ferroelectric devices as control of the ferroelectric properties would be feasible by preparation processes.

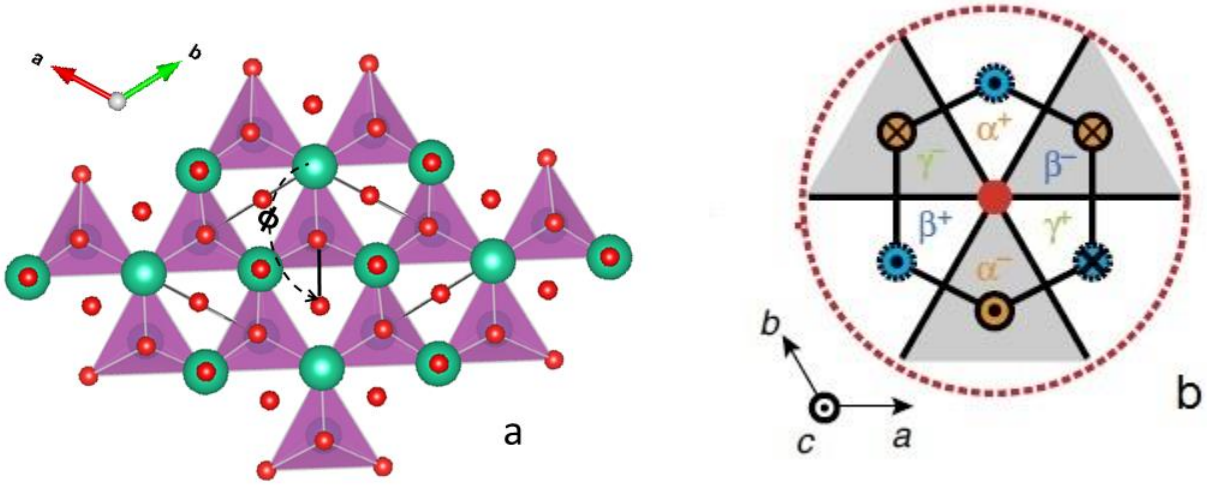

Figure 2-4. Top view of the Lu (green spheres) and Mn (embedded inside the bipyramids) ions arrangements in $LuMnO_3$ structure with oxygen ions (red spheres), the angle φ is the rotation of the central oxygen in respect to the zero position. (b) One of the possible vortex-like patterns with corresponding name of each domain due to the apical oxygen rotation (φ) as is described in the text. The colored circles are Lu ions with their direction up (dot) or down (cross)[51] .

2-6 Weak ferromagnetism in AFM ordered h-$RMnO_3$ lattices

Although h-$RMnO_3$ materials are known for the antiferromagnetic order below T_N, there is evidence of the presence of weak ferromagnetism at temperatures below T_N in these materials [10]. Four different sources or explanations of the origin of the weak ferromagnetism in h-$RMnO_3$ materials are found in the literature.

1. Presence of Mn ions of oxidation state different form Mn^{3+} most likely associated to changes of oxygen activity, antiphase-boundaries, cluster-like inclusions creating the magnetic interactions which are the signature of secondary phase Mn_3O_4 with ferrimagnetic transition around 43 K [17,62–70],

2. Spin canting driven by disordering in the lattice which had been generally assigned to Dzyalloshinskii-Moryia interaction inducing a net magnetization along the c-axis of the hexagonal lattice [31,35,71–78],

3. Ferromagnetic ordering of uncompensated spins by the effect of exchange coupling with the AFM ordered spins of the bulk lattice at interfaces, namely at the antiphase-boundaries of FE domain walls interlocked to topological defects which also creates a net magnetic moment at the interface parallel to c-axis of the lattice. Again, this ordering of spins at the interface has been partly attributed to Dzyalloshinskii-Moryia mechanism [9,10,16,48,50,51,79–81].

4. Weak ferromagnetism of nano-particles of h-$RMnO_3$ materials linked surfaces or core-shell like structures in the nanoparticles [82–86].

The weak ferromagnetic contribution of spin canting in nano-particles can seeming be excluded from the present study, as formation of nano-particle in h-$RMnO_3$ oxides has not been reported when the synthesis is done by solid state sintering in range of temperature and time of annealing adopted in this work. Since magnetoelectric coupling is one of the most relevant features of h-$RMnO_3$ materials, experimental setups have attempted to demonstrate the presence of both FE and AFM domains below T_N, providing evidence on induction of net magnetization because of spin canting on the FE domain walls to which the AFM domain walls are interlocked [9,10,16,45,48,50,79–81]. Figure 2-5 a and b give the interlocking of vortex/anti-vortex FE domains of the PFM images with AFM domains in (magnetoelectric force microscopy) MeFM image of the (001) orientation of h-$ErMnO_3$ single crystals [79]. The MeFM image was taken at very low temperature of 4 K at 8 T magnetic field. In this publication as well as in a former report of the same group [50] on $ErMnO_3$ single crystals the domain wall contrast in the MeFM images was correlated to net domain wall magnetic moments with total magnetization aligned along c-axis in a crystalline lattice which presents AFM interactions of Mn^{3+} ions in the a-b plane perpendicular to the c-axis, the orientation of the observation. A similar experiment to reveal the AFM and FE domain walls by using Second Harmonic Generation (SHG) spectroscopy in single crystals of h-$YMnO_3$ material

also concluded for the net ferromagnetic moment of the AFM domain walls from the gradual reorientation of Mn^{3+} spins on AFM domain walls locked to the FE domain walls [9]. Theoretical modelling was attempted to explain the net magnetization on the AFM domain walls interlocked to FE domain walls below T_N by taking into account the distortion of the lattice on the walls and its consequences on the spin arrangements of the Mn ions [10,16,48,79,87]. Figure 2-5.c to f demonstrate the concept of co-existence of weak ferromagnetism and ferroelectric polarization on the domain walls, where the symmetry of the lattice breaks to lower symmetry [10]. The correlation of the spin configuration of Mn^{3+} ions in basal plane of h-$LuMnO_3$ and polarization and magnetization of the lattice on the domain walls to the lattice distortion support previously experimental evidence on the role of lattice distortion to induce weak ferromagnetism coupled to electrical polarization. In Figure 2-5.d to f, lattice distortion was introduced as buckling of Lu ions, two down one up and titling of MnO_5 polyhedral or the opposite way with two Lu displaced up, one down and titling out of MnO_5 polyhedral. In Figure 2-5.e the change in polarization direction does not change the magnetic configuration of the Mn^{3+} spins, but in Figure 2-5.e the magnetic configuration is affected by change of the polarization orientation. At Q_{K3}(Å)=0 where there is no lattice distortion, polarization and c-axis magnetization are both zero, indicating the role of the lattice distortion on origin of the polarization and magnetization. The role of domain walls on producing the weak ferromagnetic contribution below T_N was introduced in Ref.[16] where the phenomenological development of the Landau free energy in combination to First-principles calculations resulted in improving the present understanding of the interplay of the symmetry broken FE domain walls and spin disordering on the domain walls.

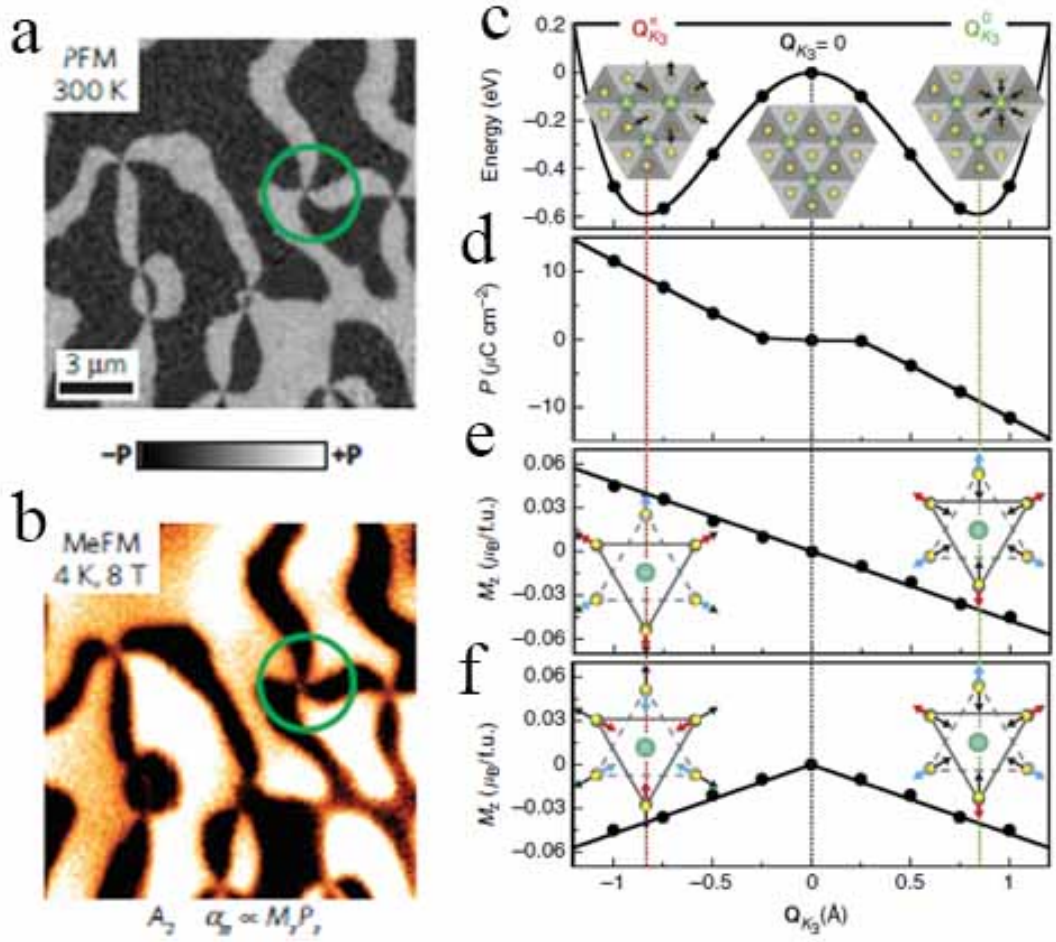

Figure 2-5.(a)) PFM image at room temperature and (b) low temperature 4 K MeFM image at 8 T magnetic field of a (001) surface of h-$ErMnO_3$ single crystal [79], (c) spin configurations and (d), (e) and (f) First-Principles calculations of polarization and magnetization both along c-axis as a function of trimer distortion Q_{K3} of the lattice, in (e) the antiferromagnetic spin configuration is fixed, in (f) it is rotated by π [10].

The presence of Mn ions with different oxidation state in a sample also contributes to magnetization of the h-$RMnO_3$ oxides. Oxidation state of Mn can change from nominal 3+ either because of oxygen deficiency [17,19,64,65,88] or presence of secondary phase of Mn namely the Mn_3O_4 [62,89–91]. The ascertaining of the presence magnetic impurities like hausmannite will be straightforward if secondary magnetic transition appears

around 43 K [90,92] since the phase diagrams of h-$RMnO_3$ materials point to hausmannite as a potential secondary phase impurity on the Mn-rich side for processes requiring temperatures above 1170 °C [93–95]. However, in some references of the literature the transition of magnetic moment at around 40 to 45 K was assigned to spin canting of Mn^{3+}, the presence of the secondary phase hausmannite was discharged by the authors based on XRD analysis [19,77]. Transitions of the magnetic moment reported below 40 K or above 45 K are rarely made dependent on magnetic secondary phase, as argued in the publications, oxygen vacancies [96,97], grain boundaries [65] or film/substrate interface [98] were given as the cause of the observed weak ferromagnetism, also in antiferromagnetic orthorhombic $RMnO_3$ oxides [99,100]. To get a comprehensive description of the causes of weak ferromagnetism in h-$RMnO_3$ materials, the measurement techniques and the scale they are detecting secondary phases, different oxidation states of Mn or the structure of interfaces will play crucial role. The importance of the detection limit of the technique selected to probe such properties was demonstrated in Ref.[99] in $TbMnO_3$ epitaxial thin films where local deficiency of Tb in the domain boundaries created additional magnetic signal below 40 K in the system. Deficiency of Tb on the domain boundaries with change in oxidation state of Mn could be detected there by using aberration corrected STEM combined with column-sensitive EELS mapping

.

3. Experimental techniques and software packages

The materials, experimental techniques for sample processing and characterization and main packages of software applied to simulation of TEM images, crystalline lattices and first-principle modelling are presented in this chapter. The more detailed description of each technique can be found in textbooks or elsewhere and it is not in the objectives of the chapter go into explanation of each technique in general. However, due to availability of different brands and variants of techniques and equipment of measurement of the studied properties which may result in change in measuring ranges, in-situ conditioning of the sample, or of sensitivity and accuracy of the measurement all main equipment that was used is identified and succinctly characterised in the following sections. Besides the measurement of properties, the procedure of synthesis and sintering of the bulk ceramics and special procedures for preparation of samples for microscopy or for particular measurement of their properties are also described because differences in adopted procedures of sample preparation may produce distinct levels of uncertainty in ascertaining the concerned properties.

In the brief introduction on the known, important software programmes and packages which were used for the purpose of data analysis or simulation and modelling of given properties the available commercial packages or free access programs are identified. Depending on the source of code, different packages may also produce simulated results with different levels of uncertainty which has to be taken into account when discussing results.

3-1 Processing of bulk $LuMn_xO_{3\pm\delta}$ ceramics

High purity oxide powders of Lu_2O_3 above 99.99% purity and MnO_2 supplied by Aldrich Co were selected for the study. The as supplied oxide powders stored in desiccators were dried at 120 °C for few hours before weighting the due amounts of the two oxides needed to formulate the nine different compositions of $LuMn_xO_{3\pm\delta}$ materials form x=0.92 to x=1.04 in steps Δx=0.02, and from x=1.04 to x=1.12 in steps of Δx=0.04 in the experimental plan. The mixed powders were hand milled in an agate mortar and pressed into cylindrical pellets of 10 mm diameter by uniaxial pressing followed by CIP- Cold Isostatic Pressing at 200 MPa pressure. The gridding and pressing into pellets with the same applied pressures was repeated for partially reacted samples after each of the intermediate steps in high temperature heat treatment described in the following.

To have the possibility of assessing the solid solubility limit of the $LuMn_xO_{3\pm\delta}$ solid solution and studying the properties in the full range of non-stoichiometry, samples for sintering were prepared with different Mn content in the range ($0.92 \leq x \leq 1.12$) in the total 9 compositions defined above. Based on the phase diagrams of hexagonal $RMnO_{3\pm\delta}$ [101–104] and considering the relevance of diffusion in solid state reactions and sintering, the plan for synthesis of the Lu-hexagonal manganite by solid state reaction and sintering was defined on three steps with isothermal holds at 850°C for 24 h, 1000°C for 12 hours, followed by a final step of sintering at 1300°C for 1 day (Figure 3-1), 5 days and 10 days in three separate batches of samples, respectively. The conditions adopted for the first set of samples with final step of 1 day sintering time at 1300 °C are often reported and can be found in the literature of the h-$RMnO_3$ oxides [37,105]. This set will provide room to compare the results of off-stoichiometric/stoichiometric ceramics in this work with available data mostly of stoichiometric compositions.

To find out the best annealing time for h-$RMnO_3$ ceramics among published literature, there is only one work on sintering of $InMnO_3$ ceramics doped with Ga ions with 120

hours annealing time, the authors claiming to be adequate on providing very high quality ceramics for studying their properties [57]. In a private communication with O. M. Fedorova (from reference [101]) the sintering conditions used by this author on producing samples reported in the phase diagram of h-$LuMn_xO_3$ ceramics were referred to as 1400 °C annealing for about 96 hours. The second set of samples was synthesized under identical conditions of the first set but with sintering time extended to 5 days. In a latter phase of the works, the study on the solid solubility range and behaviour of lattice parameters of h-$LuMn_xO_3$ ceramics influenced by sintering conditions indicated that further increasing of annealing time to at least 10 days (third set of samples) was advised in order to confirm the properties determined in samples of previous sets and the evolution of grain size with time.

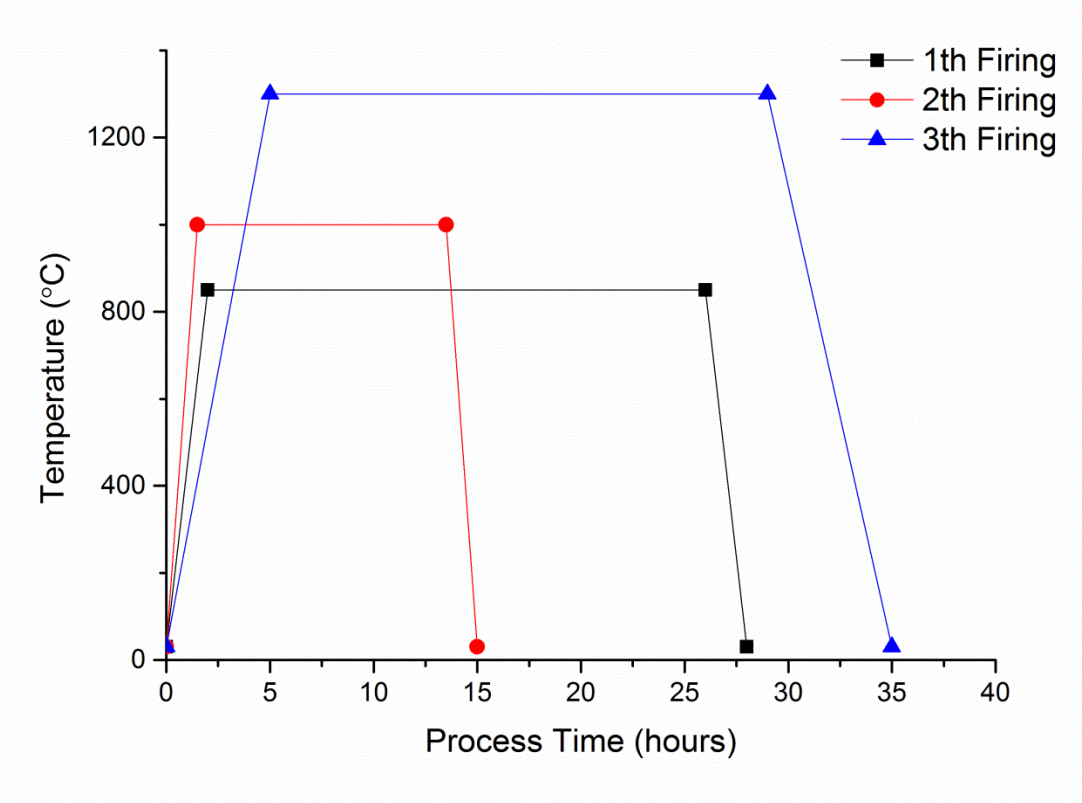

Figure 3-1. The diagram of processing temperature versus time of sintering for each step of firing of samples of one day annealing. For longer annealing time, the blue curve (3th firing) was extended to more 4 days (for 5 days annealing at 1300°C) or longer annealing time.

Equipment used for processing the bulk ceramics:

Uniaxial Pressing: Initial press, 2 MPa (CARVER Laboratory press machines); *Cold isostatic pressing*: Cold Isostatic Press (Auto CLAVE Engineering).

High temperature firing furnaces: Two furnaces were used for sintering of all pellets during PhD work one with maximum temperature of 1200 °C and another of 1500°C (Physics Department, University of Aveiro). These furnaces are of restrict use for annealing of ceramics superconductors and oxide materials only to ensure the cleanness of the furnaces from metal contaminations.

3-2 XRD phase characterization

The study of lattice parameters and phases present in the samples was done in two different XRD diffractometers with Cu ($K\alpha_1$ and $K\alpha_2$) sources and without monochromator. XRD spectra were measured with high counting and covering the range of $10°<2\Theta<80°$ or $10°<2\Theta<100°$, step of 0.013°. The samples for powder diffraction were prepared by grinding the pellets to fine powders. For each machine the LaB_6 powder with average size of 5 μm was used as a standard. The standard sample was measured to extract the parameters for the machine like asymmetry which contributes on the Rietveld refinement of the powders under study. To create the instrumental file containing shape functions and asymmetry values kept fixed during refinement of LuMnO3 samples the XRD pattern of LaB_6 standard was determined in the same experimental conditions as use for the samples.

Rietveld refinement was done using Fullprof Suit package 2.05, considering TCH pseudo-Voigt with axial divergence asymmetry for peak shape and the polynomial background model. The starting structure for the refinement was the corresponding CIF file available in the crystallography database, code ICSD 280779[29]. The refinement

proceeds by first refining the scale factor and background (6 coefficients polynomial function) and instrumental zero shift, then the lattice parameters and atomic positions and occupancy (just for the cations, the Mn and two Lu ions of different Wyckoff positions for occupancy and atomic positions), after the asymmetry correction, shape functions, grain size correction and finally adding atomic positions of oxygen ions. The grain size correction was introduced for 1 day and 5 days annealed samples of smaller grain sizes than 10 days annealed samples. The occupancy of four oxygen ions was refined after getting an acceptable reliability factor less than 5 (χ^2). Testing the influence of changing oxygen occupancy on Rietveld refinement corroborated the expected supposition that fluctuations in refinement of oxygen occupancy are of low physically relevance, as XRD is not enough sensitive to light elements such as the oxygen in order establish their occupancy within acceptable accuracy in comparison to the cations present in the same lattices [106]. The analysis on performing different cycles of the iterations and comparing the results of the refinement showed that the results have consistency on third or fourth decimal digits, depends on the quantity being determined: for unit cell parameters, the value with four digits after decimal point is repeatedly obtained even if one change some criteria to get convergence in Rietveld refinement procedure.

XRD diffractometers used in this study:

1- Philips XPERT XRD Diffractometer with Cu Kα source (CICECO, University of Aveiro). Main advantaged is the fast data acquisition, low background on high statistic of data acquisition. It is limited to room temperature measurements.

2- PANanalytical X´Pert PRO with Cu Kα source (Department of Materials and Ceramics Engineering, University of Aveiro). It offers the advantage of high temperature XRD measurements up to 1500 K with low background.

3-3 Electron microscopy techniques

The main challenge of performing transmission electron microscopy in TEM and STEM modes is preparing samples enough transparent for the electrons. Since the objective of on going through TEM/STEM analysis in this PhD work is to provide clear images of the atomic structures of the ceramics, diffraction pattern and EELS spectra of the interesting areas all in one experiment it becomes heavy dependent on the availability of thin edges in the TEM samples with enough stability for the analysis.

To prepare polished surfaces in order to determine the phases and grain sizes of the ceramics by SEM and energy dispersive spectroscopy EDS the same mechanical polishing as done for TEM sample preparation was taken. However, due to sensitivity of the EBSD technique in SEM to the perfection of surface lands after tilting the sample surface by 70°, it was necessary to finish the mechanical polishing with colloidal pastes or with lapping papers of very fine grit sizes. From the experience gained one came to the conclusion that ion milling as done for TEM or simply using the TEM thin sections for EBSD with a special sample older for SEM further improved the detectability of particles of second phases with submicron sizes by EBSD [107].

3-3-1 Methodology for preparation TEM thin sections

To overcome issues of preparing TEM thin sections of due quality, time was invested on sample preparation using methods often recommended for this purposes such as the cross sectional kit of Gatan model 601.07. However, finally we came up with a working solution based on more common sample preparation procedures of mechanical polishing and ion milling using dummy silicon slabs glued to sample that proved to be a simpler and less expensive option. The details of implementation of the method are given in the following.

The essentials of the method of TEM thin section preparation were learn from the experience of staff in Microscopy Group of Fritz Haber Institute, Berlin. The list of in-house facilities used for sample preparation is given below. The preparation starts by grinding and milling the pellets to convert them to fine powders. Experience showed that using a piece of pellet resulted in some irregular artefacts during ion milling because of the topography on the surface of the ceramics. These artefacts degrade the performance of microscopy work for HRTEM and EELS studies. However thin sections prepared from a piece of pellets were used for the investigation of grain boundaries between two neighboring particles or in the search of particles of the secondary phases. For the samples sintered 10 days the grain size is large enough to facilitate the TEM section preparation of pellets. In this case, some samples were prepared as a piece of pellet glued to dummy Si to control the thickness of the sample during mechanical polishing. For the powders, the powders were embedded into microscopy resins (G2 bond, M bond or UHU), and then two dummy silicon slabs were glued together using the prepared mixture of resin and powder of the sample. After curing, the prepared sandwich was mechanically polished down to 10 μm or less, the thickness being evaluated by the color of silicon made transparent (red color for 10 μm thickness or yellow color for thinner section). For diamond polishing, lapping papers were used in sequence of 30, 15, 9, 6, 3 and 1 μm particle sizes. Mechanical polishing was done on both sides of the prepared sandwich, on the second side it is done down to silicon transparency (red color of silicon in Figure 3-2.a).

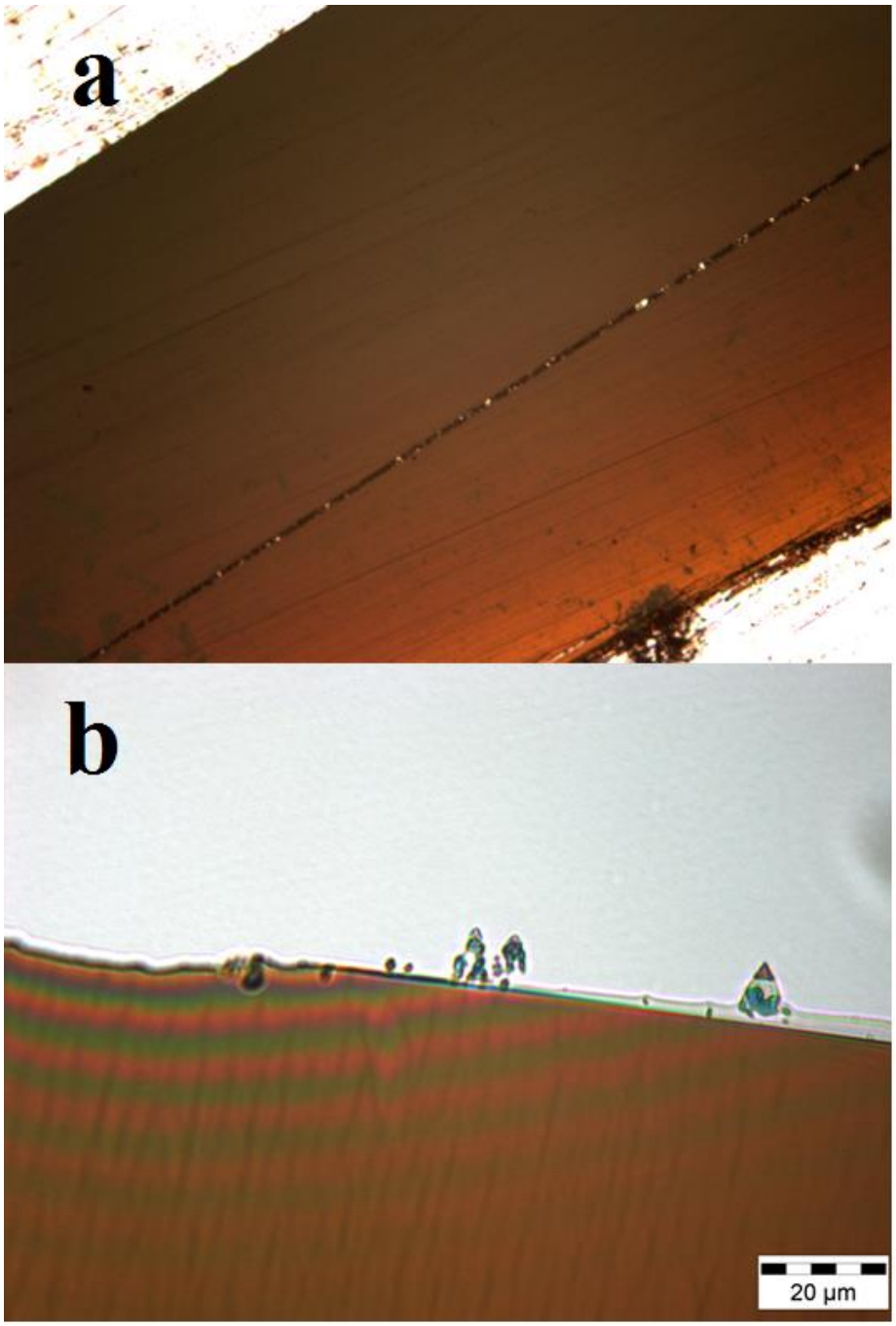

Figure 3-2. (a) Optical image of cross-section sample prepared for TEM study by mixing powders in proper Microscopy glue, brushing on a dummy silicon surface and putting second dummy silicon on the top. (b) After ion milling and removing one dummy silicon (intentionally by using single mode ion milling) there are few particles thinned enough for TEM on the edge faced to the vacuum. The glue between particles and dummy silicon is used for focus and stigmatism corrections during Microscopy.

Final step of thinning to electron transparency was made by gentle ion milling of the samples. The Ar ion energy starts from 5 keV (10 min.) then is successively decreased to 4 keV (20-40 min.), 3 keV (10-20 min.), 2 keV (10 min.) and finally to 1 keV (10 min.) with fixed angle of 4° for both, the top ion gun and the one from bellow (thin particles in Figure 3-2.b). As an option of the PIPS equipment, the ion thinning can be done either in single mode or in double mode. In single mode, ions hit the sample once in each revolution of sample. In double mode, each ion gun is activated twice pre revolution of sample. Experience showed that using the option of double mode modulation created unwanted artefacts on thin edges of the particles under study. Therefore single mode option was always used in the first steps of ion milling with high energy of the Ar beam. Only in the final step of ion etching at low energy (1 keV) was the double mode used to remove the surface damaged region on the edge of thin sections created by ion thinning at higher energy. Copper grids and copper rings are most commonly used to hold TEM samples. It was shown that the use of copper rings resulted in re-deposition of copper on the surface of the thin sections coming from hitting the ring by Ar ions during ion milling. Because the etching rate of Mo or Ti rings by the Ar ions is lower than for copper, mostly Mo rings were used to reduce re-deposition. All samples before TEM analysis were passed to plasma cleaner to remove surface contaminations.

Equipment and mounting materials used for preparing TEM thin sections:

1- Wire saw (WELL 3241)

2- Two polishing/grinder units: METASERV 2000 and PACE Technologies Nano 1000T Grinder/Polisher.

3- Dimple Grinder Gatan model 656

4- Gatan Cross Section Kit model 601.07000

5- *M-bond, G-bond No.*601 *and UHU* (PLUS SCHNELLFES) *glues*, their use depends on the preparation steps

6- Homemade Tripods for holding the samples during mechanical polishing

7- Gatan Precision Ion Polishing System (PIPS) dual milling model 691

8-Nanoclean Plasma cleaner model 1070 (4 min. under 50 W power of plasma)

9- Dummy silicon, CrysTec, P-type, 1-20 Ωcm, (100) orientation

3-3-2 Sample preparation for SEM

Polished surfaces for the EBSD analysis in SEM have to be flat, free of mechanically smear layers and of ploughing traces due to fine scratching by hard abrasive particles. They must also have very low roughness because it tends to cause shadowing when the sample is tilted 70° degrees in relation to the electron beam. In order to make polished surfaces of the $LuMn_xO_{3\pm\delta}$ ceramics ready for EBSD analysis, the same sequence of steps of grinding and mechanical polishing was done as for TEM sample preparation before the ion milling. However, due to sensitivity of the EBSD technique to the surface state it was necessary to end the mechanical polishing by using colloidal pastes or lapping papers with the particle sizes below the micron. The use of polishing pastes was abandoned as they tend to penetrate into the pores and cracks on the polished surface of samples. Instead, very fine polishing with the diamond lapping papers of 0.5, 0.2 and 0.1 μm grain sizes was adopted to get very flat surfaces of the ceramics generally meeting the demands of the EBSD technique.

Also in order to be able to study the same area of sample both in SEM and TEM, thin sections already prepared for TEM were used in SEM/EBSD with a special sample holder adapted for TEM grids in SEM Hitachi SU-70 microscope. A thin carbon coating was

applied on all samples of LuMnxO3±δ before doing the SEM to make surfaces enough conductive avoiding accumulation of the electrical charge because in EDS mapping or EBSD the region of the sample being analysed stays long time for more than an hour under exposure to the electron beam.

3-3-3 TEM/STEM and SEM microscopes used for microstructural analysis

Selected samples were analysed with Philips CM200 FEG electron microscope equipped with the GIF camera for EELS spectra of the regions of the interest in HRTEM images, by choosing an electron lost energy range to have both oxygen K-edge and Mn L3,2 edges, with the energy resolution of 0.8 eV and dispersion of 200 μV/ch.

Most samples were studied by JEOL JEM2200FS FEG TEM/STEM electron microscope using the electron gun energy of 200 kV, equipped with Omega filter for filtered energy TEM imaging and EELS in TEM mode and the EDS detector. The EDS analysis was done in STEM mode using 0.2 nm beam spot as the ultimately fine spot of this microscope.

In both TEM microscopes, all HRTEM images were taken by introducing 10 eV energy slit to filter out the high angle scattered electrons and enhancing the contrast.

None of the main TEM/STEM microscopes widely used during PhD work had C_s-corrector and sub-Å resolution or energy monochromator for better resolution in EELS. By special courtesy of FHI/MPI Berlin and of International Iberian Nanotechnology Laboratory- INL, Braga, Portugal, sessions were arranged in 200 kV Cs corrected microscopes *JEOL JEM-ARM200F* FEI Titan respectively that became essential for the direct observation displacements of Lu ions as need to resolve upward or downward polarization of the ferroelectric domains.

Main characteristics of TEM microscopes of general for the works of the PhD thesis:

1- LaB_6 Hitachi TEM H-9000NA 300 kV TEM/STEM microscope with BF STEM detector, of ultimate point resolution 0.20 nm at 300 kV in TEM, equipped with a 4 Mp digital camera and EDS detector from Bruker (Laboratory of Electron Microscopy, CICECO/DEMaC). Offers the advantage of easy use, the high gun voltage 300 kV, less sensitive sample preparation compared to 200 FEG microscopes, large angle of double tilting holder. It limited to the only mode ADF-STEM and of lesser resolution.

2- JEOL TEM-2200FS 200 kV FE-TEM/STEM microscope equipped with in-column Omega Filter for EELS of 0.8 eV zero-loss resolution and filtered energy TEM image, BF/ADF STEM detectors, electron diffraction SAED and CEBD, EDS of Oxford, INCA system (Laboratory of Electron Microscopy, CICECO/DEMaC). Ultimate point resolution 0.19 nm in TEM, 0.20 nm (BF) and 0.13(6) nm (ADF) in STEM. It offers several advantages: the high resolution with the SFEG in conventional TEM/STEM, omega filter for EELS and energy filter imaging, BF/DF STEM imaging, light element EDS detector and EDS mapping. The disadvantages are the more complex alignment of the electron beam for each image mode of microscopy and smaller tilt angles of double tilt holder. As in all HRTEM imaging it demands very careful TEM thin section elaboration.

3- Philips CM200 FEG TEM/TSEM 200 kV microscope with maximum resolution of 0.18 nm, equipped to GIF camera (Tridiem) and EDS Genesis 4000 unit. (FHI, Berlin, http://www.fhi-berlin.mpg.de). In high resolution in TEM, post-column Gatan Camera for EELS and energy filter imaging, EELS spectroscopy presents a true advantage and makes operations much easier than omega filter in JEOL. There are however some disadvantages for the advanced user: not efficient STEM, not as robust for image filtering and less efficient for EDS.

C_s/probe - corrected TEM/SEM microscopes used in exploratory sessions by special courtesy of FHI/MPI (Berlin) and INL (Braga):

4- JEOL JEM-ARM200F cold FEG TEM/HAADF-TSEM 200 kV microscope with C_s-corrected condenser and objective lenses, maximum resolution of 0.11 nm in TEM and 0.08 nm in STEM, with HAADF, ADF, ABF, BF detectors, equipped with Quantum GIF, Gatan ultrascan 4000 camera, and EDS detector. (FHI, Berlin, http://www.fhi-berlin.mpg.de).

5- FEI Titan 200 kV ChemiStem 80-200 kV FEG TEM/HAADF-STEM with probe C_s-corrector, TEM, BF/DF-, HAADF-STEM, EFTEM and EELS modes, Super-X EDX System. Ultimate resolution at 200 kV of 0.08 nm in STEM and point resolution of 0.24 nm, information limit of 0.11 nm in TEM (INL, Braga, Portugal, http://inl.int/equipmen)

Main features of the SEM microscopes of general use in the works of the PhD thesis:

1- Cold FEG-SEM Hitachi S4100 equipped secondary electron and backscattered electron detectors and Rontec light element EDS system (Laboratory of Electron Microscopy, CICECO/DEMaC). Acknowledged advantages are the high brilliancy of the electron beam and easy use. The low signal-to-noise ratio of the EDS system in comparison with more recent technology constitutes a relative disadvantage as longer time is needed for EDS analysis.

2- SE-FEG-SEM Hitachi SU-70, with Schottky thermal field emission gun, equipped with QUANTAX-400 EDS, Bruker CrystAlign QC400 EBSD systems, Raith ELPHY Plus electron lithography and Hitachi low voltage BF/DF STEM detectors (Laboratory of Electron Microscopy, CICECO/DEMaC). High resolution, fast EDS detector, EBSD and STEM options constitute advantages in the perspective of the work to be developed in this study. The higher complexity of this SEM infrastructure and the refined quality of the finishing of the polished surfaces required for the EBSD analysis are limitations to full use of the potential of the techniques installed in this SEM microscope.

3-4 AFM/PFM microscopy

Imaging of ferroelectric domains of ceramics samples using piezoforce microscopy PFM also needs polished, flat surfaces. A previous study of h-$RMnO_3$ thin films showed that the PFM response of the surface of the thin films is not disturbed by scratches with 4nm depth or dust particles with sizes of 20 nm [108]. However in case of ceramics with porosity and different grain topologies, more careful surface preparation is demanded. Damage on the surface of the sample due to excessive polishing may induce stress/strain states with consequences on the PFM response of the surface. The experience gained by dealing with some samples indicated that the best PFM response can be achieved where the RMS value of the roughness of the surface is less than 20 nm. Therefore, surfaces were mechanically polished using fine diamond lapping papers starting with 6 μm grain size and ending with 0.5 μm grain size lapping paper. The time of polishing was kept short as much as possible to avoid surface alterations. The surfaces were carefully controlled under optical microscope during polishing for the reduction of scratches.

NT-MDT NTEGRA PRIMA or NTEGRA AURA modular sensor force microscopes were used for AFM/PFM measurements at room temperature in contact mode with 10 V AC voltage and 50 kHz frequency on the tip. Cantilevers from NanoSensor Co., Pointprobe-Plus Silicon-SPM-Sensor made of n^+-doped silicon coated by Al on the detector side with the tip height of 10-15 microns and 10 nm tip radius were used for all measurements. Before the essays, all samples were heated to 130°C for few hours to eliminate surface humidity. Silver paste was brushed on the bottom of each sample as electrode to provide electrical contact between the sample and the AFM cell.

For some PFM measurements when also estimation of piezo response coefficient was feasible, contact mode was used with 10 V as voltage, 50 kHz frequency, 10 ms time constant. Silicon tip with tip curvature radius of 10 nm, height of 15 μm and Au coating on the reflective side from NT-MDT, Golden Silicon Probes (L 1462) was used.

3-5 Magnetic measurements

Sample preparation: In order to do magnetic measurements, the pieces of the ceramics were grinded to become fine powders. Then some amount of the powder was filled into a small gelatin capsule, wrapped with kapton tape to protect the instrument against contamination.

Magnetization measuring sequences: For temperature dependent zero-field cooled ZFC magnetization (M), the cycle was initiated by cooling the sample down to 5 K without any applied magnetic field. Then after stabilizing the temperature for few minutes, the heating cycle was start with the sample under applied magnetic fields (H) of 100 Oe or 500 Oe and the magnetization measured, the process being brought to room temperature or above. To measure magnetization in the field cooled FC cycle, the sample is cooled down again to 5 K under the same applied magnetic field and the measurement of magnetization is repeated on heating the sample under the magnetic field. In all cases the magnetic transition either at T_N or for hausmannite phase was calculated by taking the first derivative of M(T) curve in heating cycle of FC measurements. Then imported to Origin pro 9 software, Peak find analyzer was used to find the minimum of transition, the baseline was defined by taking the second derivative and smoothing the data (Adjacent-averaging) in a region where the transition appears.

For field dependent magnetization M vs. H at constant temperature, measurements often start at room temperature and measuring of MxH cycles is done accordingly to schedule of temperature decreasing points from room temperature down to the low value of temperature predefined for set of measurements. The field cycling is typically ±5 T, ±7 T or ±9 T depending on the instrument. For most field dependent measurements, need to accurately measure the magnetic remnant and coercive fields forced us to define finer steps of field change below 3000 Oe for T< 45 K and 1200 Oe for T> 45 K in programming of performing Mvs.H cycles.

Magnetometers used for the present study:

1- VSM Magnetometer, Cryogenic (Physics Department). Advantages: Magnetic field up to 10 T, fast time of acquiring M-H cycles at fixed temperature. Disadvantages: long time for measurement temperature dependent magnetization, noise level (sensitivity worse than 10^{-5} emu), mounting sample more difficult and temperature range limited to 4-300 K.

2- MPMS SQUID magnetometer (IFIMUP/Physics Department, University of Porto). Advantages: fast measurement temperature dependant magnetization, wider range of temperature from 4 to 380 K, easy sample mounting, low noise (sensitivity ~10^{-7} emu). Disadvantages: long time for field dependant measurements and in DC mode only.

3- QUANTUM Design SQUID MPMS3 (Physics Department). Advantages: Both DC/VSM measurements simultaneously made, fast measurements of temperature dependent and field dependant magnetization, the range of temperature from 1.8 K to 400 K, easy sample mounting, low noise, high resolution of detection of the magnetic signal (sensitivity <10^{-8} emu). Disadvantages: Careful sample encapsulation and mounting required to take advantage of the higher sensitivity of the equipment a very recent installation with the needed to be calibrated for holders used in each specific measurement.

Since most magnetic measurements of the PhD thesis was done using this magnetometer, also some of the previously measured samples were repeated using this SQUID machine, the test run was carried out on the holders without sample to assess the magnetic contribution of the holder like brass holder which is used for all measurements done in this magnetometer.

3-6 Dielectric measurements

Before measurement of the dielectric constant and imaginary part of permittivity, Au electrodes were deposited on the opposite surfaces of the samples by dc-sputtering. The POLARON E5000 plasma coater with 1.2 KV voltage and 12 mA current for Ar ions was used for coating with gold both sides of the samples.

Dielectric measurements were done using LCR meter with frequency range from 100 Hz to 1 MHz in a closed-cycle cryostat cooler allowing cooling of the sample down to 10 K. The temperature controller Oxford iTC that is used has precise control of temperature to within 0.1 K. The Precision Impedance Analyzer Agilant 429A was used for ac measurements. The software was programed for measuring the impedance parameters, amplitude and phase, in the frequency range of 100 Hz to 1000 kHz in temperature steps of 10 K from 13 K up to room temperature. From the two measured parameters the dielectric constant (ε´) and imaginary part of permittivity (ε´´) will be calculated.

3-7 Software for data analysis and simulation

1- *Visualization of crystalline structures:* VESTA 1.3.8 and CaRIne Crystallography 3.1 were used to simulate and create visualizations of crystal structures, also to simulate single-crystal and powder diffraction patterns and in calculating some parameters of the structures such as interionic distances and bond angles. Results of Rietveld refinement extracted from XRD data can be visualized with VESTA 1.3.8 where bond lengths and bond angles then can be calculated on the visualize structure.

2- *TEM based techniques*: TEM/EELS image recording and data acquisition were done both using proprietary Gatan Digital Micrograph 1.84.1282. Image processing to reduce the noise and to subtract the background from EELS spectra were also performed using

Gatan package. The details of the data analysis which are important for white line ratio of the Mn $L_{3,2}$ edge in EELS will be given in section 6-4-2.

3- *TEM image simulation:* The simulation HRTEM images was done using proprietary JEMS package and Multislice approach embedded in the package, by introducing the relevant crystal structure obtained from XRD Rietveld refinement of the given samples. Depending on the TEM microscope used to acquire specific image, a set of experimental parameters such as energy of electron beam, energy spread of the gun, values of the spherical C_s and chromatic C_c aberration coefficients, the half angle value for incoming electrons to the sample was inserted into program. The kinematical diffraction pattern simulation was often carried out in JEMS for relevant cases in this study. The supercell approach implemented in JEMS was used to build large structures and introduce line defects or vacancies to simulate their effects on the TEM image.

4- *DFT Simulations*: In order to interpret the oxygen K-edge of EELS spectra and to get the energy of unit cell for each value of composition x, the Wien2k 14.2 package was used. This application and general criteria for each calculation will be discussed in more detail in relevant parts of chapters ahead of this thesis. In general, after getting convergence in the energy (0.0001 Ry), the programs TELNES, QTL, BerryPI and Supercell were used according to needs. Most simulations were done on *Flamingo* computing cluster of CICECO Institute of University of Aveiro. In the beginning of the work access to Wien2k 14.2 package was granted by Microscopy Group to use the computation facility in Fritz Haber Institute.

5- *TEM/STEM EDS analysis*: Proprietary INCA Suite 4.09 Software for acquiring EDS spectra and performing line EDS or element mapping implemented in JEOL TEM 2200 FS was used to acquire EDS spectra in STEM mode and do off-line analysis of the same spectra.

6- *SEM EDS and EBSD analysis:* Proprietary Esprit 1.9 package was used to acquire EDS/EBSD data. The off-line analysis of the EDS data and also EBSD data were done using the same software package.

7- *XRD data analysis:* Open access Fullprof Suite 2.05 was the only package selected for XRD diffraction analysis and Rietveld refinement, visualizing the crystal structures, producing CIF files and in calculating the instrumental contributions for XRD of the diffractometers machines used in the present study.

8- *Phase transition, symmetry analysis*: Some of free software packages from Bilbao Crystallographic Server namely the Amplimode (calculate amplitudes of symmetry modes after phase transition), Symmodes (primary and secondary modes relation), Pseudo (find the parent structure of a subgroup) and so on were used.

9- *AFM/PFM image processing*: WS×M 5.0 free package was used to carry out image processing, data analysis and noise reduction of the AFM/PFM data. As complementary software, Image Analysis 3.5.0.13365 NT-MDT was used to calculate the piezoelectric coefficient for selected samples.

10- *Data analysis*: OriginPro and Microsoft Excel 2010 were generally used to analyze and plotting data and to write short iterative programs for least square fitting.

4. Lattice behaviour of $LuMn_xO_{3\pm\delta}$ ceramics and effect of sintering

The microstructure of the sintered ceramics and their crystalline unit cells are investigated in this chapter by means of XRD and SEM techniques. As in the case of the self-doped $YMnO_3$ ceramics [17], it is expected that Lu vacancies or Mn vacancies impose forces to the crystalline lattice of hexagonal $LuMn_xO_{3\pm\delta}$ that altered unit cell in a detectable way. The approach to equilibrium conditions during sintering does allow the atoms inside the unit cell to move further with time or temperature of annealing towards more regular filling up of corresponding Wyckoff positions of the $P6_3cm$ space group. However, changing sintering conditions may produce intermediary second phases or contribute to eliminate them if early formed during the reactions of synthesis, hence it may affect average composition and the homogeneity of composition the hexagonal $P6_3cm$ main phase. The study of the lattice parameters in the off-stoichiometric range of the $LuMn_xO_{3\pm\delta}$ solid solution is done by XRD and subsequent Rietveld refinement. Changes in microstructure with composition and sintering time are investigated by SEM as a complementary tool to XRD, allowing assess of grain size evolution at the fixed temperature of 1300 °C set for the final step of the synthesis process.

4-1 XRD Analysis of the lattice parameters

The lattice parameters and crystalline structure of all sintered samples were determined by XRD analysis. Rietveld refinement was done using Fullprof Suit package 2.05 with the details of the refinement steps and experimental considerations given in Chapter 3, section 3-2.

4-1-1 Crystalline lattice constants from Rietveld refinement

Table 4-1, Table 4-2 and Table 4-3 list the results of Rietveld refinement for lattice parameters, reliability factors and the crystalline phase fraction in the $LuMnO_{3\pm\delta}$ ceramics of 1 day, 5 days and 10 days sintering at 1300 °C, respectively

Table 4-1. XRD Rietveld refinement results of the lattice parameters and secondary phases detectable in the powders of the samples sintered for one day at 1300^0C in the last firing step. All sample show $P6_3cm$ space group of the main phase. The identified space group for Lu_2O_3 and Mn_3O_4 phases are I a -3 and I 41/a m d, respectively.

x (set A)	0.92	0.96	0.98	1	1.02	1.04	1.08	1.12
a (Å)	6.0448	6.0420	6.0409	6.0417	6.0427	6.0374	6.0401	6.0363
c(Å)	11.3681	11.3674	11.3682	11.3679	11.3709	11.3654	11.3671	11.3653
V_c(Å^3)	359.74(2)	359.38(2)	359.25(2)	359.362(2)	359.57(2)	358.77(2)	359.14(1)	358.64(1)
Rf-Factor	1.98	4.03	2.64	4.08	3.31	2.2	2.79	2.14
Global χ^2	5.88	5.53	4.82	6.32	4.02	3.87	4.59	9
Fraction (wt%)	97.28	99.65	99.35	100	98.25	97.75	98.81	97.42
x_r	0.955	0.965	0.989	1	n.a.	n.a.	1.035	1.021
f_m fraction, (wt%)	2.72	0.35	0.65	-	1.75	2.25	1.19	2.58
Secondary Phase	Lu_2O_3	Lu_2O_3	Lu_2O_3	-	Mn_3O_4	Mn_3O_4	Mn_3O_4	Mn_3O_4
space group	I a -3	I a -3	I a -3	-	I 41/a m d	I 41/a m d	I 41/a m d	I 41/a m d
f_H*(%)	0.49	0.21	n.a	n.a.	n.a.	0.45	0.62	0.67

f_H-hausmannite weight fraction from XRD line intensity ratio.*

Table 4-2. XRD Rietveld refinement results of the lattice parameters and secondary phases detectable in the powders of the samples sintered for 5 days at 1300^0C as the last firing step.

x (set B)	0.92	0.94	0.96	0.98	1.00	1.02	1.04	1.08	1.12
a (Å)	6.0443	6.0432	6.0426	6.0416	6.0394	6.0384	6.0364	6.0372	6.0364
c(Å)	11.37307	11.37075	11.36994	11.36868	11.36771	11.36802	11.36716	11.36841	11.36720
V_c(Å^3)	359.829	359.627	359.526	359.371	359.073	358.971	358.711	358.841	358.709
Rp	3.88	4.26	4.18	4.08	4.46	4.5	4.33	4.25	4.48
Rwp	5.1	5.46	5.46	5.31	5.71	5.69	5.58	5.65	5.86
Rexp	2.64	2.17	2.55	2.56	2.61	2.65	2.6	2.95	2.56
χ^2	3.73	6.34	4.59	4.28	4.8	4.6	4.62	3.65	5.25
weight fraction (%)	98.75	99.35	99.56	99.98	100	99.39	99.67	99.23	99.38
x_r	0.935	0.948	0.966	0.980	1.00	n.a.	1.028	1.051	1.096
f_m fraction, (wt%)	1.25	0.65	0.44	0.02	-	0.61	0.33	0.77	0.70
Secondary Phase	Lu_2O_3	Lu_2O_3	Lu_2O_3	-	-	Mn_3O_4	Mn_3O_4	Mn_3O_4	Mn_3O_4
f_H* (%)	0.18	0.18	0.18	0.21	0.22	0.21	0.28	0.33	0.46
f_{H^+} (%)	0.003	no data	0.002	0.033	0.002	0.141	0.124	1.23	0.694

f_H-hausmannite weight fraction from XRD line intensity ratio.*

f_{H^+}-hausmannite weight fraction from magnetic susceptibility, χ.(section 5-3-1)

Table 4-3. XRD Rietveld refinement results of the lattice parameters and secondary phases detectable in the powders of the samples sintered for ten days at 1300^{0}C in the last firing step.

x (set C)	0.92	0.94	0.96	0.98	1.00	1.02	1.04	1.08	1.12
a	6.0440	6.0440	6.0438	6.0421	6.0401	6.0388	6.0366	6.0369	6.0364
c	11.37464	11.37321	11.37206	11.36885	11.36764	11.36851	11.36698	11.36719	11.36716
V_c	359.852	359.797	359.746	359.436	359.158	359.037	358.724	358.762	358.704
Rp	4.12	4.15	3.96	4.21	4.57	4.79	4.49	4.46	4.73
Rwp	5.31	5.4	5.23	5.41	5.84	6.11	5.74	5.59	5.93
Rexp	2.62	2.6	2.71	2.63	2.66	3.18	2.84	2.89	2.72
χ^2	4.12	4.32	3.73	4.23	4.81	3.7	4.09	3.74	4.74
weight fraction	98.71	99.41	99.73	100	100	100	99.31	99.25	99.4
x_r	0.936	0.948	0.964	0.980	1.00	1.020	1.014	1.052	1.097
f_m fraction (%)	1.29	0.59	0.27	-	-	-	0.69	0.75	0.60
Secondary Phase	Lu_2O_3	Lu_2O_3	Lu_2O_3	-	-	-	Mn_3O_4	Mn_3O_4	Mn_3O_4
f_H*(%)	0.19	0.21	0.13	0.25	0.25	0.23	0.23	0.41	0.30

f_H-hausmannite weight fraction from XRD line intensity ratio.*

Secondary phases identified in $LuMn_xO_{3\pm\delta}$ samples by XRD and Rietveld refinement are either the Lu_2O_3 for x<1.00 samples (Lu-rich side), or the secondary phase of Mn_3O_4 in the opposite side, x>0 (Mn-rich side), Table 4-1 to Table 4-3. The XRD profiles of x=0.92 and x=1.08 samples of 1 day annealing time are shown in Figure 4-1.a and b, respectively. When present in the x<1 samples, the Lu_2O_3 is clearly identified by the

corresponding (440) and (622) diffraction lines in the XRD spectrum, as in the inset of Figure 4-1.a. The secondary phase Mn_3O_4 is detectable by the (103) diffraction line of hausmannite, $2\theta=31.69°$, in samples of lager values of x on the Mn-rich side, although the peak intensity is faint and peak is broad and easy confused with background noise as shown in the inset of Figure 4-1.b. XRD spectra were also checked for other phases like Mn_2O_3, $LuMn_2O_5$ and $Lu_2Mn_2O_7$ but no matching of diffraction lines of these phases with Bragg reflections in the experimental XRD patterns could be found.

The difficulty on carrying secondary phase Rietveld refinement rises as peak intensity of the phase becomes weaker. In the present study such limitation on allowed to refine the scale factor and lattice parameters of the secondary phase, when present. For the x>0 side, the reliability factors of the lattice refinements are poor, so only the calculated weight fraction of the secondary phase is reported here in Table 4-1 to Table 4-3. Figure 4-1 display the Rietveld refinement of two samples selected from the set of 1 day annealed samples, also with the corresponding peaks of secondary phases identified in XRD patterns. The residuals of the refinements of the two samples in Figure 4-1 are low, but reliability factors like χ^2 close to or above 5, Table 4-1, may point to the presence to strain and dislocations in the lattice or slight off-positioning of some atoms in the unit cell from their Wyckoff positions coming from composition gradients. The limited reliability of the XRD Rietveld refinement of unit cells with off-stoichiometric samples of 1 day annealing time in Table 4-1 gave inception on performing new batches of samples with the longer annealing times of 5 and 10 days. Figure 4-2 displays the XRD profiles and performed Rietveld refinements of samples with the stoichiometric composition x=1.00 for the three values of annealing time, showing the goodness of fit based on the residual of Rietveld refinement.

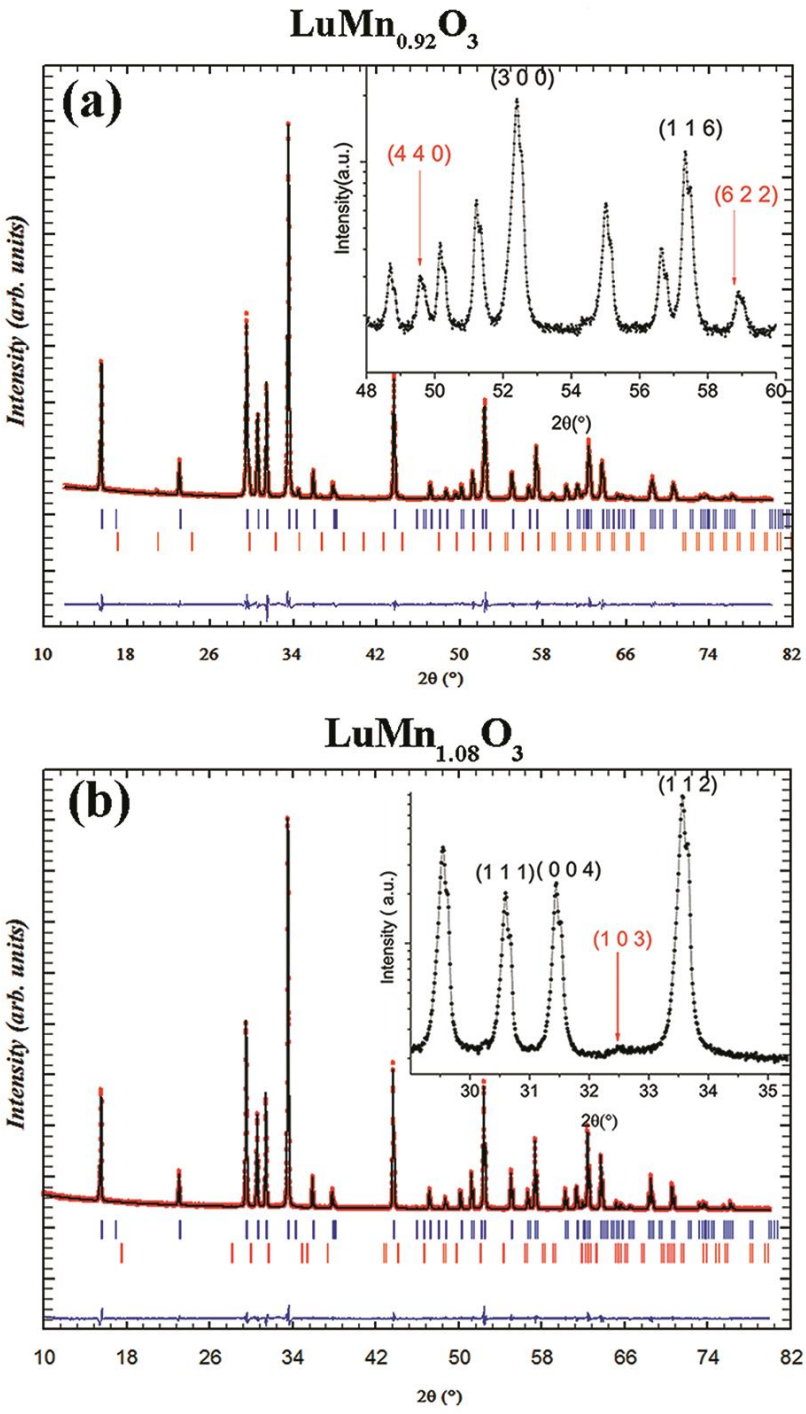

Figure 4-1. XRD data and Rietveld Refinement of the data of the $LuMn_xO_{3\pm\delta}$ samples x = 0.92 (a) and x = 1.08 (b) showing $P6_3cm$ space group of hexagonal $LuMnO_3$. Inset.a represents two peaks of Lu_2O_3 secondary phase of sample with x= 0.92 (2θ= 49.58°) and the inset.b shows the peak of Mn_3O_4 secondary phase for sample with x=1.08 (2θ= 31.69°).

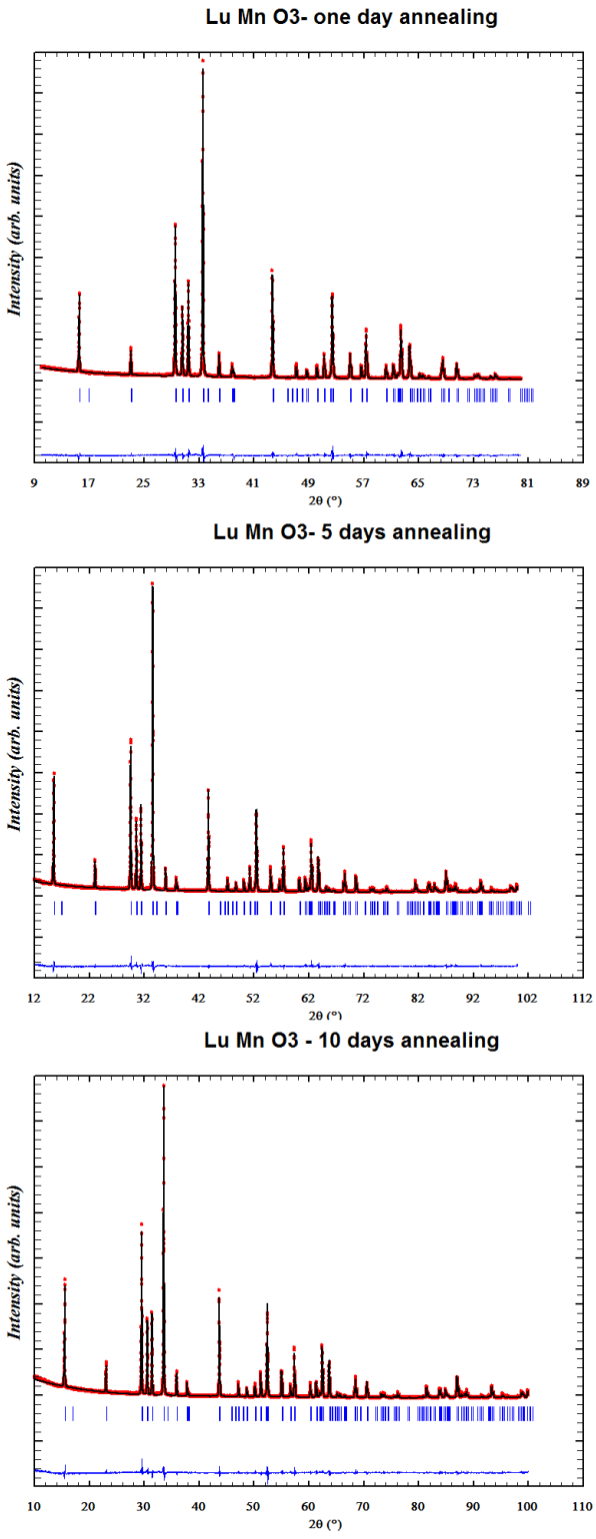

Figure 4-2. XRD Rietveld fitting of the sample $LuMn_{1.00}O_{3\pm\delta}$ after three different annealing time as written in each figure.

The behaviour of the samples annealed for 1 day confirmed how much the atomic position and even peak shapes had fluctuated in comparison to the results of the two other sets samples of longer time of annealing. Further discussion is given in the next section where the lattice parameters of samples of different sintering conditions are compared and discussed.

4-2-1 Crystalline lattice constants inside stability limits of h-$LuMnO_3$

The stability limits of hexagonal $RMnO_3$ manganites in a wide range of temperature in air and oxygen atmospheres were given in a set of publications of Fedorova and co-workers [94,95,101,103,109]. The summary with the lower (x_L) and upper (x_H) solid solution limits of h-$RMnO_3$ phases at 900 °C and 1300 °C is presented in Table 4-4. The solid solution limits of $LuMn_xO_3$ were determined from powder XRD results as the boundaries of composition where two phase fields were detected in the XRD results with the presence of a second phase a side of $RMnO_3$ main phase [95,101]. The publications of this set did not document the changes of lattice constants and other crystallographic parameters that should evolve with composition of $RMnO_3$ solid solutions [17]. However, such data are essential for modeling the dependence of properties the materials outside the strictly stoichiometric composition of $RMnO_{3\pm\delta}$ phases. To the author´s knowledge the only study available on the dependence of crystallographic parameters on the change of the Mn/R ratio in bulk hexagonal manganites is the one done in the Y-rich side of the $YMnO_{3\pm\delta}$ phase [17], also given in Table 4-4. In another study of MOCVD thin films of $ErMnO_3$ and $DyMnO_{3\pm\delta}$, the effects of off-stoichiometry on out-of-plane c-axis of the crystalline lattice showed that above a critical thickness the relaxed values of c-axis of the thin film become proportional to the R/Mn ratio, the compositions with larger Mn excess displaying the lower values of c-axis [18].

Table 4-4. Summary of the available data of solid stability limits of h-RMn_xO_3 oxides with their preparation method and maximum temperature of annealing. The result of the current study is also given in the table for comparison.

h-RMn_xO_3	**T (°C)**	**x_L**	**x_H**	**Criterion**	**Synthesis Route**	**time (h)**	**Reference**
$LuMnO_3$	900	0.94	1.03	XRD-single phase	Solid state reaction	several days	[101]
	1300	0.94	1.20	XRD-single phase	Solid state reaction	several days	[101]
	1300	0.95	1.04	Cell parameters	Solid state reaction	24	[91]
	1300	0.94	1.05	Cell parameters	Solid state reaction	120; 240	+
$YbMnO_3$	900	0.83	1.02	XRD-single phase	Solid state reaction	several days	[103]
	1300	0.83	1.20	XRD-single phase	Solid state reaction	several days	[103]
$ErMnO_3$	900	0.94	1.06	XRD-single phase	Solid state reaction	several days	[102]
	1300	0.94	1.12	XRD-single phase	Solid state reaction	several days	[102]
	850	0.88	1.39	c-axis (C_2)	MOCVD- 100 nm thin film	0.25 (O2)	[18]
$HoMnO_3$	900	0.95	1.02	XRD-single phase	Solid state reaction	several days	[102]
	1300	0.91	1.21	XRD-single phase	Solid state reaction	several days	[102]
$YMnO_3$	900	0.91	1.02	XRD-single phase	Solid state reaction	several days	[102]
	1300	0.88	1.09	XRD-single phase	Solid state reaction	several days	[102]
	1350	0.95	n.a.	Cell parameters	Pechini (citrates)	n.a.	[17]
	1450	n.a.	1.15	XRD-single phase	Solid state reaction	several days	[19]
h-$DyMnO_3$	850	0.93	1.40	c-axis (C_2)	MOCVD-50 nm thin film	0.25 (O2)	[18]

+ The results of the current PhD study.

Making use of the criterion of absence of second phase in XRD results of Mn-rich side of YMn_xO_3 bulk samples, the value of x_H=1.15 had been assigned to the upper stability limit of solid solution, Table 4-4.

The dependences of a-axis and c-axis and cell volume V_c on Mn/Lu = x ratio of the hexagonal h-$LuMn_xO_{3\pm\delta}$ phase in Table 4-1, Table 4-2 and Table 4-3 are plotted in Figure 4-3 (a, b, c), respectively.

The dependences of the same lattice parameters on the Mn/Y ratio of $YMn_xO_{3\pm\delta}$ for the high Y side ($x \leq 1$) from reference [17] are also plotted in insets Figure 4-3.(a, b, c) (secondary y-axis, with equal span of values). The relative variations of V_c of the hexagonal structure are twice more dependent on relative changes of a-axis than of the c-axis, the plots of V_c in Figure 4-3.c displaying trends similar to the plots of a-axis in Figure 4-3.a. The residuals of the Rietveld refinement of the XRD spectra of 5 day sintered $LuMn_xO_{3\pm\delta}$ samples are smaller than for those of 1 day sintered samples and the scatter of values of the corresponding lattice constants in Figure 4-3.a, b and c is also lower.

The composition x_r of the $LuMn_xO_{3\pm\delta}$ solid solution is calculated from the corresponding values of the nominal composition and the fraction of second phase (Lu_2O_3 if x<1, or Mn_3O_4 if x>1), the corresponding values being also given in Table 4-1 to Table 4-3. The root x_r is determined with the approach that the second phases Lu_2O_3 and Mn_3O_4 are stoichiometric and chemically pure. The equation to determine x_r can be univocally solved only with one secondary phase. It fails to deliver a meaningful solution in cases when the weight fraction of detected second phase(s) would lead to values of x_r in the off-stoichiometry side opposite to the one of the nominal composition x of the sample.

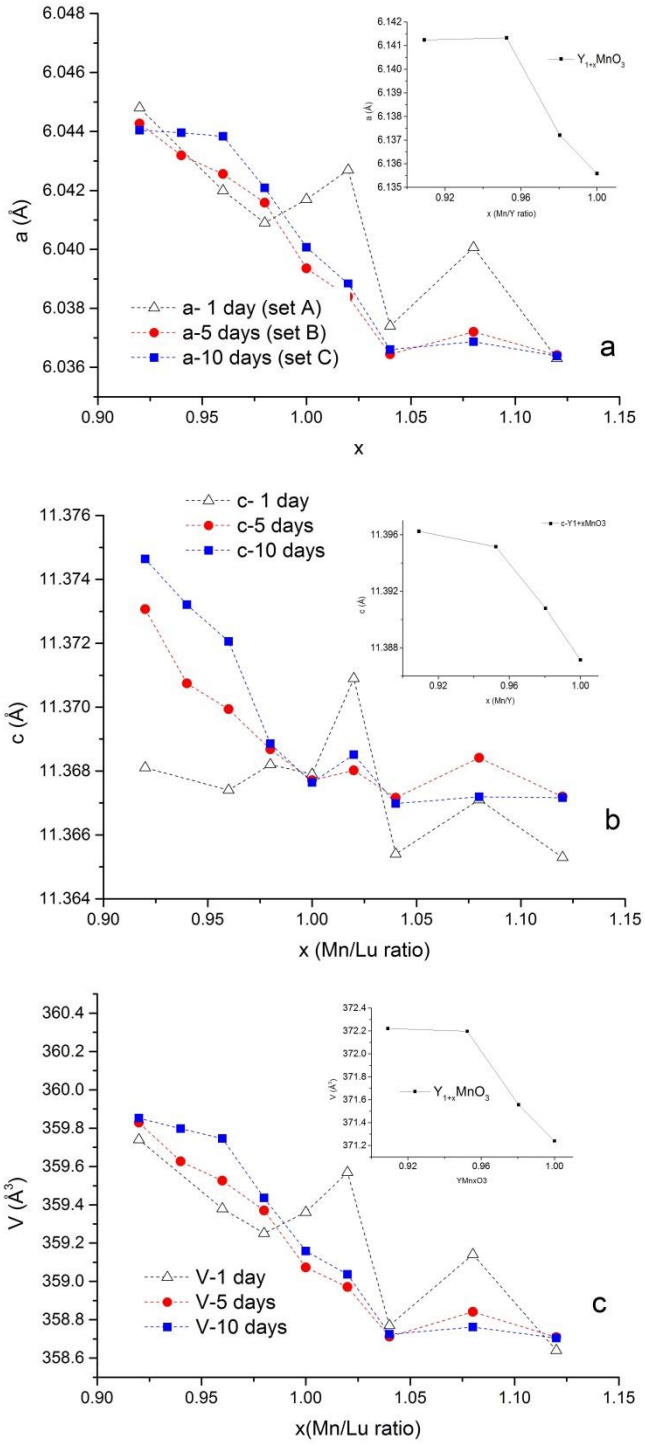

Figure 4-3. Dependence of the lattice constants on Mn/Lu = x ratio of the $LuMn_xO_{3\pm\delta}$ hexagonal manganite: (a) a-axis, (b) c-axis and (c) Cell volume V_c for different sintering conditions. Insets are the same constants of the $Y_{1+x}MnO_3$ ceramics for comparison [42].

The plots of weight fraction of second phases as a function of x_r for samples of 5 days and 10 days annealing time in Figure 4-4 indicate that the stability of the $LuMn_xO_{3\pm\delta}$ solid solution at 1300 °C is limited to the composition range x_L=0.936±0.001 ≤ Mn/Lu ≤ 1.052±0.001=x_H in the present study. The low stability limit x_L is taken as value of x_r of the two samples with maximum saturation of Lu_2O_3 (nominal composition x=0.92) coinciding with leveling of the corresponding values of a-axis and V_c in Figures 4-3.a and c. The value of the high stability limit x_H is taken as value of x_r of the two samples with net saturation of Mn_3O_4 (nominal composition x=1.08) and coincides with the leveling of all lattice parameters in the same Figure 4-3. The calculated weight fraction of Mn_3O_4 in samples x=1.12 consistent with the value of x_H≈1.05 above would be f_m=1.78 %wt, the triple of what was determined by Rietveld refinement (0.6-0.7 %wt), Tables 4-2 and 4-3. The apparent increase of x_H to the new value x_H≈1.10 determined from two x=1.12 samples has no correspondence in the values of the lattice parameters in Figure 4-3 and may result from inaccuracy of Rietveld refinement to determine such low fractions of second phases or some hausmannite in the amount of roughly 1 %wt might have reacted to form some unknown intermediary phase which remained undetected. The observed dependences of lattice axes and of V_c on the composition of $LuMnxO_{3\pm\delta}$ phase closely follow the trends reported for the Y rich side of the $YMn_xO_{3\pm\delta}$ system [17]. There is a nearly linear dependence of a-axis on the Mn/Lu ratio throughout the overall stability range of the $LuMn_xO_3$ solid solution and also of the c-axis but limited to the x<1.00 side. The trend shown by the values of c-axis in the Mn rich composition of $LuMn_xO_{3\pm\delta}$ is less clear. While the lower limit of solubility of the $LuMn_xO_{3\pm\delta}$ solid solution is close the value x = 0.942 previously reported [109], the upper limit of solubility of the present study stays well below the corresponding value of x = 1.198 reported in the same study, Table 4-4. The origin of such difference in Mn content of the main phase was investigated by HRTEM microscopy in the search for linear and planar defects of the crystalline lattice that may be present in the $LuMnO_{3\pm\delta}$ crystalline grains and could accommodate large excess of Mn [110] and it will be presented in following chapters.

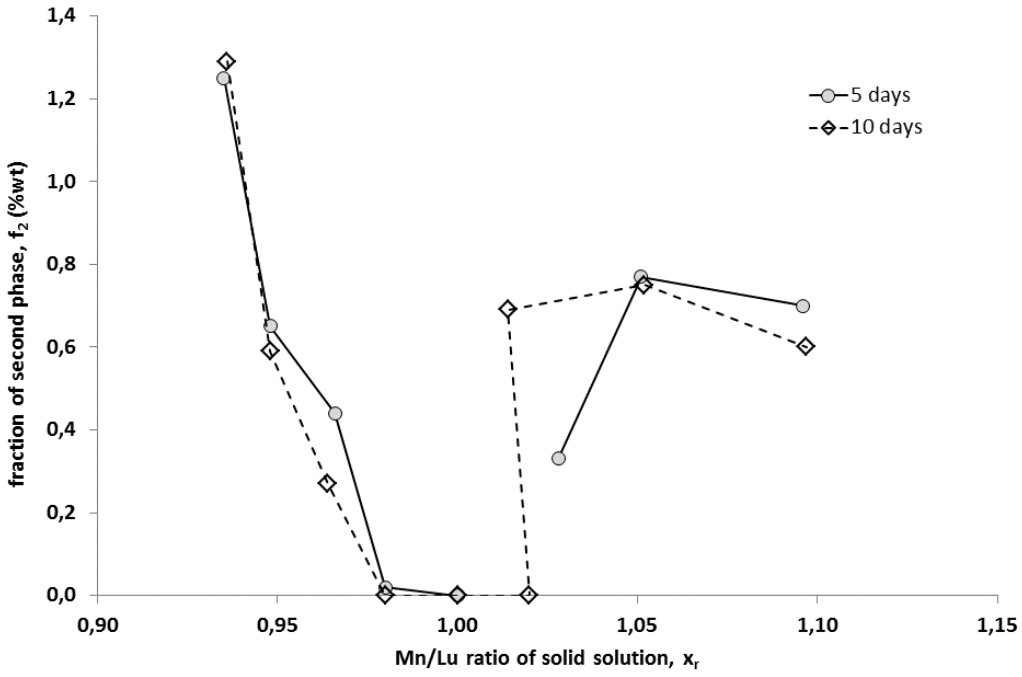

Figure 4-4. Weight fraction of second phases determined from Rietveld refinement of XRD data of 5 days and 10 days sintered samples of $LuMn_xO_{3\pm\delta}$.

Increasing annealing time was decided in order to get higher quality polycrystals [57] for the PhD work. Lattice variation in a-axis and cell volume in these samples of longer annealing time are now showing more visible the limit of solid solubility in the approximate composition range of $0.94 \leq x \leq 1.04$, as derived from 5 days samples, Figure 4-3. After 5 days annealing the straight plateau appears in the region of $x \geq 1.04$, indicating the limit of solid solubility in R-site vacancy region. Even the duplication of annealing time to 10 days allowing for ions in the lattice be relaxed to their minimum energy positions, or moving grain boundaries to assist the completion of reaction by sweeping through the volumes of the material did not change the lattice parameters for samples of $x \geq 1.04$. On the contrary, in samples with Mn-site vacancies, 5 days annealing could not completely stabilize the atomic structures which demanded longer annealing time to get such leveling plateau of a-axis and V_c values below $x<0.96$, Figure 4-3. In

general, the reliability factors of samples of 5 and 10 days annealing time do not show remarkable differences, Table 4-2 and Table 4-3, indicating that the atomic positions defined according to the space group and XRD peak shapes considered in the Rietveld refinement are adequate for both sets of samples. Figure 4-4 shows that on this side of sample composition the 5 days and 10 days annealed samples have almost identical behavior concerning the secondary phases. Rietveld refinement does not directly evaluate extended defects and dislocations inside the particles, but generally refine crystal cell parameters which may be connected to either stress/strain or grain size. Residual Lu_2O_3 secondary phase ($x<1$) which has better defined peak shapes than the Mn_3O_4 secondary phase ($x>1$), can be traced in XRD patterns, Figure 4-1.a. The broad XRD peaks of Lu_2O_3 in $x<0.96$ samples are probably indication of dispersed nano-particles of this phase in the sintered ceramics. Thin films of h-$RMnO_3$ oxides with off-stoichiometric composition developed nano-inclusions of the secondary phase of R_2O_3 at the film/substrate interface or in film [18,111].

Inspection of the faint (103) XRD line of Mn_3O_4 phase in the inset of Figure 4-1.b shows that it does not overlap with neighbor peaks of the $LuMnO_3$ phase. Accounting that this (103) XRD line is broad and poorly defined against background noise a different approach was used to make a straight estimate of Mn_3O_4 weight fraction. As shown in Figure 4-5 and Figure 4-6, polynomial forms of even order, n_p, with $n_p \geq 4$ were fitted to the XRD spectra in a fixed range of 2θ centered in the (103) Mn_3O_4 line ($2\theta \approx 32.5°$) to smooth the profile of the XRD peak. The difference of height between the maximum of the smoothed (103) peak and the straight line joining the two minima on each side of the peak was taken as a measure of peak intensity.

The relative height of the (103) XRD line was calculated by dividing the (103) peak intensity by the height of the (112) line of $LuMnO_3$ ($2\theta \approx 33.6°$) discounted for the background. The analogous procedure applied to h-$YMnO_3$ phase with the addition of 1.2 %wt of Mn_3O_4 in Figure 1.b of reference [90] yielded the peak intensity ratio $I_{(103)}/I_{(122)}=0.00642$. This value is used as calibration factor of the relative intensity

height of the (103) XRD lines to determine the approximate weight fraction of Mn_3O_4 detected in the $LuMn_xO_{3\pm\delta}$ samples given as f_H^* in Table 4-1 to Table 4-3. In the trend of the polynomial smoothed profiles of the (103) peak of 5 day annealed $LuMn_xO_{3\pm\delta}$ samples in Figure 4-5 one can always detect a maximum at the 2θ position of (103) line which suggests that there are at least traces of Mn_3O_4 in all samples of this set, even in samples of low Mn on the x<1.00 side. There is a neat increase of Mn_3O_4 content in samples of the same set with Mn excess, x≥1.04 when the upper stability limit of the $LuMn_xO_{3\pm\delta}$ solid solution is crossed. The analogous conclusions hold for samples of 10 day annealing time in Figure 4-6. For all compositions of the $LuMn_xO_{3\pm\delta}$ samples with 1 day annealing time in Figure 4-6 the detected amount of Mn_3O_4 second phase is always comparatively high and above trace levels.

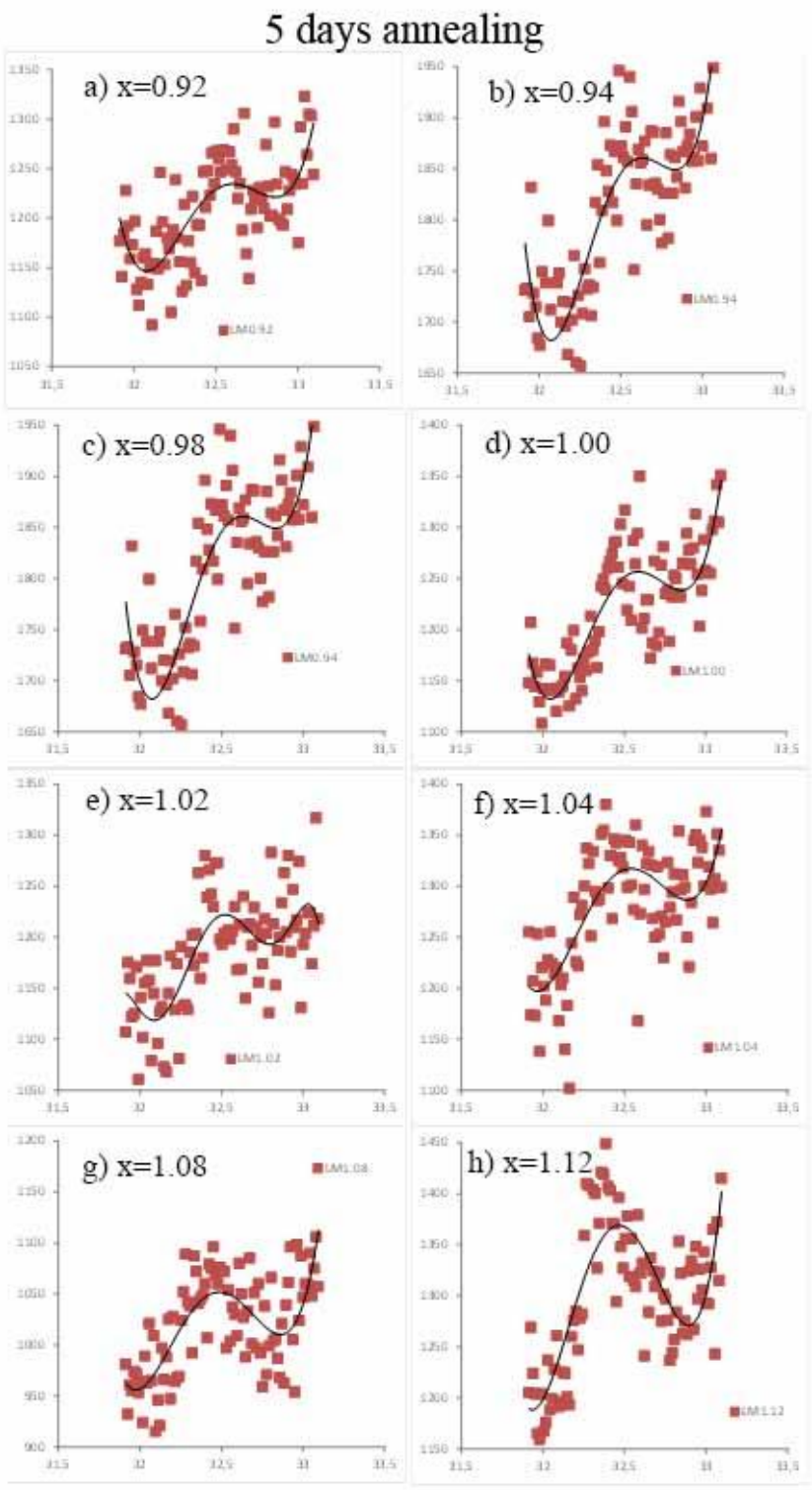

Figure 4-5. (103) peak of hausmannite secondary phase in XRD patterns of the samples after 5 days annealing.

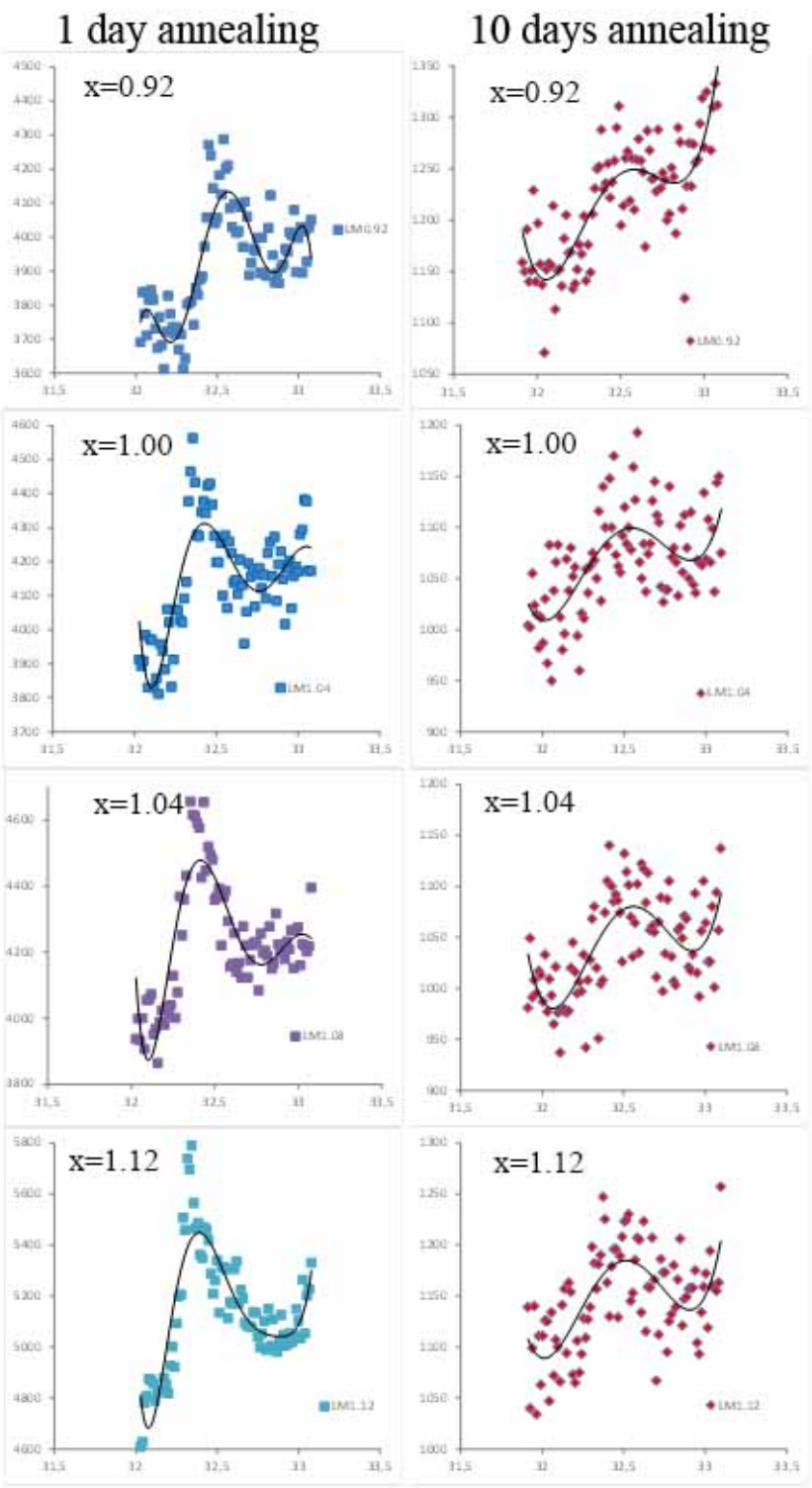

Figure 4-6. (103) XRD peak of hausmannite phase from XRD patterns of the samples after one day and 10 days annealing time showing decrease in the intensity of the corresponding peak after long time annealing.

4-2-2 R-site doped h-$RMnO_3$ materials

As implied by the results in Figure 4-3 the overall changes of unit cell axes of $LuMn_xO_{3\pm\delta}$ crystalline cells between solubility limits is minute, 0.14 % for a-axis and less 0.09 % for c-axis, the determination of their values being very sensitive to the accuracy of the XRD measurements and Rietveld refinements.

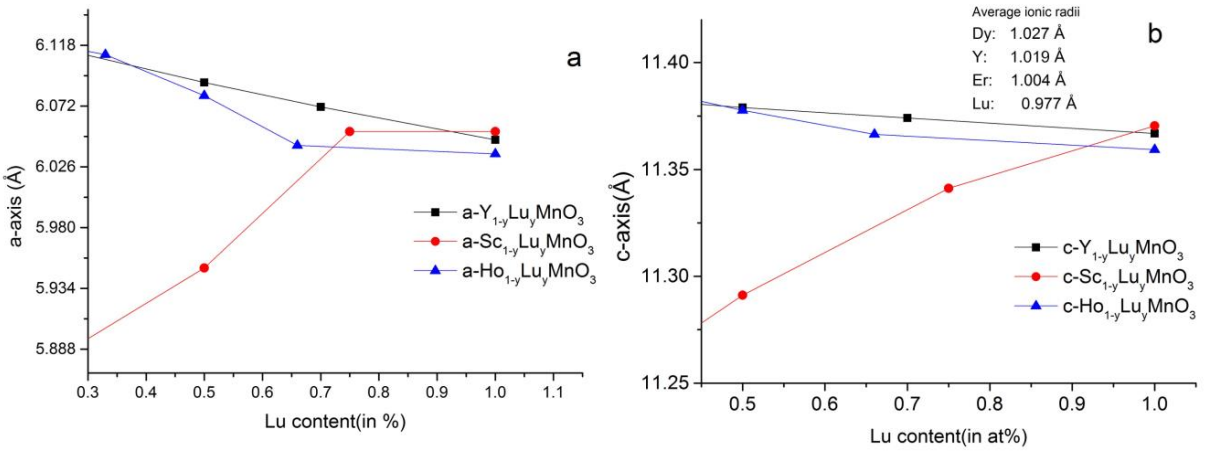

Figure 4-7. Data from bibliography on the change of (a) a-constant and (b) c-constant of R-site doped $Lu_yR_{1-y}MnO_3$ [34,72,112].

The interdependences of c-axis or a-axis of R-site doped $Lu_yR_{1-y}MnO_3$ for different solid solutions are plotted in Figure 4-7: co-doped solid solutions with stoichiometric Mn/R ratio [34,72,112]. The co-doped solid solutions (R, Lu)$MnO_{3\pm\delta}$ where R holds for Y, Sc and Ho systems show different trends in the changes of a-axis and c-axis lattice constants. Only dopants with the same charge valence of Lu^{3+} were chosen for this analysis in order to isolate the effect of ionic radius (size effect) of the dopants. Charge valence and size effect have been calculated and measured to be effective on changing the unit cell parameters and tilting of the MnO_5 bipyramids [113,114]. Doping with trivalent ions does not require any charge compensation [114]. Ion size effects were already studied

for both bulk ceramics and thin films of h-$RMnO_3$ oxides with different rare-earth ions with significant impact on changing the lattice parameters [24,115–117]. Increasing ionic radius is generally accompanied by expansion of a-axis and c-axis lattice parameters, with reducing of the buckling of planes of rare-earth ion in FE phase.

In Figure 4-7 the lattice constants for Sc-doping and for the Ho and Y dopants show opposite changes, due to differences of their ionic radii in relation to the Lu^{3+} ion. Ionic radii of Sc (0.87 Å) and Lu (0.977 Å) are smaller than the ones for Y (1.019Å) and Ho (1.015 Å), the substitution of the R_1 and R_2 rare-earth ions in case of Sc doping produces shrinkage of the lattice parameters. The later rare-earth ions have bigger ionic radius than Lu and Sc, when Lu content is being substituted into Y or Ho sites, the lattice also shrinks when the R-site is fully occupied by Lu ions. For Y-site doping of $YMnO_3$ with different rare-earth ions, it was calculated that the Sc and Lu doping are more energetically favorable particularly for Y_2 site substitution (Wyckoff position 4b) in comparison to Ho or other rare-earth ions with bigger ionic radii [114].

In the same analysis on the Y-site co-doped $YMnO_3$ system with Er, Dy, Lu in Figure 4-8 the dependency of lattice axes on average ionic radii of the both rare-earth ions implies that changes of c-axis in this system does not have the same trend for all dopants. The ionic radii of the rare-earth ions in each compound given in Figure 4-8.a, present a critical ionic radius for the behavior of the Y-site doped lattice of the $Y_yR_{1-y}MnO_3$, where the trend for change of a-axis is reversed. The graph indicates that Dy doping on Y-site has opposite trend in comparison to other dopants.

As we saw in Figure 4-7 for Lu site co-doping, Dy with ionic radius larger than Y, Er and Lu is expected to have different effect on lattice axis dimensions when it occupies the position of Y ions. On the contrary, the change of c-axis with co-doping displays a similar trend for all dopants, c-axis expanding as Y-content is increased, but presenting larger fluctuation for Er co-doping. Although not shown, for all $Y_yR_{1-y}MnO_3$ systems discussed here the unit cell volume, V_c is expanding as the Y-content increases except in case of Dy doping. One can predict that co-doping of Y-site with Ho will give rise to same behavior

of lattice as for Dy doping. It was shown in theory that Lu and Sc co-doping into $YMnO_3$ would be more energetically favorable than Ho and perhaps Dy [114]. The substitution of Lu or Y ions with isovalent dopants which have smaller or large ionic radius would force lattice to get contracted/expanded, respectively, especially as coordination number of R ions is 8 oxygen, the energy scheme of surrounding environment of the rare-earth ion in the RO_8 cage would promote lattice to respond to smaller or bigger sizes of doping of the R-site.

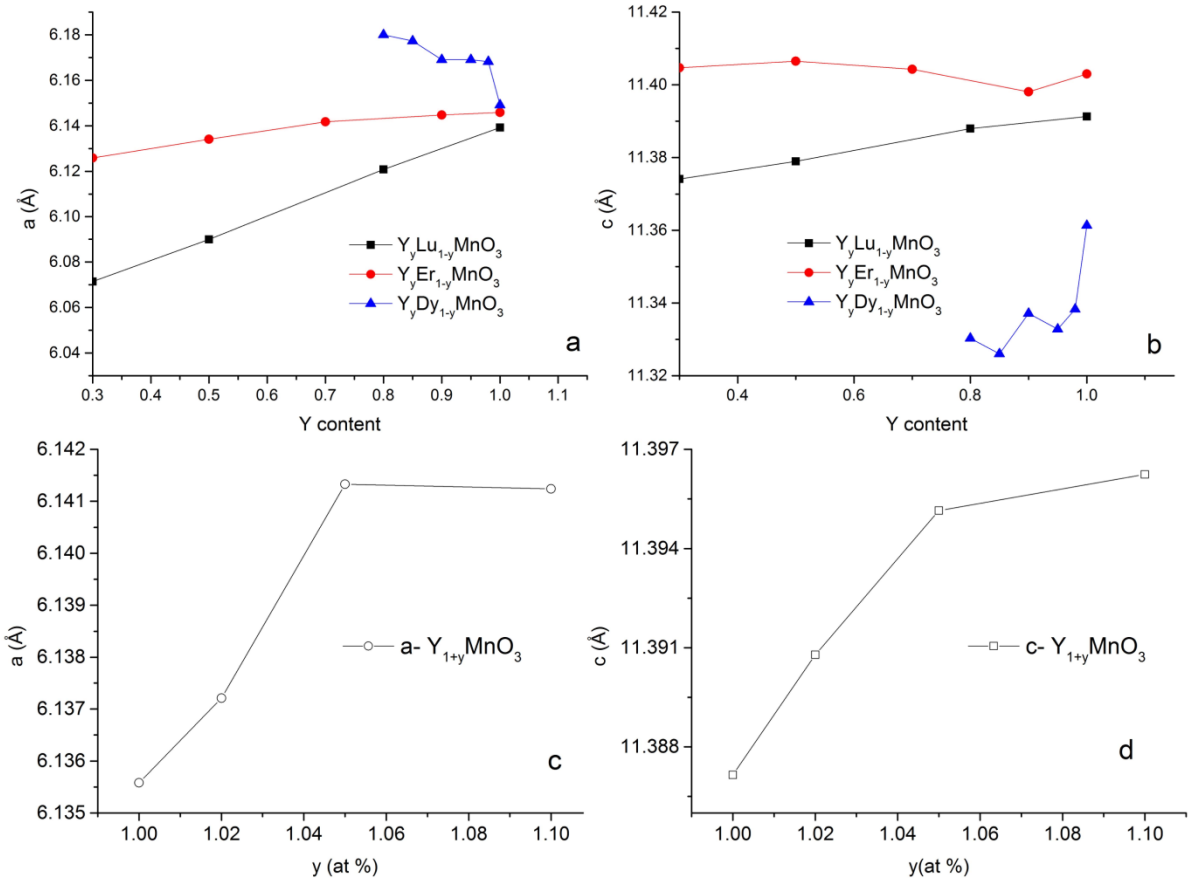

Figure 4-8. Change of the a-axis (a) and c-axis (b) of the stoichiometric R-site co-doped $Y_yR_{1-y}MnO_3$ materials [34,118,119]. a-axis (c) and c-axis (d) of Y-site self-doped $Y_{1+x}MnO_3$ was also given for comparison [17].

4-2-3 Mn-site doping in h-$RMnO_3$ materials

Mn-site co-doping of h-$RMnO_3$ materials either with trivalent dopants and vacancy doping, or self-doping are reviewed in this section. As before the study of co-doping is restrict to trivalent ions of the same valence of Mn^{3+} ion [113,114] unless the valence of the transition metals had changed due to adjustments of oxygen stoichiometry. This scenario is closer to self-doping of RMn_xO_3 oxides. Metal dopants for the Mn site are In^{3+}[120], $Cu^{2+}V^{4+}$ and $Cu^{2+}Ti^{4+}$[121], Fe^{3+}, Cr^{3+}[70], Al^{3+}[68] and Ga^{3+}[122]. Figure 4-9.a gives the change of a-lattice for ceramic samples with the ionic radii of the dopants as shown in the figure. Clearly dopants with ionic radii larger than Mn^{3+} or very close to it such as Cr^{3+} (in 6 coordination number) cause expansion of a-lattice in proportion to the fraction of dopant that occupies positions of Mn^{3+} ions in the lattice, the same trend is valid for $LuMn_xO_3$ solid solution when Mn-site is self-doped with vacancies created on the Lu-rich side (x<1) in present study, Figure 4-7.b. In the cases of Al and Ga dopants of smaller ionic radii than Mn change the a-lattice is reversed in comparison to the cases above. Higher moduli of M^{3+}/Mn^{3+} ionic radius ratio result in steeper slopes of the dependence of a-axis on co-doping fraction.

Figure 4-9.a and b does show a slightly different behavior of change of c-lattice constant by introducing dopant into Mn site. The main changes appear for Ga and Cr now behaving in completely opposite way. The radii ratio of Ga/Mn is higher than Cr/Mn but both are below unity. $Cu^{2+}V^{4+}$ co-doping also gives rise to shrinkage of c-axis constant. Calculation of unit cell volume revealed that Ga and Cr like Al dopants must force unit cell to contract, whereas all remaining dopants show expansion of unit cell when they occupy the Mn sites, even $Cu^{2+}V^{4+}$ dopant results in expansion of the unit cell [113].

The changes of a-axis and c-axis constants for self-doped h-RMn_xO_3 oxides in Figure 4-9.c and d, respectively, demonstrate expansion of the lattice axis and therefore cell volume by introducing Mn vacancies into Mn-sites (x<1 side of the solid solution) for all studied systems. The slope of the change is dependent on the ionic radius of the rare-earth ion as

shown in Figure 4-9.c and d. Values of c-axis constant from off-stoichiometric thin films of $DyMn_xO_3$ and $ErMn_xO_3$ are also given in the figure [18]. In whole range from Dy excess to Dy deficiency, c –constant is decreasing. The same holds for the $ErMn_xO_3$ thin film. The slopes of changes in c-axis parameter for both Dy and Er self-doped samples are quite similar and much larger than corresponding values of slope of self-doped $LuMn_xO_{3\pm\delta}$ samples of the present study. R-site self-doping of RMn_xO_3 oxide with R=Lu (current study), Y [17] bulk ceramics and Dy and Er thin films [18] demonstrate expansion of the c constant as the value of R ion is increasing. Available data for Y and Lu bulk ceramics give the same expansion of the lattice constants and volume of the unit cell as R-site deficiency reduces (decreasing x in the x>1 side). Therefore R-site deficiency in h-$RMnO_3$ oxide provokes retraction of the unit cell. One expects to have shorter Mn-O_{ap} bond lengths when the c-constant is decreasing with more accentuated tilting of MnO_5 bipyramids [122,123].

The size of the rare-earth ion in the plane of the unit cell which separates the MnO_5 bipyramids along c-axis may be generally used to control the amount of c-axis expansion. A simple explanation could be given to this as the R-O_{ap} and Mn-O_{ap} bond lengths are bridging R to Mn ions, therefore the electrostatic interaction of positive charged cations will affect the position of O_{ap} plus the tilting of bipyramids in the unit cell [96]. Any change in Mn sites like introducing Mn vacancies may be in favor of pushing apical oxygen towards the rare-earth due to electrostatic attraction forces. Theoretical investigations of the Mn-site doping (10 atomic %) considering dopants with different charge valence have generally shown that the splitting of Mn-O_3 and Mn-O_4 (planar oxygen ions) will be reduced upon doping and could result in a more symmetric network of Mn trimers with the subsequent effect of enhancing frustration [113]. This same study indicates the sensitivity of the tilting angle to the size factor as bigger ionic radius of dopant induces higher tilting angle of MnO_5 polyhedron. That would not be the case for divalent or tetravalent dopants as they introduce more electron/holes into the lattice.

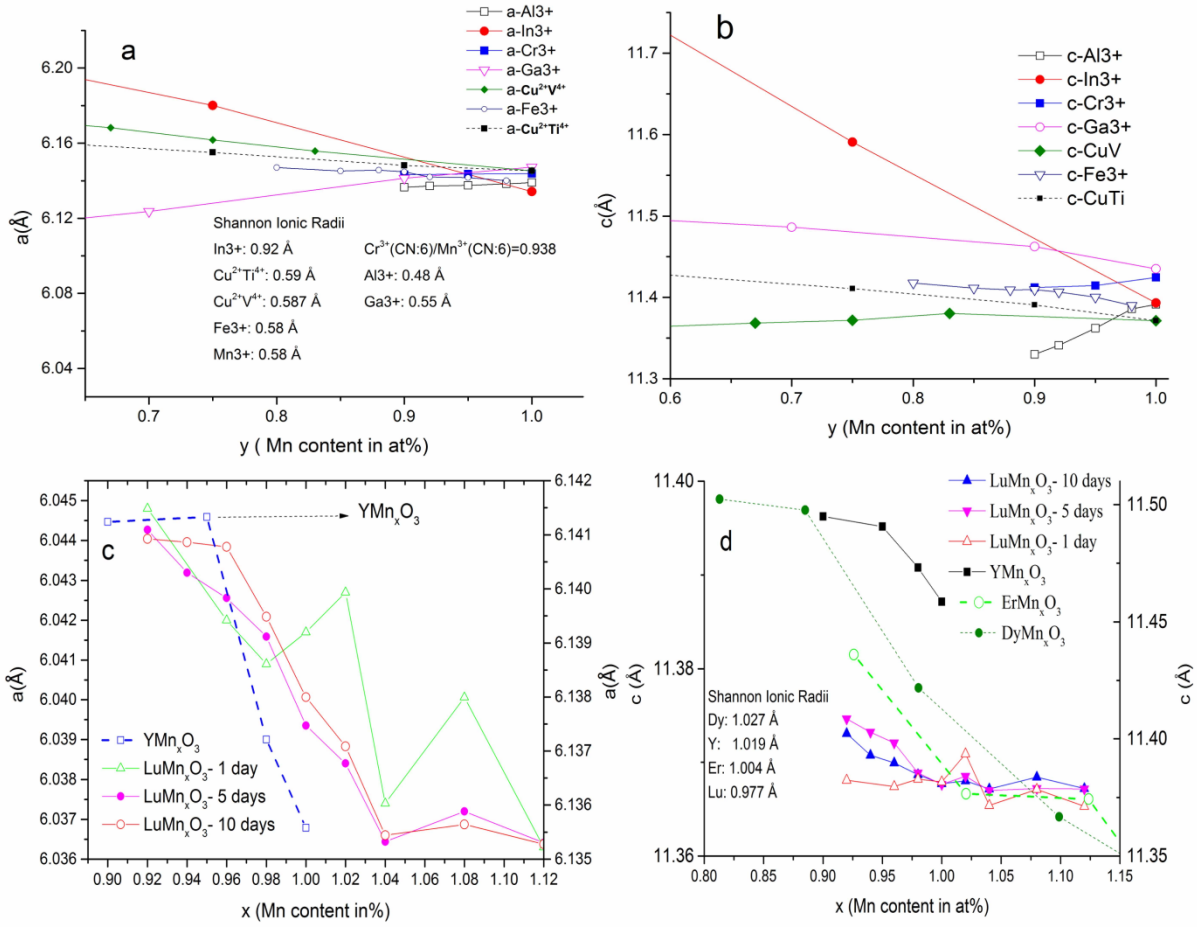

Figure 4-9. Change of the lattice parameters upon doping into Mn-site of the RMn_xO_3 oxides. (a) and (b) show lattice parameters for Mn-site co-doping with trivalent ions. The a-axis (c) and c-axis (d) constant dependence on x for self-doped $RMnO_3$ materials from current study or literature (In^{3+}[120], $Cu^{2+}V^{4+}$ and $Cu^{2+}Ti^{4+}$[121], Fe^{3+}, Cr^{3+}[70], Al^{3+}[68] and Ga^{3+}[122], Er and Dy [18]).

Moreover, the minimum energy solution for trivalent dopants can be to somehow dependent on the ionic radius [113]. In the range of ionic radius ratio of $0.9 \leq r_{M^{3+}}/r_{Mn^{3+}} \leq 1.1$ for Co, Ga, Fe and Cr the minimum energy decreases from Co to Cr, implying that Mn-site doping is more energetically favorable for dopants with larger ionic radius. On the other hand, Al with smallest ionic radius in the studied series of Mn-site dopants gives rise to lower energy than Co and Ga, emphasizing that Mn-site

substitution may suddenly change its dependency on the ionic size of the dopant. This behavior is more pronounced for tilting angles, less for Al than Cr and Ga, whereas the buckling angle closely follows the r_M^{3+}/r_{Mn}^{3+} ratio and becomes smaller when this ratio turns higher. These are important results as the energy scheme of the unit cell is the collective mechanism including all ionic displacements and tilting of MnO_5 polyhedrons, implying that dealing with Mn-site vacancies in self-doped RMn_xO_3 materials may not inevitably represent a monotonic trend in all properties or distortion of lattice parameters.

4-2-4 Tilting and buckling in unit cell of $LuMn_xO_{3\pm\delta}$ ceramics, sintering effect

Not only the change of lattice constants in R-site or Mn-site doped h-RMn_xO_3 lattices but also the tilting of MnO_5 bipyramids and shift of the Lu ions along c-axis are important on dictating the electrical polarization and magnetic interactions. Figure 4-10 a and b show the tilting of the polyhedron of MnO_5 for selected samples with off-stoichiometric compositions for 5 days and 10 days sintering time. Tilting is defined by the angle of O_3-O_4 bond to basal plane (tilting of O_{pl}) and angle of O_1-O_2 bond to c-axis (tilting of O_{ap}) [30]. The values of the O_{ap} tilt angle and Mn-Mn bond distance were extracted from VESTA 3.1.8 software which gives also the error bars of the calculated parameters from cif files of the compositions extracted from Rietveld refinement of the XRD data.

The tilt angles in Figure 4-10.a and b reveal slightly different behaviour from left to right when Mn-site vacancy doping switches into R-site vacancy doping. Refining the oxygen atomic positions using conventional XRD is a true limitation of the method and would have introduce some uncertainty in the results which may explain the fluctuation of the calculated quantities. It appears that O_{ap} tilting angle in Figure 4-10.b has more noise than the O_{pl} tilting angle in Figure 4-10.a aside, as it could be predicted from the fluctuation of the experimental data of c-axis constant. Tilting angles for both sintering

conditions of Mn-site vacancy samples (x<1) follow a clearer trend with less fluctuation of their values than the ones for R-vacancy doped samples. The better defined trend of tilting angles for Mn-vacancy doped samples becomes more evident in change of O_{pl} tilt angle, as planar oxygen ions are directly affected by Mn filled position or vacant site in basal plane

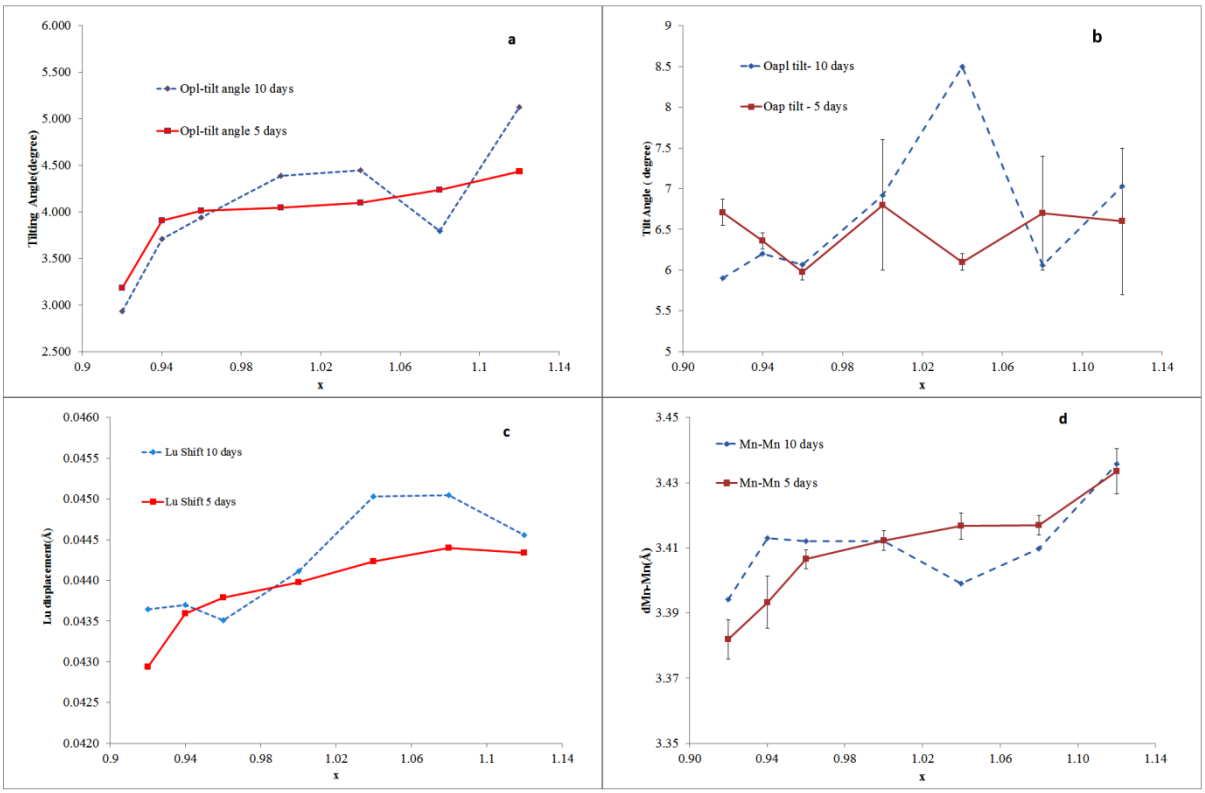

Figure 4-10. Tilting of the MnO_5 polyhedron in (a) and (b), and displacement of the Lu ions and Mn-Mn bond lengths of off-stoichiometric ceramics under study in (c) and (d).

Figure 4-10.c and d present the displacement of Lu ions and Mn-Mn bond distance in basal plane, respectively, for the same sets of samples under study. Both functions show a trend to increase with the value of x. However both quantities in x<1 region of Mn-vacancy doping follow parallel trend to the one observed in the values a-axis and cell volume, Figure 4-3.a and c, ending in a flat plateau after 10 days annealing in this region.

Again fluctuation of the data in the region of R-site vacancies appears more significantly than in the opposite side. It is suggested that Lu-vacancies would introduce more complexity in the behaviour of crystalline cell than Mn-vacancies, which it may be due to the higher coordination number of Lu (bonded to 8 O ions) than Mn sites with 5-fold O coordination [96]. The Mn-Mn bond distance has a trend for expansion with x which is contrary of the trend for shrinking of the a-axis constant with x. Such feature is important in discussing the AFM interactions of Mn magnetic moments in the basal plane. It confirms that Mn-O_{pl}-Mn bond angles also play significant roles on shrinkage or expansion of the unit cell in the basal plane.

4-2-5 Energy scheme of $LuMn_xO_{3\pm\delta}$ compositions from First-Principles Calculations

In next step of study of the crystalline lattice, it is considered helpful to have a landscape of the minimum energy of the unit cells of the off-stoichiometric materials under study to make a first time exploratory comparison with the values of minimum energy of stoichiometric $RMnO_3$ lattices. For such First-Principles calculations were carried out using the full potential linear augmented plane wave (FP-LAPW) method implemented in Wien2K code [124], by fixing atomic positions and lattice parameters to the values obtained from XRD Rietveld refinement of selected samples the 5 days and 10 days sintered batches. Since the LDA method does not give band gap in these insulator oxides [125], after getting the convergence of the calculations with set criteria the LDA+U with Hubbard potential of 6 eV on Mn 3d orbitals was applied to open the band gap [126]. More details of the same First Principle calculations and use made in the study of the $LuMn_xO_{3\pm\delta}$ samples are left to the matters in latter chapters of this thesis.

Figure 4-11 gives the outcome of First Principles calculations for selected samples of two sets under study, revealing that the energy minimum of samples with 5 days annealing

time occurs at stoichiometric composition while in 10 days annealed samples the lowest values of the calculate energy are to the left in the x<1.00 side of sample composition.

It must be mentioned that the concept of vacancy in these calculations is introduced only by the indirect via implicit in atomic positions and lattice parameters from the XRD Rietveld refinement. Introducing any vacancy into the models of the crystalline lattices demands supercell calculations, volume optimization and then determination of the equilibrium positions of all individual atoms in the supercell. Considering of AFM spin configuration will increase even more the time of First Principles calculations. A-type AFM spin states for Mn moments was considered in the present calculations, with spins parallel but of opposite signs in two Mn planes in a unit cell [10,127]. The energy scheme for x=1.12 of 10 days annealed samples in Figure 4-11.a indicates highest value of energy for this composition which may imply that instability was induced in the lattice more than in samples of other compositions.

Figure 4-11.b demonstrates that the change of band gap for 5 days annealed samples covers a broad range of energies, with stoichiometric sample in the middle of the energy range with a band gap of around 0.6 eV. The corresponding value of the band gap for the stoichiometric composition of 10 days samples is around 0.7 eV. The results of the calculation of band gaps for both sets of samples indicated Mn-site vacancy doping (x<1) leads to the crystalline lattices with smaller band gaps whereas the opposite occurs in R-site vacancy samples in the right side of the plots of this figure. As discussed in a latter chapter of the thesis, the calculated partial density of states for Mn 3d, O 2p and Lu 5d orbitals indicate that the lowest energy states at the bottom of the conduction band could be assigned to the Mn 3d – 2p O hybridization [10,128]. Therefore, it would be rational to correlate the changes Mn-Mn bond distance in previous Figure 4-8.d with the differences of energy band gap. Even though the AFM configuration was simplified to A-type AFM for the needs of the present First Principles calculations as also reported in reference [10,127]. The adoption of non-collinear spin geometry of Mn^{3+} moments has been

proven that would not change much the energy scheme and band gap values in the $YMnO_3$ system [129].

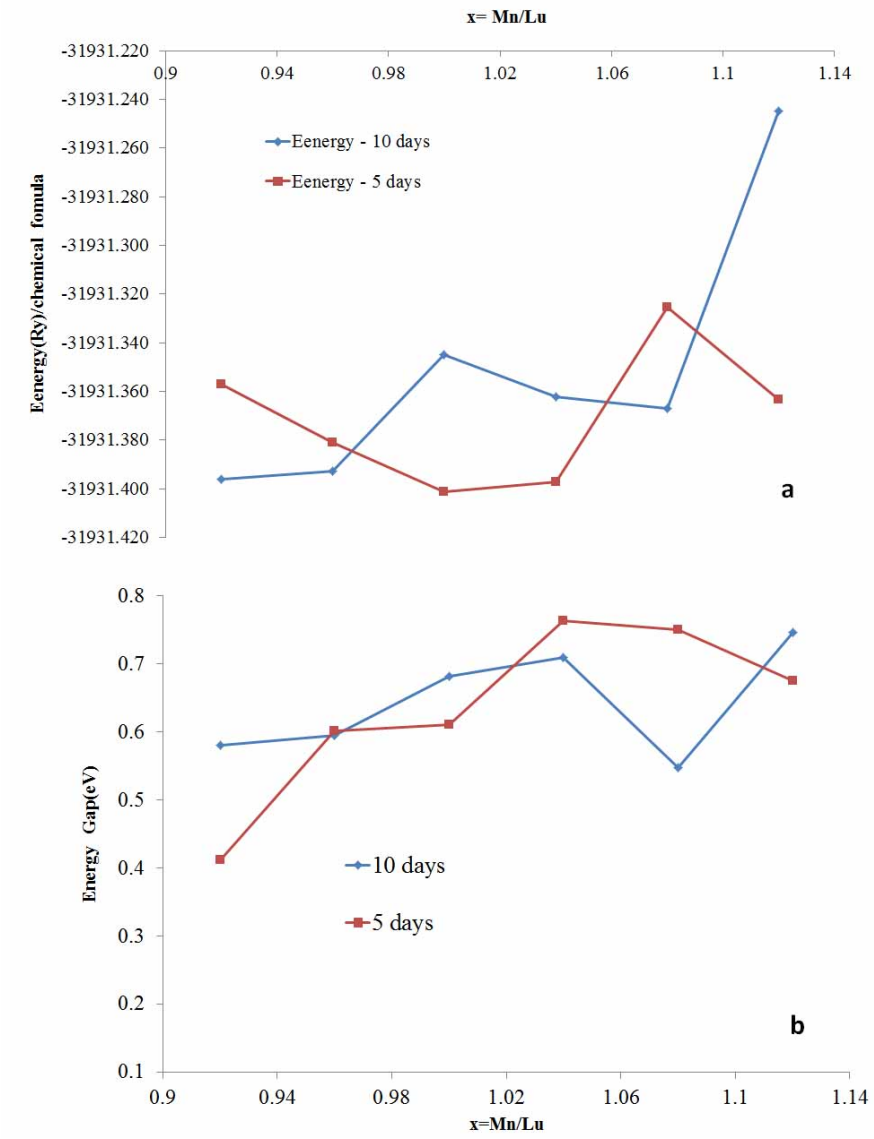

Figure 4-11. (a) Calculated energy of the off-stoichiometric $LuMn_xO_{3\pm\delta}$ ceramics and (b) evolution of the bad gap determined by First-Principles approach.

4-2-6 R-site / Mn-site vacancies through First-Principles Calculations:

Up to now literature reviewing could not give any comprehensive work or way to introduce vacancies on First Principles simulations of vacancy doped lattices of the h-$RMnO_3$ oxides. Results of the current investigation of the effect of R-site or Mn-site vacancies in the atomic positons of the ions of the unit cell are present in this section. To simplify the calculation and therefore reducing the time of the calculations which becomes prohibitively long, the structure of the paraelectric phase of $LuMnO_3$ was adopted as the sintering was also done at 1300°C very close or on the edge of the phase transition. To introduce a low amount vacancy as at the limit of present experimental study (12%), the unit cell was extended by 2x2x1. Considering the Wyckoff positions of Lu (2a) and Mn (2c), extending of the unit cell and introducing one cation vacancy per supercell would be almost equivalent to the 12 % vacancy concentration of that cation. The same potentials and Wien2K code were taken as done in section 4-2-5. To reduce time of calculation after creating the supercell and introducing either Mn vacancy or Lu vacancy non spin polarized calculations were performed going directly to determine equilibrium positions of the all atoms in the supercell. Wien2k code does find the equilibrium positions by minimizing the forces on the nuclei. We performed minimization of forces with the criteria of 0.0001 Ry for energy convergence and 0.001 e for charge and 1 meV/Å for forces.

The atomic arrangements of ions in the supercell in c-axis projection are shown in Figure 4-12. Figure 4-12.a is the starting supercell of the PE phase [41,106]. The corresponding orientation for the Mn vacancy and Lu vacancy supercells are presented in Figure 4-12.b and c, respectively.

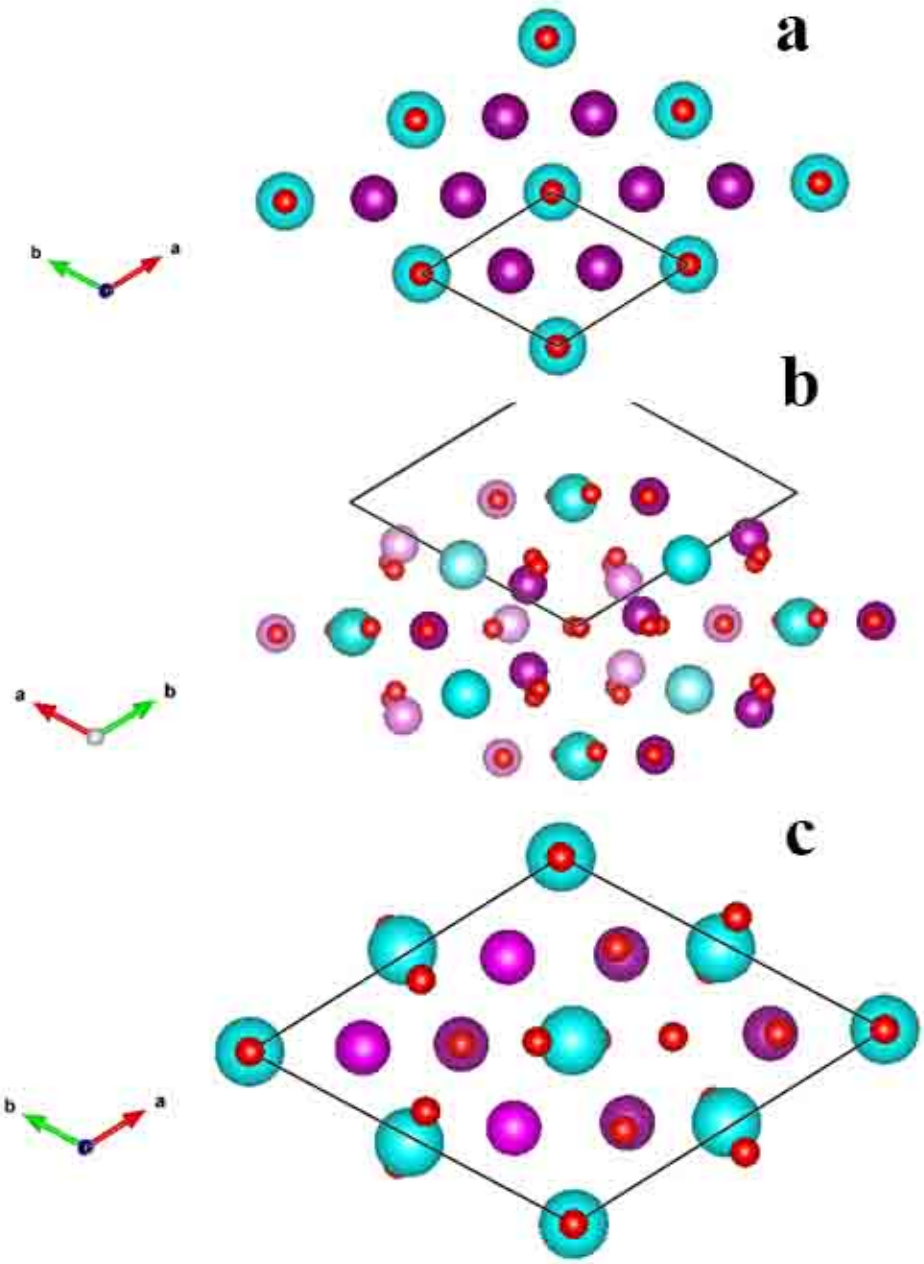

Figure 4-12. (a) PE structure of the 2x2x1 supercell of the $LuMnO_3$ stoichiometric structure viewing along c-axis, (b) Lu vacancy supercell, the place of Lu vacancy is located in the center of the image, Mn ions with different colors indicate two z-positions and (c) Mn vacancy supercell in a plane of Mn ions with pink color, other Mn ions are located at different z-coordinate.

Because converting the usual unit cell to supercell and then introducing vacancy in A-site or B-site will result in change of the space group, the unit cell dimensions in the images are not the same. In a first glance, the major disturbance in the atomic positions is for image b, Lu vacancy supercell. We should emphasize that the convergence for Mn vacancy supercell was achieved after 600 cycles of the calculations; however the one for Lu vacancy supercell could not get convergence within the defined criteria mentioned already. Therefore, the impact of the Lu vacancy on the force minimizations of the ions in the unit cell is too much as the convergence of the calculations could not be reached after many cycles (we tried 1500 cycles). However, comparing the final structure of the calculations may give useful information on the sensitivity of different species in the unit cell to the specific vacancy. In general we can summarize the result of comparison of calculated atomic positions and their initial positions as following:

ion type	**Lu vacancy**	**Mn vacancy**
Lu ions	less than 0.003 Å shift in coordinates	in x,y coordinates can be 0.01 Å, in z is smaller
Mn ions	x,y shift as large as 0.01 Å, along c-axis, much lower	no shift along c-axis, shift in basal plane as large as 0.01 Å
Opl	shift in x,y coordinates less than the ones for Mn ions	shift in x,y coordinates is more than the ones for other ions (~0.06 Å)
Oap	shift in x,y coordinates more than z, and more than the ones for Opl, but less than Mn shift	less shift in all coordinates in comparison to other species in the supercell

The analysis of the comparison shows that introducing Mn vacancy would provoke Lu ions to be displaced along c-axis more than Lu ions in a structure with Lu vacancy. Also, introducing Mn vacancy affects planar oxygen (O_{pl}) coordinates significantly, in such a way there exists a shift in x or y coordinates as big as 0.05 Å or even bigger for ions close to vacancy positions. The Mn-O_{pl} bond lengths would change from 2.08941 Å of the PE structure to 1.76677 Å for Mn vacancy supercell and 1.88595 Å for Lu vacancy supercell. In the same time, the bond angle of the Mn-O_{pl}-Mn in basal plane has values of 143.17° for Mn vacancy and 129.2008° for Lu vacancy supercells (in PE structure is 120°). In calculations of the distances and the angles we have considered those ions close to the vacancy positions to illustrate the effect of the vacancy on adjacent positions. Change of Lu-O_{pl} from PE structure (2.8 Å) is 2.7446 Å for Mn vacancy supercell and 2.57589 Å for Lu vacancy supercell. Thus, Lu vacancy has stronger effect on the Lu-O_{pl} bond lengths as it was claimed that to be a driving force for ferroelectricty via orbital re- hybridization of Lu($5d^{z2}$) – ($2p_z$) O_{pl}[33,130,131].

In complementary calculations, it would be better to first carry out the volume optimization in order to understand how the volume of the unit cell will change depending on the type of vacancy. Then using the calculated cell parameters one can proceed for atomic position minimization.

Finding equilibrium positions of the atoms in the unit cell after introducing vacancy results in giving intuitive information on the magnitude of the change of crystal parameters in previous calculations. However, in performed calculations there was no room for oxygen vacancy which may be present at least when cation vacancy are introduced. Our calculations in PE phase of $LuMnO_3$ showed that unit cell does not get convergence when vacancy in Lu site is introduced, whereas Mn vacancy lattice could get convergence after reasonable number of cycles. Thus we tried to carry out calculations at FE phase, with A-type AFM spin configuration of Mn ions to find out the effect of Mn vacancy on the volume change of the unit cell. A mesh of 5×5×3 of K-points in reciprocal space was chosen for the unit cell of $LuMnO_3$, Mn ion (0.6645000, 0.0000000,

0.4992300) and planar oxygen ions (0.33333333, 0.66666667, 0.51900000) and (0.66666667, 0.33333334, 0.51900000) which are the closest ones to the chosen Mn ion were removed. The choice of removing oxygen planar was made as neutron diffraction analysis of the $YMnO_{3-\delta}$ indicated that the planar oxygen vacancy is more favorable than apical oxygen vacancy [96]. Values set for expansion or contraction of the unit cell volume was chosen as: (-2, -1, 0, 1, 2) which covers both possibilities of expansion or contraction in unit cell. The main objective of this calculation will be finding the tendency of the change of the unit cell volume when the lattice is exposed to Mn/O vacancies. Criteria of 0.0001 Ry for energy convergence and 1.0 mRy/a.u. for the force were set.

Figure 4-13 indicates the results of the volume optimization of the unit cell with Mn/O vacancy. The x-axis gives the percentage of the change in volume with respect to initial unit cell volume (zero value), the calculated energy after reaching the convergence criteria for that specific volume change. Our calculations reveal that the minimum energy reaches for 4% change in volume of unit cell. Therefore, the reaction of the unit cell to Mn/O vacancy would be expansion of the volume of the unit cell. Results of volume optimization in Figure 4-13 confirms our experimental findings from XRD Rietveld refinement values of the unit cell in Figure 4-3 which show that for $x \leq 1$ (Mn vacancy) the unit cell becomes expanded as x value decreases.

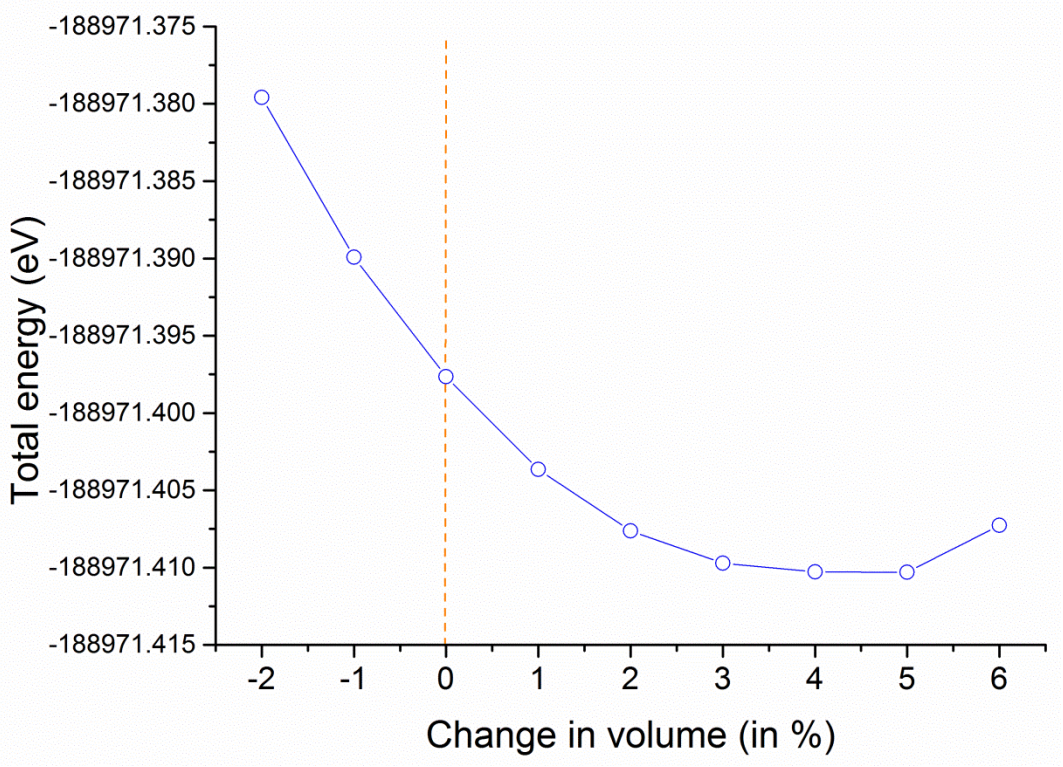

Figure 4-13. Total energy versus volume change in the unit cell of $LuMnO_3$ with Mn and O_{pl} vacancies. 4% change in volume gets minimum energy among considered changes in volume, means that the unit cell after introducing Mn/O vacancies tends to be expanded.

4-3 Morphology and elemental analysis of secondary phases

Matter transport in high temperature processing of the $RMnO_3$ materials proceeds by diffusion. Samples with different concentration of cation vacancies are expected to react differently during solid state sintering, thus yielding changes in final density and in grain size as well as in the distribution of secondary phases. Homogeneity of the crystalline particles is another matter which should also be examined because it contributes to modifying the properties of these materials. Evaluation of these issues is made in this chapter with use of scanning electron microscopy SEM/EDS analysis on polished cross sections of the ceramic samples.

4-3-1 Effects of Mn/Lu ratio on grain growth

Grain boundary grooving and intergranular fracture of as sintered samples revealed the contours of the crystalline grains with detail allowing the characterization of grain coarsening by SEM on fracture surfaces without the need of polishing and etching the surfaces.

At least five SEM images of each sample were taken for measuring the grains size. Cord lengths were determined by counting the number of grains intersected by the gauging straight lines on the SEM images and were later converted to the grain size according to the scale of the SEM pictures and averaged for each sample.

As particles of secondary phases can be found on grain boundaries and inside the grains of the main phase, polished cross-section of the samples were prepared for SEM for detection and characterization of the distribution of secondary phases by using diamond lapping paper sizes from 30 micron to 0.5 micron. Tests of thermal etching of the polished surfaces for short time at temperatures 20 % below the sintering temperature were done to reveal particle grain boundaries before SEM. Selectivity of thermal etching for the grain boundaries of $LuMn_xO_{3\pm\delta}$ was low and surface loosed quality due to increase of relief in the polished surface. Since it was not know exactly what will be the reaction of the secondary phases at high temperature, it was avoided to apply the heat treatment for thermal etching of the surfaces.

The EBSD technique in SEM was shown to be too sensitive to surface roughness, artefacts and damage of fine polishing of the cross sections. These difficulties were overcome by doing the EBSD with a special SEM sample holder to clamp the TEM thin sections prepared by mechanical polishing and with the surfaces finished by thinning with ion milling. The sample for TEM thin sections was glued between two dummy single crystal Si slabs. After mechanical polishing down to silicon transparency the thin section was ion milled and thinned to electron transparency in TEM.

Figure 4-14 shows SEM images of fracture surfaces of 5 day sintered $LuMn_xO_{3\pm\delta}$ samples of a selection of six different compositions. As seen, there is strong dependency of grain

size on x, the Mn/Lu ratio. The grain growth is increased by raising the value of the x ratio. Closed porosity at the grain boundaries is observed but with decreasing frequency in samples of larger values of x.

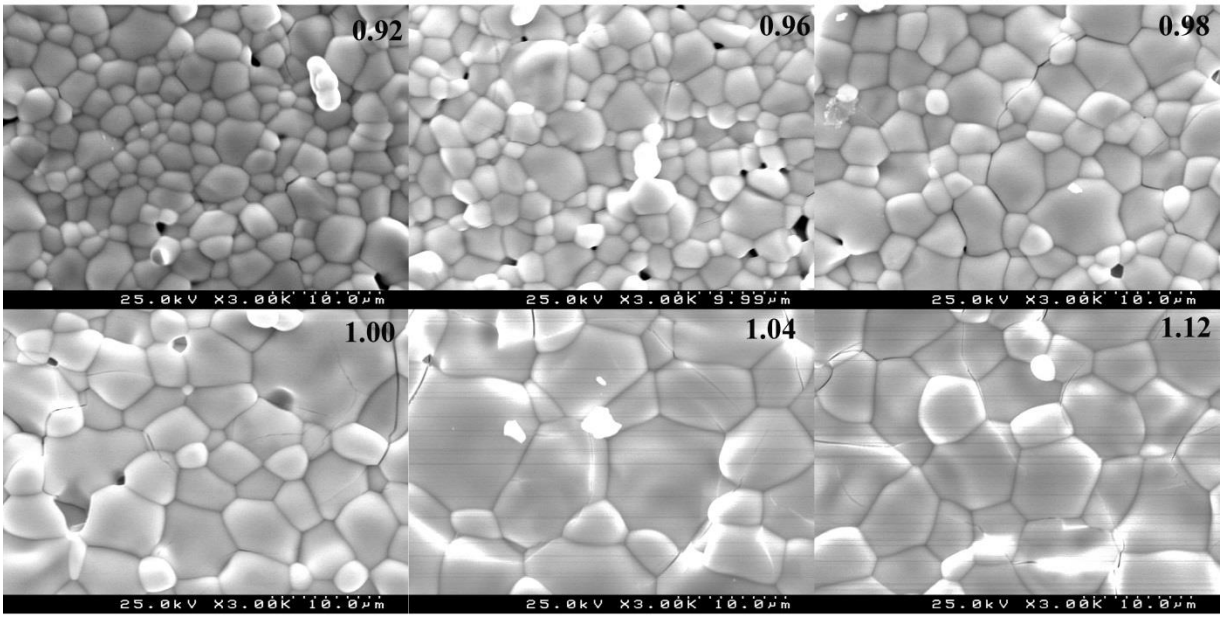

Figure 4-14. Fracture surfaces of 5 day sintered $LuMn_xO_{3\pm\delta}$ samples of six different compositions.

Figure 4-15 presents the evolution of grain size and porosity of $LuMn_xO_{3\pm\delta}$ with high temperature annealing time of three selected compositions, one from each side of the solid stability limit of the solid solution and the nominally stoichiometric composition (x=1.00). The grains are looser and the particles have poorer packing in the ceramics of lower values of x. The slow densification of compositions with Mn/Lu ≤ 1.00 is visible for the shortest time period of one day and it has direct effect on reducing grain growth by the action of pores on pinning and slowing down the grain boundaries. Grain growth of the porous samples being linked to density, samples of higher density or fully dense have larger grain sizes, as seen in samples with x≥1.

One must take into account that any deficiency in Lu or Mn in sample composition combines with the time and temperature of sintering so the whole picture of the

distribution of particles and their sizes can be changed. This means that by dealing with grain size one may modify the physical properties of $LuMn_xO_{3\pm\delta}$ as it was reported before for the rare-earth manganites [85,86,132], both of perovskite type or of hexagonal ones, either from chemical based routes or from solid state sintering.

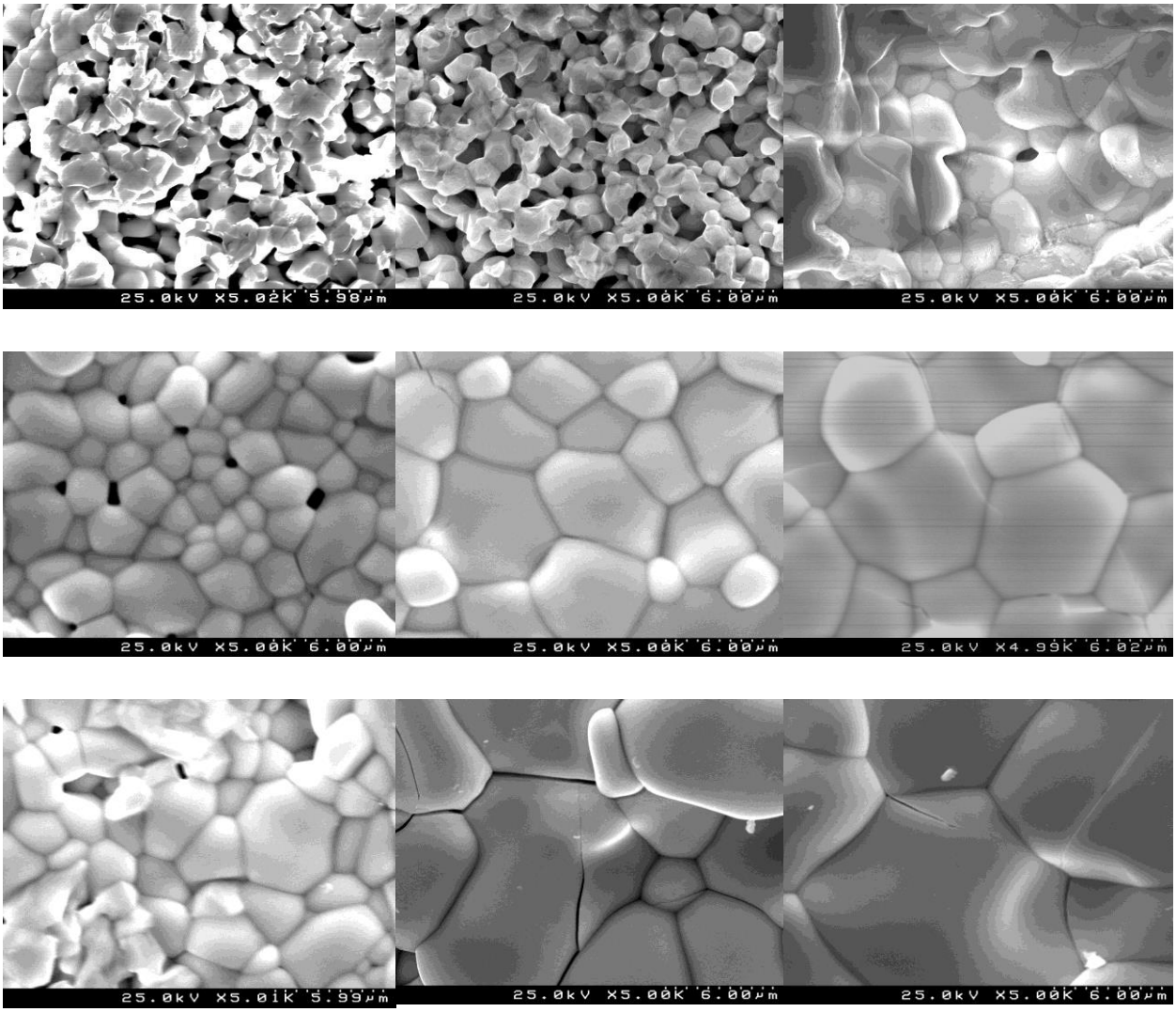

$LuMn_{0.92}O_3$ $LuMn_{1.00}O_3$ $LuMn_{1.08}O_3$

Figure 4-15. Evolution with time of annealing at 1300 °C of densification and grain size of $LuMn_xO_{3\pm\delta}$ samples of three selected compositions. First raw, samples of one day annealing, second raw of five days annealing and last raw of ten days annealing.

Figure 4-16 gives the general view of grain growth of the complete set samples of this work as a function of sample composition for fixed periods of time of isothermal annealing at 1300 °C. Grain size as found here is very sensitive to the x value. A change in x by just 4% modified few times more the size of the particles. Relating to the results of XRD in section 4-2 above, one also finds out that in x<1 range, where residuals of Lu_2O_3 phase were seen in the 1 day annealed samples, the slow grain growth and recrystallization did not assist in the redistribution of mater and in homogenization of the content by the sweeping effect of moving grain-boundaries and retarded the elimination of residuals of the reactant Lu_2O_3. The content of secondary phases will be further analyzed in following section.

The exponents of the power law plots of grain size as a function of annealing time in the inset of Figure 4-16.b range from ≈1/3 for x=0.92 and 0.98 to approximately 1/2 for the remaining 4 compositions. The observation of the $G \propto t^{1/n}$ law of grain growth is an approach of the growth kinetics given by the equation, $D^n(t) - D_0^n = K_G(T)t$, with $D_0^n \approx 0$ and G, grain szie [133]. As grain growth is thermally activated, $K_G(T)$, the growth rate constant will be given by the Arrhenius equation. Values of grain size were squared to test the hypothesis of the parabolic grain growth kinetics, n=2. The analysis of plots of $G^2 \propto t$ of samples x=0.92 and 0.98 confirmed that the parabolic grain growth equation also holds for these samples, but deviation of the corresponding slopes in inset of Figure 4-16.b from 1/n = 1/2 resulted from the initial grain size condition, D_0^2, not being much smaller than the values of $D^2(t)$. Within the limited accuracy of the present results, the values of the growth rate constant of the parabolic kinetics $K_G(T)$ in Figure 4-16.b reveal an approximately exponential growth with x for samples with composition within the stability limits of the $LuMn_xO_{3\pm\delta}$ solid solution, $0.95 \leq x \leq 1.04$ [91].

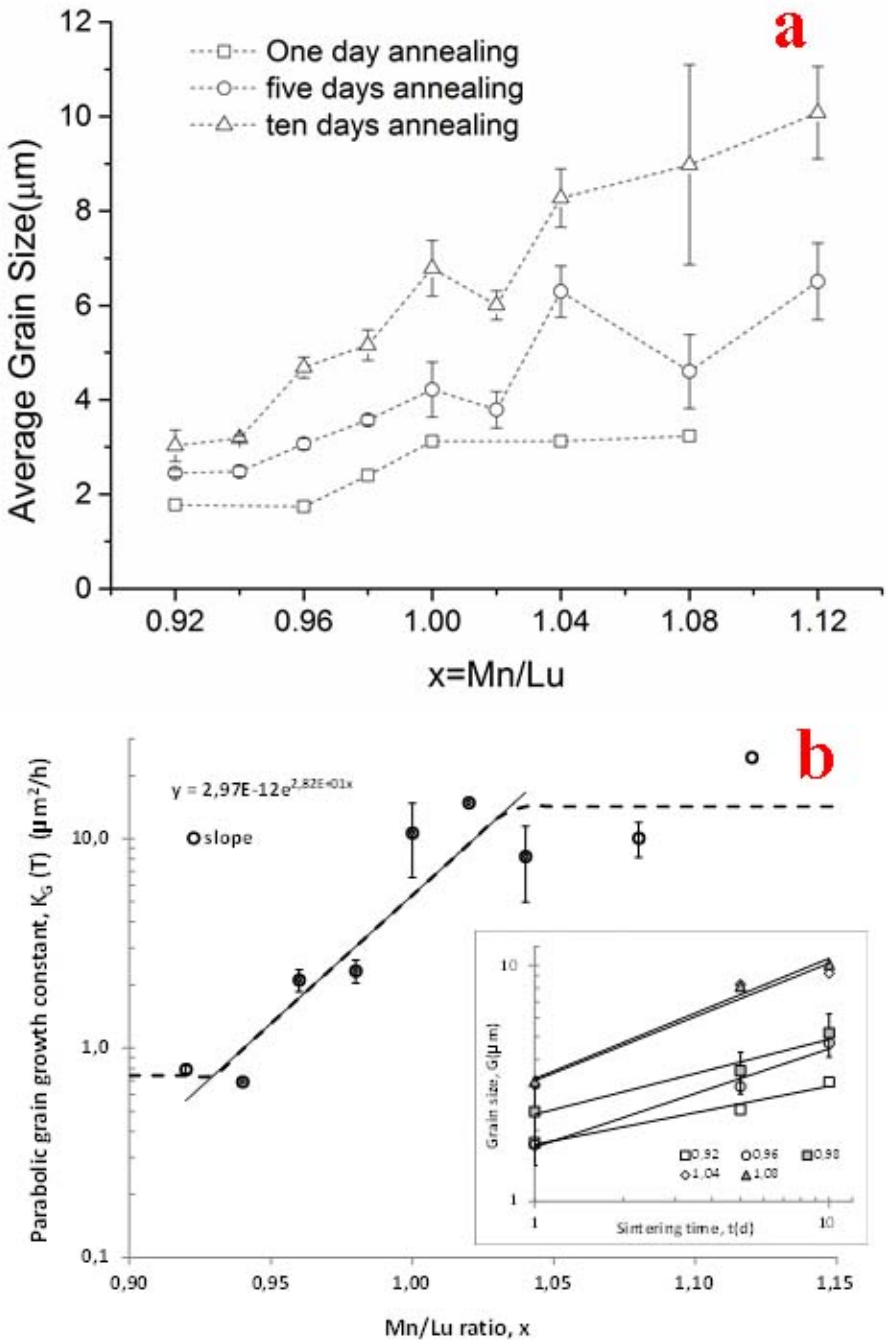

Figure 4-16. Grain growth in high temperature annealing of $LuMn_xO_{3\pm\delta}$ at 1300 °C. (a) Dependence of grain size of $LuMn_xO_{3\pm\delta}$ on x the Mn/Lu ratio for 1 day, 5 and 10 days of isothermal sintering. (b) Dependence of the constant of the parabolic grain growth kinetics KG(T) on x; inset, the power law representation of grain growth kinetics.

The most severe effect of grain coarsening on sample quality for any technological use is the appearing of thermal expansion anisotropy induced microcracking during cooling in samples with grain size above a critical threshold, G_c, caused by the anisotropy of thermal expansion coefficient (CET) of the hexagonal lattice of $LuMnO_3$ [30,134–136]. There is large thermal expansion anisotropy in $LuMnO_3$. The following maximum and minimum values of CET of $LuMnO_3$ single crystals $\alpha_a=12.8x10^{-6}\,K^{-1}$ and $\alpha_c=1.60x10^{-6}\,K^{-1}$ were determined in the range 300-1000 K from the relative increase of the a-axis and c-axis of the crystalline cell with temperature [30]. In the same range of temperature the average thermal expansion coefficient of polycrystalline YMn_xO_3 presents little variation with $0.97\leq x\leq 1.05$ [137].

Thermal expansion induced microcracking of $YMnO_3$ was early reported in samples of high relative density, above 98% of theoretical density, the extent of microcracking being enhanced after thermal etching [137–140]. The contribute to nucleation and growth of microcracks in dense, coarse grain $YMnO_3$ of strain induced by the relative volume change of the high temperature phase transition from $P6_3/mmc$ to $P6_3cm$ symmetry had been investigated [141]. The onset of intergranular and transgranular cracking formed during cooling was noticed in dense $YMnO_3$ with average grain size larger than 2 μm sintered at 1400 °C in O_2 atmosphere [142]. The analysis of the microstructure of the $LuMn_xO_{3\pm\delta}$ samples in Figure 4-16 shows that the start of microcrack development runs diagonally from the sample x=0.92 with 10 days annealing to the sample x=1.08 of 1 day annealing which corresponds to an almost constant critical grain size of $G_c \approx 3.3$ μm.

4-3-2 Dispersion of secondary phase and elemental mapping

Samples with of the shorter sintering time, 1 day, are less homogenous and offer larger probability of finding particles of secondary phases by SEM/EDS analysis. To

characterize the distribution of secondary phases in relation to the grains of the main phase, polished cross-section of the samples were prepared as describe above. The microstructure of a sample with high Mn excess, x=1.08, from one day sintering time is shown in Figure 4-17.

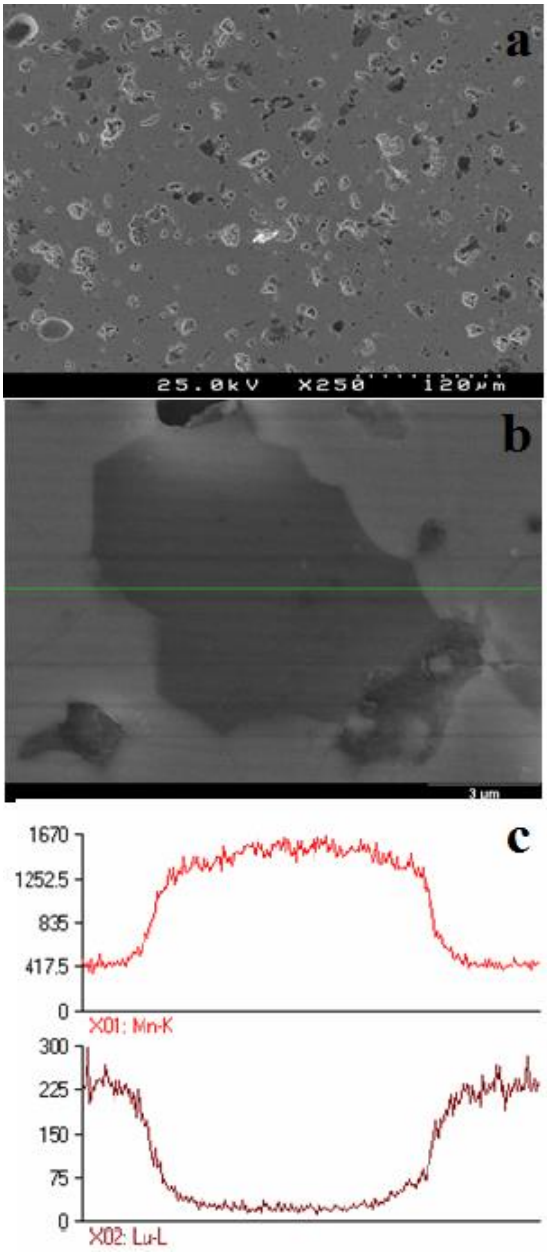

Figure 4-17. Microstructure of sample $LuMn_{1.08}O_{3\pm\delta}$ (a) The low magnification image displaying polishing pull-outs and residuals of the secondary phase (dark grey). (b) Large particle of Mn_3O_4 secondary phase and (c) corresponding Mn and Lu EDS line profiles.

The distribution of secondary phases in Figure 4-17.a and b, can be seen as disperse dark gray regions. Selective EDS analysis in dark gray regions across the surface of the sample in Figure 4-17.a showed some are as with ratio of Mn/Lu=1.08 the dark contrast being originated from polishing artifacts, others have EDS Mn/Lu ratio close to 2 or even above 10. Due to the low sensitivity of SEM-EDS technique to oxygen quantification, more accurate analysis of the phase composition was not attempted. Based on the Mn/Lu ratio determined by EDS, those inclusions with Mn/Lu ratio close to 2 could be identified with the $LuMn_2O_5$ phase which would be within the predictions of the equilibrium phase diagram of Lu_2O_3-MnO_x oxides, but for a lower temperature $T \leq 1000$ °C [17]. However, the X-rays coming out of the sample surface in EDS analysis carry information from a interaction volume a few micron deep and not just from the particles as seen on the surface. The values of the Mn/Lu ratio of thin bits of small particles of secondary phase on the polished cross-section are distorted by the fluorescent X-ray emitted from the main phase underneath. The effect is lesser relevant when the dimensions of the inclusions are well above the micron, as the inclusion in Figure 4-17.b. Figure 4-17.c displays the EDS line profiles of Mn and Lu in the inclusion of secondary phase and at both sides of the inclusion in Figure 4-17.b where there is just the main phase. Quantitative EDS analysis made on both the inclusion and main phase regions confirms that the Mn/Lu ratio in the dark gray inclusion in Figure 4-17.c is at least ten times higher than that in the matrix around, the secondary phase being tentatively identified as hausmannite.

More detailed analysis of the secondary phases and diffusion gradients of the cations at the interface between main phase and secondary phase is obtained in thin sections using TEM microscopy. For this purpose the JEOL 2200 FS TEM/STEM microscope with EDS was used.

A small particle of the secondary phase identified as hausmannite linked to the remaining piece of the main phase is shown in STEM-DF mode in Figure 4-18.a. Overlaid on the STEM image is the plot of Mn/Lu ratio calculated from EDS results collected on the marked points along the line crossing the interface of the two particles. The regions

in right ($LuMnO_3$ phase) and left (hausmannite) indicate flat plateaus meaning that the compositions there get stable values of Mn/Lu ratio corresponding to the crystalline phases themselves. The transition region at the interface extends up to 400 nm in width and shows a nearly monotonic slope in the Mn/Lu ratio; if the result of an intermediary phase of Lu and Mn between the saturated $LuMn_xO_{3\pm\delta}$ and Mn_3O_4 phases its structure could not be determined by the analysis of crystal orientations. As the contour of the inclusion in the STEM image suggests the inclusion lays sidle on the main phase. The overlapping of the two wedges of the both crystalline phases alone can explain the corresponding variation of the Mn/Lu ratio averaged by their thickness in the transition zone. A more intricate scenario was observed with another Mn rich particle ($LuMn_{1.08}O_{3\pm\delta}$) shown in Figure 4-18.b, with the corresponding EDS line profiles in Figure 4-18.c. The EDS line profiles of Lu and Mn ions reveal two stable regions corresponding to hausmannite (left side) and main phase (right side of the image). The transition zone at interface is even much wider than in the previous set of particles in Figure 4-18.a extending up to 1 micron width, with the a sharp slope of the Mn and Lu signals on the side of the main phase, then two local peaks of Mn and the large Mn rich inclusion on the left, probably Mn_3O_4, with a sharp increase of Mn concentration. Presence of wide interface between secondary phase and main phase and the difficulty to assign particular phase to it can be linked to our previous discussions of Figure 4-18 and also to the problems on identifying the correct weight fraction of the hausmannite phase from XRD Rietveld Refinement.

The same analysis was done for samples with $x < 1$ where inclusions of unreacted Lu_2O_3 phase are expected based on XRD results in Table 4-1, Table 4-2 and Table 4-3, above. Differently from the hausmannite phase in samples with $x \geq 1$ in Figure 4-17, the size of Lu_2O_3 particles in Figure 4-19 is similar to the grain size of the particles of the $LuMn_xO_{3\pm\delta}$ main phase. Residual Lu_2O_3 particles are mostly distributed on edges of pores and a few times inside larger particles of the main phase.

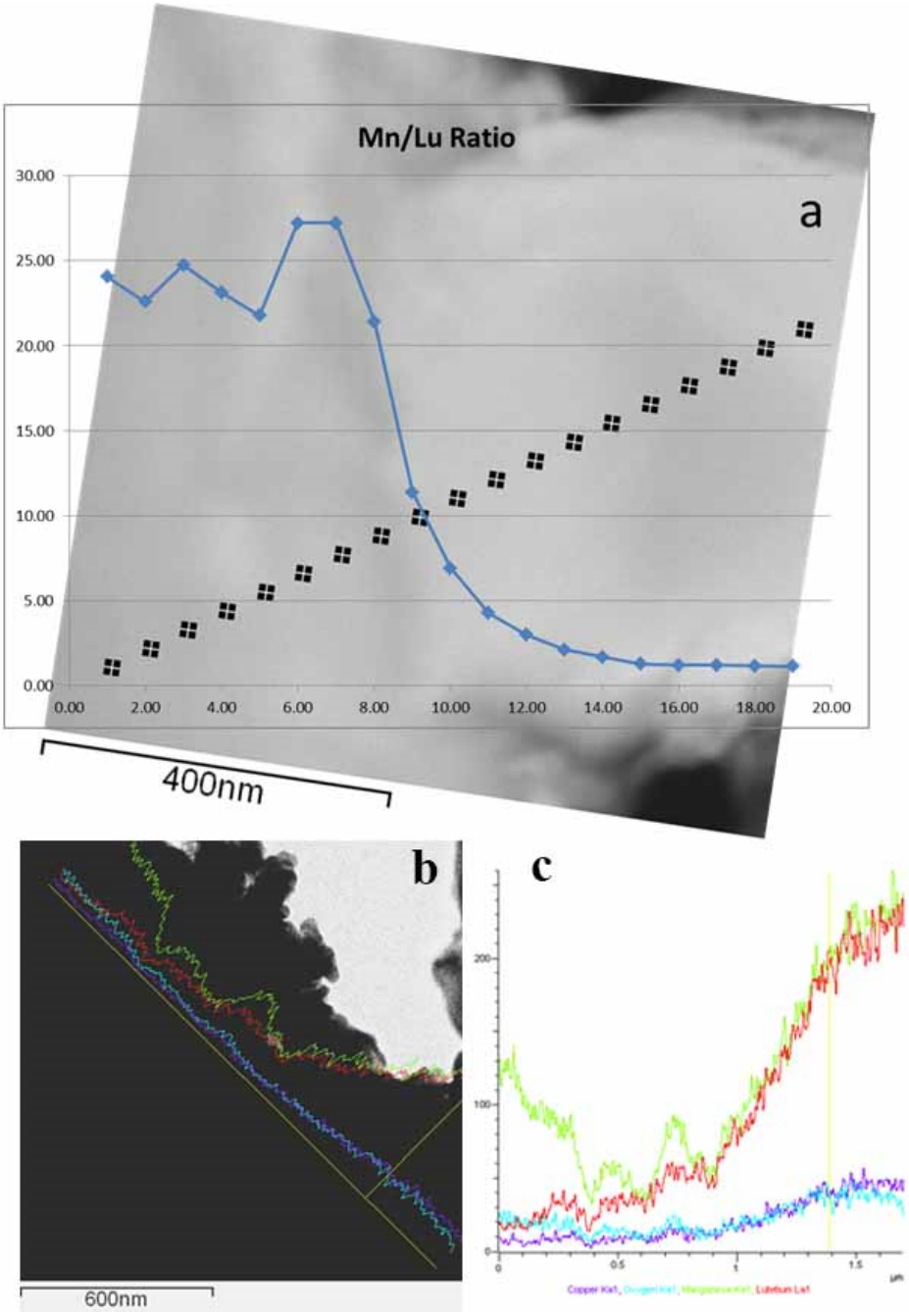

Figure 4-18. EDS element profiles of the interface zone between Mn rich inclusions and the $LuMn_xO_{3\pm\delta}$ main phase of sample x=1.08. (a) ADF STEM image the interface zone between one hausmannite particle and main phase with the profile of the Mn/Lu ration overlaid. (b) BF-STEM image of another set of hausmannite particles and main phase and (c) EDS line mapping along an interface zone between the hausmannite and main phase from (b).

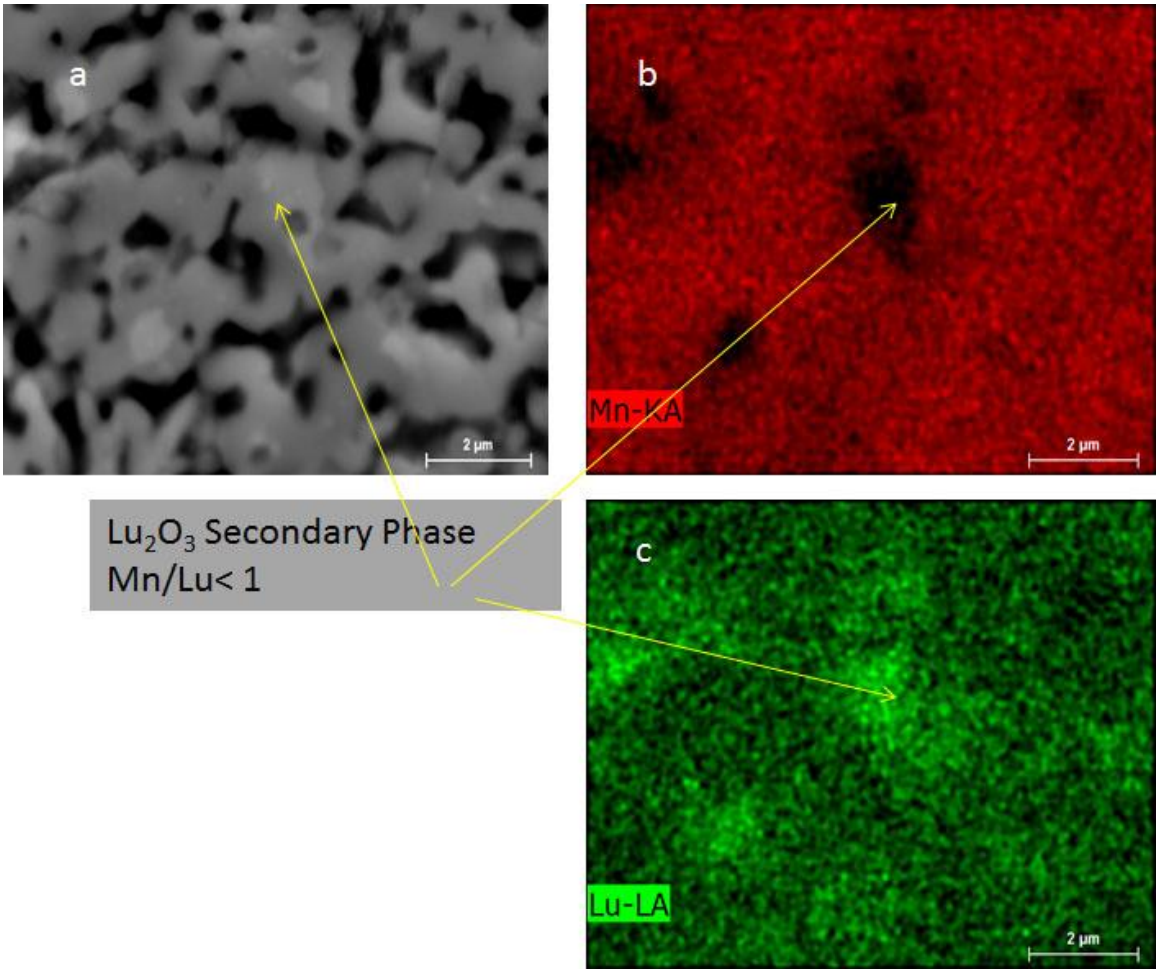

Figure 4-19. Microstructure and EDS elemental mapping of polished cross-section of $LuMn_{0.92}O_{3\pm\delta}$ sample. (a) Isolated Lu-rich particles of the Lu_2O_3 secondary phase, detected by whiter contrast in SEM image. (b) Mn-K_α EDS map. (c) Lu-L_α EDS map.

For better separation of inclusion particles that are in the surface plane from those buried underneath but detected by EDS, the study by EBSD in SEM was also done in a selection of samples. As stated above, samples prepared for TEM by mechanical polishing and thinning by ion milling were used in EBSD. The samples for EBSD analysis are tilted by 70° in respect to incident electron beam direction of the SEM. This high tilt angle provides more surface thickness for Kikuchi elastic scattering of the electrons and

lesser dispersion deep inside the material. Figure 4-20.a shows SEM image of the $LuMn_{0.92}O_{3\pm\delta}$ sample, with the grain boundary relief and grain boundary contours from EBSD. Phase identification in the EBSD is done by automatic matching with the EBSD software the Kikuchi lines in EBSD sensor with calculated electron diffraction lines for the given lattice symmetry and lattice constants provided for the most probable crystalline phases in the sample. Data for the crystalline phases of Lu_2O_3, Mn_3O_4 and $LuMnO_3$ was included in automatic search, according to the secondary phases detected by XRD. The EBSD phase map in Figure 21.b indicates the presence of Lu_2O_3 as the relevant secondary phase in $LuMn_{0.92}O_{3\pm\delta}$. The XMAP grain orientation map in Figure 4-20.c and the color code of the crystal directions in Figure 4-20.d confirm the isotropic texture of the bulk polycrystalline samples from sintering of $LuMn_xO_{3\pm\delta}$ materials. The same holds for the associated YMAP and ZMAP grain orientation maps, not shown.

Figure 4-20.b indicates the presence of Lu_2O_3 secondary phase and the places where this phase can be identified inside the sample. Differences in the relative density and grain sizes are notice between the left region (more dense and coarser) and the right region of Figure 4-20.a and b. The close observation of Figure 4-20.b confirms that the residuals of the Lu_2O_3 secondary phase are frequently located in the vicinity of pores, or on pore surfaces where, as reactant, the Lu_2O_3 particles became partially isolated and dissolution was slowed down. Thus, it would be expected that local fraction secondary phase will be diminished as the porosity is eliminated. The reaction of synthesis of the main phase is delayed in the more porous area on the right of Figure 4-20.b. Comparison of the grain sizes in Figure 4-20.a and c) with the grain size determined from SEM images, Figure 4-16, confirm that they are roughly the same, 1.5 μm on average.

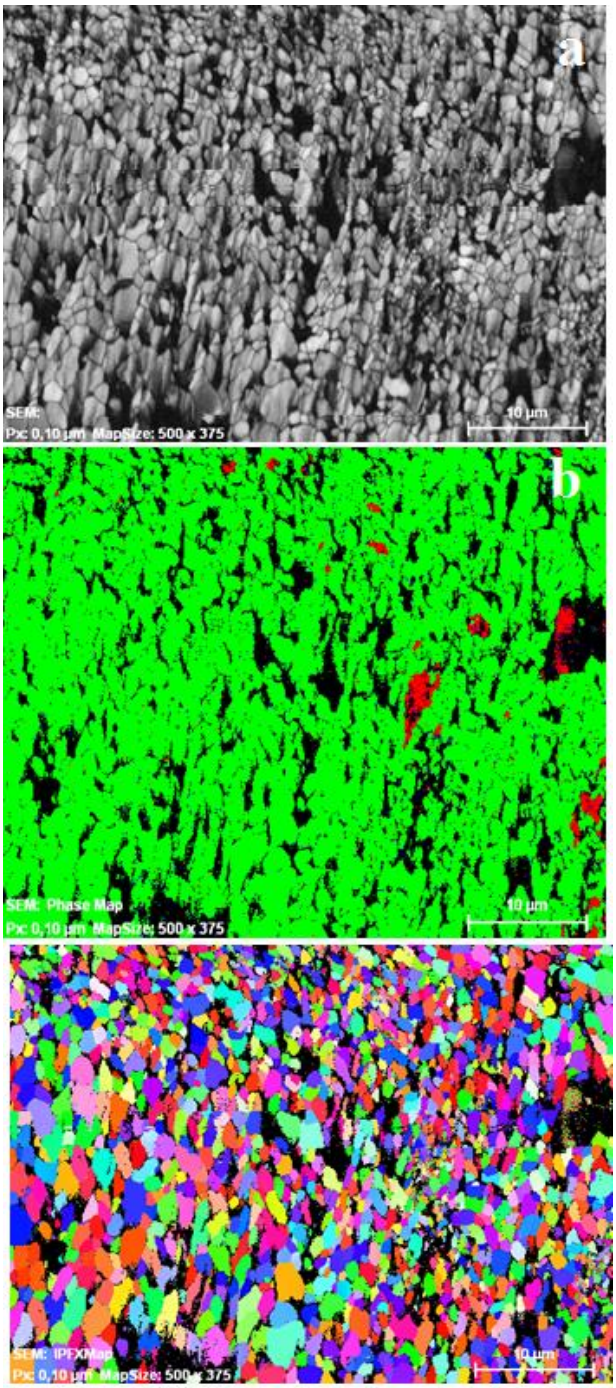

Figure 4-20. EBSD analysis of sample x=0.92, 1 day annealing. (a) SEM image with relief and grain boundary contours of EBSD. (b) EBSD phase map, $LuMnO_3$ main phase (green) and Lu_2O_3 (red), Mn_3O_4 (blue, very small regions); pixel size = 100 nm, (c) Crystal orientation map, XMAP.

The sample for the EBSD analysis in Figure 4-21 was taken from the Mn-rich side of off-stoichiometric $LuMn_xO_{3\pm\delta}$ where the XRD results in Table 4-1, Table 4-2 and Table 4-3 and SEM/EDS confirm presence of hausmannite in large particles as secondary phase, Figure 4-17.c. None of such large Mn_3O_4 inclusions could be found in the area of this sample analyzed by EBSD. Besides the main phase $LuMnO_3$ (in green color) Figure 4-21.b shows particles of the secondary phase Lu_2O_3 (red color) in less than 1% which was not detected neither in XRD nor by SEM/EDS. As it was discussed for x=0.92, Lu_2O_3 inclusions are mostly found around pores. In Figure 4-19.b the larger Lu_2O_3 particle appears on the edge of a pore. The Lu_2O_3 particle size is smaller than the grain size of main phase. One must bear in mind that the sample in Figure 4-21 was prepared after long time mechanical polishing down to Si transparency and then ion milling thinned for TEM microscopy. If the Ar ion etching rate of hausmannite is faster than for the main phase, Mn_3O_4 may have been worn away faster from the surface. Or, as EBSD image acquiring is very slow, the (2) zones tried for EBSD analysis of this sample were statistically insufficient to find such scarce inclusions. Enlarged by 10x to reveal the EBSD dot scale (pixel size of 100 nm), Figure 4-21.c and 22.d taken from the phase maps of Figure 4-20.b and Figure 4-21.b respectively, display a distribution of fine dots in blue and red automatically identified by the system as submicron size particles of the reactants Mn_3O_4 and Lu_2O_3, respectively.

It is noticed that in Figure 4-21.d of the $LuMn_{1.04}O_{3\pm\delta}$ solid solution where the reaction stage is more advanced due to faster densification and grain growth than in the $LuMn_{0.92}O_{3\pm\delta}$ sample, Figure 4-14 and Figure 4-16, the density of the Mn_3O_4 assigned blue dots is much lower than in Figure 4-21.c of the x=0.92 sample and isolated Lu_2O_3 nano-inclusions have almost disappeared too. Due to large surface area to volume ratio the hausmannite nanoparticles, even in tiny weight fractions, they are important as they have ferromagnetic ordering transition below AFM and by exchange coupling at the interface with the AFM matrix may strongly interact with the $LuMnO_3$ lattice [65,90]. Mn_3O_4 is also often reported as impurity phase for self-doped $LaMnO_3$ solid solutions [110].

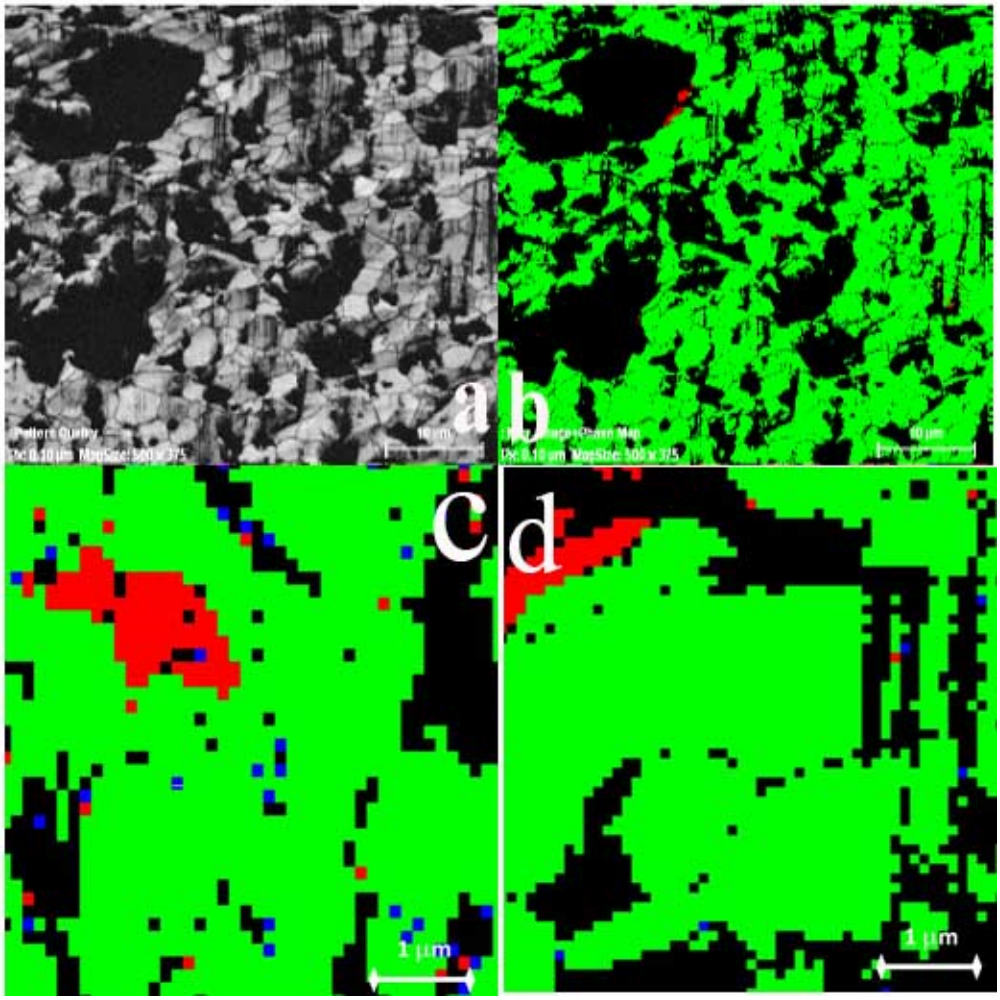

Figure 4-21. EBSD analysis of $LuMn_{1.04}O_{3\pm\delta}$: (a) SEM image with relief and grain boundary contours of EBSD. (b) EBSD phase map, $LuMnO_3$ main phase (green) and Lu_2O_3 (red), Mn_3O_4 (blue); pixel size = 100 nm. (c) (10x) enlargement of area taken from EBSD phase map of $LuMn_{0.92}O_3$ sample, Figure 21.b. (d) (10x) enlargement of area taken from EBSD phase map in figure (b). The large holes in the figure are not porosity but voids of the TEM thin section created by ion milling.

To provide further support on presence of secondary phases inside the sample captured by means of EBSD, the same sample of Figure 4-17 which was studied in TEM, was investigated by EBSD. The EBSD pictures are given in Annex B to keep the main text shorter.

4-3-3 Secondary phase in samples of long annealing time

In the initial part of this chapter it was shown that the secondary phase of Lu_2O_3 could be exhibited properly in XRD. Its amount decreases as the time of annealing is increased. However, the difficulties still persist for samples of x>1 after long time annealing where the trace of the hausmannite secondary phase could not be consistently detected in XRD results. The effort to identify the secondary phase of hausmannite in SEM images was much harder than finding the Lu_2O_3 secondary phase in samples of the Mn-site vacancy.

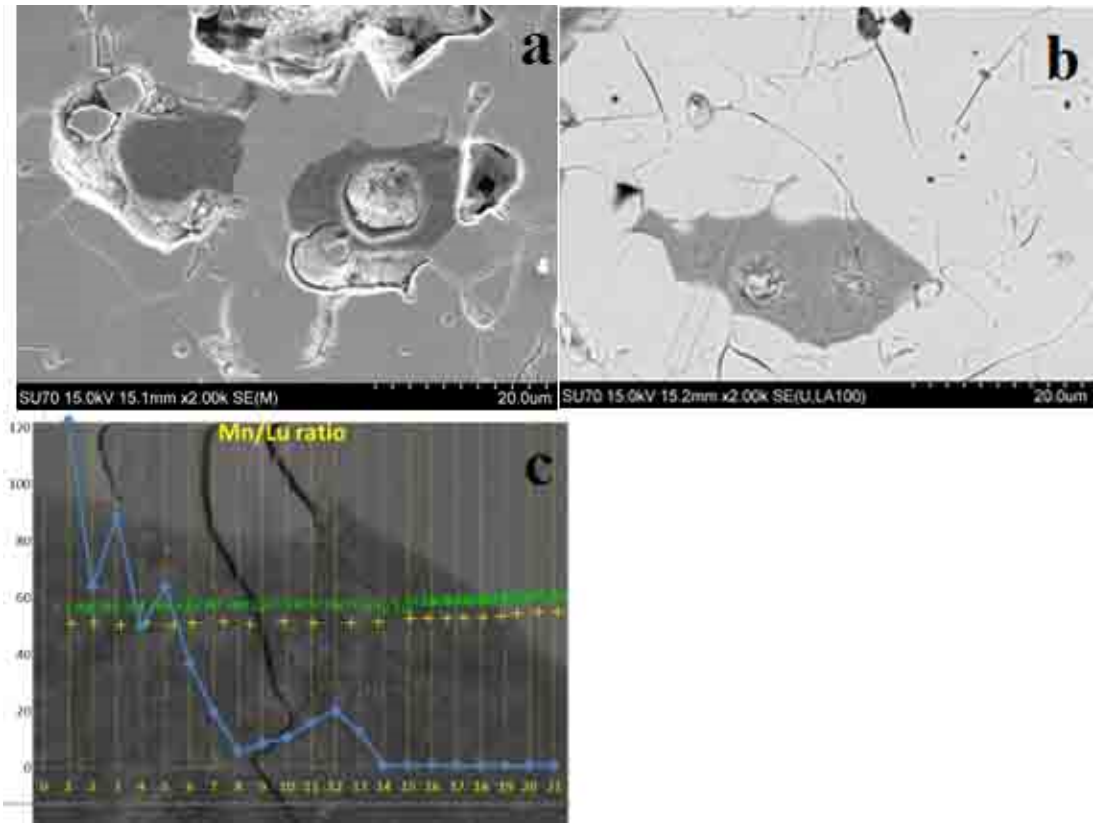

Figure 4-22. Sample $LuMn_{1.04}O_{3\pm\delta}$ after 5 days annealing. (a) SEM image. (b) BSE image of different area with enhanced contrast for atomic number Z, relief and surface cracks, both images show the secondary phase. (c) image of SEM with large particle of secondary phase with low average atomic number and profile of Mn/Lu ratio of the EDS line scan overlaid on SEM image, are taken from the upper part of secondary phase in (b).

For the study of long time annealed samples looking for traces of the secondary phases, the samples x=1.04 and 1.08 with 5 days annealing were chosen, as this last composition showed large particles of hausmannite in samples of one day annealing in previous SEM images, Figure 4-17.

Figure 4-22 is taken from a wide study of different regions of sample x=1.04 after 5 days annealing, on the attempt to detect secondary phases on dark regions, holes and inside grains. To reveal the grain boundaries this sample was thermally etched at 800 °C for 30 minutes after polishing the surface. The sample had already been investigated in SEM before thermal etching without finding traces of the secondary phase of hausmannite. The surface of the sample in Figure 4-22.a and b looks similar to the one in Figure 4-17 for short time annealing, where in that case some of dark regions showed deficiency of Lu few times lower than the atomic concentration of Mn.

The search across the center of the samples did not show any secondary phase. However upon moving the electron beam to the borders of the polished section, the secondary phase hausmannite appeared in some places. The BSE image Figure 4-22.b shows the secondary phase of hausmannite found in the $LuMn_{1.04}O_{3\pm\delta}$ 5 days annealed sample. Figure 4-22.c gives the relative concentration of Mn and Lu ions as the Mn/Lu ratio in the zone of the interface between the secondary phase and main phase on the right of the inclusion. The SEM image shows that the secondary phase may be a collection of smaller grains of the secondary phase. The plot of Mn/Lu ratio in Figure 4-22.c exhibits modifications in some places which may result from overlapping of smaller particles of Mn_3O_4 with larger particles of the main phase behind them.

Figure 4-23.a is the SEM image of a zone with two pores and grain boundaries of sample $LuMn_{1.04}O_{3\pm\delta}$ from 5 days annealing with subsequent thermal etching at 800 °C. As Lu_2O_3 secondary phase appeared mostly on the edge of pores, the image was zoomed to show the dark regions right on the edge of the pores as shown in Figure 4-23 and EDS elemental maps of Lu and Mn were taken, Figure 4-23.b and c, respectively. In both cases, the EDS mapping images of Mn and Lu show no counting rate variation for Mn or Lu that

could signal any lack or excess of one of the elements. Other points of darker contrast in SEM of the cross section of the $LuMn_{1.04}O_{3\pm\delta}$ sample were checked by EDS analysis but no shortage of Lu could be detected in relative amounts that could indicate any Mn-rich secondary phase or Mn_3O_4.

To scrutiny in more detail if there was any particle of secondary phases in the edges of the pores or in grain boundaries of the area analyzed by EDS in Figure 4-23.a, EBSD analysis was also done in this zone of the $LuMn_{1.08}O_{3\pm\delta}$ after 5 days annealed sample, Figure 4-23.d and f. This region of the sample in Figure 4-23.e was chosen because it presents some dark regions and clear grain boundaries exposed by the thermal etching.

As EBSD images in Figure 4-23 show that the grains are coarser than the grains in Figure 4-21, of the sample with shorter annealing time and composition x=1.04 close to the one of Figure 4-21. The EBSD phase map in Figure 4-23.e shows only the main phase $LuMnO_3$ phase (in green color). There is no preferential orientation of the grains in the crystal orientation maps of three Euler's angles in Figure 4-23.c to e. Increasing the annealing time did not give rise to modification of the random orientation of grains of the samples of short annealing time.

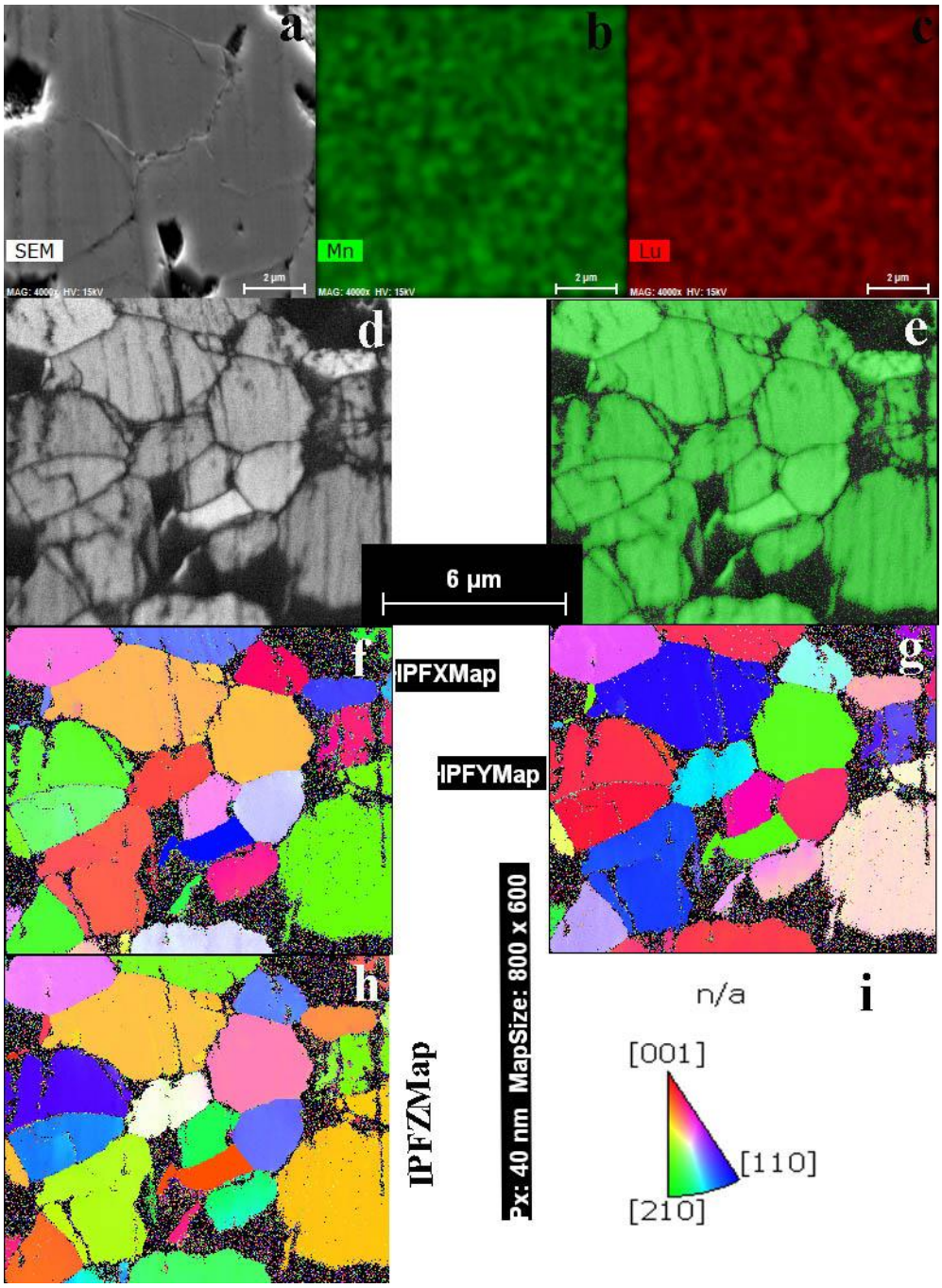

Figure 4-23. (a) SEM image of $LuMn_{1.08}O_{3\pm\delta}$ after 5 days annealing with EDS elemental mapping of Mn (b) and Lu (c) form this region, respectively. The images show pores and grain boundaries, with uniform distribution of Mn and Lu ions within the resolution of the image. (d) relief map and (e) EBSD phase map with its Euler´s components (f to g) and color code (i).

5. Magnetic behaviour of h-$LuMn_xO_{3\pm\delta}$ solid solution

The most essential aspect of the magnetic behaviour of the h-$RMnO_3$ oxides is the antiferromagnetic ordering transition at Neel temperature as it was discussed in Chapter 2. Hexagonal h-$LuMn_xO_{3\pm\delta}$ solid solution is expected to show AFM interaction with Neel ordering transition around 90 K wherever it preserves its space group in FE phase [30,34]. Since Lu does not have localized $4f^{14}$ electrons, this ion does not carry free magnetic moment to participate in magnetic interactions in h-$LuMnO_{3\pm\delta}$ lattice and hence Mn^{3+} ions are the sole magnetic ions inside the structure. The geometrical frustration results in non-collinear Mn^{3+} spin arrangement in basal plane with AFM interaction of the magnetic ions. The AFM ordering is explained by 2D magnetic interaction of frustrated Mn^{3+} ions forming trimers of nearest neighbour Mn^{3+} ions in the triangular network of the basal planes of the hexagonal lattice of the $RMnO_3$ compounds [30]. Any change in ionic positions of cations will duly modify magnetic moment (interaction), and therefore the magneto-electric coupling. The Lu-dependent or Mn-dependent properties may reveal additional details of the interlocked dependency of relevant properties on stoichiometry shifts set by excess of either of the Lu or Mn cations. Two important matters rising on the study of the magnetic interactions of polycrystalline h-$RMnO_3$ oxides are tentatively ascertained in this chapter. The first is that introducing vacancy in the lattice of h-$RMnO_3$ (R= Y, Lu and Sc) with non-magnetic rare-earth ions, can induce any plausible correlation of the strength/weakness of the magnetic interactions be explored. Second, that was seldom investigated [142] and not extensively is the effect of sintering duration on the magnetic performance of the h-$RMnO_3$ ceramics particularly of $LuMnO_3$. Present findings in Chapter 4 have shown that sintering time modified the lattice behaviour significantly, resulting in a trendy shift of the lattice parameters, namely the a-axis and volume of the unit cell with the Mn/Lu

ratio. It will be noteworthy to trace the change in T_N as function of the stoichiometry variable x and sintering time as well as in other magnetic parameters like magnetic moments and magnetic interactions associated to the values of Curie-Weiss temperature and frustration factor.

5-1 Contribution of secondary phases to the total magnetic moment

As shown in the previous chapter the presence of hausmannite secondary phase is detectable in XRD pattern and in SEM images of the $LuMn_xO_{3\pm\delta}$ samples. It will affect the magnetic properties of the $LuMn_xO_{3\pm\delta}$ main phase, the overall magnetic properties of the sample, and also measurements of such variables as the parameters of the Curie-Weiss law. External effects of random noise, dependent on the precision of the magnetometer, and of background magnetic signal originated by sample holder and equipment have also to be accounted for in the determination of the magnetic moment of the samples. The potential contribution of these disturbing effects on calculated parameters of the Curie-Weiss is established from simulations as described in the following, with details in Annex C.

Since the hausmannite shows ferrimagnetic behaviour with Curie-Weiss temperature around 43 K, deviation of the magnetic behaviour of the samples from the linear Curie-Weiss law when they have hausmannite extends up to higher temperatures [143]. It will be wise to use a function which can describe the magnetic signal of the secondary phase as a correction applied in proportion to the calculated amount of the secondary phase from the XRD Rietveld refinement and additional analysis of XRD spectrum in section 4-2. Since samples with shorter annealing time have the higher amounts of the secondary phase the analysis is focused in this set of samples. Later on we will apply the same analysis on samples with longer annealing time.

5-1-1: The influence of random noise and background signal

To make the dimensioning of the effect of random noise on the estimating of the parameters of the Curie-Weiss equation of the $LuMnO_3$ phase the magnetic signal of the pure $LuMnO_3$ sample is calculate from the susceptibility as a function of temperature with reported value of the Curie-Weiss constant for $LuMnO_3$ pure sample corresponding to the effective magnetic moment μ_{eff} ($LuMnO_3$) =4.9 μ_B, assuming spin only contribution and 880 K the modulus of Curie-Weiss temperature, early reported in the literature for $LuMnO_3$ single crystal (e.g.[35]). To match the system of units adopted in the main text of this thesis, the calculated Curie constant is expressed (emu.K/g.Oe) as:

$$C_{LuMnO3} = \frac{N_A \times \mu_{eff}^2}{3 \times MW_{LuMnO3} k_B} \qquad (5\text{-}1)$$

where N_A = 6.0221x10^{23} mol^{-1} is Avogadro´s number, k_B = 1.38064x10^{-16} $erg.K^{-1}$ is the Boltzmann constant, μ_{eff} = 4.9 μ_B = 4.9x9.274x10^{-21} $erg.G^{-1}$ and MW = 286.0701 $g.mol^{-1}$ is the molecular weight of the pure $LuMnO_3$, yielding

$$C_{LuMnO3} = 1.049542 \times 10^{-2} \frac{erg.K}{gr.G^2}$$

With the contribution of a background signal, χ_0, the modified equation of the Curie-Weiss law becomes

$$\chi_{LuMnO3} \left(\frac{emu}{gr.Oe} \right) = \chi_0 + \frac{C}{T - T_{CW}} \qquad (5\text{-}2)$$

Where C and T_{CW} are given above and χ_0 in emu/g.Oe represents any background contribution in real magnetic measurements. From the analysis of in section C-1 of Annex C, the value of background correction χ_0 was set at 1% of the average of χ of pure $LuMnO_3$ in the temperature range 150-300 K. A random noise close to 1% of the calculated value χ was added to the magnetic susceptibility χ_{LuMnO3} to simulate the experimental data. The calculated parameters of the magnetic susceptibility in Table 5-1

show a comparatively low sensitivity to the level of random noise. A change of no more than 6 K is found in the estimated values of T_{CW} which links directly to the width of the temperature range above T_N selected for least-square fitting with three adjustable parameters, Annex C, equation

(5-2) .

Table 5-1. Fitted values of the Curie-Weiss fitting, equation (5-2) for pure $LuMnO_3$, with χ_0=0, showing the reliability of the fitting approach used to extract parameters.

sample	T_{CW} (Initial) (K)	Background (fixed, constant)	Random Noise (emu/Oe.gr)	Range of Fitting	C(fitted) (emu.K/Oe.gr)	Effective Moment	T_{CW} (fitted) (K)
pure	-880	0	±1E-7	100-290 K	0.0105	4.90	-880.9
pure	-880	0	±1E-7	150-290 K	0.0105	4.89	-878.6
pure	-880	0	±1E-7	200-290 K	0.0104	4.88	-874.4

5-1-2: Effect of hausmannite on the magnetic properties of the pure $LuMnO_3$

The molecular field theory for two magnetic sub-lattices like Mn_3O_4 with Mn^{2+} and Mn^{3+} ions in different positions gives a model to describe the paramagnetic behaviour of the temperature dependent magnetic susceptibility at $T > T_C$, the results being adequately describe by the Lotgering´s equation [143]:

$$\frac{1}{\chi}\left(\frac{mol}{cm^3}\right) = \frac{T}{C} + \frac{1}{\chi_0} - \frac{\sigma}{T-\Theta} \qquad (5\text{-}3)$$

where C is Curie constant, σ, χ_0 and Θ are adjustable parameters in fitting. The values of the constants are used here from Ref. [143] Θ =10.2 K, σ = 1700 mol/cm^3.K, $1/\chi_0$ = 57.5 mol.Oe/cm^3, C=10.43 cm^3.K/mol.Oe. Equation (5-3) is converted to the susceptibility in mass using the molar mass of Mn_3O_4 as 228.814 g/mol:

$$\frac{1}{\chi_{Mn_3O_4}}\left(\frac{\text{g.Oe}}{\text{emu}}\right) = 275.6818\text{T} + 1.6533\text{x}10^5 - \frac{4.8881\text{x}10^6}{\text{T}-10.2} \qquad (5\text{-}4)$$

In present approach, the total magnetic susceptibility, Equation (5-5) is calculated as the linear combination of the magnetic susceptibility of the main phase with a relative fraction (mass fraction) (1-f_m) and of the secondary hausmannite phase with the amount of secondary phase evaluated from Rietveld refinement of the XRD patterns (section 4-2), the magnetic susceptibility of hausmannite being calculated with equation (5-4):

$$\chi_{\text{measured}}\left(\frac{\text{emu}}{\text{g.Oe}}\right) = (1-\text{f}_\text{m}).\chi_{\text{Lu}Mn_xO_3.}\left(\frac{\text{emu}}{\text{g.Oe}}\right) + \text{f}_\text{m}.\chi_{Mn_3O_4}\left(\frac{\text{emu}}{\text{g.Oe}}\right) \qquad (5\text{-}5)$$

where 1- f_m is the mass fraction of the main phase from XRD pattern (Table 4-1).

Table 5-2. Results of fitting of the magnetic susceptibility of the pure $LuMnO_3$ assuming 1-f_m weight fraction of the main phase and f_m of the hausmannite phase in equation (5-5).The overall signal of sum of magnetic signals of two phases is used as the raw data for fitting. Then the f_m was changed (as a fix parameter) during each fitting to understand how much change do we have in magnetic parameters if the amount of secondary phase estimates incorrectly from XRD. Zero as subscript holds for initial values to start least-square fitting.

	Mn_3O_4(wt fraction)	T_{CW}(K)	C(emu.K/g.Oe)	1-f_m	R-Square
1	0.05	-878.4	0.01044	0.949	0.99726
2	0.04	-876.8	0.01044	0.959	0.99671
3	0.03	-875.2	0.01045	0.969	0.99598
4	0.02	-873.7	0.01045	0.980	0.995
5	0.01	-872.2	0.01046	0.990	0.99366
6	0.005	-871.5	0.01046	0.995	0.99279

Figure 5-1 shows the values of T_{CW} and μ_{eff} of least-square fitting using a simulated sample of $LuMnO_3$ mixed with different amounts of hausmannite with magnetic susceptibility determined by the formula in equation (5-4). In these calculations, the background correction χ_0 as in previous approaches was zero (in equation (5-2). The fitting range was started from 90 K until 350 K.

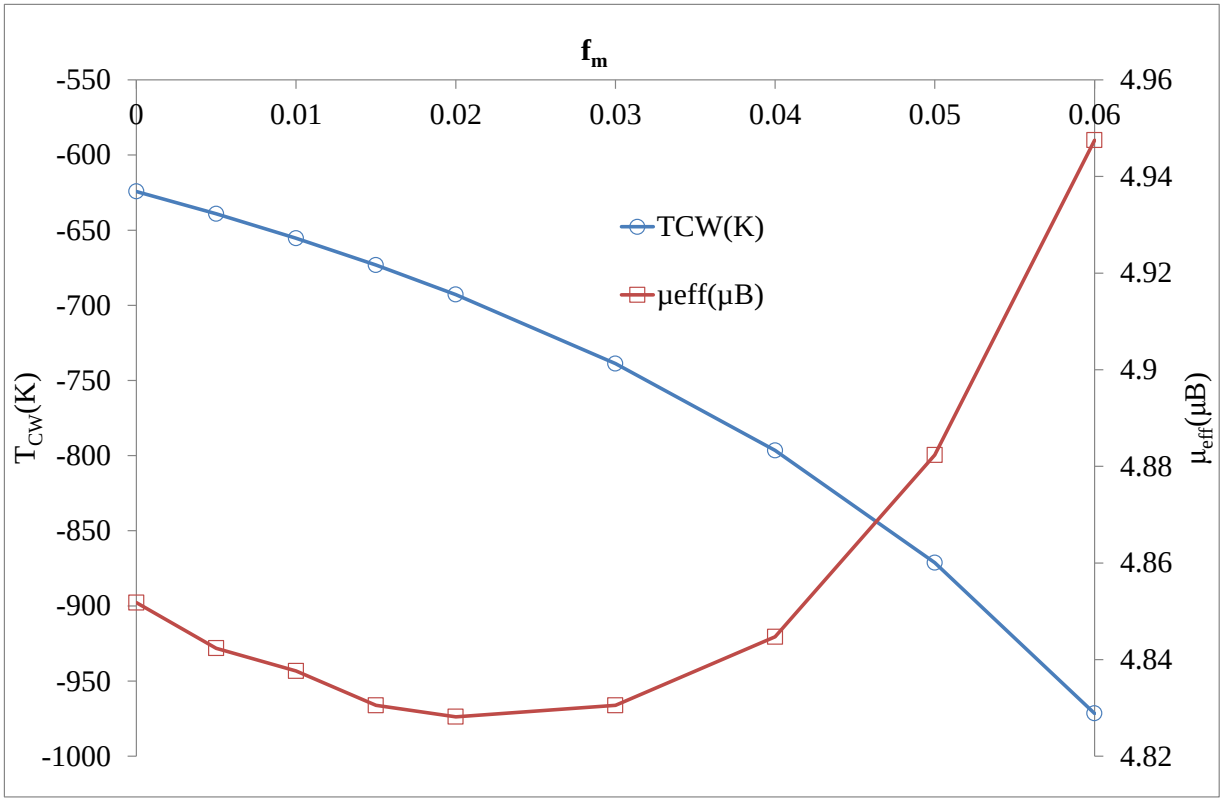

Figure 5-1. Curie-Weiss temperature of $0.95LuMnO_3+0.05Mn_3O_4$ and effective magnetic moment calculated from least-square fitting approach considering the overestimated weight fraction of the hausmanite (circle denotes T_{CW}, square, effective magnetic moment).

In Figure 5-1 within the range of temperature for fitting, one percent change in amount of hausmannite phase results in 50 K shift in calculated values of Curie-Weiss temperature, which reveals large sensitivity of the estimation of the magnetic parameters of the main phase to the magnetic signal of hausmannite. The inverse of χ is represented in Figure 5-2 for three different cases, the linear Curie-Weiss behaviour of $LuMnO_3$ phase calculated from equation (5-2), with $\chi_0=0$, the magnetic susceptibility of Mn_3O_4 given by the Lotgering equation (5-4) and the total value of $1/\chi$ for the simulated sample with 5 %wt of Mn_3O_4. The comparison of three cases portrays the non-linearity of inverse of magnetic susceptibility under the effect of the secondary phase extended up to 150 K for the mixture of two phases. Therefore, at least within this temperature range,

the use of Curie-Weiss law results in some uncertainty in the calculated parameters when samples have traces of Mn_3O_4.

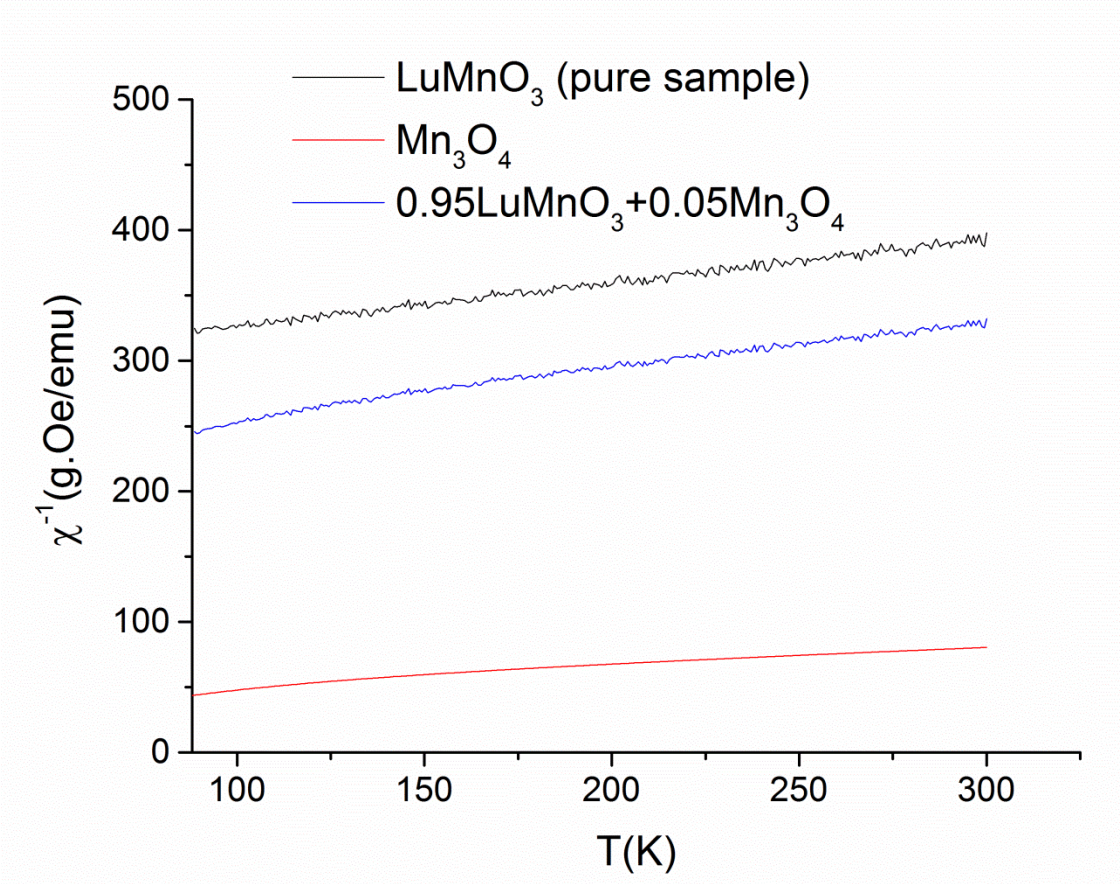

Figure 5-2. Inverse of the magnetic susceptibility for three different contributions of total magnetization indicating the effect of the hausmannite on the bending of the mixed phase sample (blue one). The red curve shows inverse of magnetic susceptibility of 5% wt. of Mn_3O_4 phase.

5-2 Magnetic behaviour of non-stoichiometric h-$LuMn_xO_{3\pm\delta}$

At the beginning of this section attention is paid mostly to samples that were sintered for one day at 1300 °C which are conditions commonly used by others in their studies on the properties of the h-$RMnO_3$ oxides [34,37,70,72,75]. This section is focused on the effect

of off-stoichiometry on the magnetic properties and presents some of the difficulties raised in their determination.

5-2-1 Irreversibility of off-stoichiometric ceramics after one day annealing

Figure 5-3 shows the magnetic susceptibility of the selected samples of 1 day annealing measured in field-cooled (FC) condition under the applied magnetic field of 100 Oe with SQUID. With increasing x a change of magnetization right just below, or at Neel ordering transition around 90 K is observed. The increasing of Mn content (x=1.08 and x=1.12) in Figure 5-3 resulted in neatly intensification in magnetic signal below T_N for the FC condition.

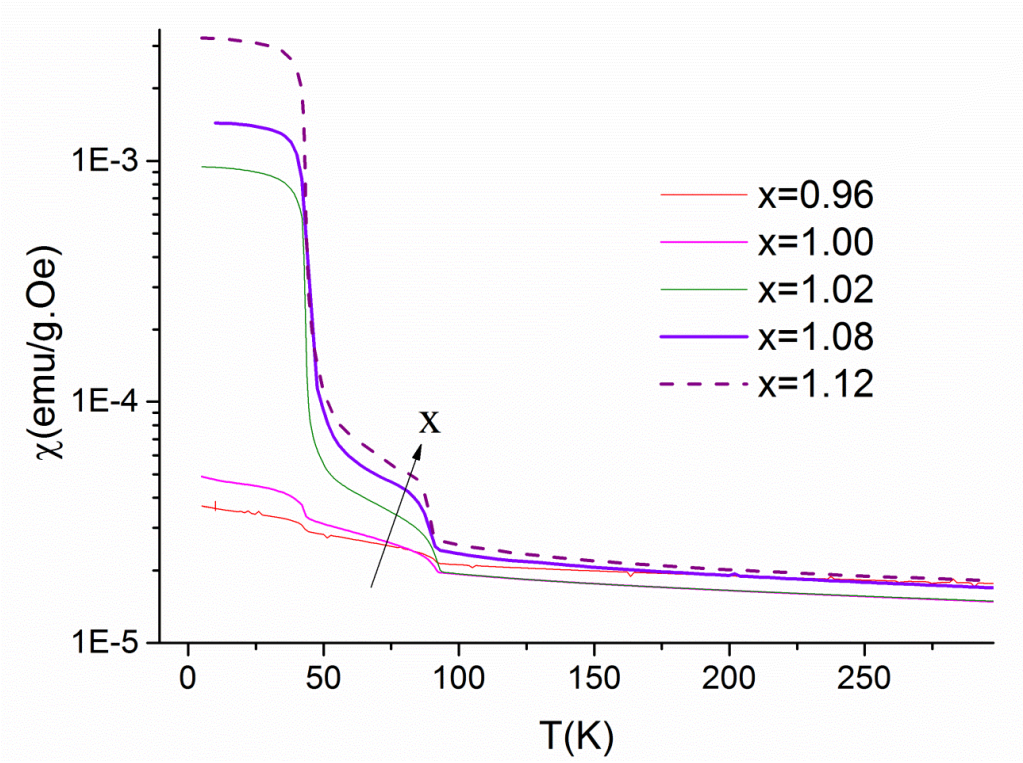

Figure 5-3. FC magnetic susceptibility of the selected samples of one day annealing measured under 100 Oe applied field, showing the effect of the off-stoichiometric on the magnetic behaviour of the sintered ceramics.

In the paramagnetic region in the temperature range above the T_N, the values of magnetic susceptibility are all of the same order. The sharp rise of χ in the temperature range below 45 K coincides with the ferrimagnetic ordering transition of hausmannite [92,143]. As found in the $YMn_xO_{3\pm\delta}$ with $x \geq 1.05$ [19], the nominal compositions with large excess of Mn displays the higher values of χ in the temperature range below 40 K. Figure 5-4 shows the temperature dependence of the magnetic susceptibility with the applied magnetic field of 500 Oe for zero-field-cooled (ZFC) and field-cooled (FC) conditions of three samples with x = 0.92, x=1.00 and x = 1.08, respectively.

Antiferromagnetic (AFM) ordering is seen for both sides of the off-stoichiometric range and in the stoichiometric composition at values of T_N all close to 90K. Fitting of the reciprocal of the magnetic susceptibility, χ^{-1}, to the Curie-Weiss law, determined by SQUID magnetometer under 100 Oe applied magnetic field, is presented in insets of Figure 5-4.a, b and c. Figure 5-4.a to c for x=0.92, 1.00, 1.08, respectively, demonstrate the difference on the magnetic behaviour observed for all samples when the ZFC and FC conditions used in the magnetic measurements. With increasing x ratio large differences of the magnetic susceptibility measured in ZFC and FC conditions appeared below T_N, the behaviour already reported for h-$RMnO_3$ materials exhibiting spin-glass behaviour or irreversibility in ZFC/FC magnetic measurements [67,70,75–77]. The reciprocal of magnetic susceptibility, χ^{-1}, deviates from the linear dependency on T expected from Curie-Weiss law in the paramagnetic region approaching T_N, as previously reported by others for h-$LuMnO_3$ [34,35]. The deviation from Curie-Weiss law in measurements makes it difficult to estimate the parameters of the Curie-Weiss law itself for the overall set off-stoichiometric samples of the present study as discussed above in section 5-1.

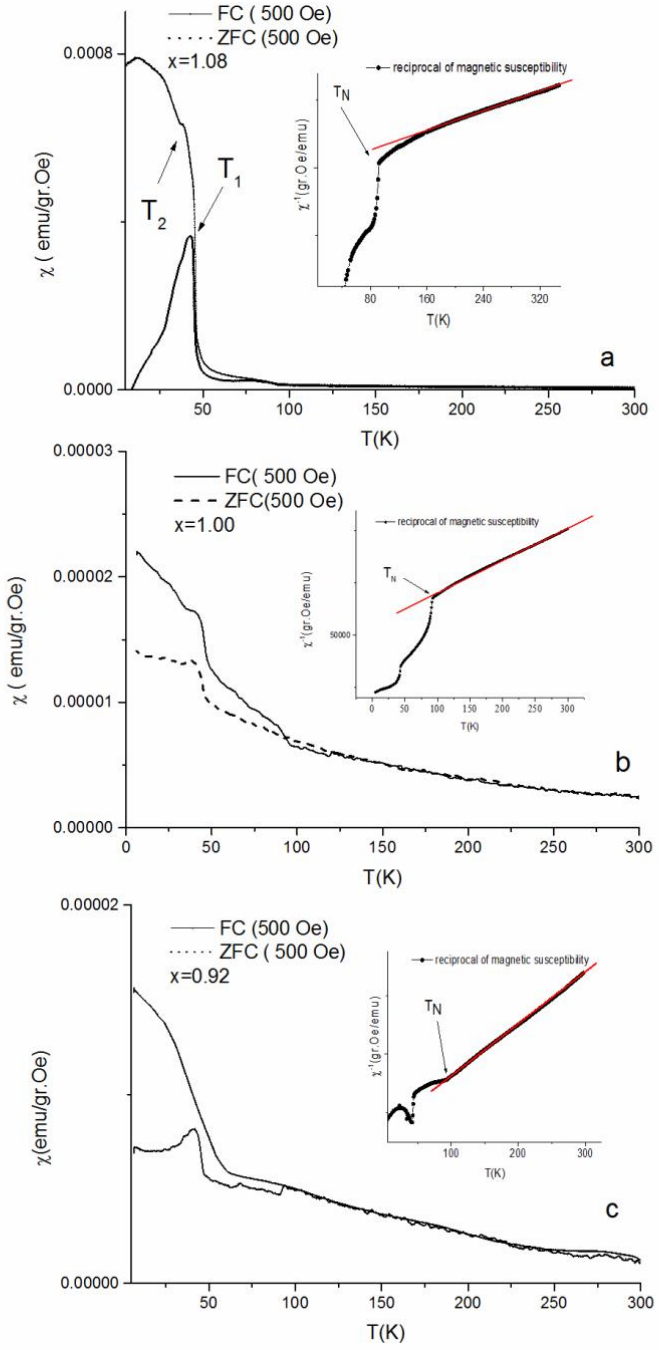

Figure 5-4. ZFC vs FC magnetic susceptibility of $LuMn_xO_{3\pm\delta}$ samples, 1 day annealing, with nominal composition, (a) x=1.08, (b) x=1.00 and (c) x=0.92, indicating the differences in ZFC and FC magnetic signals appeared at Neel ordering transition (500 Oe applied magnetic field). The inset of each figure shows the reciprocal of χ measured by SQUID under 100 Oe applied filed, and deviation of the apparent linear Curie-Weiss law for the sample of larger Mn content.

The co-existence of frustrated AFM order and weak FM order below T_N has been observed in the temperature dependent magnetization of $LuMnO_3$ and $YMnO_3$, and it was attributed to diverse origins such as the exchange coupling between AFM and FM orders [68], Mn spin reorientation and Dzyalloshinskii –Moriya interaction [62,76,77,144], double exchange interaction of Mn^{2+}/Mn^{4+} and Mn^{3+} ions [63] or local MnO_5 distortions [45]. Previously reported results of magnetic susceptibility in $YMn_{1+x}O_{3\pm\delta}$ ceramics samples with large Mn content as in the Mn-rich side of $LuMn_xO_{3\pm\delta}$ samples in the present study also resulted in weak-ferromagnetism co-existing with the frustrated antiferromagnetic order [19,76]. By accounting for the secondary phases detected in off-stoichiometric samples, section 4-2, in the Mn-rich side (x>1) the Mn_3O_4 phase will contribute to the magnetic signal below the 43 K transition temperature [92] in proportion to the fraction of this phase present in the samples. That would not be expected for the case of samples in the Lu-rich side with x≤1 which still show a rising of magnetic susceptibility below T_N although of lower intensity with no indication of Mn_3O_4 on results of Rietveld refinement of XRD (Table 4-1, section 4-2). The detailed analysis of the XRD lines for the presence of faint traces of Mn_3O_4 in Figure 4-6 indicates that samples of 1 day annealing time in the Lu-rich side are not completely free of this phase. The difference between the values of FC and ZFC magnetization is sensitive to the intensity of the weak ferromagnetism in the sample [71].

The origin of the weak ferromagnetic component of χ had been explained by Dzyaloshinskii-Moriya exchange interaction, because of geometrically frustrated trimers of the Mn ions in the basal plane [70,71,74]. The plot of χ^{-1} of Figure 5-4.a for the sample with x= 1.08, shows two anomalies or transitions in the magnetic susceptibility below $T_N \approx$ 90 K. The first transition at temperature T_1 in the range of 40 - 45 K is most likely correlated to the ferrimagnetism of the Mn_3O_4 phase. The origin of the second transition corresponding to T_2, below 40 K is hardly known; it may originate from the spin reorientation of Mn^{3+} moment in $LuMnO_3$ [62,77,145]. The coexistence of different configurations of AFM order below T_N in $ScMnO_3$ as well as in other h-$RMnO_3$ materials was already observed in a Second Harmonic Generation (SHG) experiments having been

assigned to inhomogeneity in the crystalline lattices [145]. In the Lu-excess side of the samples of the present study, the difference between ZFC and FC magnetization below T_N becomes weaker as the ratio x decreases. On the contrary, addition of Y ions in excess to $YMn_{1+x}O_{3\pm\delta}$ ceramics ($x < 1$) resulted in more pronounced irreversibility below T_N with a slight decreasing of T_N matched by an important increase in Curie-Weiss temperature, lower $|\theta_{CW}|$ [17]. The rising of θ_{CW} with minor changes of T_N implies a decrease of f_m, the frustration factor indicating that self-doping with Y weakens the geometrically frustrated magnetic interactions of Mn^{3+} ions in the basal plane of $YMnO_3$ ceramics [30].

5-3 Effect of sintering time on irreversibility of magnetic behaviour

The evolution of the parameters the unit cell of off-stoichiometric $LuMn_xO_{3\pm\delta}$ samples proved to be strongly influenced by the annealing time, as shown in chapter 4. The dependence of the lattice constant on x revealed a stable solid solution with the approximate range of stability of $0.94 \leq x \leq 1.04$. This scenario was repeated for the observed evolution of grain size. The possibility of observation of the secondary phase of hausmannite as an impurity phase in the materials in samples of extended annealing time was investigated too. The trends for change of the magnetic behaviour of the samples annealed for different periods of time are examined in this section.

5-3-1 Irreversibility of magnetization

Figure 5-5 compares the field cooled (FC) magnetic susceptibility of samples of two different compositions in the high Mn-rich side with one day and 5 days annealing time. The magnetic signal of samples of both compositions after the longer annealing time has been visible reduced, the reduction being more prominent in the region below 50 K. The

magnetization in this region of temperatures can also display the contribution of ferrimagnetic hausmannite below 43 K [90]. The decrease in magnetization below 50 K in Figure 5-5 is matched by a parallel decrease in Mn_3O_4 fraction in XRD results in Table 4-1 and Table 4-2. Minor amounts of hausmannite remain in these samples after 5 days and 10 days annealing time and are detected by XRD.

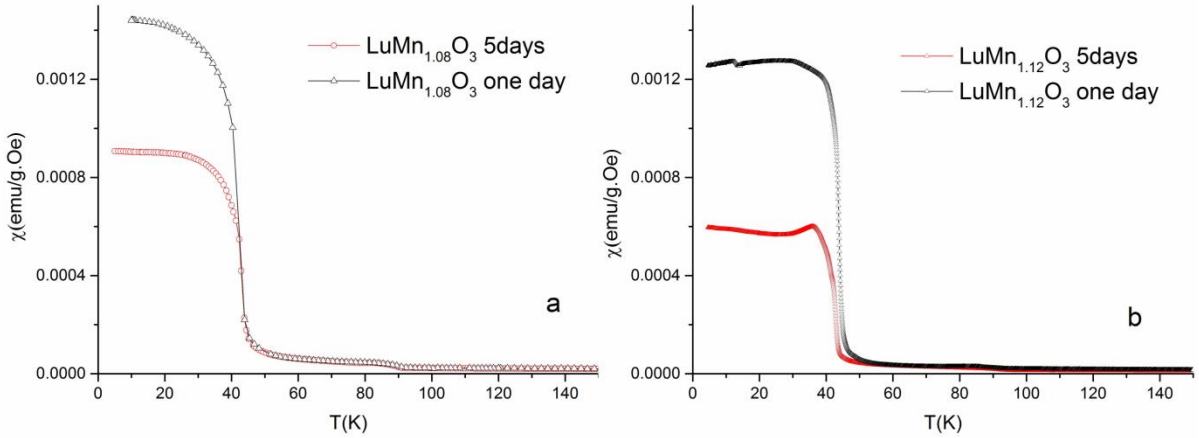

Figure 5-5. FC magnetic susceptibilities of the two $LuMn_xO_{3\pm\delta}$ samples after one day and 5 days annealing. (a) x=1.08 and (b) x=1.12 (100 Oe applied field).

The reduction of the signal of the magnetic susceptibility from 0.0014 emu/g.Oe to 0.0009 emu/g.Oe for x=1.08 samples and comparing the values of the residual secondary phase in section 4-2 from XRD data (1.19% weight fraction for one day and 0.77% weight fraction after 5 days annealing) quantitatively confirm that most part of the signal below 50 K comes from Mn_3O_4 secondary phase. The decrease in amount of secondary phase after 5 days annealing of 65% and the observed reduction in the signal of magnetic susceptibility 64% are roughly the same within the limit of error of the XRD detection for minor amounts of the secondary phases.

It was found that for temperatures between 15 K and 45 K the shapes of ZFC magnetization of sample x=1.04, 5 days annealing, and of sintered hausmannite,

Figure 5.a in reference [92], determined under the same applied magnetic field of 1000 kOe were almost identical, Figure 5-6.a. The fraction of hausmannite determined by Rietveld refinement in the same x=1.04 sample is 0.33 wt%,Table 4-2. The fitting of Lotgering´s equation (5-4) to this set data of pure hausmannite for temperatures above $T_C \approx 43$ K was found adequate with the following values of the parameters Θ =15.0 K, σ=1720 mol/cm^3.K, the other two parameters $1/\chi_0$ and C keeping the same values as given above in section 5-1-1, from Ref. [143]. Differences in the samples of hausmannite and in magnetic field 1000 Oe in Ref. [92] and 200 Oe in Ref. [143] used to determine the magnetic susceptibility of hausmannite in the paramagnetic region yielded the variation in values of parameter θ and the small correction of the parameter σ of Lotgering´s equation. Values of χ of hausmannite and of the $LuMn_{1.04}O_{3\pm\delta}$ sample are brought to close matching between 15 K and 45 K in Figure 5-6.a with a calculated fraction of hausmannite of f_H=1.8 wt%. For this same fraction of hausmannite and temperatures above T_N of $LuMnO_3$ the corresponding values of χ determined with the Lotgering´s equation represents just 7-8 % of total magnetic susceptibility χ of the $LuMn_{1.04}O_{3\pm\delta}$ sample, Figure 5-6.a. As also shown in Figure 5-6.a, above 80 K the difference in the values of χ of hausmannite resulting from using one set of parameters of Lotgering´s equation or the other is no more relevant. Differences of aggregation and dispersion of the hausmannite phase in the well-sintered pellets and as disperse impurity in the $LuMn_{1.04}O_{3\pm\delta}$ sample may account for the large difference in the results of quantification of the hausmannite present in the sample by Rietveld refinement and by the fitting of values of χ in Figure 5-6.a. In the inset of Figure 5-6.b the values of FC magnetic susceptibility of $YMnO_3$ with 1.2 wt% added hausmannite and of sample $LuMn_{1.08}O_{3\pm\delta}$, 5 days annealing, determined with the same applied magnetic field of 100 Oe, are much closer together than for the previous case analysed in Figure 5-6.a. As shown in the same inset, close matching of the two functions of χ below 43 K is obtained for a calculated fraction of hausmannite of f_H=0.88 wt%. The corresponding fraction of hausmannite determined by Rietveld refinement in this same x=1.08 sample is 0.77 wt%, Table 4-2. On accounting for this finding, the difference in values of FC susceptibility between 39 K

and 46 K of $YMnO_3$+1.2 wt% Mn_3O_4 was determined as 5.85 10^{-4} emu/g.Oe, original data from Figure S4-down, Supporting Information Ref. [90]. In a similar way, for all samples of the set with 5 days annealing time, the differences in values of FC susceptibility between two fixed values of temperature 42.3±0.3 K and 48.3±0.5 K, below and above the observed T_C points of hausmannite, respectively, were also determined and used to calculate the fraction of hausmannite (f_H^+, last row of Table 5-2) present in the $LuMn_xO_{3\pm\delta}$ samples in proportion to the value above of the difference in χ values and the known fraction of hausmannite in the $YMnO_3$+1.2 wt% Mn_3O_4 taken as a reference. When the this same procedure is applied to the values of χ of $ScMnO_3$ and h-$YMnO_3$ in Figures 3.a and 4.a of Ref.[90], respectively, the following values f_H=0.11 wt% and f_H=0.005 wt% are obtained, the same as given by the author in Ref. [90]. The value hausmannite fraction in the $LuMn_{1.08}O_{3\pm\delta}$ sample determined with this procedure from two independent measurements of χ is f_H^+=1.23 wt%, last row in Table 4-2. As given in Figure 5-6.b, there is a linear proportion between the fraction of hausmannite determined by this procedure and from the analysis of heights of the (103) XRD line of Mn_3O_4 in Figure 4-5, values in row one before the last in same Table 4-2. As also seen in the values of f_H gathered in this table, while the detailed analysis of the (103) XRD line of Mn_3O_4 cannot detect traces of this phase below the threshold of 0.2 wt%, the large sensitivity of SQUID magnetometers reveals the presence of hausmannite in the magnetic signal and allows semi-quantified determination of weight fractions hausmannite as low of 0.005 wt% in the samples of h-$RMnO_3$ materials [90].

Figure 5-7 presents the magnetic susceptibility of samples of two compositions x=0.92 and x=1.00 at ZFC and FC conditions after 5 days and 10 days annealing. Spin-glassy state of the h-$RMnO_3$ materials were discussed above in this chapter [67,70,75–77]. There is evidence in Figure 5-7 that the spin-glassy state of the stoichiometric $LuMnO_3$ samples and off-stoichiometric Lu-rich samples has not been much affected by annealing time.

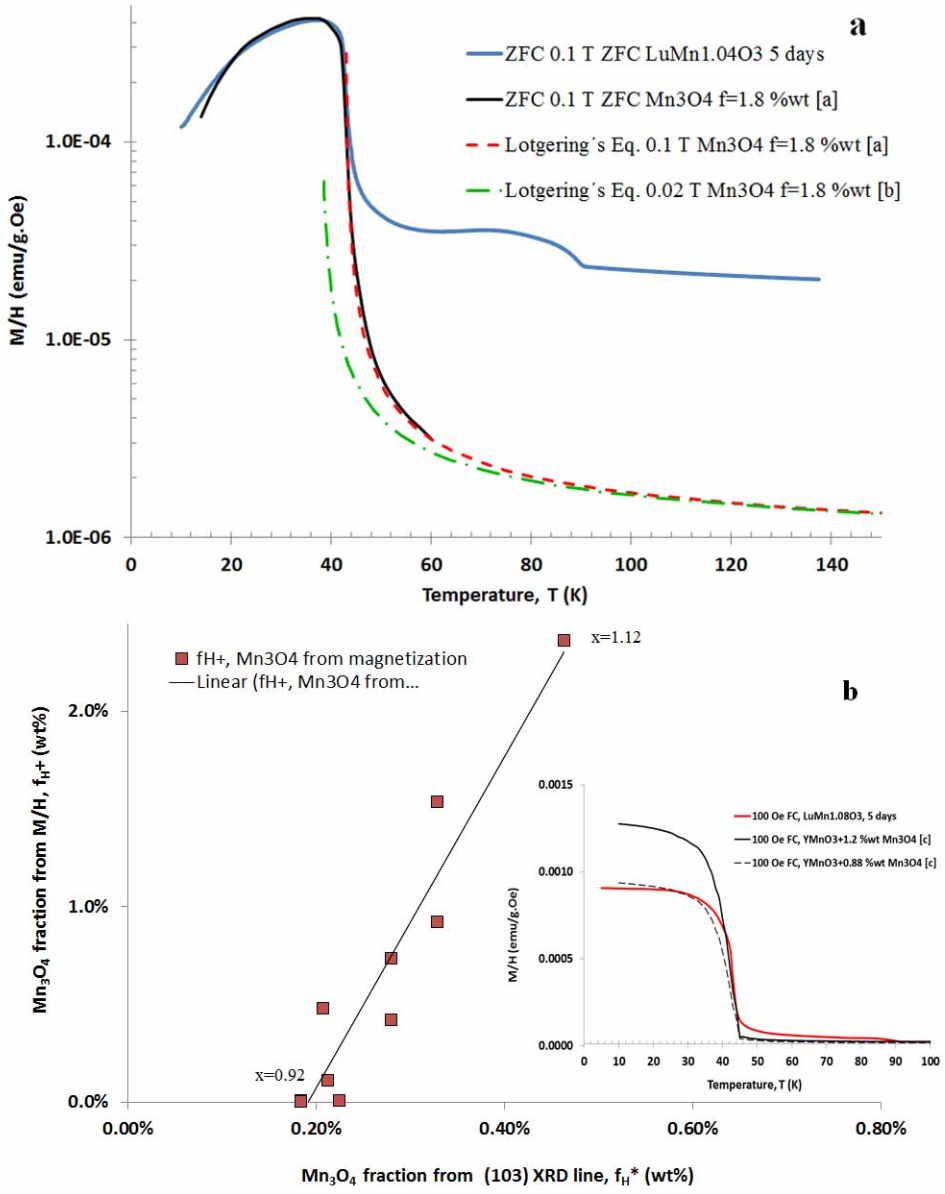

Figure 5-6. Comparison of magnetic susceptibility of hausmannite below 45 K and of samples of the present study. (a) Overlapping of values of ZFC χ of hausmannite for a calculated fraction f_H= 1.8 wt% and values of ZFC χ of $LuMn_{1.04}O_{3\pm\delta}$, 5 days annealing, same applied magnetic field of 1000 Oe. (b) Linear correspondence between values weight fraction of hausmannite in samples of 5 days annealing determined by the method given in the inset and from the intensity of the (103) XRD line of Mn_3O_4 in Figure 4-5. Inset: FC magnetic susceptibility of $YMnO_3$ with 1.2 wt% added hausmannite and of sample $LuMn_{1.08}O_{3\pm\delta}$, 5 days annealing, same applied magnetic field of 100 Oe, with close overlap for calculated f_H=0.88 wt%. Data sources, (a) Ref.[92] , (b) Ref. [143], (c) Ref.[90]

In samples x=0.92 after 5 days and 10 days annealing, still there is a small peak in the magnetization around 43K, which indicates traces of Mn_3O_4 or intergrowths of planes of Mn_xO_{1-x}, eventually of a phase very close to Mn_3O_4. Although evidence of secondary phase of hausmannite could not be found in XRD Rietveld refinement, in SEM and EBSD analysis of samples of x≤1 after 5 days or 10 days annealing and corresponding values of f_H* in Table 4-2 and Table 4-3, there is an indication in Figure 4-4 that the presence of hausmannite is traceable directly by the almost extinguished (103) XRD line in XRD patterns. For the $LuMn_xO_{3\pm\delta}$ samples with composition in x<1 side the values of fraction of Mn_3O_4 f_H^+ in last row of Table 4-2 determined from the correlation between the local increase of magnetization of the $RMnO_3$ materials below 50 K and the content of the impurity yielded values of f_H^+ above or at the level of the low threshold of 0.005 wt% for detection of Mn_3O_4 in $YMnO_3$ in magnetization results determined by SQUID [90]. The observation of a faulty stacking sequence of atomic planes with a missing plane of Mn-O in the layered sequence of Lu-O/Mn-O/Mn-O/Lu-O in TEM images of the same x=0.92 sample after one day annealing to be discussed in the next chapter is not evidence of free Mn_3O_4 in the form intergrowth planes but points towards the presence of mechanisms with the potential to accommodate matter of impurity phases intercalated in the crystalline lattice of the h-$RMnO_3$ phase. There is evidence that the in-situ formed nano-layers of Fe_3O_4 observed by HAADF-STEM in MOCVD thin films of hexagonal $LuFeO_3$ are thermodynamically stable [46].

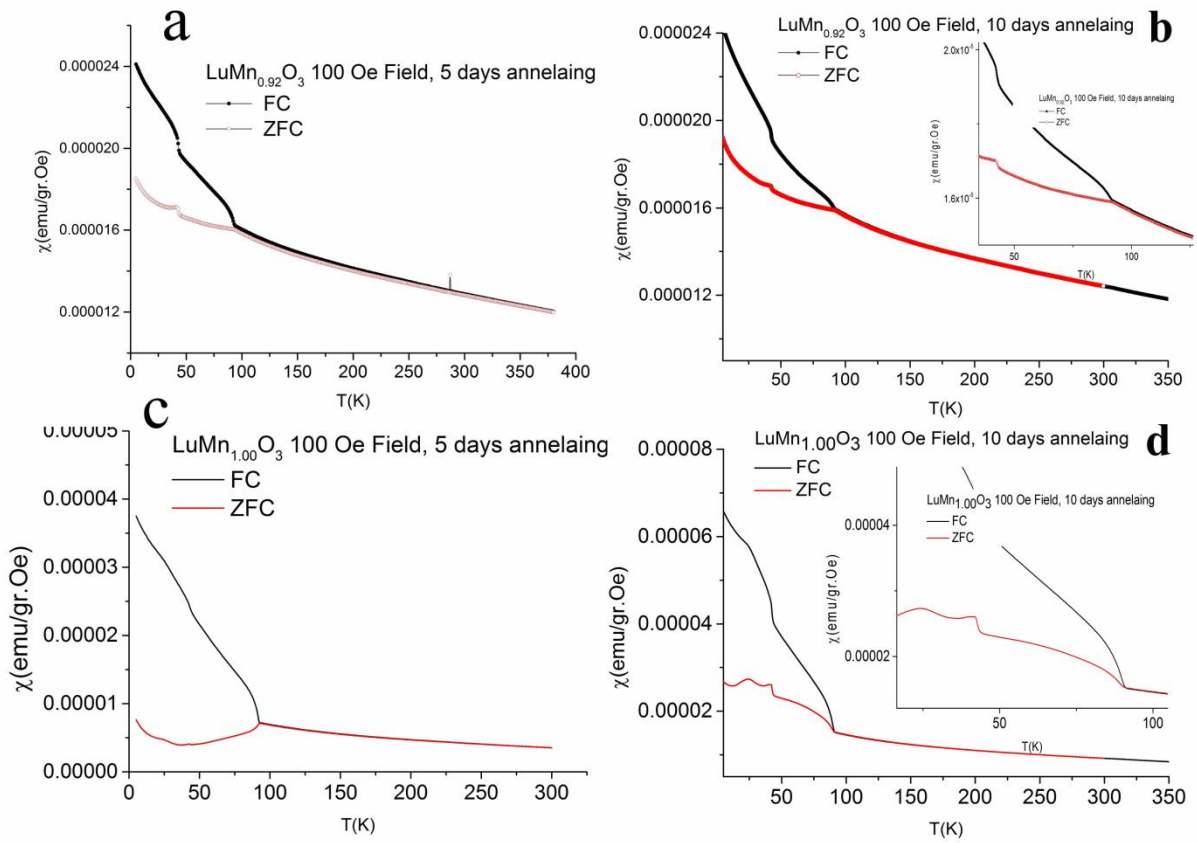

Figure 5-7. Long annealing time effect of the sintering of ceramics on spin glass state of the two samples taken by FC vs ZFC conditions under 100 Oe applied magnetics field, x=0.92 (a) and (b) and x=1.00 (c) and (d).

For sample x=1.00, the spin-glass state is stronger than x=0.92 after 5 days annealing, as the slope of FC curve sharply increases below T_N, the region well above the Curie temperature of Mn_3O_4 secondary phase, Figure 5-8. The strength of the spin-glass state for undoped and vacancy doped lattices indicates the effect of doping on modification of magnetic interactions inside the lattice structure.

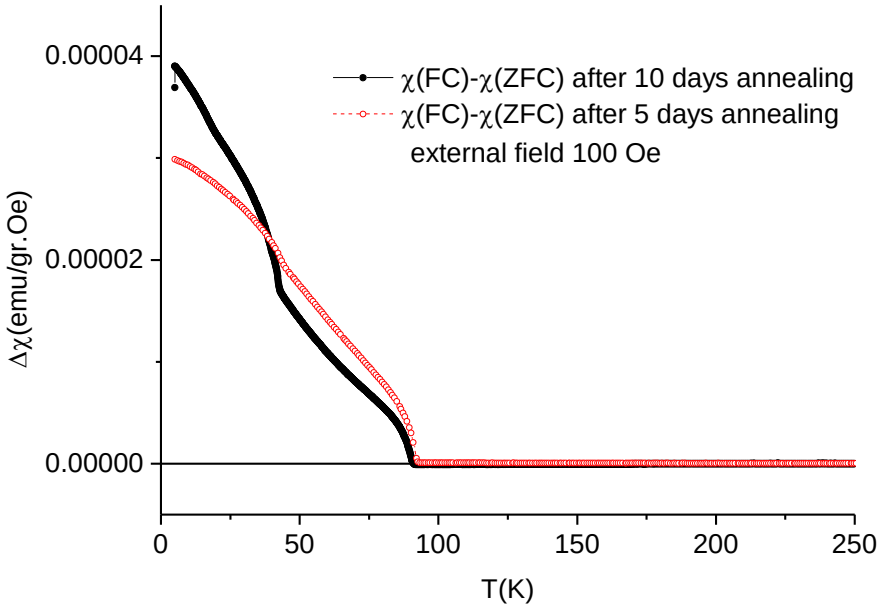

Figure 5-8. Subtraction of ZFC signal from FC signal of FC vs ZFC curves in previous figure (c and d) for sample x=1.00, which shows irreversibility in AFM region.

Figure **5-8** gives the difference in FC and ZFC magnetic susceptibilities of the sample x=1.00 for two different sintering times. In the $LuMnO_3$ results in Figure 5-7 as in $ScMnO_3$ and $LuMnO_3$ magnetic susceptibility results previously reported [36,62,72,76] the presence of small ferromagnetic component appears right just at T_N and its intensity is continuously enhanced below T_N until the lowest measured temperature is approached [71].

5-3-2 Neel temperature of antiferromagnetic ordering

Since multiferroicity in h-$RMnO_3$ materials comes from spin ordering of Mn^{3+} ions in AFM phase at it is coupled to electrical polarization, the study of cation vacancy effect on T_N may also assist on creating a deeper understanding of the role of cations in the

properties of these materials. Figure 5-9 indicates the change of the Neel temperature of the $LuMn_xO_{3\pm\delta}$ samples after different annealing times (method of extracting T_N from data was explained in section 3-5). The overall trend is for a decreasing of T_N with increasing values of x.

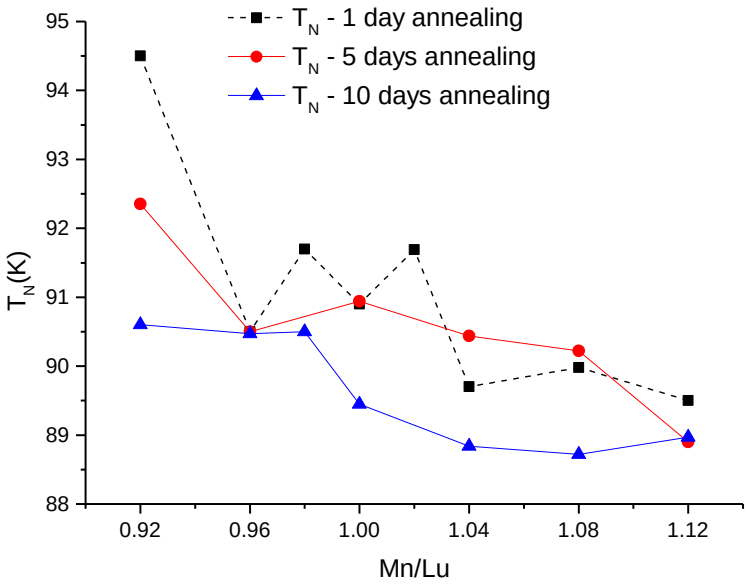

Figure 5-9.Evolution of Neel ordering transition measured for selected samples at different sintering conditions.

The clear change on having more trendy behaviour without significant fluctuation appears in set of samples sintered after5 days and 10 days. This is more evidenced on Lu-rich side (x =0.92) when sample with one day annealing is almost out of range of values for other compositions. Because AFM interaction among Mn^{3+} ions in basal plane of h-$LuMnO_3$ oxide depends on both atomic distances of the magnetic ions and the angle between bonds of Mn-O3(4), in driving any conclusion we have to take into account both factors. The AFM interaction energy can be approximately expressed by the following equation:

$$U \cong \frac{1}{2} J_{ave.} \sum \hat{S}_i . \hat{S}_j$$

(5-6)

a function of the $J_{ave.}$, the super-exchange integrals mediated by the oxygen ions between the nearest neighbour Mn^{3+} ions in basal plane [146,147]. $J_{ave.}$ in h-$RMnO_3$ materials in basal plane consists of two components J_1 and J_2 because there are two oxygen ions in basal plane, O_3 and O_4, which mediate the super-exchange interaction of Mn^{3+} ions. Also, any distortion inside the Mn trimers can change the values of J_1 and J_2 and subsequently the energy of AFM interaction. Therefore, the alteration of distance of two transition metal ions in basal plane and the bond angle of Mn-$O_{3(4)}$-Mn would result in the real energy of AFM interactions in basal plane.

5-3-3 Curie-Weiss temperature and frustration factor

The Curie-Weiss temperature of the $LuMn_xO_{3\pm\delta}$ samples was calculated by the method described in section 5-1 and Annex C with subtraction of background correction χ_0 and the component correspondent of the Mn_3O_4 secondary phase from the total magnetic signal of the sample. The values of T_{CW} and effective magnetic moment are given in Table C-6 in Annex C. Figure 5-10.a presents the change of the T_{CW} of the given samples from three sets of samples, the composition with x<1 yielding more negative values of T_{CW}. Inside the stability bounds of the $LuMn_xO_{3\pm\delta}$solid solution T_{CW} increases in a regular way with x, behaviour opposite to Mn-vacancy compositions. T_{CW} values of x<1 ranges from -1100 K to -700 K. On the x>1 side T_{CW} increases up to -500 K in samples with Mn content above the upper stability limit of the solid solution. Curie-Weiss temperature of x<1 shows sensitivity to the sintering time, values of T_{CW} increased as time of annealing is extended. Within the error of the calculation there in no much sensitivity to annealing time for samples on x>1 side of composition. Comparison is made in Figure 5-9Figure 5-10.a of the results of this study with the dependence of T_{CW} of YMn_xO_3 on x from two independent studies, for x≥1 [19] and x≤1 [17]. The effect of Mn/Y ratio on

the values T_{CW} is opposite to the one observed in $LuMn_xO_{3\pm\delta}$ in the present study, the two sets of T_{CW} data converging to similar values only for samples with nominal compostion above x>1.05. Linked at the same time to T_N values in Figure 5-9 and to T_{CW} the frustration factor $f=|T_{CW}/T_N|$ ([30]) in Figure 5-10.b gives an indication of the diminished frustration of the Mn trimers in basal plane of the hexagonal lattice as composition moves from the high excess Lu-side to the high excess Mn-side of the $LuMn_xO_{3\pm\delta}$ solid solution. This frustration has been discussed as driven by the titling of the MnO_5 bipyramids and buckling of the Lu planes inside the unit cell [25,30,34,127]. Frustration factor f covers a range of values from 11.5 for x=0.92 to 5.6 for x=1.08. Both T_{CW} and f demonstrate the important role of type of vacancies and their concentrations in self-doping of h-$RMnO_3$ lattices. T_{CW} for $LuMnO_3$ of nominal composition in the present study stays between -700 K and -600 K, the corresponding f factor changes from 7 to 8. Values of the frustration factor f and T_{CW} of $LuMnO_3$ polycrystals of nominally stoichiometric composition were reported as 5.8 (T_{CW}= -519 K) [36], 6.76 (T_{CW}= -602 K) [115], 8.25 (T_{CW}= -750 K) [34] and for $LuMnO_3$ single crystal 10.3 (T_{CW}= -887 K) [35]. The measured values of polycrystalline ceramics in current study fit well the range of values of $LuMnO_3$ materials of the same composition reported in the literature.

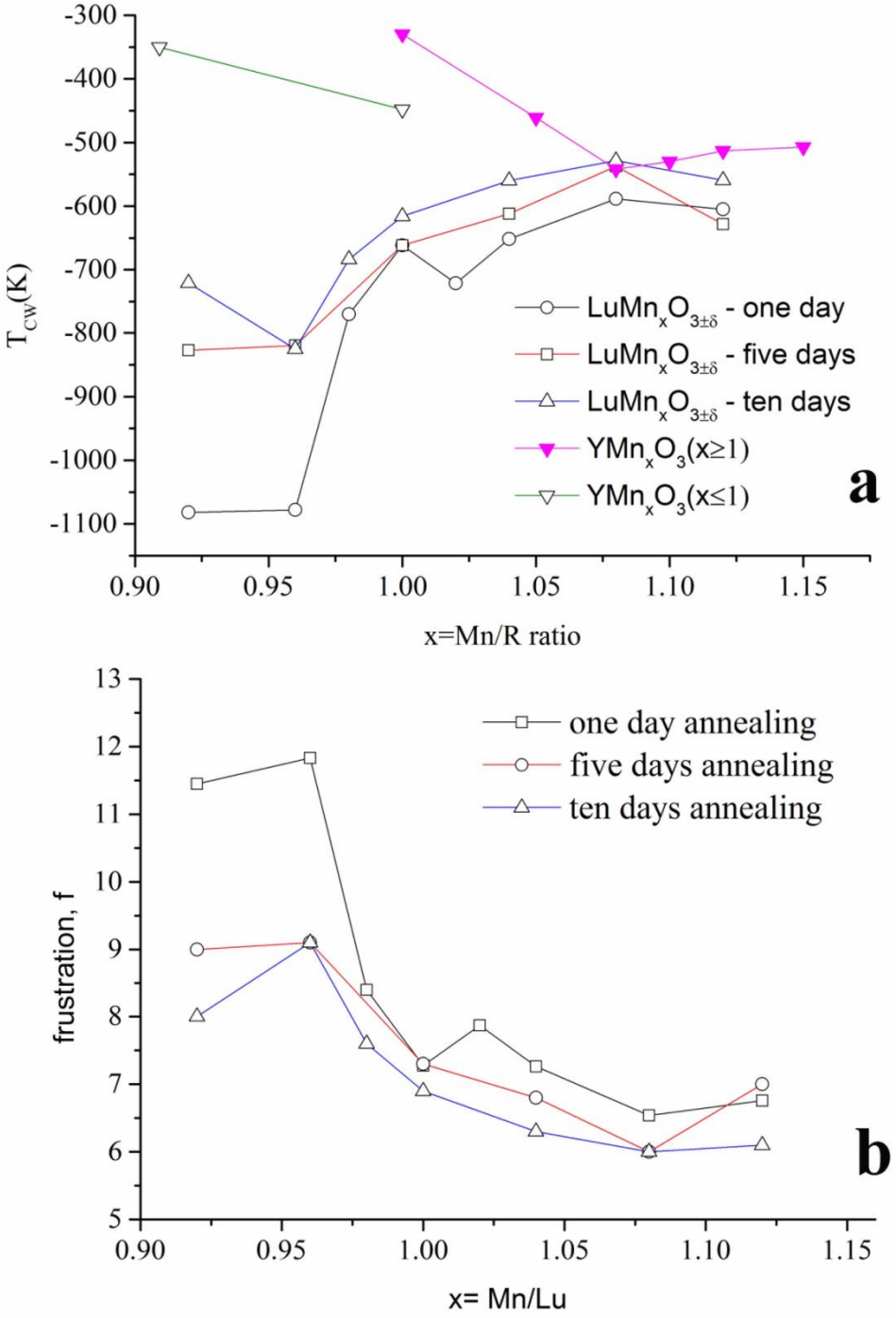

Figure 5-10. Curie-Wiess temperature T_{CW} (a) and frustration factor f (b) calculated after subtraction of secondary phase signal [91], for a selection of all three sintering conditions. In (a), comparison is made to the dependence of values of T_{CW} of YMn_xO_3 on x for x≥1 [19] and x≤1 [17].

The broadening of the range of values of the magnetic parameters like T_{CW} might result from the fact that preparation conditions and high temperature annealing schedules may significantly change some of these parameters but necessarily all of them. In a rare study of the effect of annealing temperature on the properties of the h-$RMnO_3$ phases, hexagonal $YMnO_3$ polycrystalline samples were prepared by sintering for short periods of 4 hours in oxygen at different annealing temperatures from 900 °C to 1400 °C [142]. The increasing of annealing temperatures yielded faster grain growth, improvement in the final density and changes in crystalline unit cell parameters as well as in magnetic properties, electrical conductivity, dielectric permittivity and electric polarization of the $YMnO_3$ sintered ceramics [142]. The c-axis of the unit cell was increased, whereas a-axis constant showed shrinkage with increasing annealing temperature. The unit cell volume follows these changes with a maximum for samples sintered at 1100 °C. In the same study, T_{CW} becomes negative and $YMnO_3$ samples display antiferromagnetic ordering only for sintering temperatures above 1100 °C, the values of T_{CW} decreasing to more negative values as the temperature of annealing was increased. The present study on the effect of annealing time on the magnetic properties of sintered $LuMn_xO_{3\pm\delta}$ materials reveals that the sintering time above 24 hours actually is barely effective on changing the main trends in Curie-Weiss temperature and frustration factor.

Lattice parameters in Figure 4-3 of section 4-2 may in part explain the observed change of T_{CW} and f parameter in Figure 5-9. Upon 5 days annealing cell volume and a-axis of the crystalline cell of x>1 compositions in Figure 4-3 converge to nearly steady values and the observed trends are not modified by increasing annealing time to 10 days. However, samples of the x<1 compositions showed some instability in the experimental values of the lattice parameters that made difficult setting the value of composition corresponding to the stability limit at x≈0.94 even for longest annealing time of the present study. As stated above, the observed trends in T_{CW} and frustration parameter f are linked to features of the unit cell namely to tilting of the MnO_5 polyhedral and buckling in planes of the unit cell. In support of such hypothesis, the dependency of the magnetic parameters on the ionic radius of the rare-earth elements in h-$RMnO_3$ oxides reveals that by

increasing the ionic radius from Sc to Lu and then from Lu to Y, the tilting of MnO_5 polyhedral and buckling of R planes decrease as also decrease in parallel T_N and $|T_{CW}|$ the magnitude of Curie temperature, even for single crystals [30,115]. Volume of unit cell and a-axis constant both indicate expansion by increasing ionic radius of rare-earth ion, but the trend in c-constant is not monotonic. It is also the c-axis in samples of x<1 compositions in Figure 4-3.b that showed the least monotonic evolution with annealing time. In the same way as h-$RMnO_3$ oxides with different R ions did show the dependency of the lattice parameters and magnetic parameters linked to the distortion in the unit cell, Figure 5-9 and Figure 5-10 of the current study also indicate that analogous effects of changes of the unit cell on magnetic properties are also created by self-doping.

5-3-4 Remnant magnetization and coercive field of $LuMn_xO_{3\pm\delta}$ solid solution

As stated in section 5-2, field dependent magnetization of $LuMn_xO_{3\pm\delta}$ samples sintered for one day at 1300 °C have magnetic hysteresis with ferrimagnetic like behaviour, the combination of AFM and weak ferromagnetic components. Although the presence of secondary phase of hausmannite contributes to the magnetization in field dependent magnetization below 40 K, a ferromagnetic-like component above T_C of Mn_3O_4 is still measurable for samples of x≥1. The contribution of hausmannite at 10 K can be estimated based on fraction of hausmannite assessed from XRD data. For bulk hausmannite, magnetic saturation occurs around 1.2291 μ_B/f.u. or 30 emu/g [92]. The presence of more than 1% hausmannite would produce a magnetic signal above 0.3 emu/g (0.01229 μ_B/f.u.) in magnetic remanence of the measured M-H loops. In Figure 5-11, a signal as large as 0.5 emu/gr is observed at 10K with one day annealed sample of x=1.08. Assuming the 1 wt% of Mn_3O_4 secondary phase from XRD refinement in Table 4-1, still half of this value of the magnetic remanence must originate from the

remaining $LuMnO_3$ matrix. The property of remnant magnetization in AFM matrix can be seen in measurements of the M-H loops above 43 K, like the one in Figure 5-11.b.

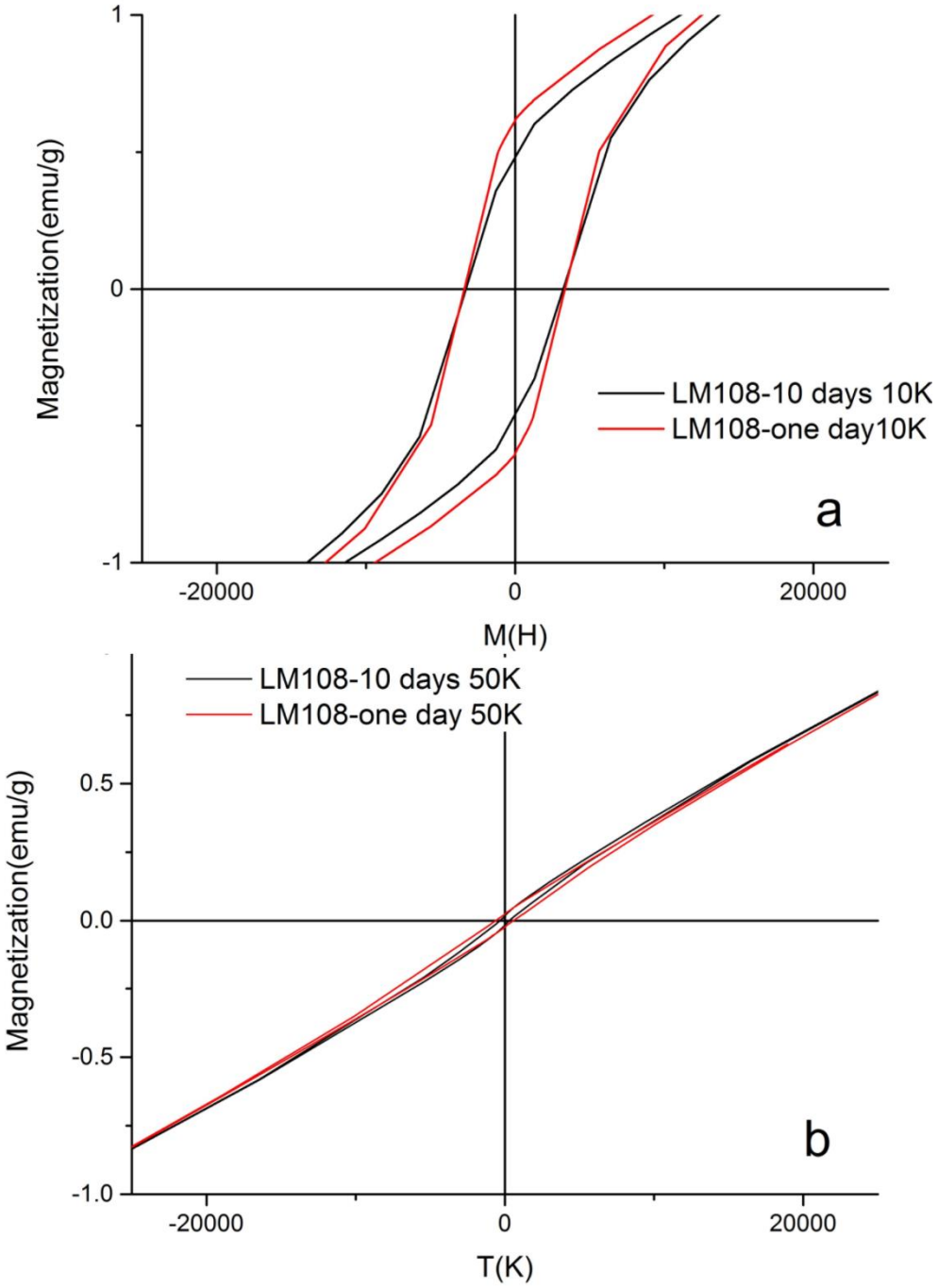

Figure 5-11. Field dependent magnetization of sample x=1.08 annealed for one and 10 days measured at 10 K (a) and above 43 K at 50 K(b).

Zooming of magnetization versus magnetic field of 5 selected samples from one day annealed samples at 80 K is shown in Figure 5-12.a. This temperature is selected as it is far above the T_C of the Mn_3O_4 phase, and just below values of T_N of the main phase in Figure 5-8. The coercive field, H_c, of 200 Oe of two samples, x=1.04 and x=1.08 is visible and half of this value for other samples. All together these observations prove that there is an additional component, a ferromagnetic like component in the magnetic interactions of the AFM $LuMn_xO_{3\pm\delta}$ matrix.

Analogous measurements are shown in Figure 5-12.b for sample x=1.04 after five days annealing at two different temperatures of 40 K, below T_C of hausmannite and at 50 K. The main features to retain here are the slope of the M-H curves when they enter the linear parts at high fields associated to the AFM behaviour of the material and the opening of the M-H loops revealing the additional magnetic component besides the AFM one. The effect of second magnetic component below 43 K is visible modifying the magnetization versus field. Above 43 K it is expected that most of the revealed hysteresis in magnetic loops must come from the main phase either originated in the crystalline lattice or from internal interfaces. The difference in the M-H curves below and above 43 K is less visible in samples with x≤1. As seen in sections 4-3-2 and 4-3-3 and shown in Figure 4-18 the interface region of Mn_3O_4 phase with main phase can be broad and presenting gradients of the Mn/Lu ratio yielding differences of magnetic behaviour. This has larger probability of occurring in samples of x>1 and short annealing time.

Figure 5-13.a shows the values of remnant magnetization, M_R, versus temperature from 5 K until 90 K for a selection of samples with different annealing conditions. Samples in this figure can be divided into two sets according to their behaviour. In one set, samples of x>1 have a large decreasing in M_R between 40 K and 50 K. It closely replicates the analogous decrease of FC magnetization under 100 Oe applied field in the same range of temperatures in Figure 5-3 and Figure 5-5. As discussed in previous section 5-3-1, this knee in M_R must also be assigned to the Mn_3O_4 secondary phase or else to planes with intergrowths of Mn-O phases. In the second set, those samples with x≤1 show a rather

regular decrease of M_R with T with just a slight bending of M_R when crossing the same range of temperatures. Above T_C of hausmannite the values of M_R of samples with x>1 become of the same order of magnitude as the M_R of the samples with nominally stoichiometric composition (x=1.00).

As non-null exchange-bias magnetic field was detected in the samples, coercive field, H_c, in Figure 5-13.b was calculated as $H_c = |H_+ - H_-|/2$ and the exchange bias field in Figure 5-13.c as $H_{EB} = (H_+ + H_-)/2$ where H_+ and H_- are the coercivity fields on increasing field and decreasing field branches of the M-H loop, respectively [65,90,148]. Almost the same division in two groups of samples is observed concerning the dependence of the H_c on T, as it was found for the M_R. Figure 5-13.b gives the values H_c as a function of T and reveals the presence of a drop in values H_c in the range of 40 – 45 K for samples with x>1.

While by analogy with the values of M_R one would expect to observe for compositions with x>1 a decreasing trend of H_c as temperature rises from T_C of Mn_3O_4 and approaches the value of T_N of the main phase, in fact the values of H_c of some of these samples rise again at temperatures above 50 K and latter converge to the values of coercive field H_c determined in the samples with nominally stoichiometric composition (x=1.00). At this stage of the present research any explanation can hardly be attempted for the observed discontinuity of H_c between 40 K– 45 K of some of the samples of the $LuMn_xO_{3\pm\delta}$ solid solution with x>1 in Figure 5-12.b. The same behaviour was observed for wet chemical synthesis of $LuMnO_3$ nano-crystalline where H_c gave different trend in the midway of temperature range of measurements from 5 K to 90 K (Fig.4 of Ref.[77]). The H_c values for x≤1 samples present a slow and continuous drop as T goes up which accelerates as T approaches T_N. As for M_R values, the net decreasing of H_c for x>1 samples at 40-50 K can be assigned to the presence of impurity phase of Mn_3O_4 or nano-regions with composition close to hausmannite left behind from incomplete reaction at some places inside the main phase after firing the samples and it is generally corroborated by the findings of Mn_3O_4 in samples by XRD analysis and by electron microscopy.

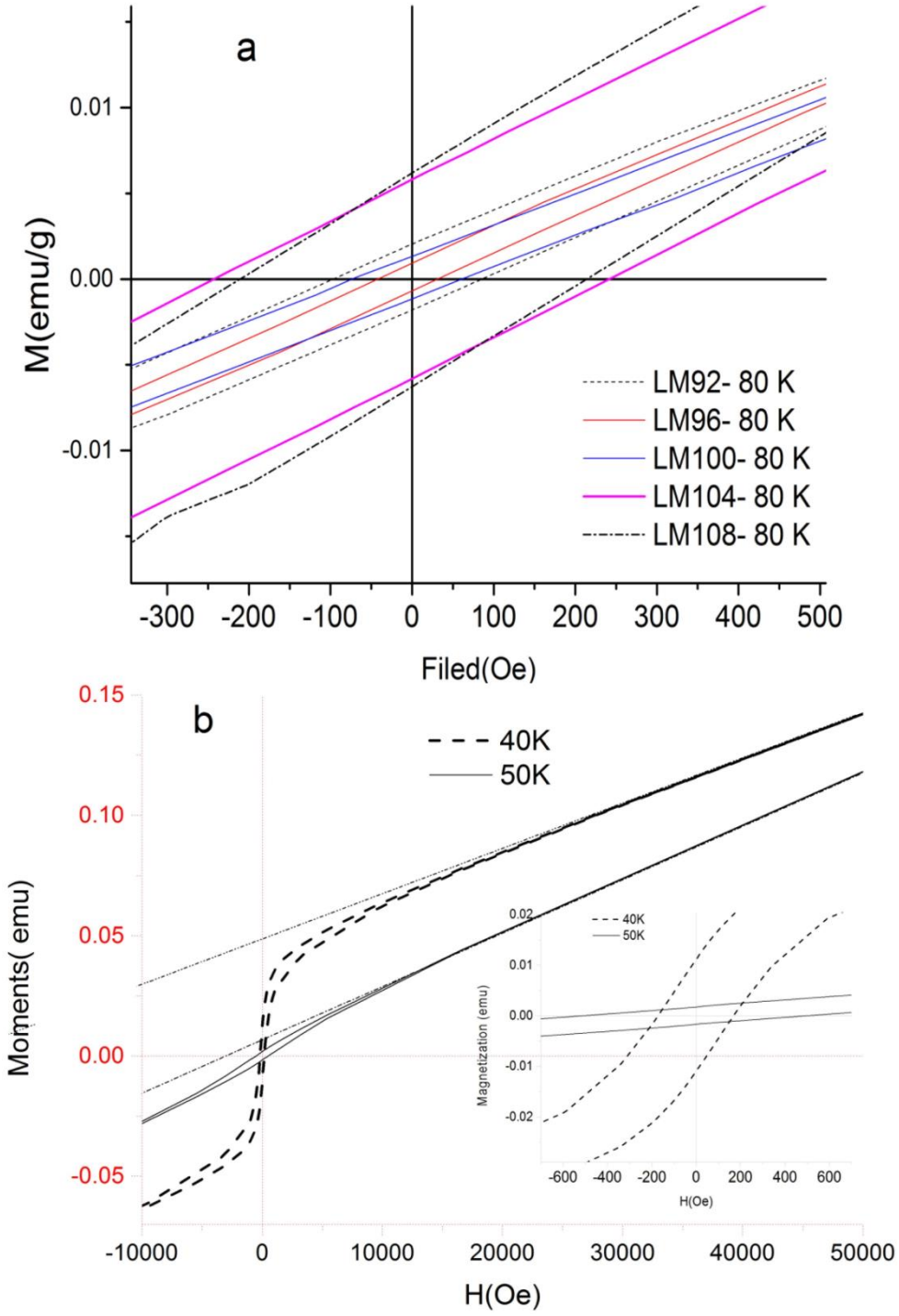

Figure 5-12. (a) Field dependent magnetization of samples with different compositions showing hysteresis even at 80 K for samples annealed for one day. (b) Magnetic hysteresis loops of sample $LuMn_{1.04}O_{3\pm\delta}$ after 5 days annealing measured at 40 K and 50 K, and the dashed lines are showing the linear parts of the loops at high fields (inset is magnifying parts close to H=0 region).

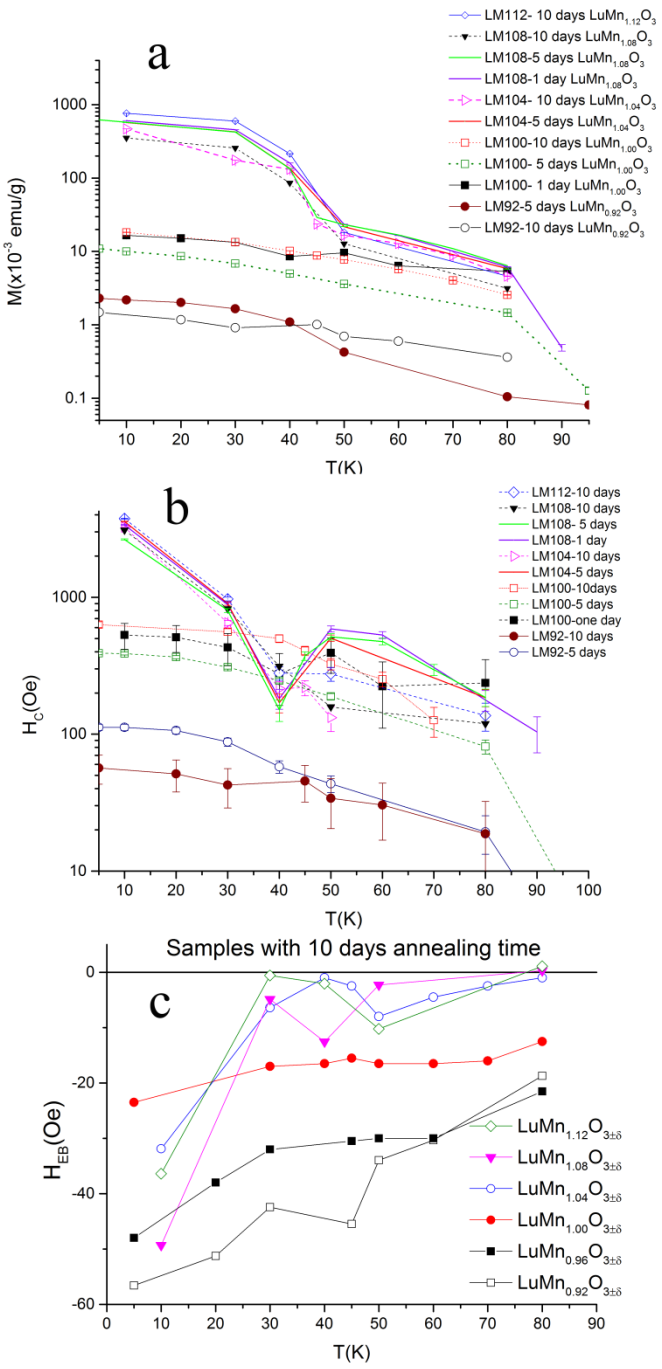

Figure 5-13. Parameters of weak ferromagnetism of selected $LuMn_xO_{3\pm\delta}$ samples from applied fields of 5.5 T to -5.5 T. (a) Remnant magnetization M_R as the average of magnetization of M-H hysteresis loops at H=0. (b) The corresponding coercive fields, H_c. (c) Exchange bias values H_{EB} at the given temperatures for selected compositions of 10 days annealed samples.

Careful observation of M-H loops revealed that the symmetry of the loops around H=0 was generally missing. The exchange bias (EB) effect can be seen in the magnetic hysteresis loop of sample x=1.04, 5 days annealing, in inset of Figure 5-12.b. The values of H_{EB} for a representative selection of samples with 10 days annealing time determined at different temperatures are plotted in Figure 5-13.c. The values of H_{EB} disclose quite new features and again separate the behaviour of x>1 samples from the samples with x≤1. For samples with x>1 H_{EB} shows the negative values (M-H loop shifts position in relation to the origin, H=0) of H_{EB} at 10 K, with dropping the $|H_{EB}|$ to low values at 30 K. As in case of H_C in Figure 5-13.b, from 40 K to 50 K, the trend of $|H_{EB}|$ shows discontinuity, first increasing of $|H_{EB}|$ followed by decreasing of values as temperature rises to T_N. The exchange bias for samples of x≤1 also indicate negative values, in general the values of H_{EB} are more negative for these samples in comparison to the ones of x>1. Sample x=0.92 reveals higher values of $|H_{EB}|$ among all measured samples. On the contrary of x>1 samples, x≤1 regime does keep the trend of change in values of H_{EB}. Outside the solid stability limit determined in this study, the x=0.92 sample shows most negative values at 10 K which may point out the effect of lattice distortions on the magnetic behaviour.

The H_{EB} field can be due to presence of a secondary phase as it was reported for h-$RMnO_3$ and orthorhombic $YMnO_3$ ceramics [90]. On the same grounds one would not expect stronger H_{EB} effects for x≤1 samples at temperatures below T≤40 K, since the study of these samples did not show any relevant signals of the magnetic secondary phase above trace levels in samples annealed for 5 or 10 days. However, for the two samples with x≤1, H_{EB} fields have significant amplitude in whole range of T below T_N. These observations may be contrary to the role attributed to the Mn_3O_4 secondary phase in the exchange bias of the manganites. In thin films of Mn-rich $YMnO_3$ it was noticed that presence of Mn^{2+}/Mn^{3+} valence states in the film became a possible source for the observed EB effect below T_N by the accumulation of Mn^{2+}/Mn^{3+} on grain boundaries instead of being located inside the grains of polycrystals [65,149]. If such scenario is also the correct one for sintered ceramics, the x≤1 samples with smaller grain sizes and larger specific surface

area of grain boundaries would have more intense signals of M_R, and in correspondence the values of H_c and H_{EB} could also be stronger as composition variable x moves to the x≤1 side of the solid solution. But this is not seemingly the case of the results of the present study with Mn- vacancy or Lu-vacancy doped samples. Nano-particles of $YMnO_3$ prepared either via chemical routes [68,82] or conventional solid state sintering [150] showed presence of negative exchange bias, attributed to the exchange interaction of spins in AFM state and uncompensated spins on surface of the particles. Reversal of exchange bias field under the effect of electric field was reported for h-$LuMnO_3$ which offers the control of sign of magnetization switchable by an applied external electric field for possible applications [81]. This matter was not investigated in the PhD thesis; however presence of negative exchange bias with change of its magnitude by x may suggest the preferred compositions to be used for the stronger exchange bias response to an external electric field. Reversal of sign of exchange bias field H_{EB} from (usual) negative to positive was early reported in FeF_2/Fe bilayers coupled to the increase of the magnetic cooling field [148]. H_{EB} became a tuneable property of YVO_3, $BiFeO_3$–$BiMnO_3$ solid solutions and perovskite $NdMnO_3$ materials as both negative and positive H_{EB} fields and states of reversed magnetization can be created in one same sample [69,90,151,152].

To explain the presence of exchange bias effect and irreversibility in sintered h-$LuMnO_3$ ceramics, one looked inside the crystalline lattices for defects that could be indication of loss of necessary regularity. The details of the nanostructure and the more extensive study by TEM and STEM of the crystalline lattices of the materials of this study will be left to the next chapter where they will be discussed. The observation of the TEM images of crystalline lattices in Figure 5-14 reveal that the lattices of off-stoichiometric samples, x=1.08 and 0.92, are both composed of nanostructured domains.

The hexagonal symmetry of atomic arrangement in the HRTEM images in Figure 5-14 shows the Lu ions (bright spots, a hexagon) and trimers of Mn ions (both z=0 and z= 0.5, less bright spots) as grey spots inside the hexagons of Lu ions. Images of the basal plane of the lattice show different structural zones inside the same crystalline structure but

they appear separated by structured domain walls of diffuse contour. The dimension of the nanostructure domains of sample x=1.08 in Figure 5-14.c are smaller than in the corresponding image of sample x=0.92 in Figure 5-14.d.

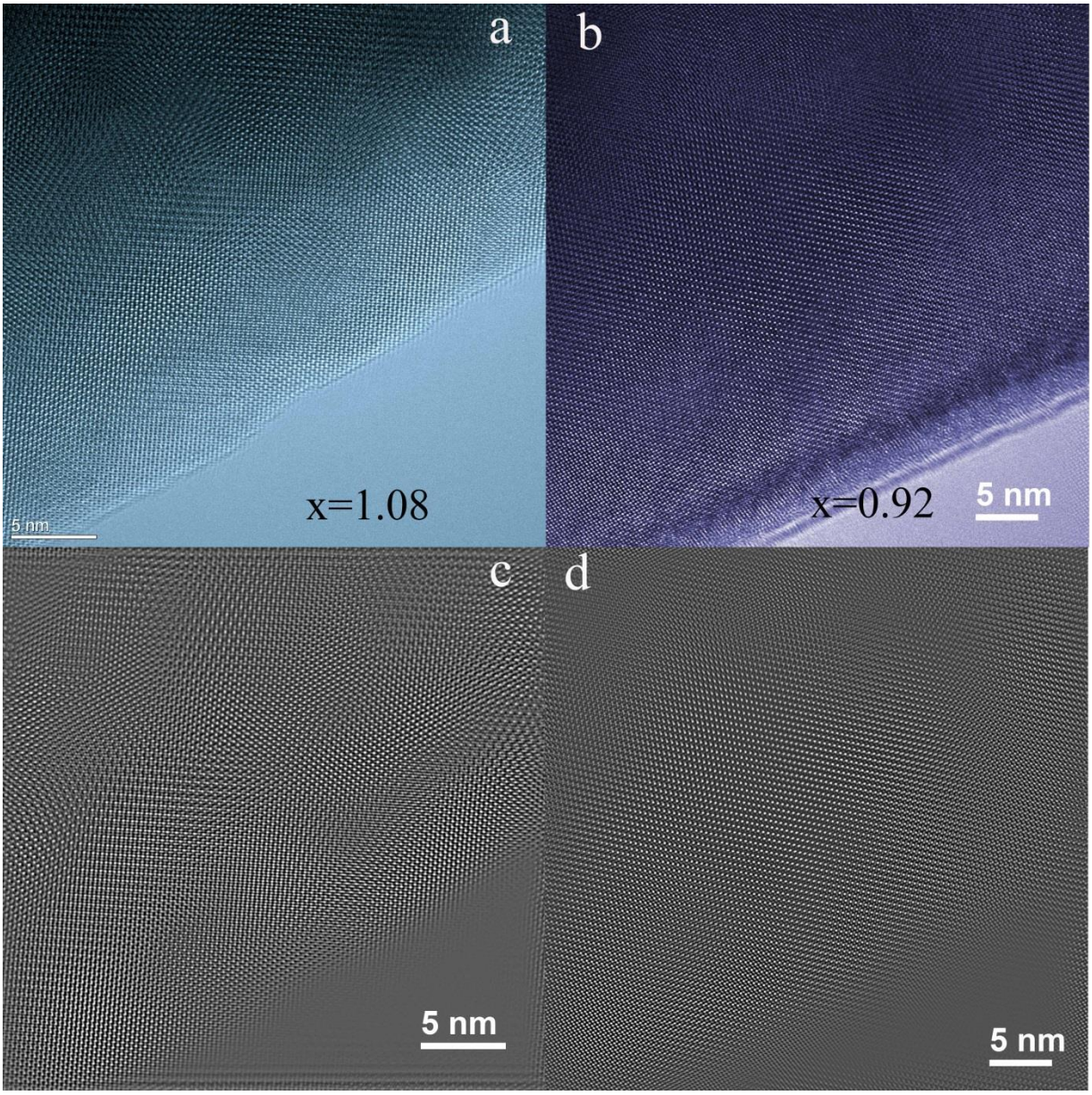

Figure 5-14. HRTEM images of $LuMn_xO_{3\pm\delta}$ samples along [001] zone axis where atomic arrangements of the basal plane can be seen (the images were colorized to show up better different nano-regions in each image): (a) x=1.08 and (b) x=0.92, both from short annealing time (c) and (d), are corresponding IFFT images of the lattices where the change of the lattice regularity at the nanoscale can better be visualized.

Since magnetic and ferroelectric domains in h-$RMnO_3$ materials are inter-locked together [9] and further linked to structural distortions of the crystalline lattices like APB (anti-phase boundaries) on domain walls [79], the presence of nanostructured zones throughout the crystalline grains of the sintered ceramics may dictate changes in the magnetic behaviour. It must be mentioned that the dependencies of magnetic properties like spin-glassy state and exchange bias on nanograin size were already reported in h-$RMnO_3$ materials[77,82,84–86,132,150]. The observed low temperature magnetic properties of nanoparticles were explained by the presence of ordered spins in AFM state of the core interacting with uncompensated spins of FM state on the shell of the nanoparticles. Although in the present study of conventional solid state sintering of off-stoichiometric h-$LuMn_xO_{3\pm\delta}$ ceramics grain size changes with the x=Mn/Lu ratio, grain sizes assessed in section 4-3-1 are of the order of few microns, at least the smallest ones can be half a micron size, much larger than what was found in case of the synthesized nanoparticles. Nonetheless, lattice images from inside the crystalline grains clearly reveal that nanostructured regions with the interfaces separating them from neighbouring zones can provide the equivalent scenario of compensated AFM spins inside the ordered crystalline lattices of the nanodomains and uncompensated FM spins on the interfaces. For both samples in Figure 5-14 in a small area of roughly 30 nm x 30 nm there are several nano-regions with their wide interfaces which would promote even stronger interfacial effect than area on the surface of h-$RMnO_3$ nano-particles of few tens of nanometer in size if they do not show such regular nanostructure inside their cores. Atomic structures shown in TEM images of Figure 5-14 clearly depict the Mn ions arrangement in basal plane, where the main component of AFM interaction exists [26,32]. Linked to the discussion on the effect of interfaces on the magnetic properties of h-$RMnO_3$ materials, several studies were made available mostly focused on the role of structural/FE domain walls and their coupling to magnetic and ferroelectric properties of hexagonal $RMnO_3$ oxides [9,10,16,48,79,99].

5-3-5 Anomalous magnetic contribution below Neel ordering transition

In FC and ZFC measurements of magnetization under 100 Oe field of $LuMn_xO_{3\pm\delta}$ samples in Figure 5-3, Figure 5-6 and Figure 5-7 the weak ferromagnetic component appears immediately below T_N and becomes more intense in the subset of samples with x>1. Figure **5-15** presents the increase in magnetic signal of sample with x=1.08 when the system becomes AFM ordered. In the following, we will discuss the change in ZFC or FC magnetization from T_N to lower temperatures for ease of discussion, but as usual the measurements were done on heating cycle. The magnetic signal increases rapidly in a narrow range of temperature when one looks at temperature range from $T_N \approx 90$ K down to 80 K. The ZFC magnetic susceptibility reaches a maximum around 80K and smoothly decreases as temperature reduces to 75 K. Comparison of ZFC and FC results shows that once the magnetic signal begins to increase below T_N, the FC and ZFC curves almost overlap together. But, after the local maximum of ZFC magnetization the FC magnetization presents a steady increase with cooling opposite to the decreasing trend in ZFC magnetization. The appearance of the sharp increase in magnetization right below T_N implies that the component of weak ferromagnetism has the origin in the main phase or in a part of the system which has the magnetic moments definitively coupled, or exchange coupled with the antiferromagnetic ordered spins of the Mn ions in basal plane of the $LuMnO_3$ phase.

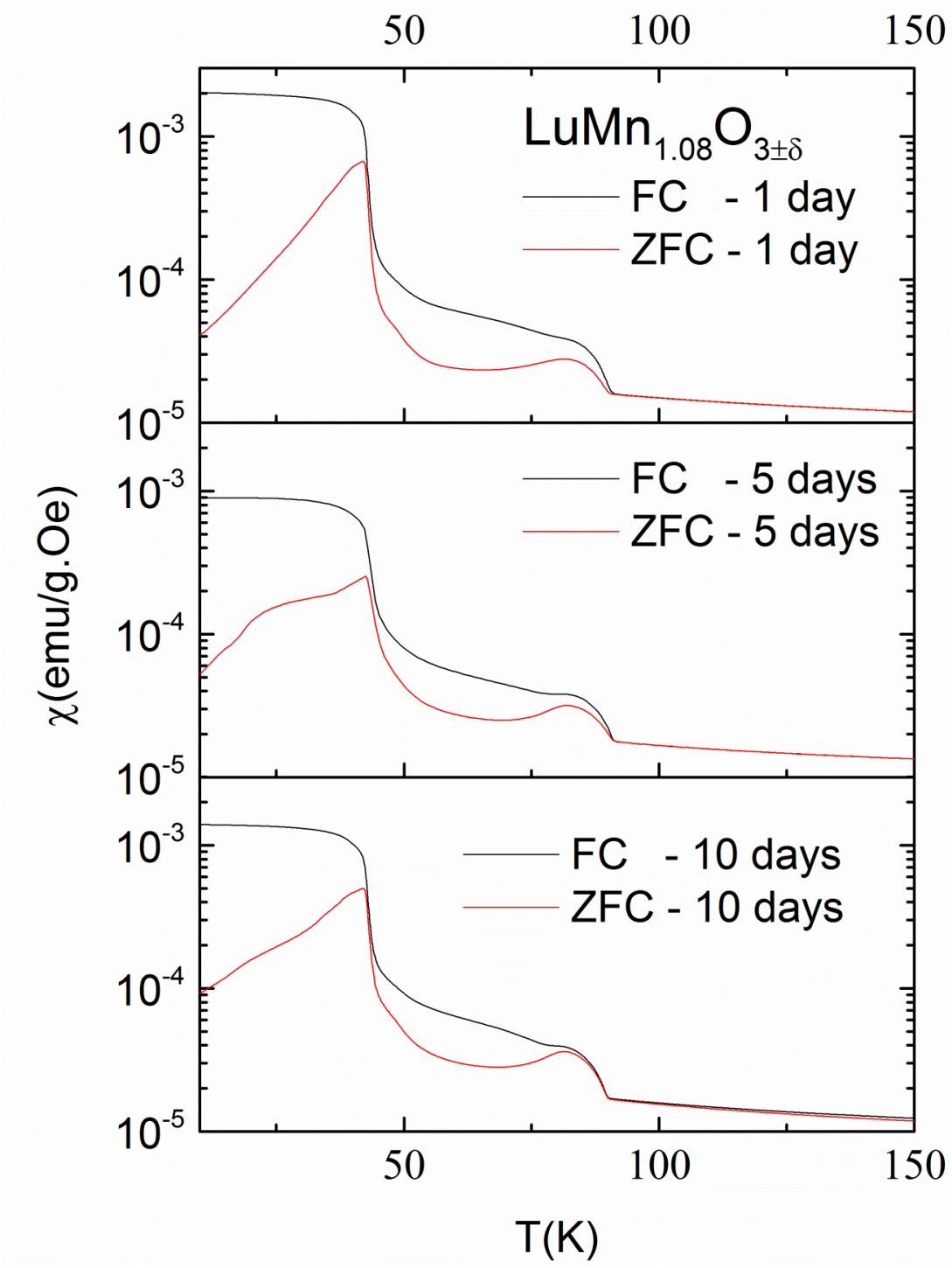

Figure 5-15. FC and ZFC magnetic data (100 Oe external field) of sample $LuMn_{1.08}O_{3\pm\delta}$ annealed at different time shown the additional magnetic component on the contrary of expected basal plane AFM interaction at T_N and below it.

Additional characterization of the component of weak ferromagnetism and the peak of ZFC magnetization observed between 70 K and 90 K was done by determining the effect of different magnetic fields in the range 0.01 T to 1 T on the ZFC magnetization (M/H) of a representative sample, the x=1.04 of 5 days annealing, given in Figure 5-16. In region below 45 K, as the applied magnetic field increases the shape of the magnetic peak becomes smoother and almost flat for the highest applied magnetic fields. With shapes similar to magnetization of Mn_3O_4 [92] smoothing of the magnetization peak below 45 K demonstrates well the effect of the magnetic secondary phase on the total magnetization of the sample [90]. The magnetic behavior of sample x=1.08 observed right below T_N in Figure 5-15 is also present in sample x=1.04 as shown in Figure 5-16.a. One could not find any correlation between the intensity of the component of the weak ferromagnetism and the fraction of hausmannite, especially in the range of temperatures far above the T_C of hausmannite. Therefore, the magnetic contributions observed above 43 K in Figure 5-15 and Figure 5-16.a might have the origin in the crystalline lattices of the $LuMn_xO_{3\pm\delta}$ phase. The magnetization normalized by the magnetic field, i.e. M/H, in the intermediate range of temperature 45-65 K is approximately field independent. Values of FC magnetization for the different magnetic fields are plotted in Figure 5-16.b Like magnetization in Figure 5-15 for x=1.08, FC magnetization in Figure 5-16.b does not display visible magnetic anomalies between 50 K and 90 K at least as clear as was seen in corresponding ZFC magnetization measurements. On the contrary to ZFC measurements, in the whole temperature range of FC measurements for all values of the applied magnetic field the M/H presents field dependency. In the region of temperature just below T_N the values of M/H are field dependent and the relative contribution of the component of the weak ferromagnetism to total magnetic moment of the sample becomes gradually weaker and almost disappears as the magnetic field increases above 0.5 T. For the highest applied fields (1 T) of the assay, M/H values of both FZC and FC measurements coincide at temperatures above 50 K

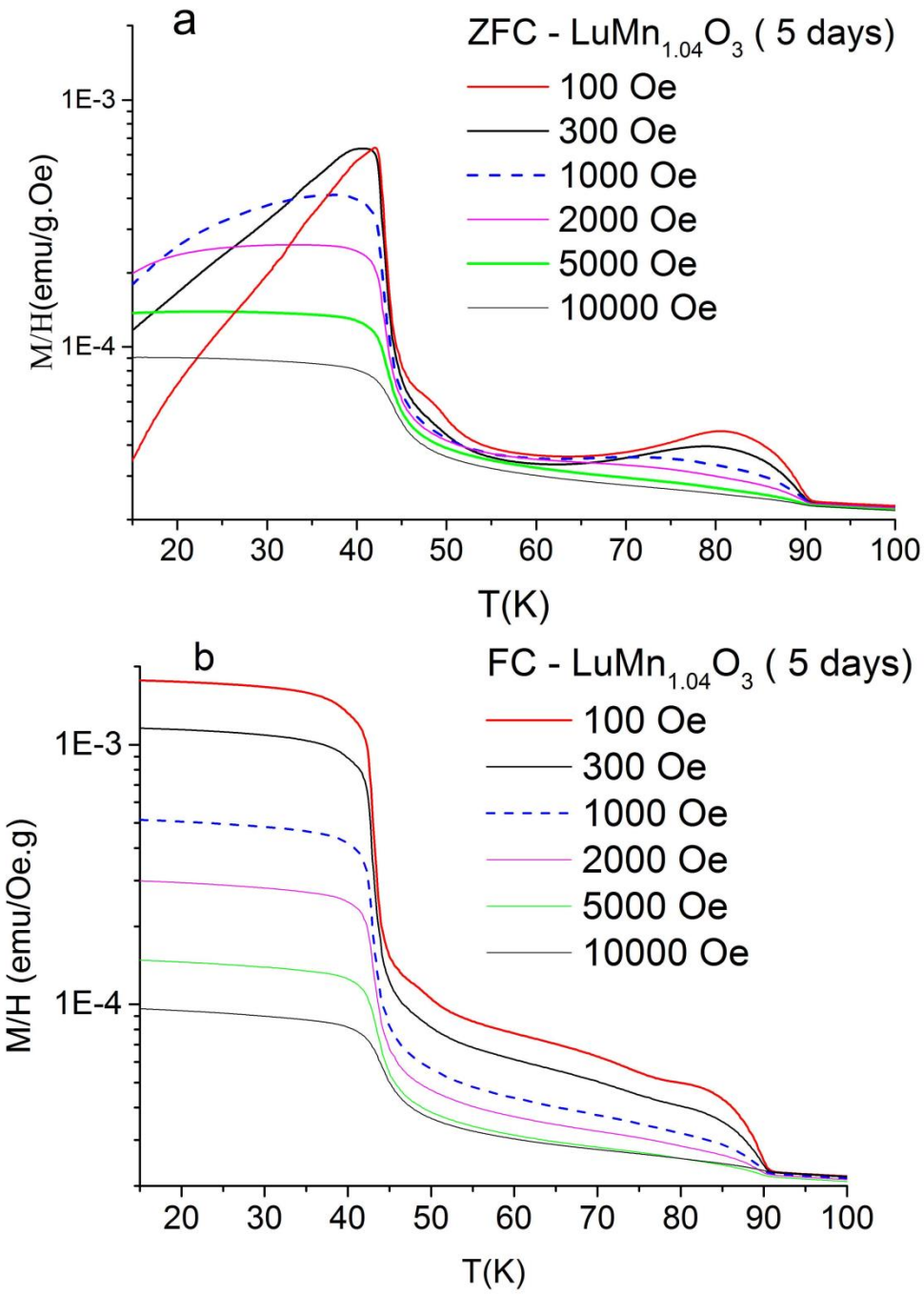

Figure 5-16. Magnetization normalized by the applied magnetic field, M/H, of the sample x=1.04 after 5 days annealing under different applied magnetic field. (a) ZFC zero-field cooled M/H. (b) FC, field-cooled M/H.

The dependence x of the local maximum of the ZFC magnetic susceptibility on sample composition, with fixed measuring magnetic field of 100 Oe, observed at T≈81 K, is plotted in Figure 5-17.a for selected samples of the 5 days and 10 days annealing time. As displayed by the figure the intensity of this component of weak ferromagnetism of the $LuMn_xO_{3\pm\delta}$ phase develops mostly in self-doped samples with Mn-excess, starting at x≈1.00 and saturating at x=1.04 close to the upper limit of stability of the solid solution. The analysis for the effect of magnetic field on magnetization M of the $LuMn_{1.04}O_{3\pm\delta}$ sample in Figure 5-16.a, at the same local maximum of the magnetic signal reveals that M has a non-linear dependence on the magnetic field given by the empirical power relation $M \propto H^{\eta}$ (adapted from Ref. [65]), as shown in the plots of Figure 5-17.b. As implicit in the values of M/H in the intermediate temperature range 45-65 K being almost independent of magnetic field magnetization, the magnetization M at the constant temperature of 55 K is proportional to the magnetic field, the exponent η becomes almost identical to one in the corresponding power law plot in Figure 5-17.b. Below the Curie temperature of hausmannite, at the temperature of the maximum of M/H curves (ZFC) approximately 40 K, the exponent η of dependence of magnetization M on magnetic field is close to ½, caused by the effect of hausmannite on the magnetization of the sample. The values of the exponent η from the same analysis of FC magnetization for sample x=1.04 in Figure 5-16.b, as well as for the selected samples, x=0.96 and x=1.00 in same range of applied magnetic fields and for both ZFC and FC conditions are given in Annex D.

The increased magnetic susceptibility below T_N does not follow the characteristic change of χ in magnetically ordered phase with AFM ordered Mn^{3+} ions in basal plane, as one would expect the magnetic signal to be reduced upon entering AFM region with decreasing T [35]. Instead magnetic behaviour that can be described as spin fluctuation appears significantly in the samples with Mn-excess and annealed for long times [30,153]. The lacking of this increase in magnetic susceptibility immediately below T_N for samples with x≤1 or even the observation of the opposite trend as in Figure 5-6.c would back the interpretation that the Mn-excess in the lattice of the $LuMn_xO_{3\pm\delta}$ phase with x>1.00 creates these positive cusps in ZFC magnetic susceptibility.

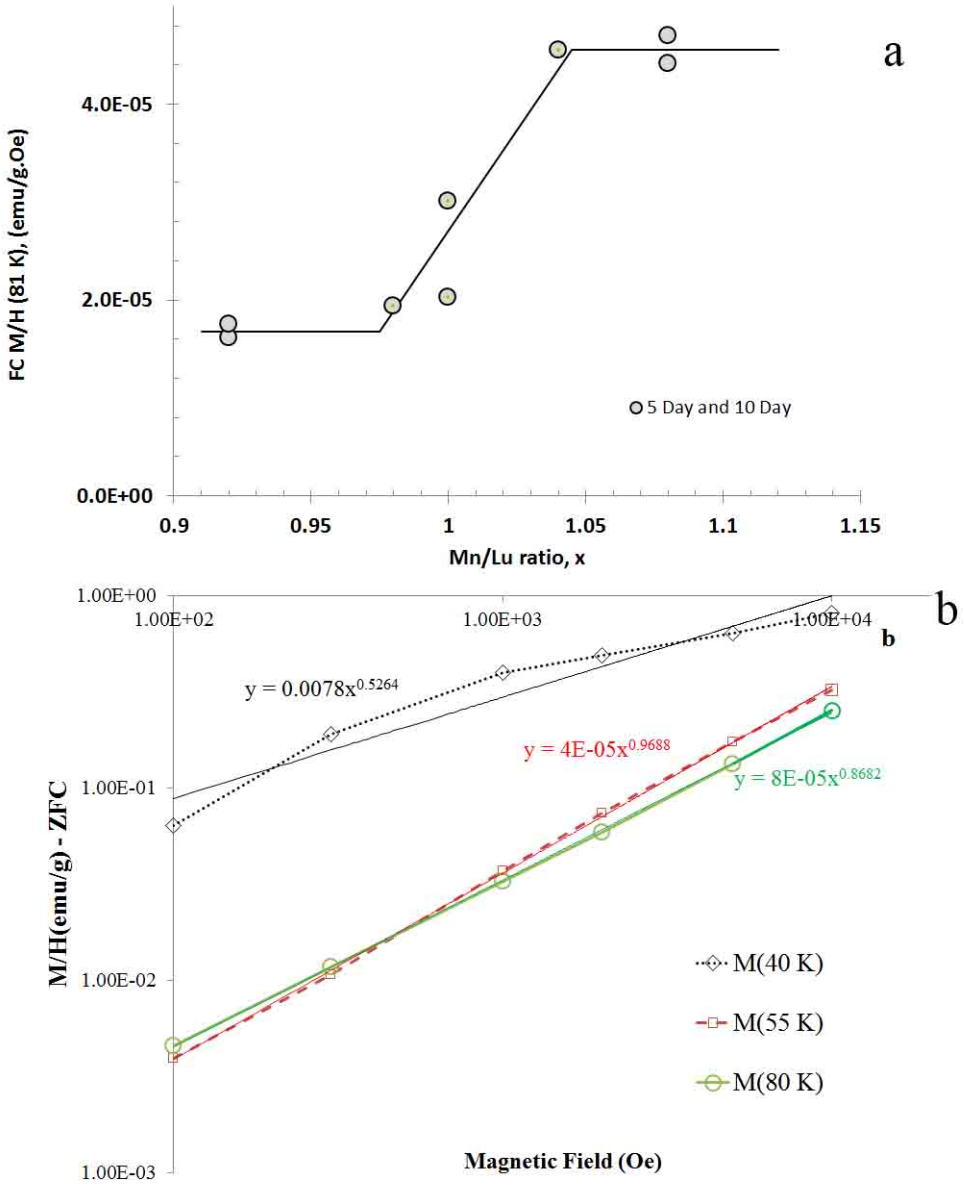

Figure 5-17. Dependence of magnetization $LuMn_xO_{3\pm\delta}$ at given values of temperature in the temperature below T_N. (a) Dependence M/H at the maximum of ZFC, T≈81 K, on the Mn/Lu ratio x of selected samples of 5 days and 10 days annealing time, with measuring applied field of 100 Oe. (b) Dependence of magnetization M on applied field H of sample $LuMn_{1.04}O_{3\pm\delta}$, 5 days annealing at the given temperature T=40, 55 and 81 K, from M/H (ZFC) data in preceding Figure 6-16.a.

Increasing Mn concentration in the lattice of $LuMn_xO_{3\pm\delta}$ solid solution enhances the relative height of these magnetic cusps, Figure 5-17.a indicating that spin disorder can be driven by distortions of the lattice induced by Mn-excess. The analogous increased contribution to magnetic susceptibility just below T_N was noticed in an early study of magnetic properties of polycrystalline $ScMnO_3$ [35] and later reported in other works in polycrystalline h-$RMnO_3$ materials of $ScMnO_3$ [76,90], $InMnO_3$ and $YMnO_3$ [90] and also in orthorhombic $ScMnO_3$ thin films [100]. The relative increase in the magnetic susceptibility just below T_N is most intense in polycrystalline $ScMnO_3$ prepared by the solid state method with the final step of reaction at 1150 °C for 34 hours with a very limited fraction of hausmannite impurity of about 0.11wt% [90]. The same increase of FC and ZFC magnetic susceptibility of $ScMnO_3$ starting just below T_N is also reported for materials that present no indication of hausmannite in the temperature range 40-45K and have quite monotonous χ dependences down to temperatures of 10-20 K [36,72]. Among the polycrystalline h-$RMnO_3$ that display this anomaly below T_N is the polycrystalline $LuMnO_3$ material of nominal x=1 stoichiometry also prepared by the solid state reaction method with final step of reaction at 1100 °C and accumulated time at this temperature of 25 hours [117].

5-4 Unit cell of $LuMn_xO_{3\pm\delta}$ ceramics and magnetic moments from the DFT approach

Simulated results plotted in Figure 5-1 proved that significant variation of the effective magnetic moment μ_{eff} determined from the fitting of the Curie-Weiss law to experimental values of χ in the paramagnetic state can be obtained when the sample is a magnetic composite made of the AFM main phase and the ferrimagnetic Mn_3O_4 secondary phase. The background correction and the fraction of hausmannite detectable in the samples were taken into account in the determination of the Curie-Weiss temperature T_{CW} of the

$LuMn_xO_{3\pm\delta}$ samples with different times of annealing in Figure 5-10.a, the corresponding experimental values of effective magnetic moment per Mn ion for 5 days and 10 days of annealing times are plotted in Figure 5-18.a. There is a trend for μ_{eff} to increase from an experimental value below the theoretical value of μ_{eff} in samples with Lu-rich composition to values well above this reference in the set of samples with Mn-excess. The values of μ_{eff} of the samples in the lower and upper limit of the composition, x=0.92 and x=1.12 respectively, present large scatter for set of samples annealed for 5 days and deviate to some extent from the dependence of μ_{eff} on x inside the stability domain of the $LuMn_xO_{3\pm\delta}$ solid solution.

It was shown in sections 4-2-5 and 4-2-6 that the first-principles calculations of the unit cells of the samples in current study can give the effect of lattice on the energy and band gap. It was seen that the lattice parameters such a-axis and volume of the unit cell change in a trendy way with the Mn/Lu ratio x and are also dependent on annealing time. The same first-principle method is applied here to calculate the magnetic moment obtained as in sections 4-2-5 and 4-2-6 by taking LDA+U approach and considering the A-type AFM configuration. In this configuration, the spin direction of Mn^{3+} ions in one z-coordinate is fixed up, whereas the spins in another z-coordinate are aligned downwards. Therefore the net magnetic moment preserves the AFM state of the whole unit cell. These calculations only convey the effect of the unit cell inner structure on the magnetic properties and necessarily ignore any interaction with features of the actual crystals like interfaces and secondary phases and the contributes they may have in creating additional magnetic components in the system. The values of magnetic moment per Mn^{3+} ion of the first-principles calculation for the 5 days and 10 days annealed samples are plotted in Figure 5-18.b. All values of the magnetic moment in Figure 5-18.b are lower than the theoretical value of magnetic moment for the h-$LuMnO_3$ phase (4.9 μ_B). In previous first-principles calculations on $HoMnO_3$ material which used the current approach (AAFM) and spin-lattice coupling, magnetization for Mn^{3+} ions was 3.79 μ_B and 3.99 μ_B respectively [154]. DFT approaches for $YMnO_3$ with only Mn^{3+} ions as magnetic entity gave 3 μ_B [155], 3.5 μ_B [31] and 3.9 μ_B [125] in previous reports, the low magnetic

moment was assigned to ignoring the spin-lattice coupling [155]. Single crystals of $LuMnO_3$ and $YMnO_3$ gave values of magnetic moment less than 3.5 μ_B [30]. Two main features emerge on comparing the two sets of the samples together in Figure 5-18.b. One is the scatter in values of magnetic moment/Mn ion of samples with composition in the extremes or near the limits of the range of composition fixed for the present study, the samples with x=0.92 and those with x≥1.08. The coincidence is possibly fortuitous but, the unit cells of composition x=0.92 and x=1.08 returned almost the same values of magnetic moment in each set of samples.

The second feature to be noticed is that values of magnetic moments of samples with composition in the range of 0.96≤x≤1.04 present a decrease with increasing x in same range of composition where the crystalline lattices are expected to be inside the solid solution limits of $LuMn_xO_{3\pm\delta}$ phase and parameters of the unit cell like the cell volume showed a smooth change with no flat plateau in Figure 4-3. Comparison between the values of magnetic moments in Figure 5-18.a and b reveals different trends with increasing values of x and suggests that in samples with higher values of x the magnetic moment includes important contributes of other magnetic components besides the AFM ordered magnetic moments of the crystalline lattice, or disordering in the lattice may favour spin-lattice coupling. One of such magnetic components might seemingly be in the origin of the anomalous magnetization observed below T_N and object of the discussion in section 5-3-5 above.

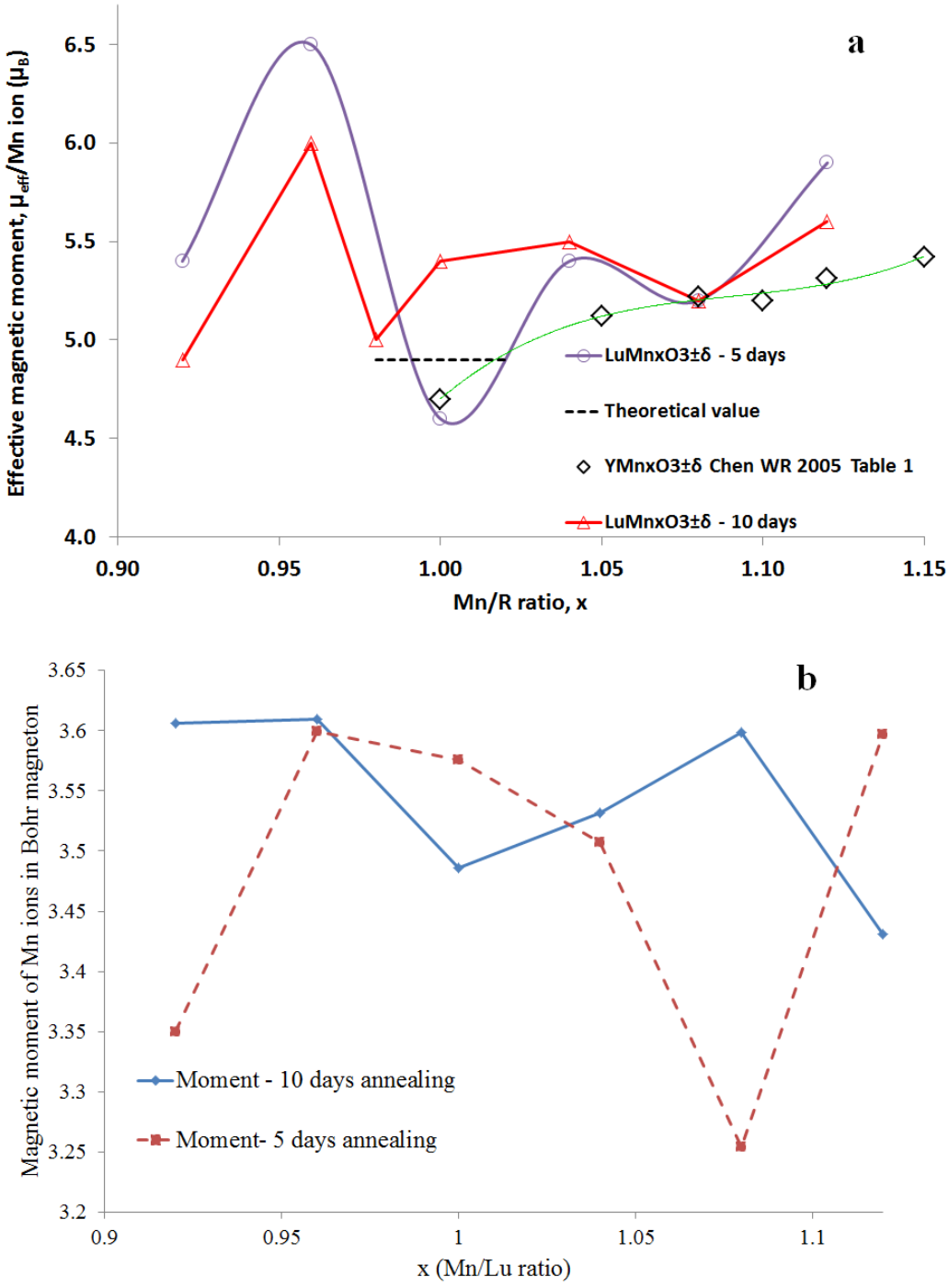

Figure 5-18. Magnetic moment of Mn ion of $LuMn_xO_{3\pm\delta}$ solid solution (a) Effective magnetic moment determined from the fitting of Curie-Weiss (Table C-6), 5 days and 10 days annealed samples. The data of effective magnetic moment of $YMn_xO_{3\pm\delta}$ were calculated from Ref.[19] (b) Magnetic moment of the Mn^{3+} ions from first-principles calculations considering collinear A-type AFM configuration.

6. TEM study and DFT calculation of electronic structure of $LuMn_xO_{3\pm\delta}$

The crystalline lattice of vacancy-doped $LuMn_xO_{3\pm\delta}$ oxide is expected to present different phenomenology for x>1 or x<1 sides of the solid solution as Mn or Lu are located at two different crystal positions in the building block of the $LuMnO_{3\pm\delta}$ unit cell. Mn ions are positioned in the centre of the bipyramids surrounded by five oxygen ions with their magnetic moment ruling the magnetic interactions. On the other hand, Lu ions coordinated with 8 oxygen ions separate sheets of the Mn ions along c-axis, where shifting of their positions induces electrical polarization aligned with c-axis. The XRD characterization and magnetic measurements showed that volume of the unit cell and AFM strength are both function of the Mn/Lu ratio. However, the cases of poor residuals of the Rietveld refinement of XRD data and presence of extra transitions in magnetic moments below T_N with broad Neel ordering transition, all signal changes in crystalline lattices linked to two different types of vacancies, Mn or Lu, created by the self-doping in the present study. In this chapter, the nanostructure of the LuMnxO3±δ samples is studied with detail to separate the potentially different roles of Lu and Mn vacancies on creating defective atomic arrangements, dislocations and chemical inhomogeneity in crystalline lattice of $LuMn_xO_{3\pm\delta}$ samples. Since clustering of point defects in the lattice may affect the local atomic arrangement of the unit cell, there is a probability of local changes in the electronic structure of the ions as it was more often reported for perovskite $RMnO_3$ materials. To this end, the electronic structure of the Mn^{3+} ions in basal plane as the main responsible for the AFM basal plane interactions was also studied to get through a broader picture of magnetic interactions in samples with off-stoichiometric composition. Combined to the HRTEM characterization, there is also the need to take EELS spectra of the regions under study looking at the Oxygen K-edge for information on

the Mn 3d-orbitals and Mn $L_{3,2}$ for assessing the presence of the different oxidation states of this ions beside the Mn^{3+} valence. Another remarkable matter of study in h-$RMnO_3$ materials is their improper ferroelectricity resulting from the interlocking of the structural distortions and the electrical polarization of the R^{3+} ions, that gives rise to six Antiphase (AP)/Ferroelectric(FE) domains in the ferroelectric phase that is present in a large range of temperature including room temperature. The ferroelectricity arises from displacement of the R^{3+} ions along c-axis, upwards and downwards, which dictates 180° rotated domains. Lowering temperature from high temperature, the highly symmetric $P6_3/mmc$ paraelectric phase changes to the reduced symmetry $P6_3cm$ ferroelectric phase, tripling the unit cell in the ferroelectric phase [53,58]. The tripling of the unit cell and the translation lost in ferroelectric phase generates three possible choices for the unit cell, therefore 3 types of domains are aroused. Combination of the 180° ferroelectric domains and three structural translation domains gives 6 APB/FE domain walls in h-$RMnO_3$ like $LuMnO_3$ materials. The study of the effect of transition metals or rare-earth vacancies on the crystalline lattices has impact on the understanding of magnetoelectric coupling as it was argued that this coupling has its origin in the Mn trimers and it would be modified by any change of atomic arrangements in the basal plane [35,127]. Since translation symmetry lost during PE to FE phase transition is the reason behind of existing APB/FE domain walls in FE phase [156], it was investigated if the topology of interlocked ferroelectric to structural defect has to be revisited by chemistry change or interfacial defects in h-$RMnO_3$ oxides [56,157,158].

6-1 Study of crystalline lattice of off-stoichiometric samples

The behaviour of the lattice parameters shown in Table 4-1, Table 4-2 and Table 4-3 indicating that Lu vacancy forces the unit cell to shrink whereas Mn vacancy expands the unit cell in relation to the dimensions of the unit cell of the stoichiometric $LuMnO_3$, which results in different levels of distortion in the unit cell whenever complete chemical

homogenization is not attained. The reliability factor and residual of fitting of the given crystalline structures and phases demonstrate the presence of distortions in the lattices. Due to distortions, atoms are energetically favoured to be little off their regular positions in lattice sites. TEM investigation of selected samples is used to unravel the kind of distortions in the lattice of off-stoichiometric samples and the effect of the Lu and Mn vacancy self-doping on the density and type of the distortions and in-homogeneities in the atomic arrangements.

6-1-1 Ferroelectric domains in TEM images

Figure 6-1.a shows the low magnification dark field TEM image of sample with x=1.04 obtained by tilting the sample little off-parallel to the (110) zone axis and taking the dark field (DF) image to excite spots (-220) and (-330) and enhance the contrast of the anti-phase/ferroelectric domains. Since looking at the $LuMnO_{3\pm\delta}$ along (110) zone axis shows the arrangement of the Lu ions and their polarization direction properly, any vacancy driven disordering in the arrangements of the Lu ions can be investigated. Figure 6-1.a clearly exhibits the small size of the 6-fold anti-phase/FE vortex-like patterns in the left part of the image, others being elongated most-likely because of distortion in the lattice. Analysis of the images of the different parts of the sample demonstrates the 100 nm as the size of the vortex/anti-vortex domains, in some cases even smaller than this. The chemical effect of substitution of Mn ions by Ti ions in $YMn_{1-x}Ti_xO_3$ ceramics (x=0.175) resulted in reduced size of the FE domains from few microns for pure $YMnO_3$ to 10-20 nm in $YMn_{0.925}Ti_{0.175}O_3$ [159,160].

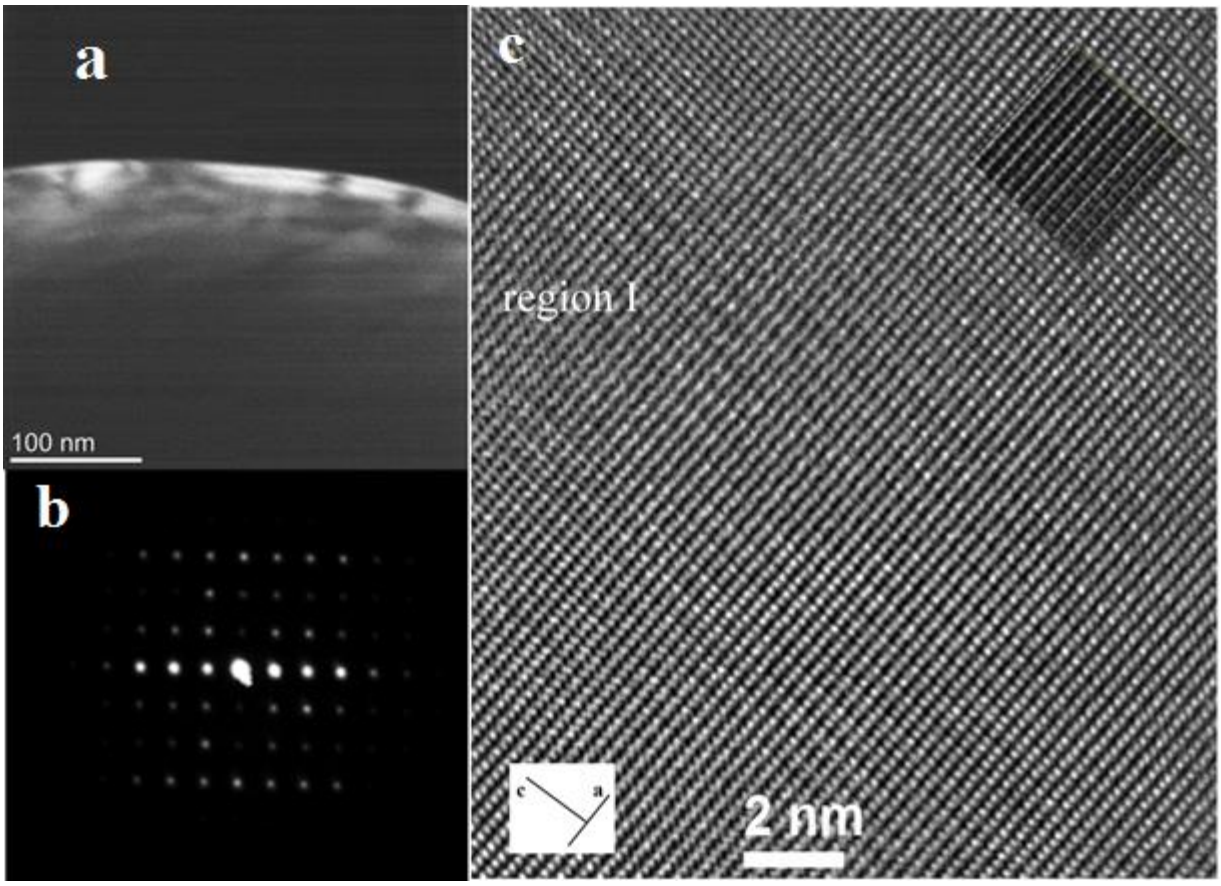

Figure 6-1. (a) The dark field image of the $LuMn_{1.04}O_{3\pm\delta}$ sample taken by choosing four spots in the SAD pattern showing small antiphase ferroelectric domains, (b) SAD diffraction pattern of the same particle oriented along (110) zone axis. (c) HRTEM image of the sample exhibiting the switching of the Lu ions observable due to contrast change; inset shows simulation of the image overlapped with the experimental one.

Figure 6-1.b is the SAD pattern of the same sample taken with the thin section oriented along (110) zone axis showing the two main spots chosen to take dark field image in the Figure 6-1.a. Figure 6-1.c shows the corresponding HRTEM image, part of area in Figure 6-1.a, illustrating the switching of the shift of the Lu ions from top of the image to the bottom. The switching is observed because of shift of the positions of the Lu ions and the oxygen ions connected to them all appear as change in the contrast. The analysis of the switching of the Lu ions results in identifying the two ferroelectric domains where

the simulation is overlaid with image. The contrast of the bright spots and then their change of contrast from two bright, one less bright to two less bright, one bright is interpreted as phase shift of the ferroelectric domains from α- to β+ separated by a type I domain wall [161]. Part of the image is overlaid with the simulated image, showing well-matched simulated and experimental images. Although the atomic arrangement of this sample is nearly well-defined everywhere, a part of the image shows out-of-registry marked as region 1 in the Figure 6-1.c, where atomic planes along c-axis appear distorted, which may be indication of chemical inhomogeneity. The region of distortion extended more than one unit cell in wide and consists of inter-diffusion of the Mn and Lu planes along c-axis, resulted in the tilting of the unit cells. Figure 6-1.c proves that the size of the each separate ferroelectric domain should be in the scale of few tens of nanometres, as seen the Figure 6-1.a, because of the density of the distorted regions which can be seen in this image and in images taken from other parts. Lu vacancies and chemical in-homogeneities, although not intensively disturbing the ions out of their positions in the lattice are directly restricting the ferroelectric domains to a nano-scale, by forcing the Lu ions to shift their displacement quickly wherever the lattice faces distorted regions. The effect of oxygen vacancies on FE domains of $YMnO_3$ on changing the FE domains of stoichiometric $YMnO_3$ to ordered stripe patterns once the oxygen deficiency is introduced was already reported [97,162].

Figure 6-2 demonstrates the methodology used here to identify the type of domain walls and the phase of ferroelectric domains on both sides of the domain wall. The basic concept was taken from Zhang [58] and is shown in the inset of Figure 6-2.a, where three different phase angles of the FE domains (translation domains) and their relation are depicted. Each box with dash line in the inset corresponds to a unit cell and each division to a Lu ion with up or down orientation. To take the same procedure as Zhang, a network of lines with equal distances (yellow lines in the image) is made where each line should coincide with the first atom of the unit cell when one moves along atomic lines (b-axis) in the model image of two domains with opposite orientations (Figure 6-2.b). Therefore in

Figure 6-2.c one expects that the lines to be always on the edges of the unit cells if the displacement of the Lu ions remains always up or down.

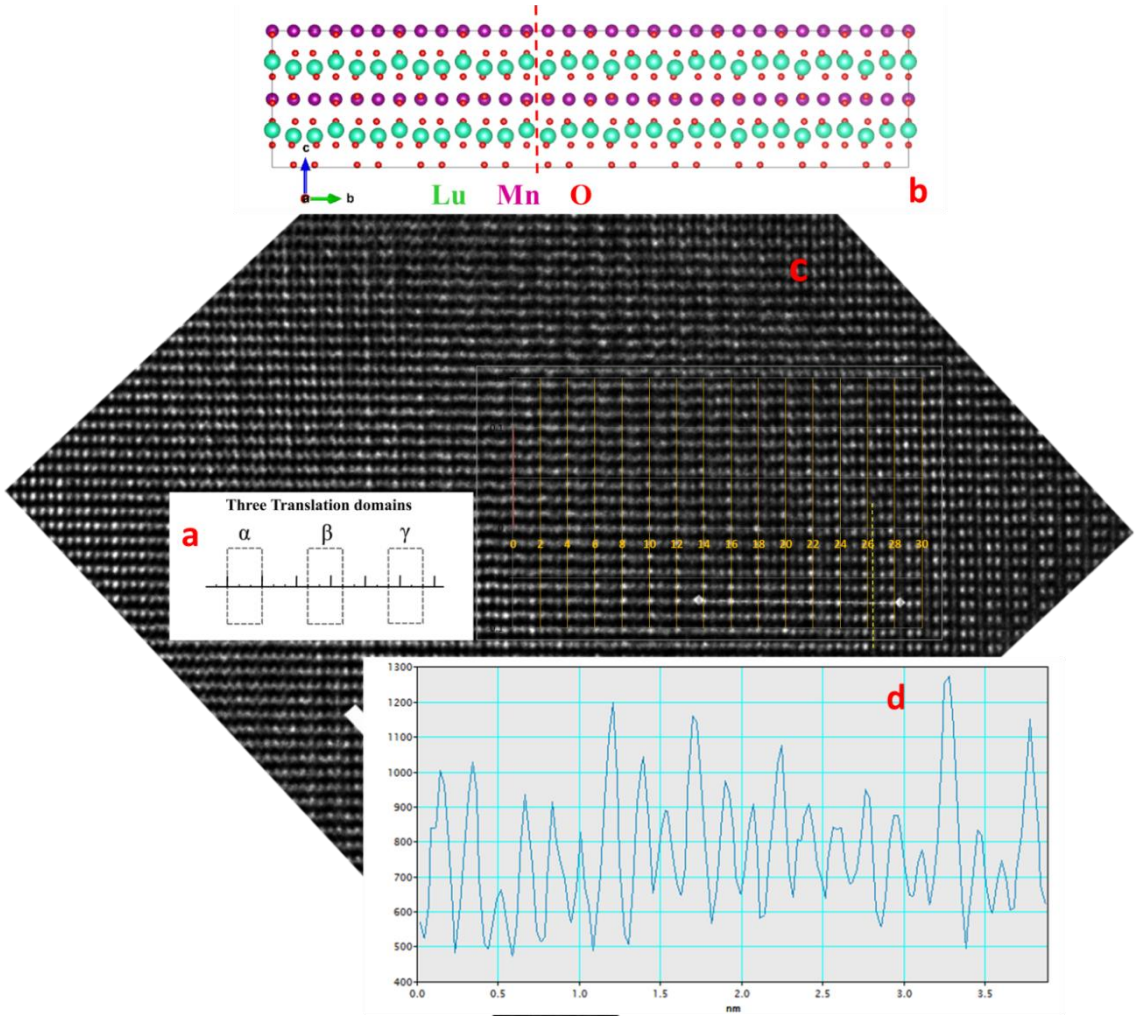

Figure 6-2. . The methodology used to find ferroelectric domain switching considering the phase shift of Lu ions positions on the domain walls. The network inside the TEM image is used to locate the positions where domain wall appears and what type of domain exists on both sides of the domain wall. (a) The box on TEM image used in Ref.[58] to define the type of domain wall and phase shifts of Lu ions on both sides of the domain wall. (b) The model image of two FE domains with opposite polarization along (100) zone axis. (c) The TEM image of sample $LuMn_{0.92}O_{3\pm\delta}$ and network of lines; each one marks the first atom of the unit cell starting from left side. (d) The intensity profile of the line drawn on the TEM image clearly indicates the fluctuation of the up or down atoms along an atomic plane with transition of period from 1 down – 2 up on left, to new period 1 up – 2 down on right side.

The lines reveal that somewhere in the image they no longer match with the staring of the unit cell as one moves away from left side, the bright spots indicating the Lu ions are displaced downward. Counting by numbers, on position 26 the ordering of the bright spots is like one grey, two bright in opposite to observation in the region between numbers 4 and 24. Figure 6-2.d shows the intensity profile of the white line in Figure 6-2.c given the fluctuation of intensity of the contrast of Lu ions, confirming the displacement of the Lu ions in the unit cells, as higher intensity corresponds to upward polarization and vice versa. The classification of the two types of domain wall follows reference [161]. Type A domain wall includes one space between Lu ions whereas type B is made of 2 Lu spaces and engages 3 Lu ions.

The HRTEM image of sample $LuMn_{1.12}O_3$ shown in Figure 6-3 is taken from the sample with composition at the extreme of Mn-excess in this work. In the upper part of the image ordering of the atoms in the atomic arrangements of Lu and Mn ions, with Lu as white spots, is different from the one in the lower left part, manifesting itself as change in contrast. In the upper part of the image, between pairs of bright spots, there are two less bright spots, whereas in the lower left part of the image, the reverse is observed. The inset gives the simulation of the image overlaid with the atomic positions of each element along (110) zone axis. As the simulation shows the shift of Lu ions and their connection to oxygen can be seen by the change in the contrast for up or down movements of the Lu ions. On the contrary of the previously observed in single crystals with domain walls one unit cell wide [52,161], here in Figure 6-3.a the domain walls are diffuse and wide and they create transient regions for atomic planes of Lu ions between regions where they are displaced upward or downward. These transition regions can be associated with chemical inhomogeneity which introduces changes in the regular ordering of the ions.

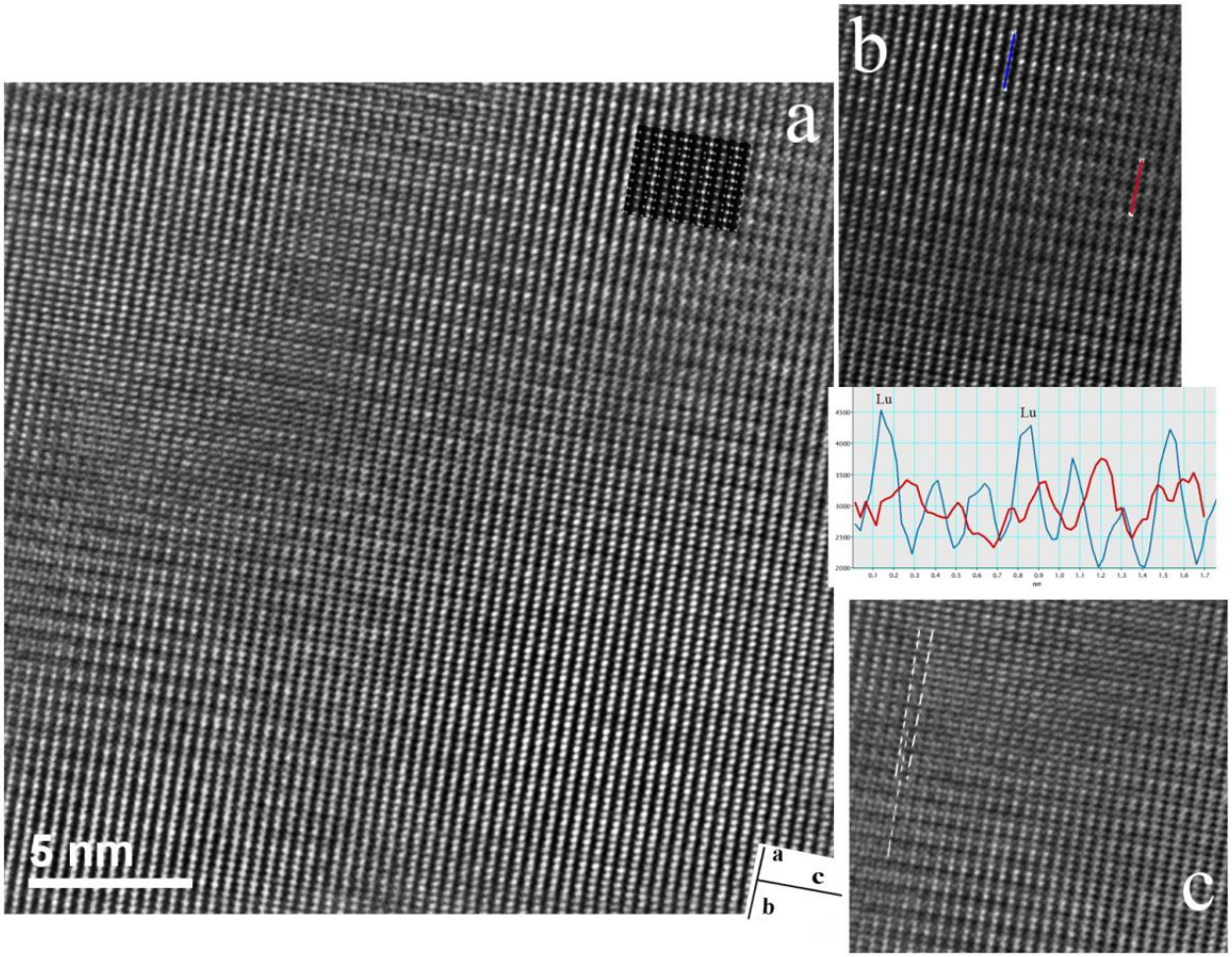

Figure 6-3. (a) HRTEM image of the sample $LuMn_{1.12}O_{3\pm\delta}$ taken along (110) zone axis with simulation overlaid in the upper part of the image. (b) Right part of the image in a), indicating distortion in the atomic planes of Mn and Lu ions. The intensity profiles on the bottom of the image display ordering in the peaks of the blue line and disordering in the atomic arrangement in the lattice along c-axis in the red line. (c) Left part of image a) showing the APB in the region marked by dash lines along basal plane.

Figure 6-3.b and c give two regions of Figure 6-3.a form the right and left sides, respectively, of the image appearing to be out of registry and which have planar defects. In Figure 6-3.b, the distortion is bending the planes of Lu and Mn ions along c-axis. This chemically driven defect locally disturbed atomic arrangement of the lattice as it is

shown in the intensity profiles below Figure 6-3.b, taken along the two marked lines in same Figure 6-3.b. By moving from one line to the other in the Figure 6-3.b, one sees that the pattern of intensity of the profiles is changed, indicating the degradation of the organization of the atoms along the second line (red line) on the right side of the Figure 6-3.b. In Figure 6-3.c, a planar defect appears as APB along a-b plane (basal plane), indicated by dashed lines for easy recognition. The region where APB´s starts is little out of registry due to distortion of the lattice there. In both sides of this region, up and down displacement of the Lu ion switches showing different electrical polarization.

The low magnification TEM image Figure 6-4.a was taken of a structure distortion with few hundred nanometres length observed in the sample with x=0.92 taken by tilting sample to the (110) zone axis. The lines in TEM image present the stripe patterns similar to those observed in $ErMnO_3$ single crystals exposed to shear strain above FE Curie temperature [56]. The stripes in $ErMnO_3$ were explained as the shear strain creates energy competition between the vortex/anti-vortex and stripes in the lattice. It was assigned to the lattice change around vortices making stripes energetically more favourable by promoting the vortex/anti-vortex to move far apart from each other, finally stabilizing in the form of stripes. In Figure 6-4.a, the angle between lines and ab-plane is less than 30°, right after the point where they appear. However, the lines are changing their angle with respect to ab-plane as they are going further away of their origin. Ordered stripes of FE domains were also observed in oxygen deficient single crystals of $YMnO_{3-\delta}$, the oxygen deficiency forced the 6-fold cloverleaf patterns to convert to parallel stripes across the sample [162].

Figure 6-4.b is the HRTEM image of the joining area of the stripes showing high intensity of distortion. In the image, distortion mainly contains the APB, either at the place of the walls or in the centre of the distortion occurring along c-axis, or the bending of the atomic planes accompanied by twisting of the unit cell around central defect.

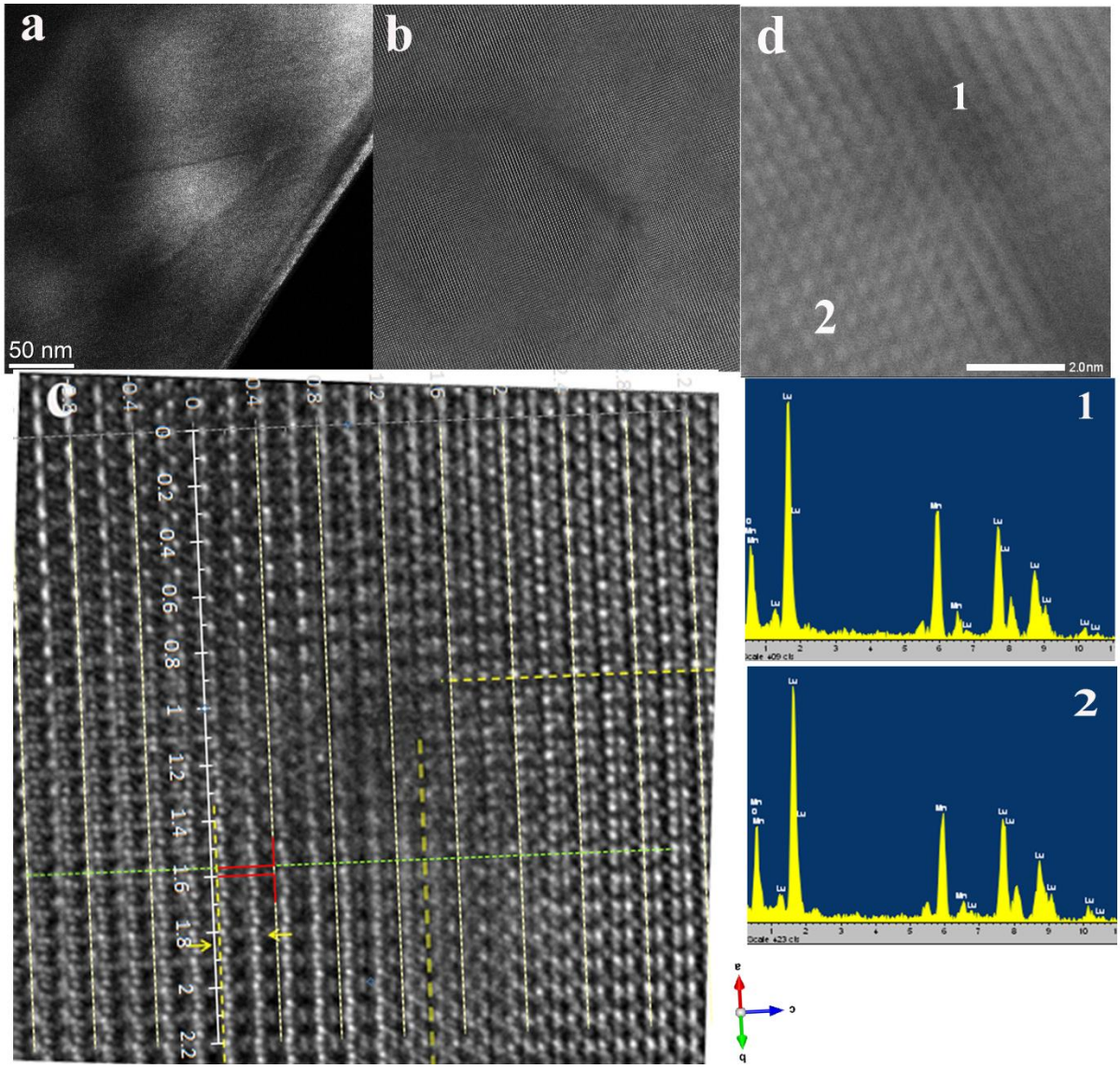

Figure 6-4. Structural distortion observed in sample x=0.92. (a) Low resolution TEM image taken by introducing the contrast aperture for better contrast along (110) zone axis, showing two lines of the APB (anti-phase boundaries). (b) HRTEM image of the place where the APB lines join together showing nanodomains around the joining point. (c) Magnified HRTEM image of the joining point of the APB lines indicating the high intensity of distortion. The scale in the image is a guide to find the FE switching as was discussed in Figure 6-2. The yellow, dashed lines indicate regions with different polarizations. (d) STEM image of the same joining point of the APB lines, below the image the EDS spectra from points 1 and 2 marked in the same image.

In Figure 6-4.b and c, few structural domains are distinguished being separated by wide boundaries, where distortions like APB or twisting of the atomic planes have changed the contrast in these regions. In Figure 6-4.c few structural domains are distinguished being separated by wide boundaries, where distortions like APB or twisting of the atomic planes have changed the contrast of these regions.

In the effort to identify the driving force to stimulate lattice on creating stripe lines and distortions in this sample, EDS characterization in STEM mode was also performed, looking for chemical in-homogeneity. The EDS analysis from some points in the centre and around this region indicated fluctuations in elemental composition. The broad area EDS analysis, on the contrary of the point analysis around central defect gives more Lu than Mn in a proportion closer to the nominal x=0.92 composition. Figure 6-4.d shows BF-STEM image of a disorder area observed in Figure 6-4.a, and the two selected points, on the disordered region (marked as 1) and lattice (marked as 2) and their respective EDS spectra with a clear change of the ratio of Mn (K-line) to Lu (L-lines) in the two adjacent regions. Therefore, the formation of the nanodomains may be associated to change of chemical composition across the region. The same disturbance of the regularity of the crystalline was confirmed with a second particle, EDS results exhibiting change of the Mn/Lu ratio inside and outside of the disordered region. Therefore, as confirmed by Figure 6-4, the sample with high deficiency in Mn and large concentration of vacancies (x=0.92) shows high density of strain inside the grains associated to shifts in chemical composition in local regions which results in expansion/contraction of crystalline lattice as previously demonstrated by XRD analysis in chapter 4. This is hypothesized to result in stripe lines whereas vortex/anti-vortex structure is being annihilated as it is not energetically favourable.

6-1-2 Image Simulation in relation to ferroelectric switching and ion vacancies

All simulation of the HRTEM images were carried out by JEMS v4, and the crystal structure data were obtained from the Rietveld refinement of the XRD data of the corresponding composition. In the simulation conditions corresponding to 200 keV voltage, C_c=1.1 mm, C_s=0.5 mm and energy spread of 0.3 eV were used.

Figure 6-5 shows the simulation on the unit cell done by switching the polarization direction of the Lu ions with one image in upward (arrow direction) and other in downward polarization along (110) zone axis. The left part of the image gives the atomic arrangement of the unit cells, whereas in the right panel the corresponding simulated HRTEM images are shown.

The simulated images with Lu in up and down polarization clearly demonstrate the possibility of detecting the two states of polarized ferroelectric domains, even though the resolution of the TEM microscope is not competitive with the C_s corrected ones. In this case, it is not really possible to image the displacement of Lu ions with the resolution that can be done in Cs corrected STEM mode, but the overall sum of the atomic potential of the oxygen planes and Lu ions or Mn ions follows the fluctuation in the z-direction of the Lu ions. The difference in the contrast of the Lu-O planes with two Lu ions in downward position gives sharper contrast than the image of upward polarization.

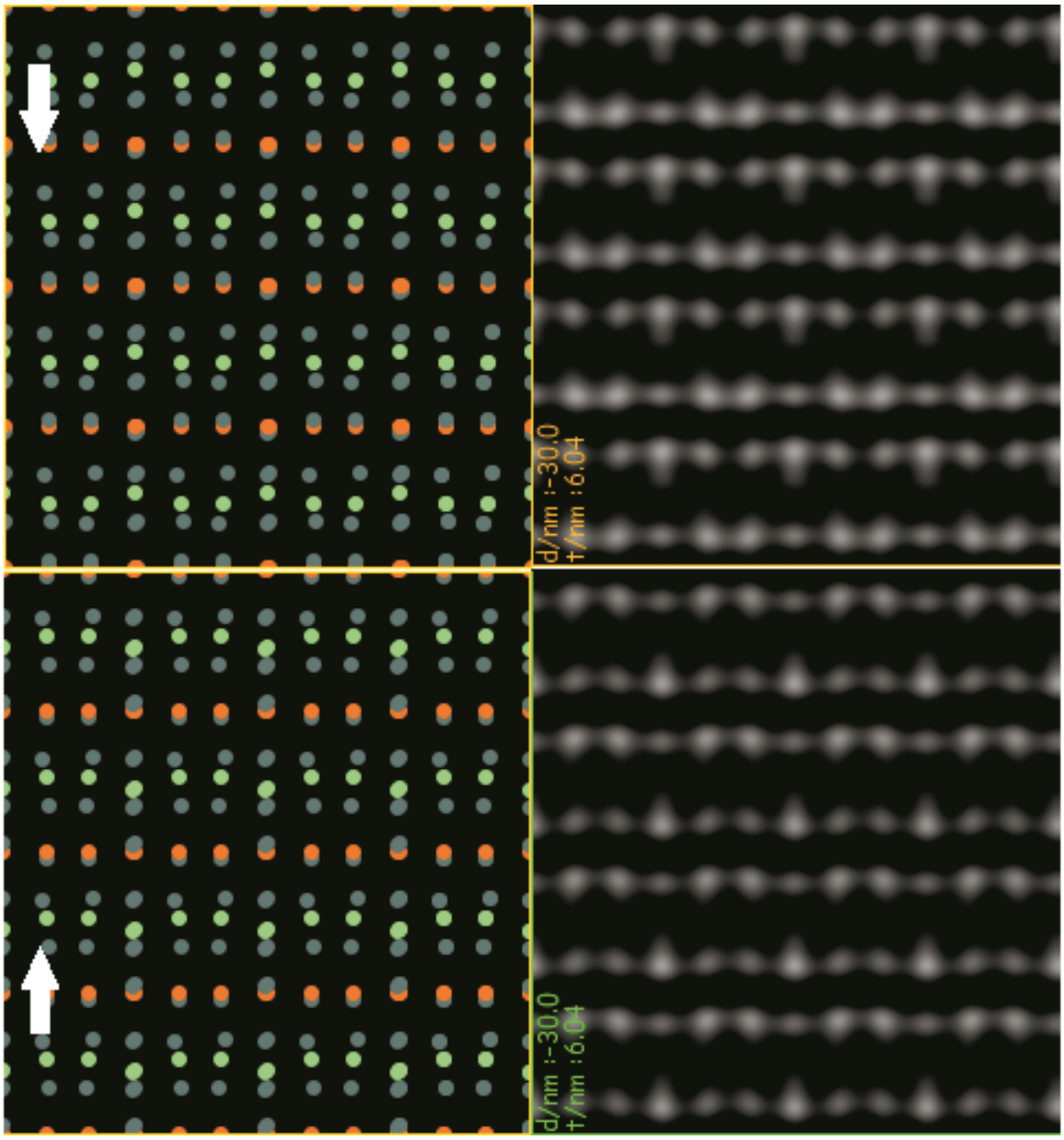

Figure 6-5. Left panel are the atomic arrangements of the ions of the up and down polarized unit cells viewed along (110) zone axis. Right panel are the HRTEM simulated images corresponding to these two atomic arrangements; the difference in the contrast of the atomic rows makes it feasible to distinguish the polarization of FE domains even in non-Cs corrected TEM/STEM.

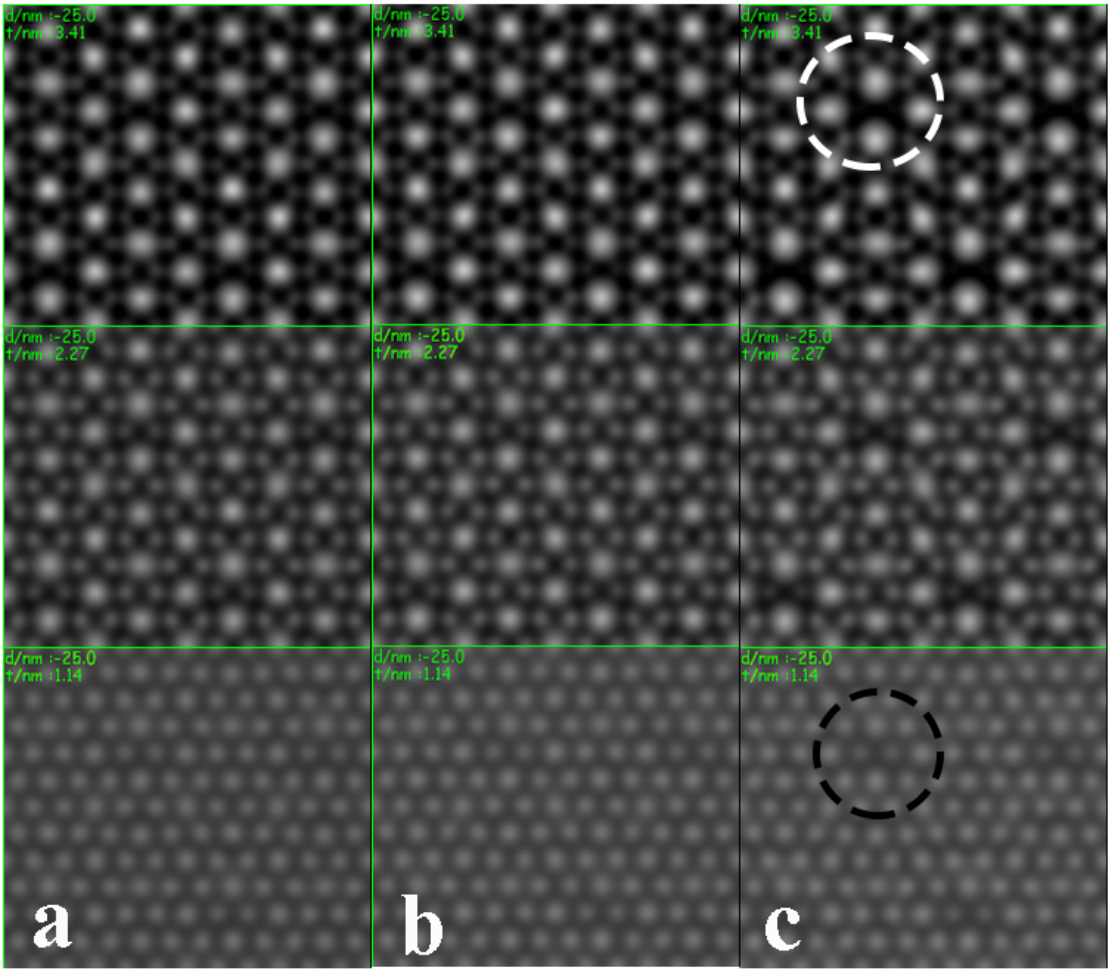

Figure 6-6. Simulated HRTEM images of the $LuMn_{0.92}O_{3\pm\delta}$ structure using 2x2x1 superstructure and imposing presence of vacancies. a. 2 Mn ion vacancies in z=0 and 1/2, b. 6 oxygen ion vacancies surrounded the Mn ions with their positions as the ones in (a) and (c). 2 Mn ion in (a) and 6 oxygen ion vacancies in (b). The dashed circles indicate places of vacancies, in each image, it is repeated four times according to the size of the supercell simulated here.

Figure 6-6 and Figure 6-7 deal with theoretical hypothesis based on defect chemistry of vacancies, showing possible pictures related to the presence vacancies of R-sites and Mn-type in TEM images with the operation condition of the microscope identical to that used in the previous simulation. Because in a unit cell of $LuMnO_3$, there are 6 chemical

formula units, introducing one vacancy in either Mn or Lu sites would represent a high percentage of vacancies. Taking out one Mn ion out of 6 Mn ions in unit cell (Wyckoff position 6 a), would result in a concentration of more than 16% of Mn vacancies.

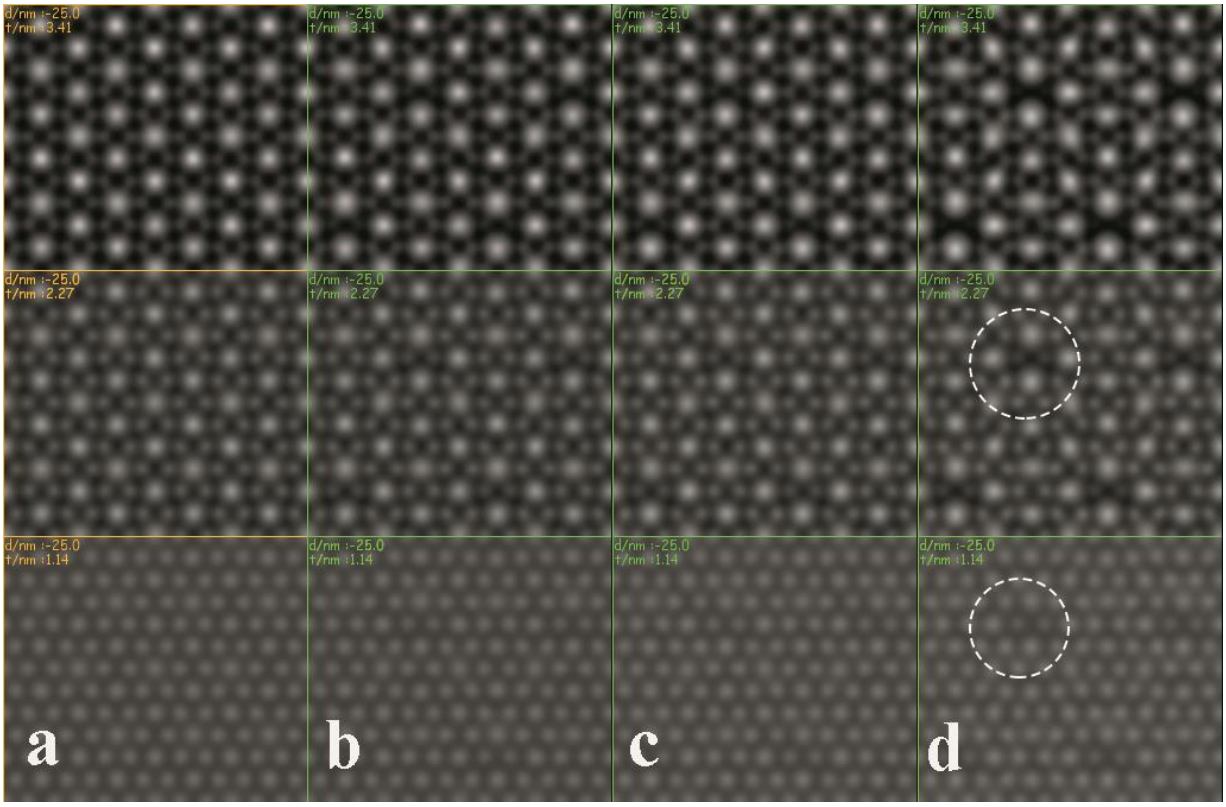

Figure 6-7. Series of HRTEM image simulation of $LuMn_{1.08}O_3$ sample considering (a). no vacancy in 2×2×1 superstructure, (b) 2 Lu ions vacancy located in a sheet of Lu ions between two Mn basal planes in unit cell, (c) six oxygen vacancies around the 2 Lu ions considered in (b) and (d) vacancy of 2 Lu ions and 6 oxygen ions. Circles are showing one of the four Lu+O deficient regions in the model considered here.

To figure out this problem, we had to build a superstructure of 2×2×1. In this structure, it is easy to introduce 8% of vacancies of Mn or Lu. Our hypothesis of neutrality of charge inside unit cell would dictate introducing also oxygen vacancies according to the following formula of the simplified effective charge neutrality condition:

$$3[V_{Mn}'''] = 2[V_{\ddot{O}}] \qquad (6\text{-}1)$$

$$3[V_{Lu}'''] = 2[V_{\ddot{O}}] \quad (6\text{-}2)$$

The oxygen ions to be considered as vacancies by changing their occupancy to zero are chosen around the cation vacancy positions to simulate the clustering of vacancies. Simulated images before including the vacancies, with vacancies of the cation and additionally oxygen vacancies are shown. Regions marked by the circle clearly indicate different contrast, darker contrast than the in remaining of the superlattice. This may occur in TEM images, that the changed contrast can come from vacancies, however it will remain difficult to be proven in a single TEM image. Performing STEM using HAADF detector will eventually be more useful to discriminate by contrast of cation deficient regions.

6-1-3 Imaging defects in the basal plane by TEM

Since in h-$RMnO_3$ materials the in-plane Mn-O-Mn AFM interaction is stronger in basal plane rather than inter-plane Mn-O-O-Mn between two planes of Mn ions (AFM along c-axis)[26,31,32], and the bond angle and bond lengths of Mn-O-Mn in a basal plane will affect the AFM interaction[34], it is important to investigate the effect of the off-stoichiometry on the atomic arrangements of the ions in basal plane. In single crystals of stoichiometric h-$RMnO_3$, it was already revealed that the presence of the domain walls creates planar defects like anti-phase boundaries at the position of the walls [18,49,89]., Theoretical modelling was also successful to predict presence of the anti-phase boundaries on the walls of the FE domains coupled to structural distortion [16,51]. Moreover, interest is rising on the effect of doping in h-$RMnO_3$ lattices, where room for appearing different topologies of structural translation domains is opened [57,58]. To shed light on the presence of the planar defects like anti-phase boundaries in basal plane which affects the geometry of the Mn-O-Mn bond angles and lengths of trimers, the

vacancy doped samples were analysed by orienting the samples parallel to the (001) zone axis. Figure 6-8.a gives the HRTEM image of a $LuMn_{0.92}O_{3\pm\delta}$ particle oriented along (001) direction, the inset of the figure is the simulated lattice view of the TEM image, showing the arrangement of the atoms in the TEM image, matched to the simulation. The bright spots show Lu ions forming hexagons, and the grey spots in the hexagons are the two sets of Mn trimers in z=0 and z= ½ planes, respectively. Figure 6-8.b is the schematic representation of the atomic structure of the unit cell along the same (001) zone axis.

The arrow in image in Figure 6-8.a points to the plane of the Mn ions which plays the role of a mirror plane for the nano-twins on the both sides of this Mn plane. Two coloured triangles are overlaid with two Mn trimers right at both side of the Mn plane, revealing 180° rotation of the structure below the Mn plane respect to the one above the Mn plane. The schematic representation in Figure 6-8.b of the atomic structure with the twins and the Mn mirror plane in between two Mn trimers shows up better the 180° rotation which is permitted by the symmetry of the structure about (001) axis. The distance between two adjacent Lu ions in a hexagon is typically 5.6 Å, whereas this distance between two Lu ions at both side of the Mn mirror plane is just 3.9 Å. Shrinkage of the distance between two Lu ions can be explained as the Mn plane is probably formed in direction of the basal plane which has stronger columbic repulsion interaction with other Mn ions forces them to go further away. Moving of Mn ions away in opposite directions will tilt the pyramids in such a way that the top Lu ions in tilted bipyramids get closed together. Although the composition under study is Lu-rich sample, the magnetic measurement showed a magnetic peak between 40 and 45 K in temperature dependent magnetic measurements both in zero-field–cooled and field-cooled measurements under 100 Oe applied external field. This extraneous peak at the position of Mn_3O_4 magnetic ordering transition was the only indication of having extra magnetic interaction beside of conventional basal plane AFM interaction among Mn^{3+} ions.

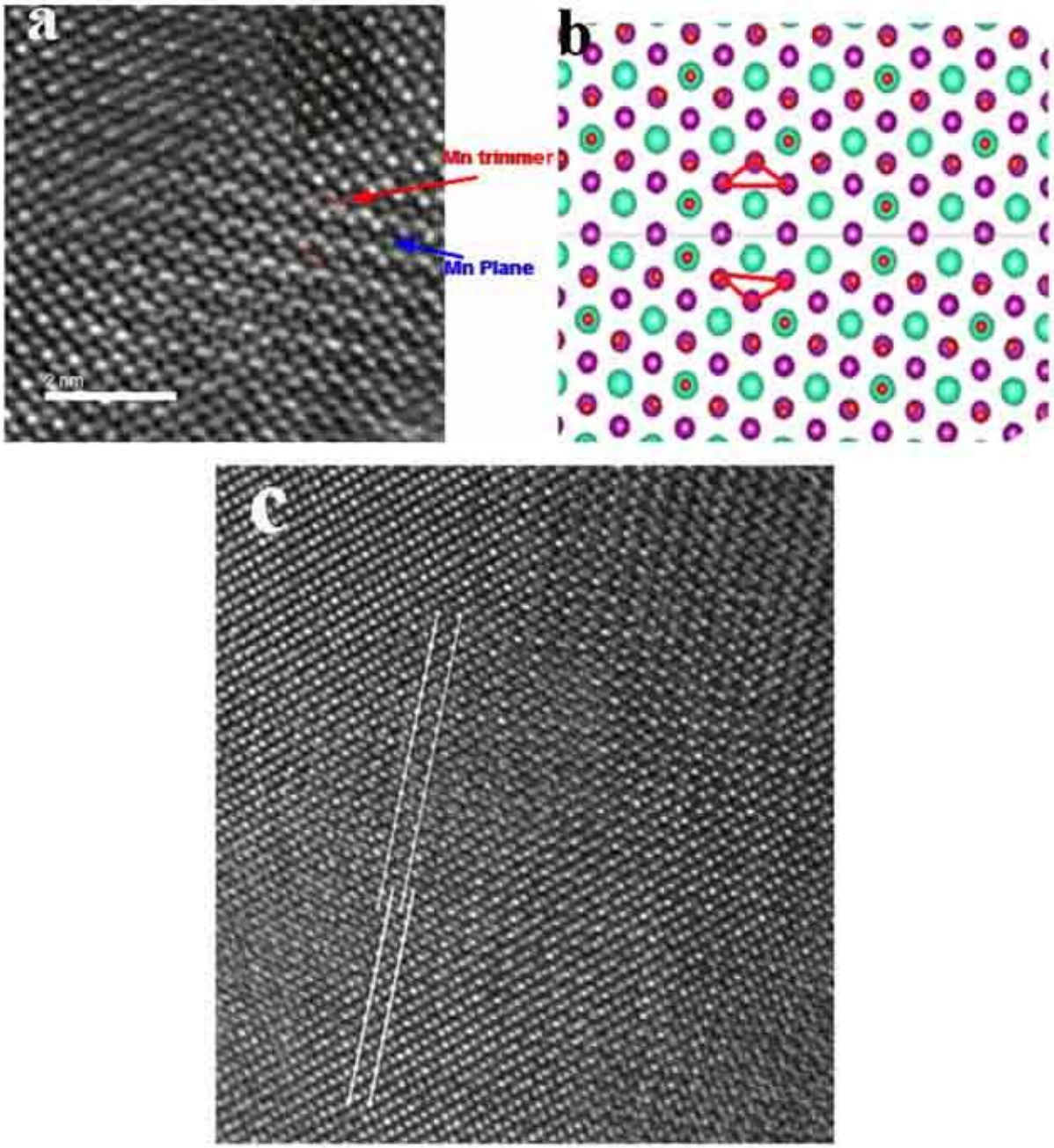

Figure 6-8. (a) (001) zone axis HRTEM image of the sample $LuMn_{0.92}O_{3\pm\delta}$ showing one plane of the Mn in-between the two planes of the Lu ions. The inset shows the simulation matched with the undistorted part of the image. (b) Modelling of the disordered in the lattice resulted in losing one Mn plane out of two Mn planes between planes of Lu ions. (c) Anti-phase boundary of Lu planes indicating shift of half spacing in planes of the Lu ions with the angle of 30^0 in respect to a-axis.

The EELS study did not show any clear deviation from 3+ oxidation state in the Mn $L_{3,2}$ edges using white line ratio method to be discussed later in this paper. Planar defects as these found in Figure 6-8.a are likely sources for magnetic interactions in basal plane other than the essential AFM interaction of Mn ions in trimers with Neel magnetic ordering temperature around 90 K, that characterises h-$LuMnO_{3\pm\delta}$ materials. TEM images of (001) zone axis showed the basal plane arrangements of Mn trimers together of Lu ions forming hexagons. Further observation confirmed the density of interfaces of structural domains in basal plane of the crystalline lattices for x>1 samples. Still one could not find out changes in chemical composition of the interfaces. The same analysis also indicated wide interfaces in order of 2 or 3 unit cells which promotes higher density of disordering occurring there. The detailed study of the chemical shifts at interfaces requires resolution of EELS analysis which is beyond the resolution of TEM instrument being used.

In Figure 6-8.c, the APB of Lu planes appears along the plane 30° inclined in respect to a-axis, where the TEM image shows little out of registry (APB´s are marked by lines in the Figure 6-8.c). The same situation happens for the Lu planes, 60° turned counter-clockwise with respect to the APB´s planes (not shown here), still in a region out of registry. As it was discussed in relation to previous images, a region out of registry where disordering in the lattice appears seemingly has its origin in fluctuations of chemical composition of the lattice. According to XRD analysis in chapter 4, fluctuation in Mn/Lu ratio inside the lattice and the subsequent change of unit cell volume can create states of strain energy in the lattice, the formation of planar defects being a way to balance and release the energy accumulated in the lattice. The analogous picture appeared in a recent study on $Y_{0.67}Lu_{0.33}MnO_3$ single crystals [58], where partial edge dislocation as an extra plane (030) divides two polarized domains. Although in that case, the authors could not find any evidence of chemical in-homogeneity, the present studies with self-doped samples reveals that change in the volume of the unit cell from x=0.96 to x=1.04 is approximately the same as value change of cell volume determined by the change of composition from z=0.30 to z=0.35 in ceramic samples of $Y_{1-z}Lu_zMnO_3$, around 0.16%

[34]. The microstructure and atomic arrangements of the ions in 0.08% vacancy doped or less $LuMn_xO_3$ lattices would dictate sensitivity of the lattice to any oscillation of chemical composition across the fields being examined by TEM.

The level of chemical in-homogeneity detected across a crystalline particle of $LuMn_xO_{3\pm\delta}$ phase in sample with x=1.08 (one day annealing time) is further characterized in Figure 6-9. Figure 6-9 exhibits two parts of one BF-STEM image very close together of one same particle. The values of the Mn/Lu ratio determined from EDS results in Figure 6-9.a and b show local fluctuations in composition of the analysed spots with different ranges of fluctuation.

The STEM image in Figure 6-9.a presents uniform contrast. The average composition determined by EDS yields x=1.035 close to the upper stability limit $x_H \approx 1.05$ of $LuMn_xO_{3\pm\delta}$ solid solution established in section 4-2-1. As also seen in Figure 6-9.a, there is almost no change in x along the line of analysis, x being constant within the experimental error of the EDS analysis. On the contrary, the contrast of the image in Figure 6-9.b shows larger variability, some regions darker than others. Such contrast change is matched by variation of Mn/Lu ratio along the line of EDS analysis. The average value of the x ratio is 1.051, higher than the average x above. Local chemical composition changes from values of x below 1.00 with Mn-deficiency in the upper left corner of the image, to values of x in the range of the average composition at the middle and to Mn-rich side at lower right corner. The values of x of these last points are well above the upper stability limit $x_H \approx 1.05$ of $LuMn_xO_{3\pm\delta}$ solid solution determined from XRD in the present study and approach the maximum value of x=1.20 in polycrystalline $LuMnO_3$ materials at 1300 °C reported in bibliography [109], given in Table 4-4. The ratio of distances of atomic planes along the line of analysis from lower right to upper left is 1.018. The behaviour of a-axis and b-axis lattice constants are related to the basal plane and cannot be assessed in the images in Figure 6-9 taken along (110) zone axis perpendicular to basal plane, but changes in atomic distances along c-axis can be evaluated.

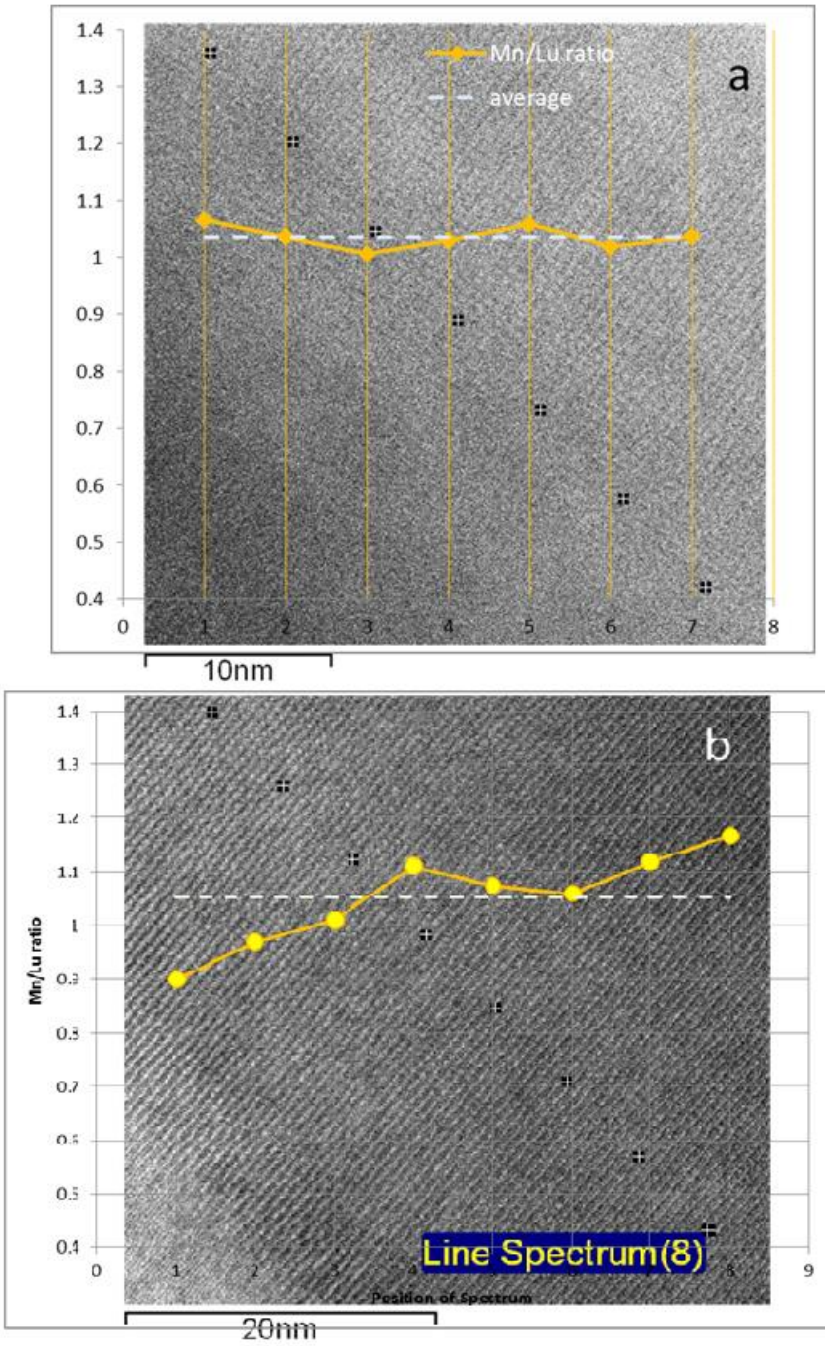

Figure 6-9. BF-STEM images of two adjacent parts of one same crystalline grain of $LuMn_xO_{3\pm\delta}$ phase of sample x=1.08 taken along (110) zone axis. For each image, EDS analysis was made of the all area and at the given points and the corresponding results of the Mn/Lu ratio for point analysis (yellow) and average ratio (dashed white line) are given in overlaid plots. (a) Area of nearly uniform contrast and average Mn/Lu=1.035. (b) Area with regions of dark contrast and average Mn/Lu = 1.051.

The relative change of distances between atomic planes above is much higher than the total change in dimensions of c-axis in Table 4-1 to Table 4-3 and suggests the formation of intergrowths with atomic planes of large Mn excess in the lower right zone of the image in Figure 6-9.b. The investigation of local fluctuation of chemical composition of crystalline particles and the observed misfit between the actual values of Mn/Lu ratio and the expected ones based on average composition of polycrystalline samples or single crystals will have important consequences on the interpretation of properties like ferroelectricity, magnetic behaviour and transport of the h-$RMnO_3$ materials [18,57,99].

Our investigations on the local fluctuation of the chemistry of the particles and observed shift in the chemistry of the expected composition would have important consequences on the interpretation of physical and chemical properties like ferroelectricity and magnetic behaviour [18,57,99].

Considering the secondary phase formation in vacancy doped samples in the x<0 side of the solid solution from XRD Rietveld refinement and clear peaks in XRD patterns, segregation of Lu_2O_3 secondary phase is a way to remove extra Lu ions from the lattice of main phase. High temperature oxygen annealed epitaxial grown $YMnO_3$ thin films also showed indication of Y_2O_3 precipitates [111,163–165]. This was explained as the oxidizing potential of Y and Mn being different, causing the Y/Mn ratio to become larger than unity in some regions like the interface of film/substrate. The secondary phase Lu_2O_3 forms residual particles in the present study. One finds only very few particles of $LuMnO_3$ with precipitation of Lu_2O_3 nano-regions in sample x=0.92. On the contrary, the same clear evidence of the Mn_3O_4 secondary phase was not found in XRD patterns of samples with x>1, only as faint peaks, Figure 4.4, but with pronounced effects in magnetic measurements, Figure 5-6. Above the lower limit of solid solubility in this region lattice images are evidencing better defined atomic arrangements in the particles of main phase. Going down from x=0.96 to x=0.92, lattice distortion appears in many particles of the main phase. Excess in Lu_2O_3 brings in some degree of metastability of the nanostructure and strain and planar defects are seen in sample x = 0.92 more often than

in x = 0.96 and x = 1.00 samples. XRD Rietveld refinement as well as TEM images confirm that atoms within the unit cells of the main phase in sample x=0.92 could not properly stabilize their positions during the short time of the sintering process according to the expected $P6_3cm$ space group and allowed Wyckoff positions.

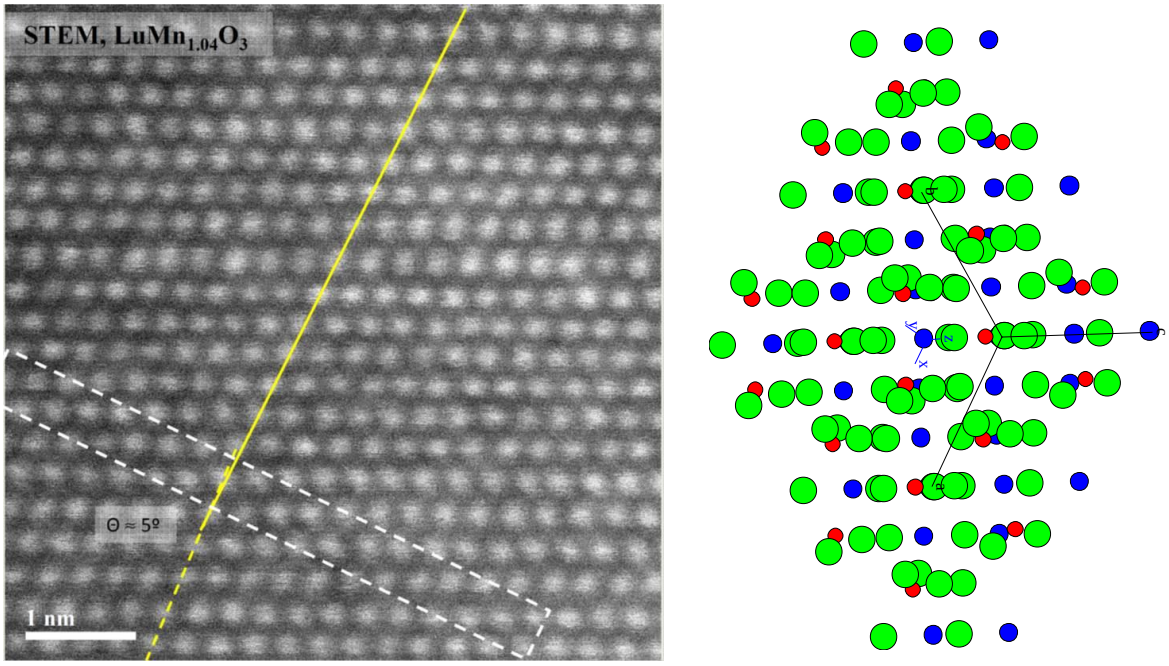

a) b)

Figure 6-10.(a) STEM image of the crystalline structure of x=1.04 $LuMn_xO_{3\pm\delta}$ solid solution for zone axis close to the $[\bar{1}\,1\,6]$ direction and (b) corresponding view of the crystal structure evidencing the columnar alignments of Lu^{3+}-O^{2-} ions in hexagonal symmetry centred in the origin of the crystalline cell were an identical columnar alignment of the Lu^{3+}-O^{2-} ions is also found. O^{2-} ion (green), Lu^{3+} ion (red), Mn^{3+} ion (blue), crystalline lattice simulation done with CaRIne Crystallography 3.1 software.

The STEM image of atomic resolution in Figure 6-10.a of a crystalline domain of the main phase in sample $LuMn_{1.04}O_{3\pm\delta}$ displays a sub-grain boundary with the low misfit angle θ ≈ 5°. The corresponding view of the crystal structure simulated by using CaRIne

Crystallography software in Figure 6-10.b evidences the columnar alignments of purely Lu^{3+}-O^{2-} ions in hexagonal symmetry centred in the origin of the crystalline cell. The composition of the solid solution has Mn in excess and lacks Lu ions in comparison to the perfect $LuMnO_{3\pm\delta}$ lattice. Close observation of the sub-grain region (highlighted in Figure 6-10.a) shows that the positions of the columnar alignments of the Lu^{3+}-O^{2-} ions maintain the hexagonal coordination in the sub-grain boundary structure but hexagons become slightly irregular thus allowing for the small misfit of 5° in plane orientation. The corresponding minute shrinkage of the sides of the hexagons in the sub-grain boundary creating the directional shift may be caused either by segregation to the subgrain boundary of Lu vacancies ($V_{Lu}^{'''}$) or of Mn ions (eventually with decrease of valence to Mn^{2+}) in antistructure configuration ($Mn_{Lu}^{'}$), the ($Mn_{Lu}^{'}$) defects representing a species of smaller ionic radius than the Lu^{3+} ions.

6-4 Density functional theory and EELS spectroscopy

6-4-1 Oxygen K-edge and crystal field environment of Mn

The microstructure of the off-stoichiometric lattices and the respective distortions and defects in the lattices imply changes in the electronic structure of the ideal h-$RMnO_3$ [18]–[20]. Thus, the TEM study is followed by EELS analysis of the oxygen K-edge of the selected samples with the objective of disclosing the effect of cation vacancy on the electronic structure of h-$LuMn_xO_{3\pm\delta}$ ceramics. The oxygen K-edge around 532 eV contains hybridization of the O-2p orbitals to unoccupied states of the conduction band of the Lu-5d and Mn-3d orbitals [142,166–170]. Figure 6-11 shows EELS spectra of samples of 3 compositions, exhibiting corresponding peaks of the Mn-3d/4sp or Lu-5d/6sp bonds to the oxygen ions. The spectra are background subtracted using power law approach embedded in Digital Micrograph Suit 1.8.4. Data acquisition of the EELS

spectra in HRTEM was intentionally not too long to avoid excessive exposition of samples to the electron beam, with probable change in the oxidation state of the Mn or oxygen content [167]. Previous reports on the XANES O-K edge of $YMnO_3$/$HoMnO_3$ polycrystals [142,166,168] and XAS of O-Kedge of single crystal $YMnO_3$ [131] and $TbMnO_3$ [170] provide the guidelines to interpret the features appeared in EELS spectra of the O K-edge of h-$LuMn_xO_3$ oxides in Figure 6-11. The oxygen pre-peak below 532 eV appearing in EELS spectra of Figure 6-11 was also reported on EELS spectra of some rare-earth manganites [99,167]. Accordingly, the peaks "a" and "b" correspond to bonding of Mn 3d orbitals to apical and planar oxygen ions, therefore their intensity gives a scale of the population of the unoccupied states for each peak. The following two peaks, labelled as "c" and "d" are related to the Lu(5d)-O(2p) with the last peak marked as "e" linked to Mn(4sp)-O(2p) hybridized orbitals, respectively. Although the statistics of the acquired EELS data is changing in different measurements mostly because of thickness variation, EELS spectra demonstrate all these features within the energy resolution of the measurement in all samples (x=0.96 and 1.04 are not shown here). EELS spectra were always calibrated with reference to ZLS spectrum. The energy of the analysed features in EELS spectra does not change with Mn/Lu ratio x.

To clarify the contribution of the unoccupied orbitals of ions involved in EELS spectra, DFT calculations were performed using GGA+U approximation (with U, on site Coulomb interaction energy 6eV) implemented in the Wien2K package, with A-type antiferromagnetic configuration of the Mn^{3+} ions and -6.5 Ry energy to separate core and valence states. Calculation was done for the three compositions of Figure 6-11.a, with the crystal structure of the corresponding Rietveld Refinement of XRD patterns.

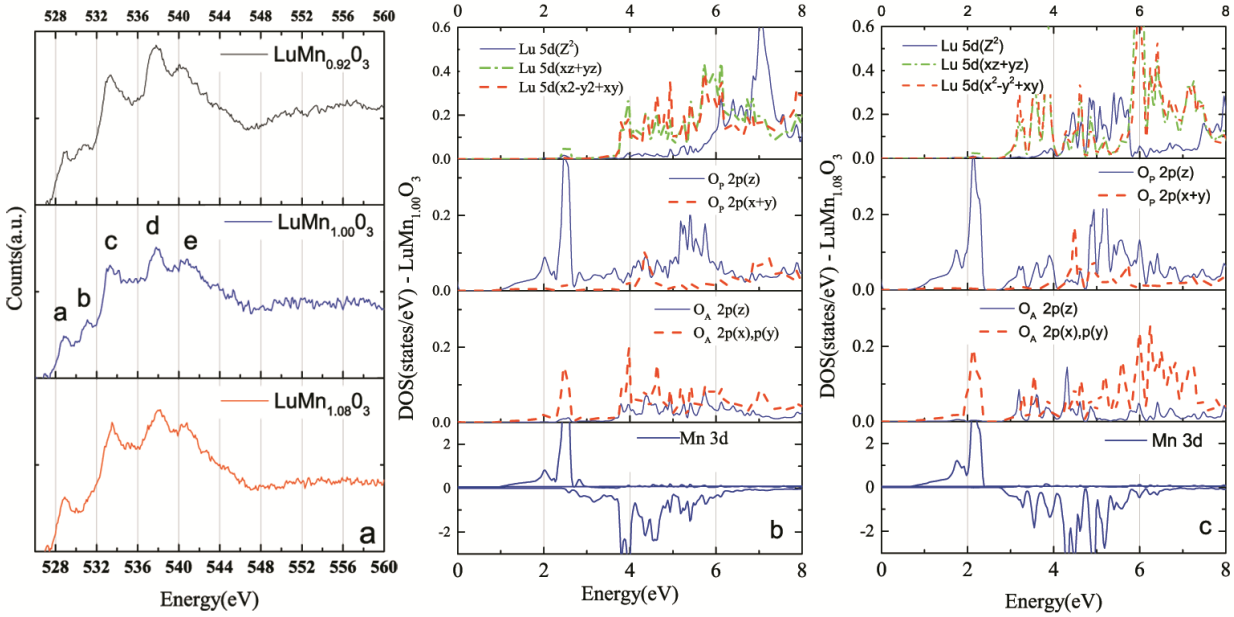

Figure 6-11. (a) EELS spectra of the O K-edge of the three selected compositions, indicating slight change in intensity as the type of vacancy is changed. Density of unoccupied States calculated for sample x=1.00 (b), and 1.08 (c) (the x=0.92 is not shown here) for the orbitals of the involved ions which have contribution in EELS spectra.

Figure 6-11.b and c shows density of states for 3d, 5d and 2p orbitals of the Mn, Lu and oxygen respectively. In the conduction band close to the Fermi level, large contribution comes from hybridization of Mn(3d) orbitals with O(2p) orbitals, mostly planar oxygen as expected [127]. On the contrary to the reported O K-edge measured by XAS in some h-$RMnO_3$ materials [131,142,171], the energy resolution and statistics in present spectroscopic method in the pre-edge region of O K-edge does not allow to distinguish different unoccupied states of the Mn(3d) orbitals separately. DOS of Mn (3d) in Figure 6-11.b implies that the first peak below 530 eV corresponds to the mixture of the unoccupied states of the Mn-3d($3z^2$-r^2)↑, (xz↓-yz↓) and (xy↓-x^2-y^2↓), and the second peak above 530 eV shows Mn-3d($3z^2$-r^2)↑ unoccupied states with strong hybridization to the O(2p) unoccupied states. The region after 533 eV in Figure 6-11.a shows the Lu(5d)-O(2p) hybridized states, with two successive peaks with higher intensity than those

peaks in the pre-edge region, revealing the strong nature of the bonding of Lu(5d)- O(2p) unoccupied states[172,173], claimed as the probable driving force of the ferroelectricity [130,131,172].

6-4-2 White line ratio and oxidation state of Mn

The EELS spectra of the Mn $L_{3,2}$ edges of the same samples of Figure 6-11.a are shown in Figure 6-12.a. The $L_{3,2}$ edges of the transition metal ions have been extensively studied as they provide information of the oxidation states of the transition metals and coordination of the transition metal environment [174,175]. The L_3 and L_2 edges of the Mn^{3+} ions in Figure 6-12.a are the result of electron transition from $2p_{3/2}$ and $2p_{1/2}$ states to Mn 3d unoccupied states, respectively. They have almost similar shape and energy onset within the resolution of EELS spectroscopy. The ratio of L_3/L_2 edges of Mn ion gives the Mn oxidation states, which can be quantified by the method so-called "white line" ratio described elsewhere [176–179]. To apply white line ratio method on the Mn $L_{3,2}$ edges of the EELS spectra in Figure 6-12.a, the multiple scattering contribution was subtracted using Digital Micrograph Suit, then a 10 eV window was chosen as scaling window in the region immediately after L_2 peak to be used as Hartree-Slater cross section step function. The so subtracted $L_{3,2}$ peaks from the extracted step function were both integrated in the same energy window. The average of L_3/L_2 ratio of the EELS spectra of two different particles of each composition for 5 different compositions is plotted as a function of Mn/Lu ratio in Figure 6-12.b. Based on the relation between the L_3/L_2 ratio and the corresponding Mn valence in the literature [174–177,179], the present analysis in Figure 6-12.b confirms a rather constant value of valence of three for the Mn oxidation state for most measurements, or very close to it, as the nature of covalent bonding may result in slight change of the valence state. Besides of Mn valence state, $L_{3,2}$ edges were used to determine the crystal field environment of the Mn ions

because of their sensitivity to the coordination number of Mn and therefore to the bonding of Mn to its surrounding oxygen ions [170,174,180]. Compared to EELS of h-$YMnO_3$ [174] where the Mn environment is very close to the one in h-$LuMnO_3$, the $L_{3,2}$ edges of the off-stoichiometric samples in Figure 6-12.a are in good agreement with the ones of the stoichiometric the x=1.00 sample and the one for h-$YMnO_3$ stoichiometric sample of S. Nishida [174], confirming the stability of valence state for Mn ions in the analysed regions.

Two visible changes can be observed by comparing EELS spectrum of x=1.00 sample with EELS spectra of the off-stoichiometric ones in Figure 6-11.a. First in the Mn(3d)-O(2p) hybridized region below 533eV for x=1.08, the shape of the second peak is almost step-like instead of being a distinct peak as it is for the two other samples. The second change is observed in the relative intensities of the peaks correspond to the Lu(5d)-O(2p) hybridized states for x=1.00 which is rather lower than the one for off-stoichiometric samples. In the first case, the O pre-edge, either in the spectra of XAS [131,142,166,168,173,181] or EELS [99,167,176,182–187] were interpreted as the hybridization of transition metals to the O(2p) orbitals. The change of the intensity or shape of the peaks was attributed to the oxygen off-stoichiometric or structural distortions and defects. It was argued that presence of oxygen off-stoichiometric is followed by change of the Mn^{3+} valance state to keep total electrical charge neutral in the case of e.g. $TbMnO_3$ [99] or $SrMnO_3$ [186]. However, very rare studies on the effect of the oxygen off-stoichiometric on the properties of h-$RMnO_3$ materials indicate at least that oxygen deficient $YMnO_{3-\delta}$ may undergo change of the valence state of the Mn^{3+} [96,188] or keep it as 3+ [97,167]. In both cases the bond length of the Mn-O is modified, which in turn, changes the Mn(3d)-O(2p) hybridization as it is distinguished in oxygen pre-edge of the EELS spectra (peaks a and b in Figure 6-11.a). Since in Figure 6-12.b. there was no clear evidence for any deviation from the expected Mn^{3+} valence in the analysed regions, it would be rational to assign the change in the shape of the oxygen pre-edge of the sample x=1.08 compared to x=0, to the crystal field environment of the Mn^{3+} ions, either

due to oxygen vacancies (case of h-$YMnO_3$ [167]) or Lu vacancies (like Tb deficient in $TbMnO_3$ domain walls [99]) in order to keep charge neutrality.

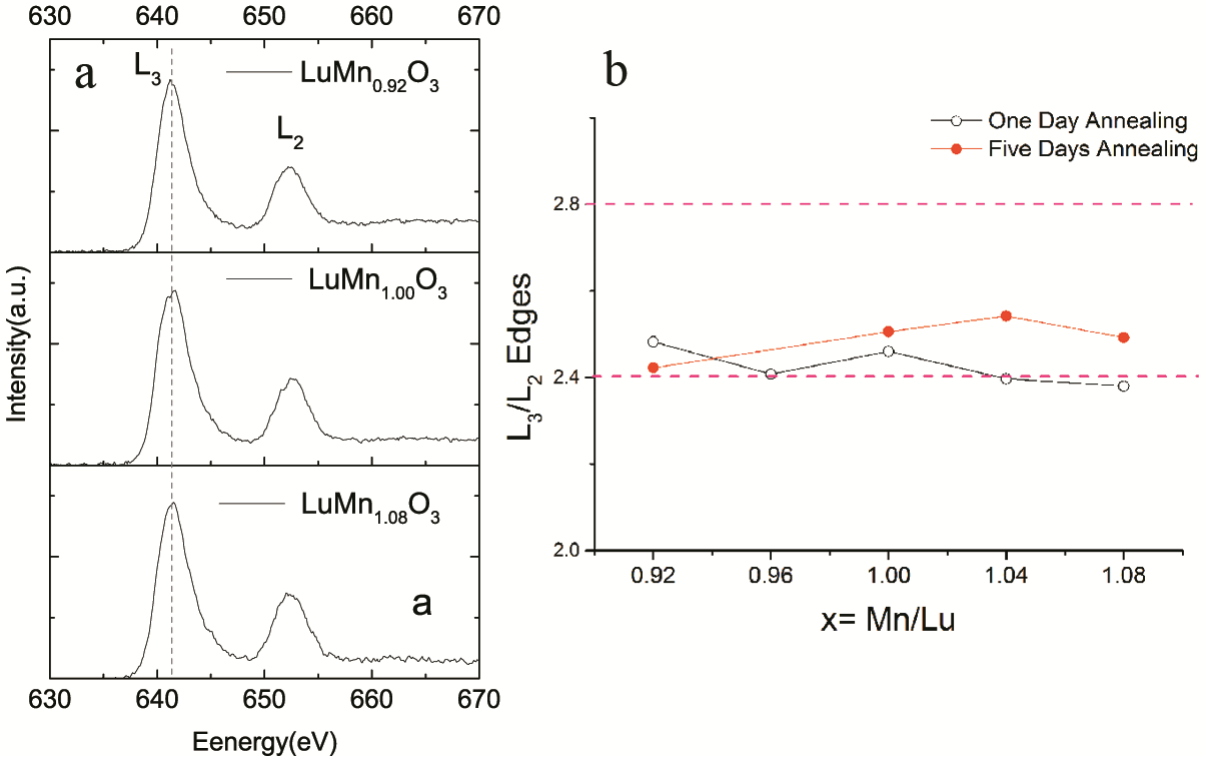

Figure 6-12. EELS spectra of the Mn $L_{3,2}$ edges of the three samples in the Figure 6-11.(a) (all compositions of the one day annealing samples). constant energy onset, also the apex of L_3 peaks have almost the same energy (dashed line in the figure). (b) Average "white line" ratio of two different particles for each of the given sample compositions of samples of one day and 5 days annealing time. Points between the limits of 2.4 and 2.8 are considered representative of 3+ oxidation state of Mn ions.

The DOS of Mn(3d) and O(2p) for x=1.08 sample in Figure 6-11.c shows spreading of the Mn(3d)↓ unoccupied states in a wider energy region towards higher energies in conduction band rather than more localized DOS of Mn(3d) for samples x=1.00 (Figure 6-11.b) and x=0.92 (not shown here). The higher population of unoccupied states in the energy window of 4 eV to 5.5 eV is mostly due to the bonds of 3d(xz-yz)↓ and 3d(xy-(x2-y2))↓ orbitals of Mn to O(2p) orbitals of planar and apical oxygen ions in the

unit cell. It would be expected to have these bonds present as separated peaks in pre-peak of O K-edge, however, energy resolution better than 0.8 eV is needed to distinguish them with higher statistics. Therefore, what appears as a step-like region below 532 eV in Figure 6-11.a (peak b) is in fact overlapping of Mn(3d)↓-O(2p) unoccupied states for x=1.08, different from that in x=0.92 and x=1.00 as a result of change in the unit cell of off-stoichiometric h-$LuMn_xO_{3\pm\delta}$ ceramics.

The second feature is the slight difference due to sample composition in the intensity ratio of the peaks c and d in O-edge, Figure 6-11.a, in the energy region corresponding to Lu(5d)-O(2p) hybridization. Samples out of stoichiometry show more pronounced c and d peaks than the x=1.00 one. Previous EELS studies on the same peak ratio in Y_2O_3 materials have shown that the ratio of the peaks of Y(3d)-O(2p) hybridized orbitals varies if the octahedral environment of the Y ions changes either because of oxygen vacancy or other defects [189–191]. In either case, the intensity of the peak c is higher or at least the same as the intensity for peak d, and the defective region or oxygen vacant region both indicate the reversal of the c to d intensities, higher for c than the one for d. This trend may help us to understand the variation of the relative intensities of the peak c to d for x=1.00 and x≠1.00 samples in Figure 6-11.a. As shown by the XRD results, the lattice parameters change with x, which in turn affects the crystal field environment of the Lu ions in respect to 8 surrounding oxygen ions in the unit cell. Since in Figure 6-11.b, the DOS of unoccupied states of the Lu(5d) and O(2p) are main constituents of the peaks c and d in O K-edge with strong bonding, the change of the bond lengths of the Lu to oxygen ions directly results in slightly different situation of the Lu(5d)-O(2p) hybridization, which in turn appears as variation of the relative intensities of the unoccupied states in this region. Stronger bonding of Lu(5d)-O(2p) for both planar and apical oxygen ions in Figure 6-11.c for sample x=1.08 in comparison to one in Figure 6-11.b for x=1.00 leads to the effect of chemically driven unit cell distortion on the Lu(5d)-O(2p) bonds, that results in peak ratio variation of corresponding peaks in O K-edge in EELS spectra of Figure 6-11.a.

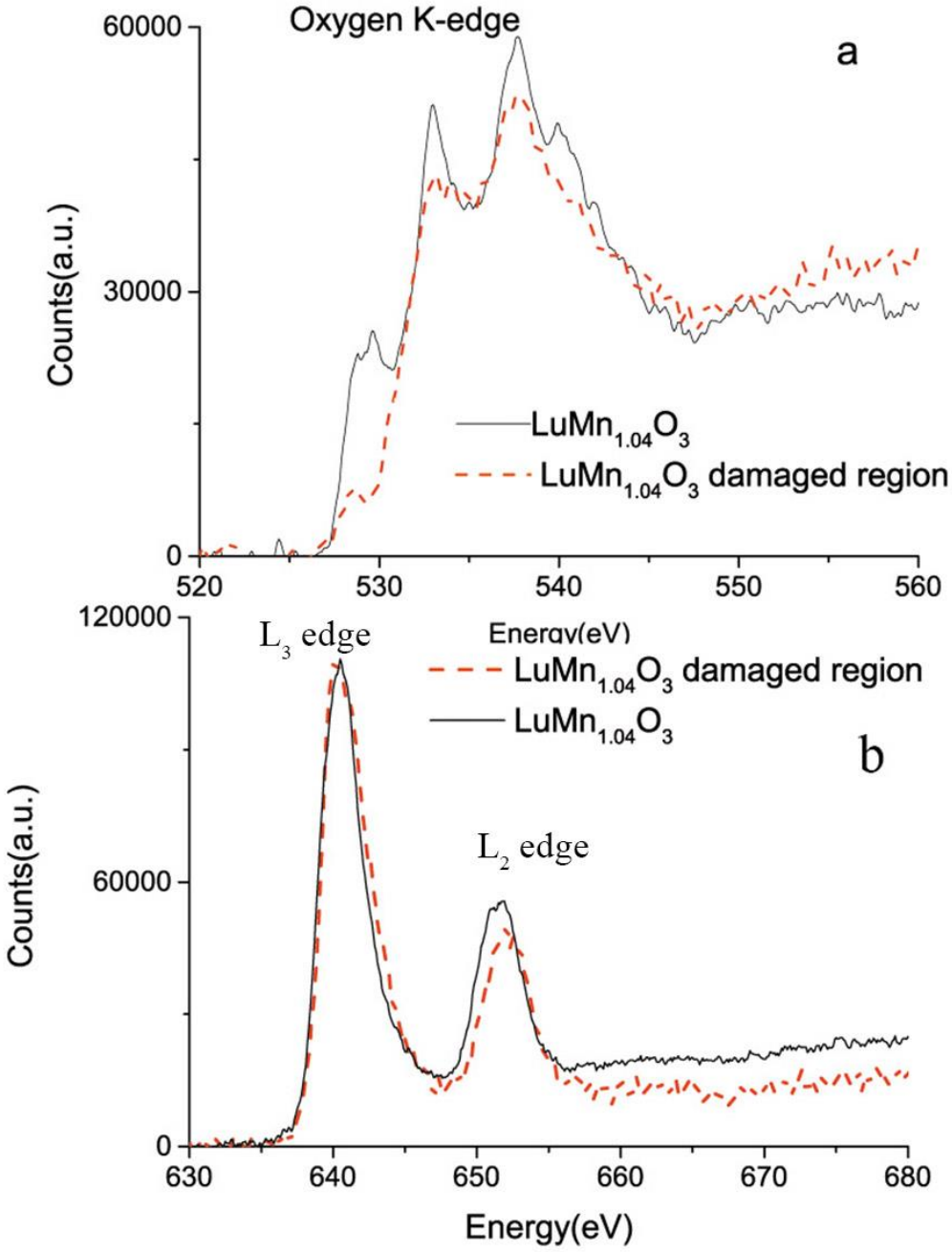

Figure 6-13. Comparisons of EELS spectra in two regions of the crystalline grain of the main phase of $LuMn_{1.04}O_{3\pm\delta}$ sample, damaged area at the edge of the particle (dashed-line) and slightly to the inside the particle (solid line). (a) oxygen K-edge and (b) $L_{3,2}$ edges of Mn^{3+}.

It is instructive to analyse and give the dimension of the effects of beam damage coming from ion milling in TEM sample preparation or high energy electron irradiation of the sample in TEM. Figure 6-13.a and b compare the EELS spectra of Oxygen K-edge and $L_{3,2}$ edges of Mn for two different regions of one same grain of the main phase of x=1.04. The spectra were taken from the damaged region on the edge of thin section and from a second area little to the inside of the grain where no damage was observed. Beam damage (most probably Ar ions in ion thinning process) changed the pre-peak of oxygen, which would be explained by a completely different crystal field for Mn and reducing the hybridization of Mn to its surrounding oxygen ions. Damage effects are not so clear in the Mn $L_{3,2}$ edges [167]. The "white line" ratio analysis gave 2.68 which is visibly above the values that were obtained in Figure 6-12.b. The same analysis was done on the damaged region of sample x=0.92 which gave 2.27 from white line ratio, below the boundary line defined for Mn^{3+} oxidation state in Figure 6-12.b.

6-4-3 Hausmannite and Mn ion oxidation state

Since hausmannite secondary phase was observed on some h-$RMnO_3$ oxides [18,65,90] as well as in samples of the present study and being still not clear if there are intergrowths of planes of hausmannite or of other phase of Mn-O compounds, the analysis of the EELS spectra of Mn_3O_4 secondary phase was added to the matters of the present research. Sample x=1.08 one day annealing with some lean particles of hausmannite thin enough for EELS spectroscopy was selected for the study. Figure 6-14.a gives the lattice image of hausmannite secondary phase composed of many nano-structural domains. The elemental composition was checked with EDS. The particle gives roughly the stoichiometric of Mn_3O_4 within the error of EDS. The scale of the nanodomains that constitute the Mn_3O_4 particle is far below the large sizes of some of hausmannite inclusions found in SEM analysis of samples with Mn-excess, section 4-3-2.

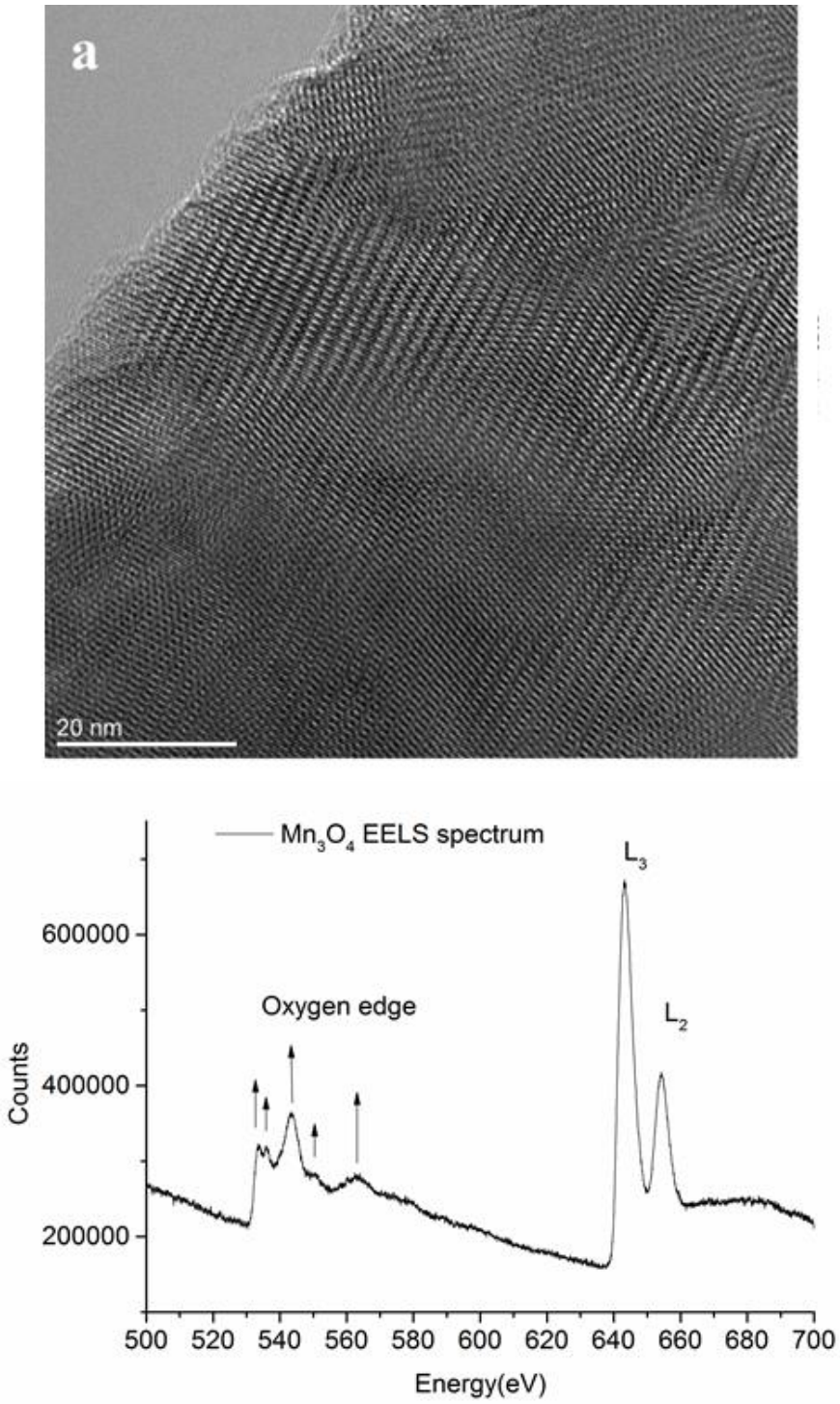

Figure 6-14. Sample $LuMn_{1.08}O_{3\pm\delta}$, one day annealing time. (a) Particle of hausmannite showing different domains inside the lattice and (b) EELS spectrum of a region less than 10 nm in size inside the same particle.

The fine nano-texture of the hausmannite particle divided into nanodomains will cause XRD line broadening and may explain the difficulty on detecting the total fraction hausmannite by XRD described in section 4-1. Figure 6-14.b displays the EELS spectrum with both oxygen K-edge and $L_{3,2}$ edges of Mn of the same particle taken from narrow area of less than 20 nm diameter. In a first glance, it is absent the pre-edge of oxygen related to Mn-O hybridization in $LuMnO_3$, Figure 6-11.a and Figure 6-13.a. The 5 peaks in the O-K edge of hausmannite in Figure 6-14.b have relative intensity in close correspondence with the sequences of a1, a2, b, c and d peaks or the oa1, oa2, oa3, ob* and ob peaks of two other EELS studies of Mn_3O_4 [192,193].

The analysis of the intensity of EELS peaks is difficult as there are two sub-lattices for Mn^{2+} and Mn^{3+} in the inverse spinel structure of hausmannite which result in different environment of the Mn ions and their surrounding oxygen ions and may be seen in fine structure of the oxygen edge and split of L_3 line of the Mn edge [177,192–194]. Values of the white line ratio of L-edges of Mn in Mn_3O_4 were reported in the literature as signature of the average oxidation state of Mn ions in the hausmannite [177]. The values of "white line" ratio evaluated by using Double Arctan method [195] implemented in Digital Micrograph suit in some other points inside the same particle to stay between 2.47 and 2.8 and the energy difference between L_3 and L_2 edges between 11.1 eV to 11.2 eV. In the literature [175,177], the values white line ratio of 2.8 (0.2) were assigned to average oxidation state Mn ion of 2.67 for hausmannite the corresponding energy difference being 11.2(0.1) eV. Although data on white line ratio and energy difference determined from EELS spectra collected from the particle in Figure 6-14.a are close to values of the same parameters reported for Mn_2O_3 compound (2.4 (0.1) for white line ratio and 10.8(0.1) eV energy difference, respectively [177], the fine structure of oxygen edge excludes the Mn_2O_3 phase and can only be assigned to the hausmannite phase [192,193]. The explanation for the differences of the white-line ratio of this study and values reported for hausmannite in the bibliography have to sought hidden on the

microstructure of the phase as in TEM image of the particle of Figure 6-14.a with a fine texture which may affect the shape of Mn L-edges [174].

6-3 Regularity of the atomic structure after extended annealing time

6-3-1 Defects of the crystalline lattices after long time annealing

In the XRD analysis in section 4-2-1 the dimensions of unit cell of the $LuMn_xO_{3\pm\delta}$ ceramics changed in a more regular way with x and present lesser dispersion of values after 5 days and 10 days of annealing time. In parallel, the parameters of fitting of Curie-Weiss equation to the paramagnetic behaviour, the anomalous remnant magnetization between T_C of hausmannite and T_N of the main phase also presented improved repeatability and lesser scatter after extending the time of annealing of the samples. The aim of this last section of the chapter on TEM and STEM microscopy of the off-stoichiometric $LuMn_xO_{3\pm\delta}$ samples is to present indications of improvement of regularity of the crystalline lattices at the atomic and nanoscale in the samples with longer annealing time that may elucidate the observed improvement in properties.

Figure 6-15 shows defects present in sample x=1.04 after 5 days annealing. They appear as lines of dislocations in a part of the image whereas the remaining area of particle looks defect free with a rather regular structure. This kind of line defect which has been observed in different samples under study occurs in localized areas, leaving the remaining of a large particle undisturbed. The dark field image of Figure 6-15.a was taken to detect dislocations along (001) zone axis. The image shows strain due to the presence of line dislocation blocking the expansion of FE domains. As image indicates the dislocations promote the bright (marked as 1) and dark (marked as 2) contrast around them which implies up and down polarization. Considering the contrast around line

dislocations of the DF image in Figure 6-15.a it can be concluded that even in a small scale uniform contrast exists in areas far apart from dislocations. However, right on the regions close to dislocations, contrast of DF image changes quickly in correspondence to the stress field around the dislocation core. It may even promote appearance of smaller FE domains in comparison to domain sizes in the remaining the image.

The reaction of the lattice of the h-$ErMnO_3$ to shear strain promoting the appearing of different patterns of APB/FE domains was already observed [56]. Single crystal $YMnO_3$ also shows different patterns of vortices like four state vortex patterns created in the lattice because of the presence of partial edge dislocations [59]. Such kind of domain pattern needs in atomic structure imaging to be observed and it is not visible in DF images.

The low magnification BF image in Figure 6-15.b shows that the dislocation line is a few hundred nanometers long. Figure 6-15.d is the enlargement from a small area around defects in dark field image of Figure 6-15.a. IFFT image in Figure 6-15.c of the image in Figure 6-15.d displays in a clear way the distortions of the atomic planes from the main spots of the FFT (and the only spots in the FFT). The planes of the Lu ions are clearer in right part of the IFFT image. This displacement definitely is accompanied by equal displacement in the Mn planes, which from this view are the positions of bipyramids. The IFFT and HRTEM images of the images shown in Figure 6-15.c and d give enlarged views at the 5 nm scale of the straining and inclination of the atomic planes in the distorted zone of the defect (Figure 6-15.e and f). Distortions in bipyramids can also be represent by tilting of bipyramids where the two atomic planes of Mn in this zone axis (between each pair of Lu atomic planes) are coming closer together or moving apart from each other, see model in Figure 6-8.b. Hence, it would be expected that the magnetic or dielectric properties of these materials are being affected by any distortion in the bipyramids caused by the strain around the dislocation lines.

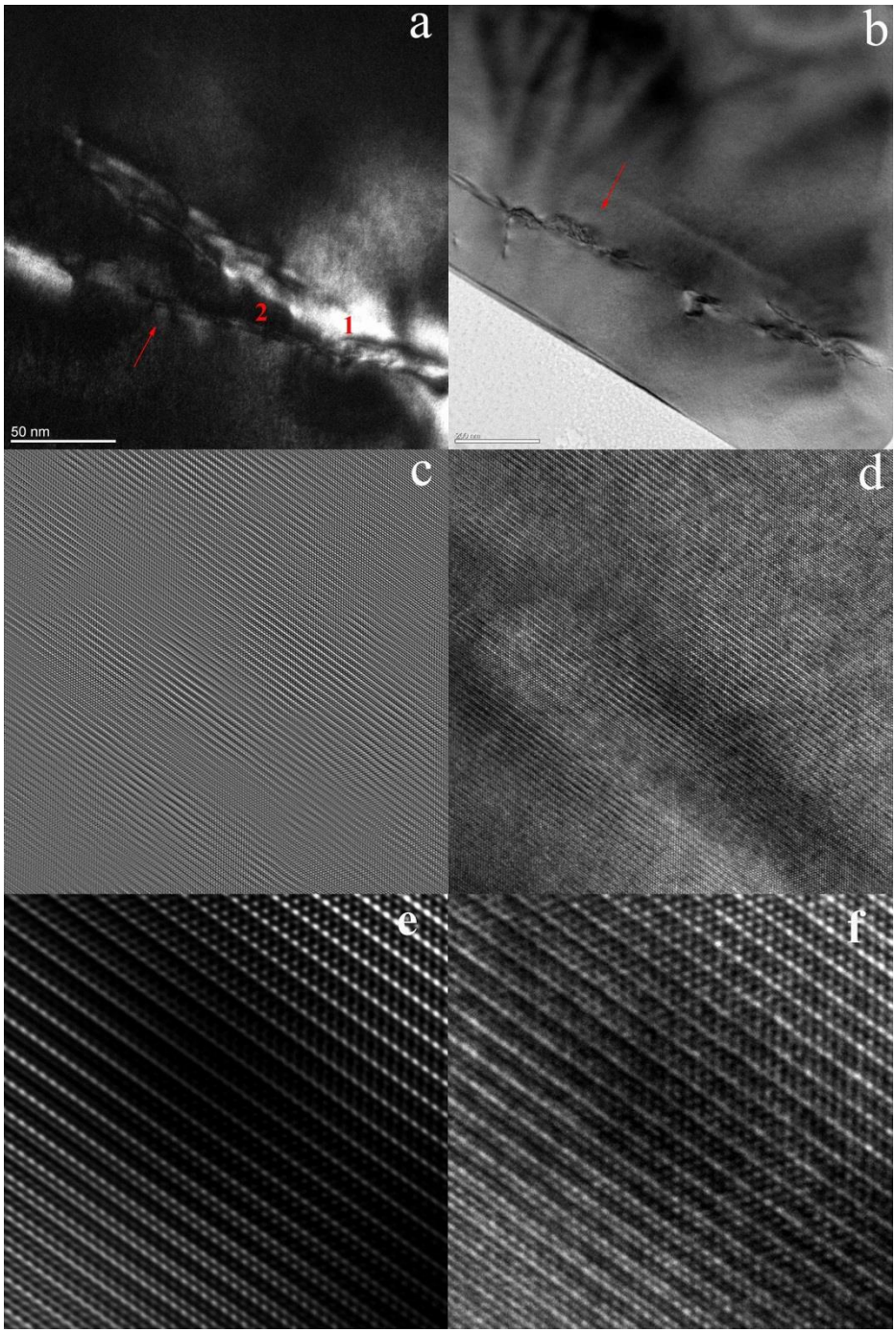

Figure 6-15. (a) Dark field image of a particle of sample x=1.04 after 5 days annealing taken along (001) zone axis and (b) dislocations in the same particle in BF image. (c) IFFT of the HRTEM image in (d) showing disordering of the lattice sapcing across the image. (d) HRTEM image of a defect in images (a) and (b). (e) IFFT and (f) lattice images of the defect presenting distortions in the bipyramids.

TEM images in Figure 6-16 are of two compositions, x=1.04 and x=0.92, after five days annealing and show the presence of line defects with different orientations. It is important to investigate the images of the (110) zone axis where ferroelectric domains coupled to topological defects can be distinguished. First image, Figure 6-16.a, displays one alignment of dislocation which were also observed in TEM images of the samples of only one day annealing. The lattice image of the dislocation in Figure 6-16.b exhibits the organized lattices at top of the image, whereas when entering the distorted region displays disordering on the atomic planes.

This feature was already observed in this family of materials, pointing towards the effect of stress/strain or chemical inhomogeneity on forming stripes instead of vortex/anti-vortex FE domains [58,59,157]. For sample x=0.92, which is in the opposite side of the solid stability limit of the $LuMn_xO_{3\pm\delta}$ solid solution, the stripe-like distortion along the linear defect is more pronounced. The lattice image of a part of the stripe is shown in in Figure 6-16.d. The lattice image of the distorted region in in Figure 6-16.d reveals the existence of different structural domains, being separated by diffuse domain walls. Such diffuse domain wall in APB/FE domains were observed in $Y_{0.67}Lu_{0.33}MnO_3$ single crystals [58]. In the present study this type of defect is not limited only to Mn-site vacancy samples, as it also appeared and more often on R-site vacant samples. In addition, doping $YMnO_3$ with Ti indicates that after a certain concentration of doping, the displacements of the Y ions in APB/FE domains can be reduced to values that switch the polar mode to non-polar mode, again highlighting the role of chemistry on atomic structure and properties of the h-$RMnO_3$ materials [160].

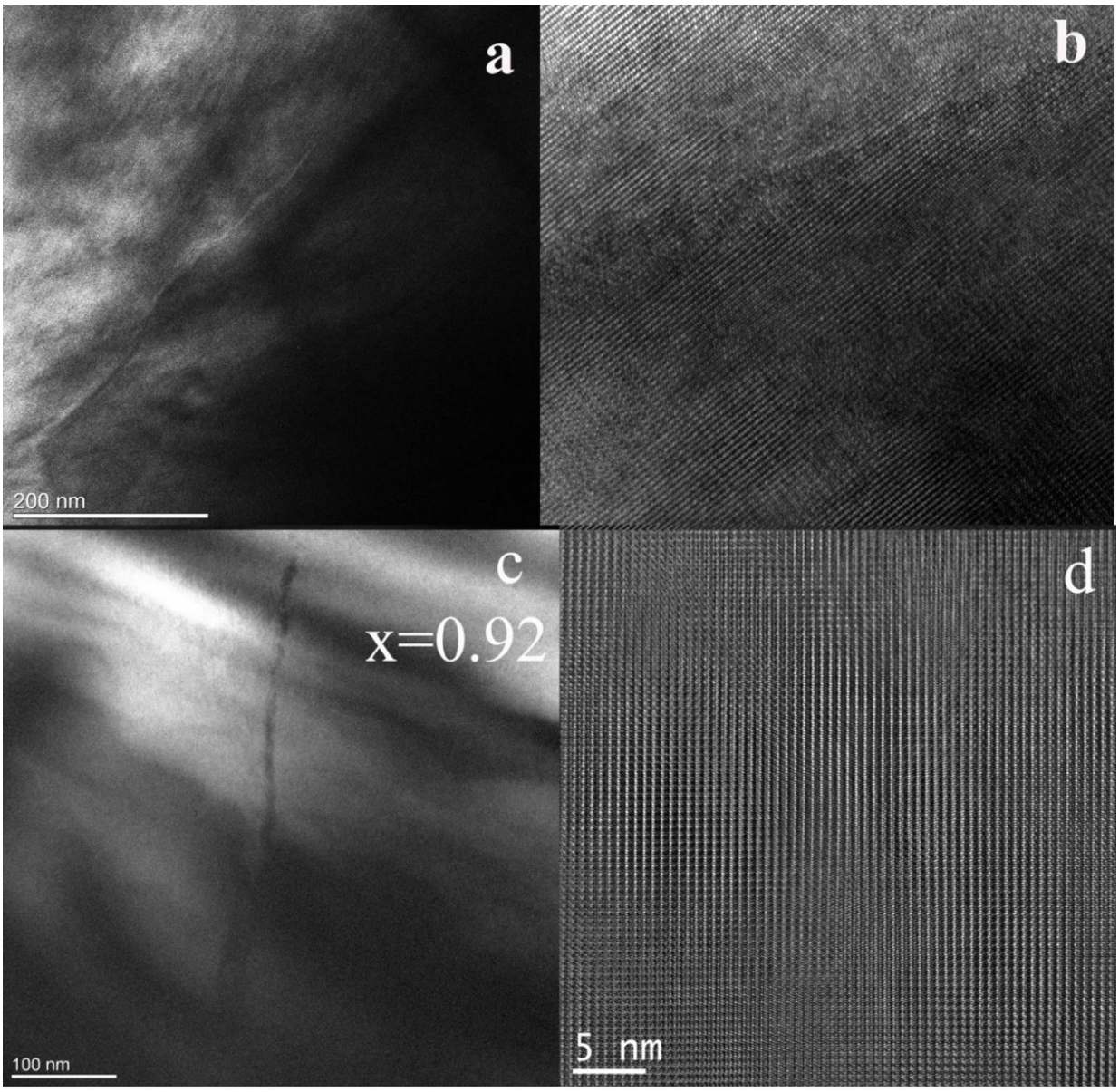

Figure 6-16. TEM images taken along (110) zone axis of sample x=1.04, 5 days annealing: (a) Low resolution image with one alignment of dislocations forming a low angle boundary. (b) Dark field image of the lattice in the region of image (a) where the aligned dislocations are observed. TEM images from sample x= 0.92, 5 days annealing: (c) DF image of a long linear defect like a dislocation. (d) In HRTEM image there are regions out of registry due to distortion. DF images were taken by slightly tilting the sample away from the (110) zone axis to enhance the contrast of the defects.

6-3-2 Ferroelectricity from STEM observations

To overcome the limitation of resolution of the available in-house electron microscope access was granted under collaborative research to the Cs-corrected STEM in Fritz Haber Institute, Berlin, to observe the displacements of Lu ions in one off-stoichiometric sample. The sample with composition x=1.04, 5 days annealing, at the upper stability limit of the $LuMn_xO_{3\pm\delta}$ solid solution was selected. The image in Figure 6-17.a was taken in STEM mode using HAADF detector with the electron beam parallel to the (110) zone axis. The observed displacements of the Lu ions correspond to electrical polarization pointing downward. The image in Figure 6-17.b is the enlarged view of part of the image in Figure 6-17.a. The downward polarization of the FE is general no just in Figure 6-17.b and c but also in the total area in Figure 6-17.a. with no indication of APB/FE domain walls or switching of the polarization. It is concluded from this observation that the FE domains must be above 20 nm in size.

Figure 6-17.c taken from another part of the same particle close to the area in previous image exhibiting again the same downward polarization of the Lu ions of Figure 6-17.c. The corresponding IFFT image in Figure 6-17.d reconstructed from FFT spots of the whole image, after noise subtraction, gives a better resolved view of the displacement of Lu ions. It can further be deduced that the fundamental mechanism of FE polarization of the h-$LuMnO_3$ phase remains active in samples with Mn-excess up to the solid stability limit and was not diminished by the change in chemical composition.

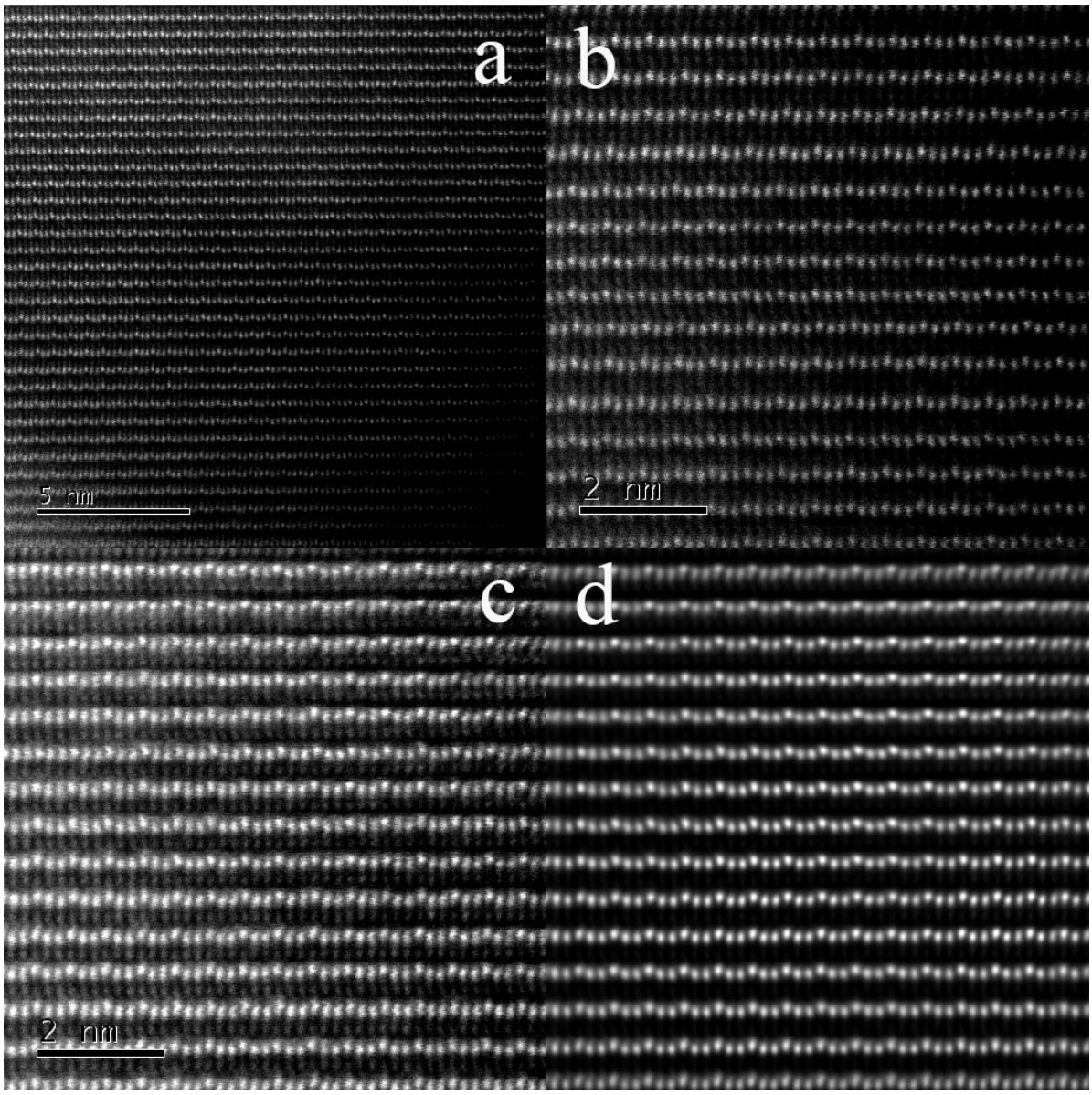

Figure 6-17. HAADF-STEM image of sample $LuMn_{1.04}O_{3\pm\delta}$ of 5 days annealing time, [110] zone axis. (a) Large area with single direction of FE polarization as determined from displacement of Lu ions. (b) Enlarged image taken from lower left corner of a). (c) Enlarged image of a second area of the same particle close to a. (d) IFFT of the image of (c).

6-3-3 Lattice distortion, oxidation state of Mn after long time annealing

The TEM observation of some particles in this study showed high density of dislocations which causes strain with local disordering in the atomic arrangement of the Mn ions in basal plane. In the investigation of the magnetic behaviour of these samples, spin-glass like dynamics was observed as a function of Mn/Lu ratio, extended from T_N to 5 K the lowest measured temperature, section 5-3-1. Field dependent magnetization, complementary to the measured temperature dependent magnetization also indicates irreversibility below T_N, with maximum of magnetic remanence and coercive field around 30 K, section 5-3-4. The same holds for the dielectric response of the samples measured for x≥1, below T_N, with a maximum around 30 K showing polaron like thermal behaviour, to be discussed in last Chapter 7. The enigmatic weak magnetization in the AFM matrixes of h-$RMnO_3$ oxides, as recently calculated, was assigned to the magnetic interaction occurring in the domain walls of APB/FE domains [9,10,16,43,48,79,99]. It is argued that symmetry breaking on APB/FE domain walls allows net magnetization along c-axis, also known as asymmetric Dzyaloshinskii – Moriya interaction, commonly found in geometrically frustrated magnetic systems [196,197]. In addition, atomic scale images and theoretical calculations of topological defects (APB/FE domain walls) progresses in explaining the findings in properties like net magnetization besides of AFM of basal plane interaction in h/o-$RMnO_3$ stoichiometric or off-stoichiometric materials [63,66,76,98,198]. The relevant point here of these studies to the current study is the mutual relation of the structural distortions on internal interfaces of particles or inside single crystals and ferroelectric and magnetic properties.

Following the methodology of the Mn $L_{3,2}$-edge “white-line” ratio to determine Mn oxidation state from EELS spectra applied in sections 6.2.2 and 6.2.3 above, given samples form 5 days annealing times were selected for characterization by EELS. The corresponding results of calculation of the L_3/L_2 ratio using atan fitting for both peaks of L_3 and L_2 [195] are given in Figure 6-12.b above. In comparison to the first set of samples

with one day annealing time, longer annealing time gives rise to less diversity on the extracted values of the Mn oxidation state inside the crystalline grains of the main phase.

As in the first set of samples, no clear deviation of Mn oxidation state from 3+ was found for the five day annealed samples. It is important to analyse some points about the method being followed. The white line ratio shows slight deviation from right value of 3+ which may be due to inaccuracy in fitting of the profiles of the $L_{2,3}$ lines in the present calculations [179]. Two other factors must also be considered. In the present study EELS analysis was done in TEM mode using high magnification, usually in an area of 5 nm side, which does not allow site-sensitive analysis. Atom site sensitive EELS can only be done in STEM. Assuming 4% Mn-vacancies in sample composition is equivalent to one Mn^{3+} ion out of 24 Mn^{3+} ions be missing in a supercell of 2x2x1. This supercell is the analogous of a unit cell with 1.2 nm a-constant in basal plane. Therefore, if Mn or Lu vacancies have been uniformly distributed as point defects at such levels of concentration or below, sensitivity of the EELS technique to vacancies would be too low and will not be enough to detect it. Second, the crystal field environment of Mn will affect L_3 and L_2 edges and may bring some change to white line ratio [174,175,182]. Our TEM images have revealed the presence of dislocations on the walls of the structural domains where we do not expect ideal unit cell and atomic arrangements of the ions in $LuMnO_3$ structure. As was shown in case of $TbMnO_3$ [99], the matter also needs better resolution in EELS spectroscopy than that the one can be provided, 0.9±0.1 eV resolution, of the Ω-filter of the TEM microscope.

Dark field images of this study in relevant zone axes to display the ferroelectric domains showed that there are vortex/anti-vortex states at the nano-scale which may result in net magnetization on the domain walls of internal interfaces or in the core of dislocations observed in the particles. The density of structural nanodomains and APB/FE domain wall patterns in polycrystalline materials is of difficult assessment in semi-quantitative way by electron microscopy methods. It may be supposedly assumed as the parameter which controls the magnetization strength either via variation by expansion/retraction

of the unit cells on the defective regions or through modification in arrangements of spins if symmetry changed there. The values of $L_{3,2}$ Mn-edge "white line" ratio did not provide evidence of the presence of Mn^{2+} or Mn^{4+} ions in the lattice of $LuMn_xO_{3\pm\delta}$ solid solution which would modify the nature of magnetic interactions between Mn ions in the structure of crystalline grains. Also, low fraction of Mn_3O_4 secondary phase detected in samples inside the range of solid solubility in this study can explain the weak magnetization measured below its Curie temperature of $T_C \approx 43$ K but cannot produce the remnant magnetization observed well above 43 K in M-H measurements, as it is observed until 80 K. This general assumption is not free of questioning in view of results that showed residual magnetization and exchange bias fields above T_C of the FiM phase in AFM/FiM binary pairs in the form of core-shell nanoparticles and mechanical mixture of powders where Mn_3O_4 is the FiM phase [90,199]. The crystal field environment of Mn^{3+} however would show dependency on the value of x in off-stoichiometric samples, given by DOS calculations and the pre-edge profile in O K-edge of EELS spectra, generated by defects in the crystalline lattice from different processes of vacancy doping.

However, not all nanodomains in the samples under study are necessarily APB/FE coupled domains, particularly when dealing with off-stoichiometric structures, A-site or B-site vacancy doped [18,23,89]. That can be the case of the image of sample x=0.92 in Figure 6-18. The particle shows net contrast fluctuation across the image. The similar picture was taken for $La_{0.66}MnO_3$ particles [110]. In either $LuMn_{0.92}O_3$ or $La_{0.66}O_3$ cases, defects like anti-phase boundaries and secondary phases of Lu_2O_3 in former case and of Mn_3O_4 in later exist inside the particles. Thin films of the $DyMn_{0.94}O_3$ and $ErMn_{0.96}O_3$ also show inclusions of Y_2O_3 and Er_2O_3 respectively; whereas Mn_3O_4 secondary phase was observed only for $DyMn_{1.56}O_3$. Thin films with composition in the remaining range of Mn-rich compositions did not show up Mn_3O_4 secondary phase [18]. Not only in off-stoichiometric films, but also in stoichiometric thin films of $YMnO_3$ the presence of Y_2O_3 nano-precipitates was noticed [163,165], which can serve the argument that effective Mn/Y ratio would be lower than unity in the starting composition of the amorphous layers.

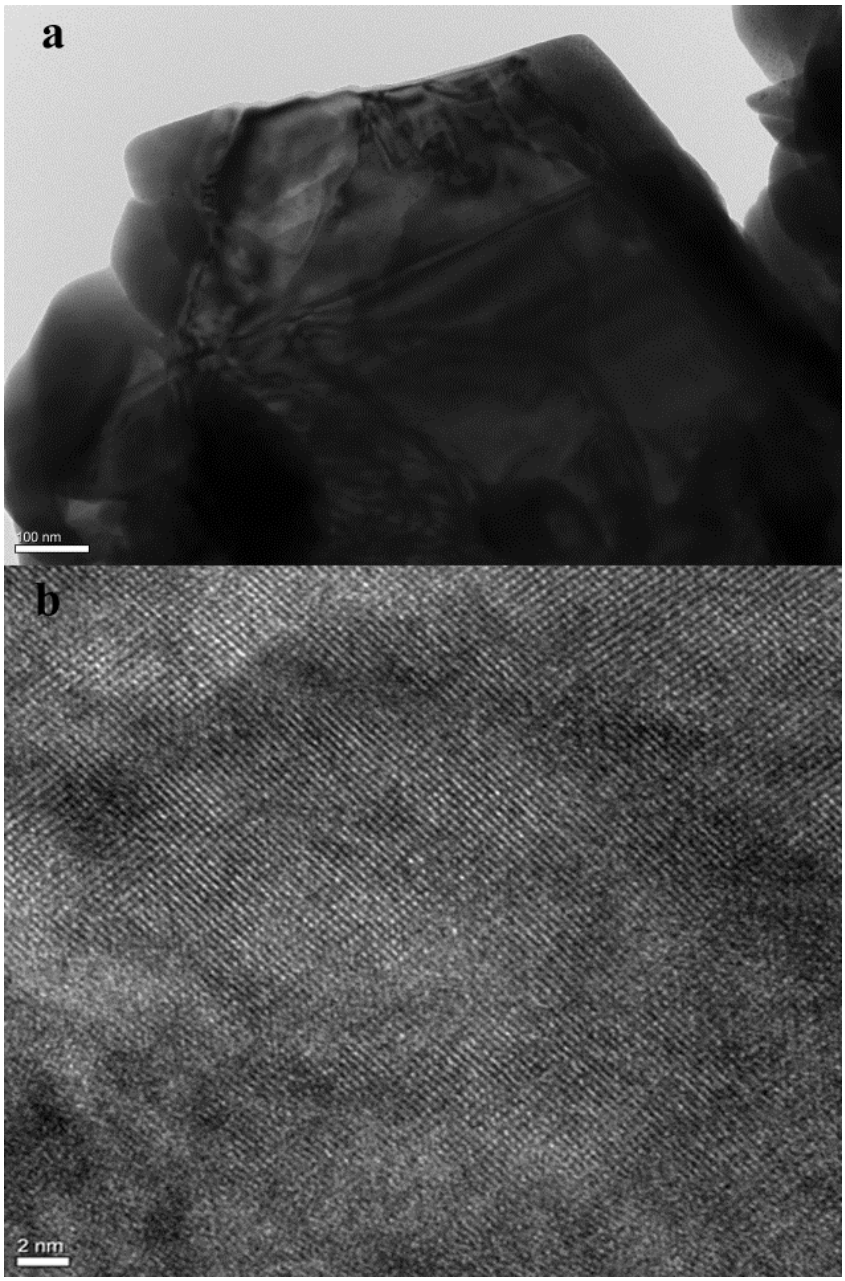

Figure 6-18. (a) Dark field image of a region of sample $LuMn_{0.92}O_{3\pm\delta}$, one day annealing, with contrast fluctuation across the particle, defects like APB and nano-clusters of defects are thought to be responsible for the contrast change. (b) High magnification of the same area with fine inclusions inside the crystalline lattice of the $LuMn_{0.92}O_{3\pm\delta}$ particle.

Microscopy studies in the current work indicate the existence of the nano-structures and dislocations, planar defects like APB or twinning planes with slight changes from R-site vacant to Mn-site vacant samples. Generally Lu-vacant samples show smaller structural domains and more interfaces. For x=0.92 composition wider nanodomains are observed, but the distortion on the domain walls cover more unit cells, mostly partial edge dislocations which are extended. It is known that microstructure and defects modify the regular magnetic behaviour of the materials like the exchange bias, section 5-4 [65,200]. The objective of identifying the magnetic signature of each type of defect and the role they may have on magnetoelectric coupling and dielectric polarization has large complexity and remains mostly inaccessible [201]. The objective is even further away when dealing with complex nanostructure bulk polycrystalline h-$RMnO_3$ materials and the several types of extended defects revealed by detailed studies with HRTEM and the best HAADF-STEM instruments. To this point, the microscopic study helped to assess the role of hausmannite as an impurity and in identifying its signature in the magnetization of the $LuMn_xO_{3\pm\delta}$ solid solution. Other features of this solid solution present magnet signatures that were tentatively decoded here as well in other studies before this one. Finding the causal links between those magnetic signatures and the features of microstructure being analysed with atomic detail is outside the present state of knowledge and can only be attempted as exploratory exercises.

In the HAADF-STEM image in [110] zone axis in Figure 6-19.a from sample $LuMn_{0.96}O_{3\pm\delta}$ annealed for 5 days (taken using the FEI Titan C_s/probe corrected microscope with 200 kV, by courtesy of the International Iberian Nanotechnology Laboratory- INL, Braga, Portugal) the displacements of Lu ions are well resolved and show upward polarization. The EDS map of Mn from the same part of image is shown Figure 6-19.b. The Mn ions fill in the crystalline rows of weaker contrast between the rows of Lu ions, in accordance in the crystalline structure of $LuMnO_3$ phase. All parts of the particle where polarization was analysed exhibit the same upwards FE polarization. Looking through different parts of the same image, Figure 6-19.c, evidence was found of a boundary separating the regular hexagonal phase with $P6_3cm$ symmetry (on the left) from a modification or

distortion of this phase (on the right) with an inclination of the c-axis of approximate 2° in relation to its regular direction orthogonal to the a-b plane. The yellow lines in Figure 6-19.c indicate one FE period of the Lu-displacement and are perpendicular to the a-b planes. The white line on the right gives the direction of the origin of the same FE phase period as one goes to the right. It meets one of the yellow lines in the middle of the image at a point where a boundary plane parallel to the a-b planes separates the regular hexagonal $LuMnO_3$ lattice (left) from the distorted hexagonal-like crystalline lattice (right) with $\alpha \cong 90°$, $\beta = 87.7°$, and $\gamma = 120°$.

The end of the lines on the right indicates the position of the vertical plane where the crystalline lattice returns to the regular hexagonal alignment, the distorted hexagonal phase presenting a width of $4c_0$. The total displacement of the regular lattice on the right in relation to the regular lattice on the left is given by the partial ribbon dislocation of Burger vector, $\overrightarrow{b_p} \cong 1/6\,[1\bar{1}0]$, the total width of the partial ribbon dislocation being $4c_0$ [202]. The low angle of the inclination of c-axis in the distorted area of Figure 6-19.c has analogy with the low angle tilt in the atomic planes described above in Figure 6-10.a.

By continuing the examination of the same sample a defective area including stacking faults was found which deserved additional attention. The analysis of images taken from defective region reveals that FE polarization direction given by the displacement of Lu ions switches from upward to downward at several places. In region 1 in Figure 6-20.a middle right of this figure, there are a-b planes of Lu ions with two opposite directions of polarization, the planes being facing each other (marked by arrows). The distance between these Lu planes of different polarization does not give room for any Mn plane between them. Also the image in that specific region does not produce the same contrast of Mn planes as in non-defective regions. The modification of the atom arrangements in this region is associated to the stacking fault which roughly removed one Mn-O layer. The loss of Mn plane with the connected planar oxygen ions may be the driving force for the new atomic structure which is tentatively explained in detail below. The loss of the Mn plane corresponds to elimination of Mn-vacancies in excess dissolved in the lattice,

and some of the Lu in excess is fixed in the new atomic structure. The topology breaking role of oxygen vacancies on introducing new patterns of APB/FE domains besides of the 6-fold vortices was recently demonstrated in h-$RMnO_3$ single crystals and resulted in the presence of 4 vortex/anti-vortex patterns, or of core fragmentation and stripe patterning [60,162,203,204].

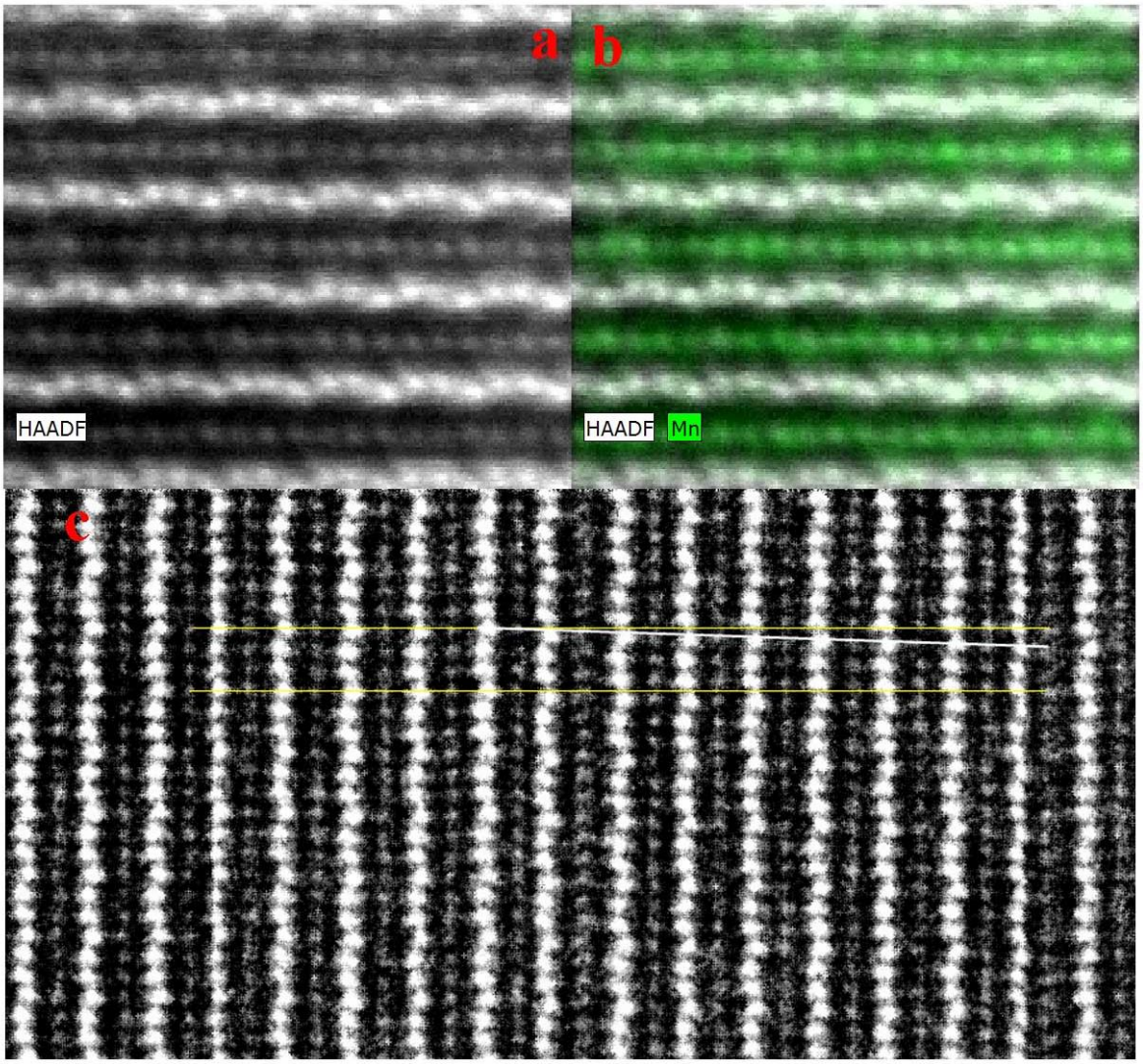

Figure 6-19. (a) HAADF-STEM image of lattice of $LuMn_{0.96}O_{3\pm\delta}$ taken along (110) zone axis. (b) EDS mapping of the Mn ions overlaid on the image. (c) One (001) boundary plane separates the regular hexagonal $LuMnO_3$ lattice (left) from distorted hexagonal crystalline lattice (right) with $\alpha\cong90°$, $\beta=87.7°$ and $\gamma=120°$ (partial ribbon dislocation, [202]).

In region 2 of Figure 6-20.b there is another FE domain with downward polarization with the size of few unit cells. The auxiliary scale in this image gives a way to determine the phase shift of the two FE domains [58]. Switching of polarization occurs on number 46 on the scale from up (right) to down (left) and corresponds to a type I APB/FE domain wall [161]. Scale on the image indicates α+ FE domain in left and γ- FE domain on right of the domain wall. Switching of polarization is also observed on the edge of the sample (not shown here, located on left side of region in Figure 6-20.c). Therefore from left to right of the defective region the phase shift of FE domains are: β- → α+ →γ-.

The defect was also analysed by EDS line mapping in order to get any evidence on shifts in the concentration of Mn, Lu or O ions, as shown in Figure 6-20.d and e. The line EDS taken along line marked in Figure 6-20.c gives fast change of the net Mn/Lu ratio of the elements in the defective region. Although the EDS analysis here may not transfer the accurate change of the Mn and Lu concentrations along each atomic plane, using probe corrected electron beam we can look at the change of the Mn and Lu in a wider range. As shown in Figure 6-20.d and e, after smoothing the EDS data using Adjacent-averaging method (15 points per window) in Origin Pro 9 the irregular change appears on the defective region (marked as hatched area), the average drop comes for Mn rather than Lu more visibly.

Figure 6-20.f presents the enlarged view of window marked with yellow line on left of Figure 6-20.a. The observed structure of modified sequence of atomic planes in Figure 6-20.a and b represents a stacking fault with displacement of atomic planes parallel to c-axis corresponding to the partial dislocation with Burger vector, $\overrightarrow{b_p} = 1/6\,[001]$. The atomic structure of this planar defect is different from the main phase but retains elements of the $LuMnO_3$ crystalline lattice. The new stacking of planes is formed along c-axis by a triple-layer of pairs of Lu planes with mutual cancelation of their FE polarization. The yellow dashed vertical lines in this figure are eye guides indicating preservation of FE phase at the bottom (negative) and $\pi/3$ phase shift with reversal of FE polarization at the top (positive). The limits of triple layer of the planar

defect are marked by the dashed red line. The triple layer creates a new 2D phase just 1.91 nm tick inside the crystal of the h-$LuMnO_3$ phase [99]. The simulated crystalline structure of this new 2D phase overlaid on the HAADF-STEM image in Figure 6-20.f results from two operations, the reflection on the (001) of the mother structure of $LuMnO_3$ with $P6_3cm$ symmetry is followed by translation of the reflected structure parallel to c-axis with translation vector given by the partial dislocation $\overrightarrow{b_p} = 1/6\,[001]$ of the stacking fault. The new crystalline structure is the reunion of the parent structure with the reflected-and-translated structure. It would retain the hexagonal $P6_3cm$ symmetry group of the $LuMnO_3$ parent phase. But, the real structure of the 2D layered phase as seen from the [110] zone axis much have a much more complex crystalline cell than suggested by this only view. Inspection of distances between atomic positions from other views of the modelled cell indicates that contact and overlapping of ions in the structure of the new cell is unavoidable when they are represented with full values of their ionic radii. At first sight that would be solved if the two blocks of the crystalline cell with relative orientation as described build a regular stacking of alternate layers forming a superlattice with the given width or if that part of the image as seen results from overlapping of two blocks of the original $P6_3cm$ structure, with relative orientation and displacement as described above.

A partial dislocation with Burger vector parallel to c-axis of the same modulus as $\overrightarrow{b_p} = 1/6\,[001]$ and total width $\approx 2|[1\bar{1}0]|$ was reported as the displacement at the antiphase boundary in h-$DyMnO_3$ thin films deposited by MOCVD on $ZrO_2(Y_2O_3)$ created at the film/substrate by a monolayer atomic step of the substrate surface [116]. The antiphase boundary becomes the sub-grain boundary separating two crystalline domains. Away from the film/substrate interface the antiphase boundary is extinguished by the creation of the stacking fault relaxing the strain in the lattice.

The idealized model there presented to describe the stacking sequence at the anti-phase boundary and in the same way at the corresponding stacking fault shows that the plane of apical oxygen moves to the position of the next basal plane, the displacement along c-

axis being given by $\overrightarrow{b_p}$ above. This idealized model inspired the interpretation of the new 2-D phase in Figure 6-20.f and of the associated partial dislocation and served it with accuracy. The planar defect in in Figure 6-20.f is associated to the change of polarity and $\pi/3$ phase of the FE domains contacting with it. Hence it plays the role of a single APB/FE wall although it extends over 6 Lu-layers and not just the one Lu-Lu distance or the two Lu-Lu-Lu distance of type A and type B of the APB/FE walls, respectively, described for the 6-fold topology of FE domains of the h-$RMnO_3$ lattices.

Although the present study does not have the tools to disclose the chemical shifts in vacancies of oxygen in defective regions, there are several causes which affect the FE domain walls like the already mentioned oxygen vacancies, shifts in chemical composition like in $Y_{0.67}Lu_{0.33}MnO_3$ [58] single crystals and $InMn_xGa_{1-x}O_3$ poly-crystals [57] which showed different pictures of APB/FE domain walls, or even stress/strain in the lattice which converts vortex/anti-vortex patterns to stripes [56]. The present study reveals that the interaction of topological defects not just with vacancies but also with extended defects forming atom clusters, nano-inclusions, stacking faults and extended partial dislocations may result in new features of vortex/anti-vortex patterns which still have not been explored.

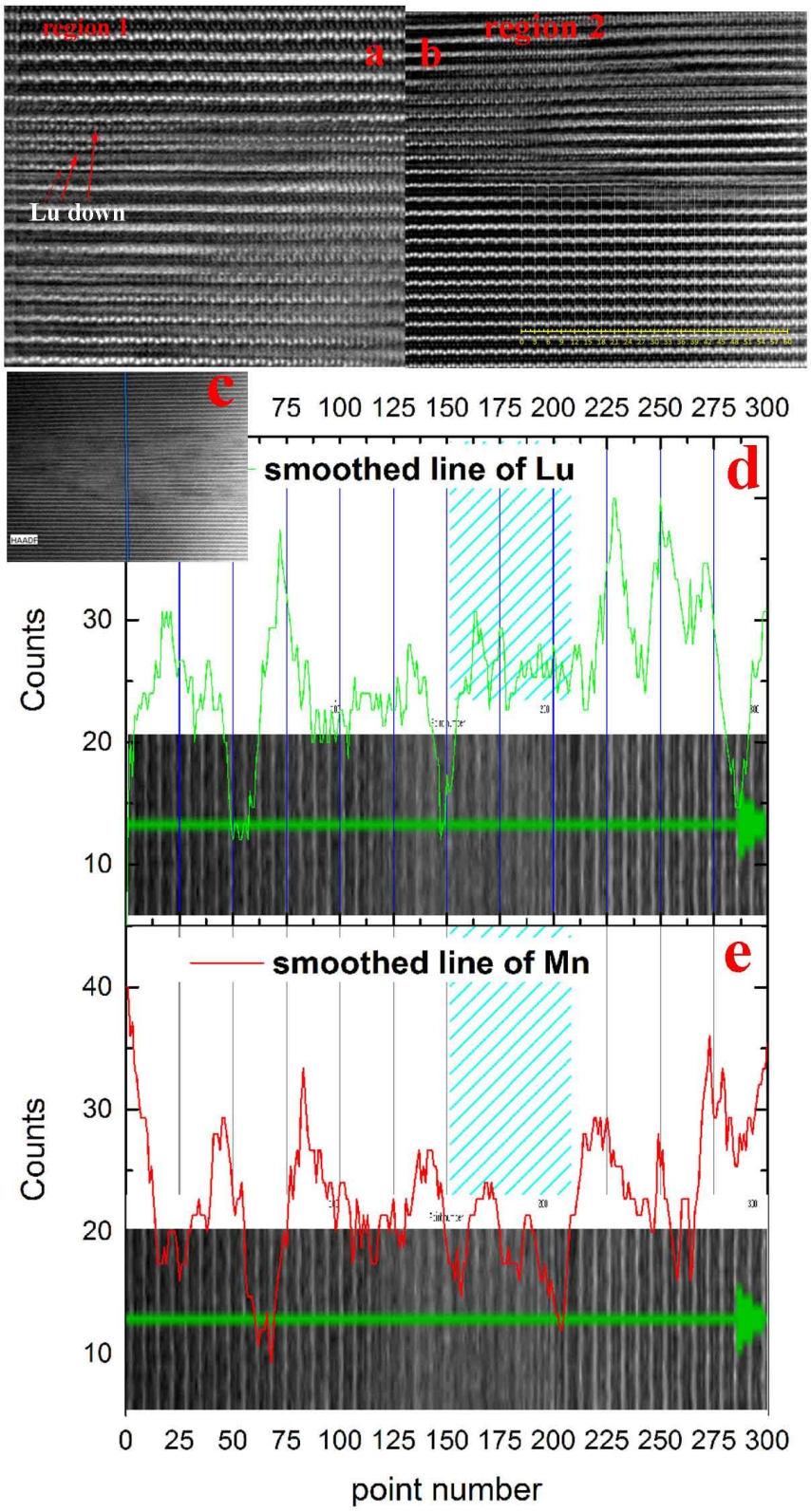
region 1
a
b
region 2
Lu down
c
HAADF
75 100 125 150 175 200 225 250 275 300
smoothed line of Lu
d
Counts
30
20
10
smoothed line of Mn
e
40
30
20
10
Counts
0 25 50 75 100 125 150 175 200 225 250 275 300
point number

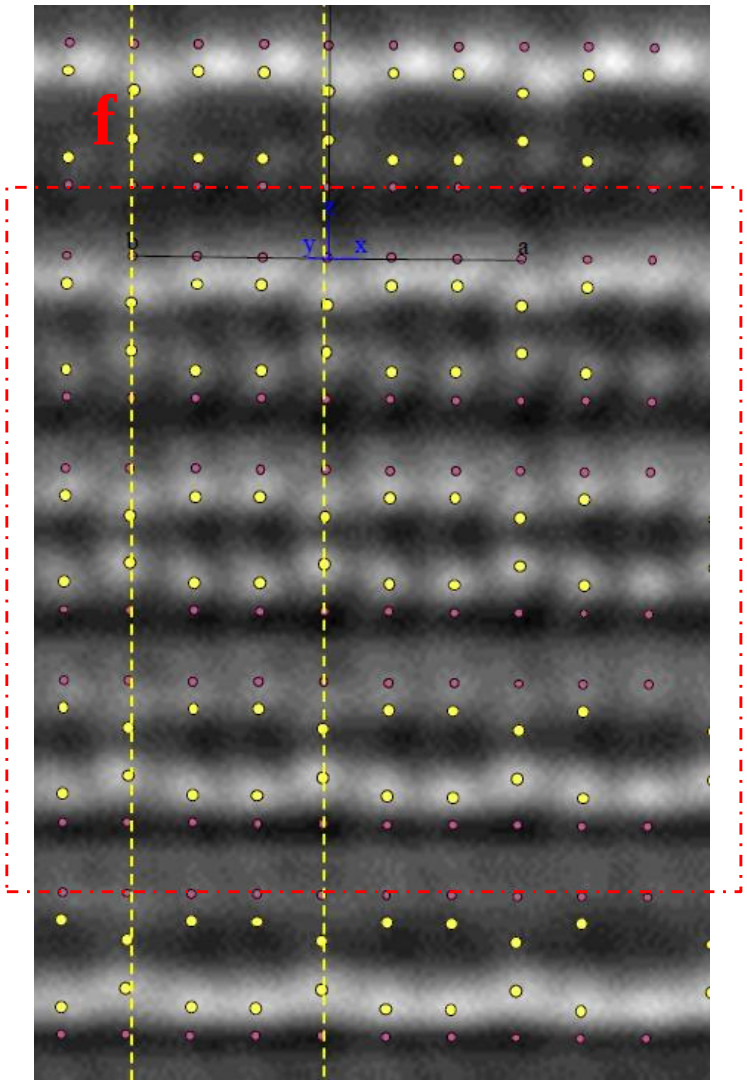

Figure 6-20. (a) and (b) show two different regions of a defective lattice of sample x=0.96 containing stacking faults in image (c). In (a) at the right, up part of defect in (c) there are 3 visible planes of Lu ions with downward polarization (shown by arrow). In (b) at the left, down part of defect in (c) there are two opposite polarizations indicating two ferroelectric domains. The scale in image (b) is used to identify the phase shift of two FE domains. (c) Line drawn across defective region to take EDS, (d) Lu line EDS profile (green) and e) line profiles of Mn (red) across the line in (c) after their data being smoothed. (f) Enlarged view of the window marked on left of (a) with a stacking fault $\overrightarrow{b_p} = 1/6\,[001]$ formed by the triple-layer structure of pairs of Lu planes with mutual cancelation of FE polarization, dashed vertical lines in yellow are eye guides indicating preservation of FE phase at the bottom (negative) and phase shift of $\pi/3$ with reversal of FE polarization at the top (positive), Lu^{3+} ion (yellow), Mn^{3+} ion (purple), O^{2-} ion hidden; the new 2D-phase is delimited by the box of the dashed-red line

7. Dielectric constant, magneto-electric coupling and ferroelectricity

The promising magneto-electric coupling of the multiferroic h-$RMnO_3$ oxides were first noticed to hide interesting physics and chemistry behind of coupling of the spin ordering and dipole polarization when the sample goes to the AFM region [35]. During years it was matter of extensive studies to understand the underlying physics of this kind of coupling which happens exactly at Neel ordering transition. Further research immediately explored that the coupling also extended to ferroelectric domains existing below paraelectric-to-ferroelectric PE/FE transition at high temperatures [9,48]. As it was discussed in Chapter 2, the existence of both ferroelectric and AFM domains were experimentally and theoretically proven. Since then there has been large research around this kind of coupling and ways to tune or modify it. In this chapter, one looks for both dipole polarization coupled to magnetic behaviour by measuring the dielectric constant at low temperature. In addition, Piezo Force Microscopy (PFM) was proven as a powerful tool of research on the area of ferroelectric domains by disclosing the variation of the ferroelectric domains from one composition to another one and the effect of sample preparation methods. Due to lack of access to temperature dependant PFM facilities, the present study is restricted to room temperature measurements.

7-1 Study of dielectric behaviour of off-stoichiometric ceramics

The dielectric constant ε which represents the electric dipole moment for a given intensity of the applied electric field, usually determined in a wide range of frequencies, is an important tool of research to study the magneto-electric coupling phenomena in

multiferroic oxides [27]. Measurements of the dielectric constant have been done from very low temperatures up to PE transition temperature of h-$RMnO_3$ oxides, each realm of temperature had helped on understanding of some properties of these materials. In this PhD work the focus has been on low temperature part of the behaviour of off-stoichiometric $LuMn_xO_{3\pm\delta}$, due either to ease of access to available equipment or strong emphasis of the work on magnetic behaviour around Neel ordering transition and below T_N.

7-1-1 Dielectric constant of Mn-rich samples

Magnetic studies of off-stoichiometric samples in Chapter 5, section 5-3 after one day annealing have shown that there is enhancement of the magnetic susceptibility signals by increasing Mn content above the x=1 stoichiometric composition. Although the impurity phase hausmannite presents a transition at 43 K, comparing the results of short time and long-time annealing in temperature dependent measurements of coercivity and remnant magnetization showed a transition at 30 K likely due to spin reorientation also observed for some other h-$RMnO_3$ materials [27].These experimental observations and searching for magneto-electric coupling mostly on x≥1 side, are the driving force for performing the dielectric measurements reported in this section. It should be mentioned that since hausmannite does not show dielectric transitions like those of $LuMnO_3$, this experiment can also clarify some of ambiguities of the magnetic measurement results if they originate from hausmannite secondary phase or the $LuMnO_3$ matrix.

The dependence of the complex dielectric constant ε^* on temperature from 10 K to room temperature is assessed here both to clarify if the magnetic transitions already described also resulted in changes of dielectric polarization [2,30] and in searching for changes of spin-phonon coupling and domain wall switching in off-stoichiometry $LuMn_xO_{3\pm\delta}$ samples [67,205,206]. Figure 7-1.a shows the temperature dependence of the dielectric

constant, ε′(T), of samples with x = 1.00, 1.04 and 1.08 measured at 1 MHz. The T derivative of ε′(T) of sample with x = 1.04 in the range 100 kHz to 1 MHz, is given in Figure 7-1.b. The main drop of ε′(T) of three $LuMn_xO_{3\pm\delta}$ samples at T_N coupled to the AFM ordering of the magnetic moments is clearly apparent in Figure 7-1. The derivative of the dielectric constant indicates that the transition at T_N is athermal, not dependent on the frequency. Although called T_N in this context, transition in dielectric constant is commonly denoted as T^*_N, which may have slight change from T_N value extracted from magnetic measurements [77].

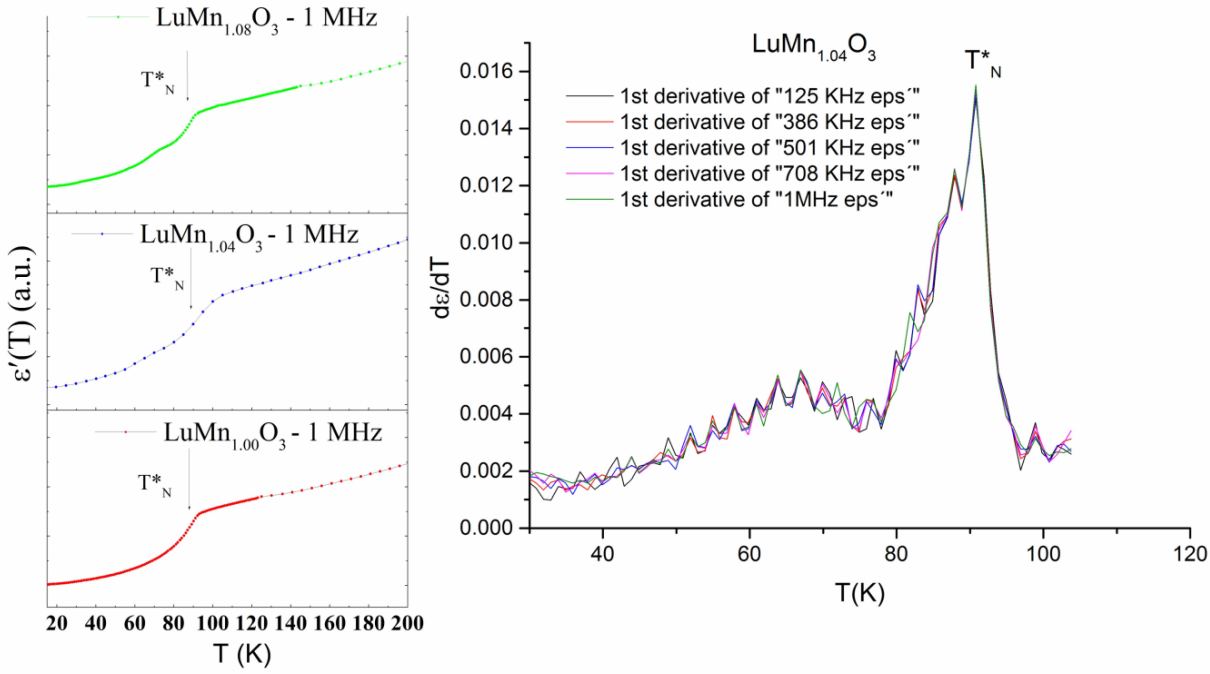

Figure 7-1. Temperature dependence of dielectric constant, ε′(T), of selected $LuMn_xO_{3\pm\delta}$ samples with x = 1.00, 1.04 and 1.08 at 1 MHz evidencing the drop of the dielectric constant ε′ at T^*_N. The right side of image is the first derivative of the dielectric constant (ε′(T)) at some frequencies, showing independency of the transition to the frequency.

Figure 7-2.a and b compare the transition points with temperature of two different physical properties, inverse of the magnetic susceptibility measured by SQUID under 100 Oe external field and the dielectric constant as given in Figure 7-1 for sample x=1.08. Although, the value of Neel ordering transition from measurements of the magnetic susceptibility and dielectric constant is not always equal [117], within the experiment error of techniques they match within 1 K or 2 K difference. Besides the clear Neel ordering transition around 90 K, a second transition below 90 K is obvious in Figure 7-2, which may be caused by spin reorientation also proved to induce change in dielectric polarization [205]. These two observed transitions of two different physical properties points to the magneto-electric effect not only at Neel ordering transition, but also below this temperature in $LuMnO_3$.

The same behaviour of sample x=1.04 can be also observed for sample x=1.08. Besides the transition of ε´(T) with maximum of the derivative at $T1_{max}$ = 89 K ≈ T_N, Figure 7-3.a, the derivative of ε´(T) of sample $LuMn_{1.08}O_{3\pm\delta}$ also indicates two other transitions: the one starting at 80 K which is broad and has the maximum of the derivative ε´(T) at $T2_{max}$ = 69 K and another at lower temperature with the maximum of the derivative ε´(T) at $T3_{max}$ = 31 K. Analogous anomaly of the dielectric constant coupled to a transition of the magnetic susceptibility was early observed in $YMnO_3$ polycrystalline samples also prepared by the solid state route of this study at a relative temperature similar to the $T2_{max}/T_N$ ratio above [35,47]. The transition of ε´(T) at $T1_{max} \approx T_N$ closely coincides with the observed transitions in the magnetic susceptibility of the same sample. The two other transition temperatures $T2_{max}$ = 69 K and $T3_{max}$ = 31 K are seen on the second derivative of the magnetic susceptibility (not shown) of the same sample in Chapter 5, section 5-3, respectively.

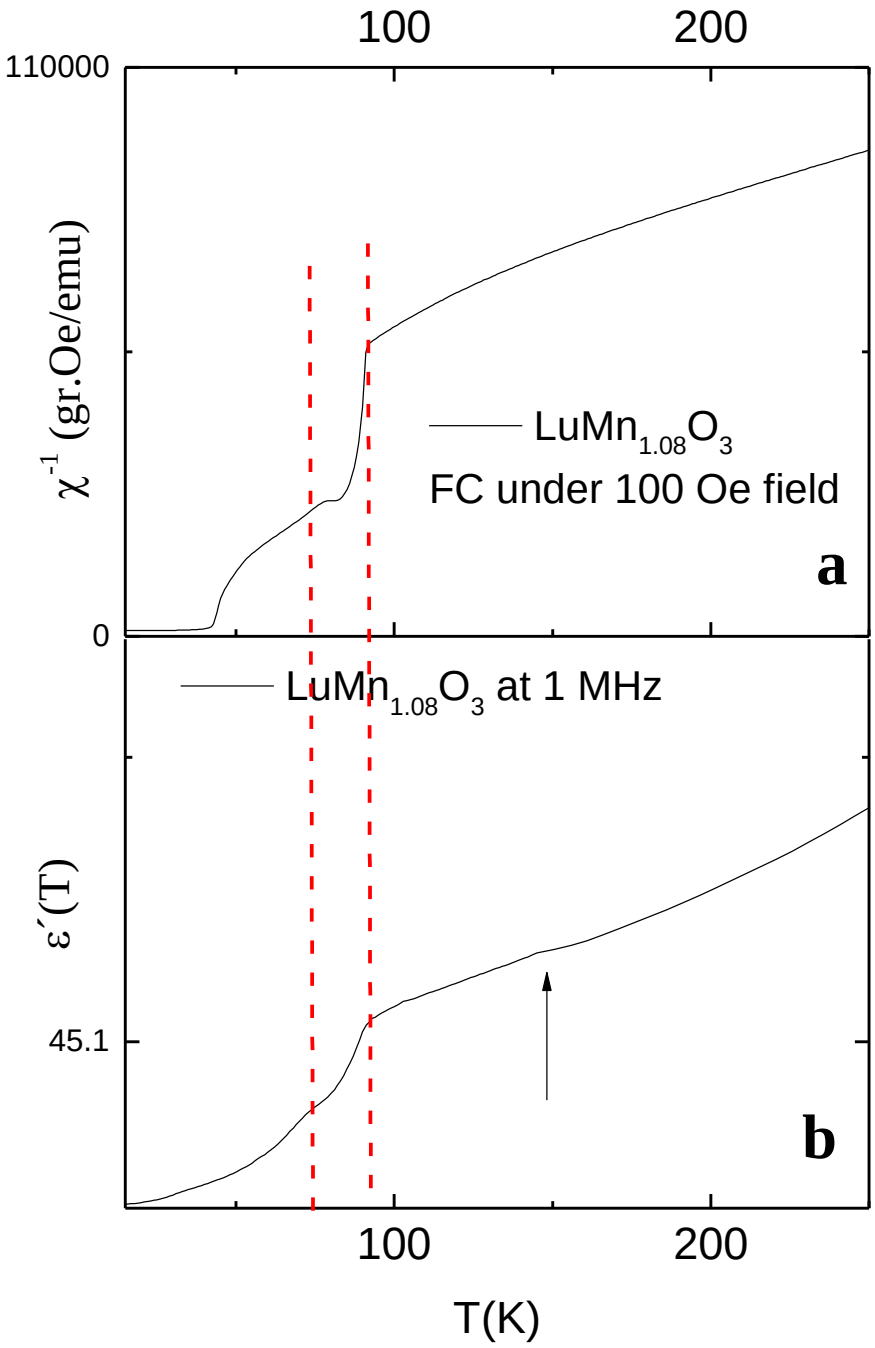

Figure 7-2.Inverse of magnetic susceptibility for sample with Mn excess (x=1.08) (a) and dielectric constant at high frequency (b) both indicate transitions around 90 K and 70-80 K, also a knee in dielectric and rarely in magnetic measurements above Neel transition temperature but at different temperatures.

The temperature dependence of the imaginary part of permittivity, ε´´(T), of sample $LuMn_{1.08}O_{3\pm\delta}$ determined in 11.2 kHz to 1 MHz frequency range is shown in Figure 7-3.b. The derivative of ε´(T) of sample $LuMn_{1.08}O_{3\pm\delta}$ in the transitions at $T1_{max} \approx T_N$ and $T2_{max}$ for the different frequencies of the given range in Figure 7-3.a exhibit inverse S-shape anomaly, not just when the sample entered AFM magnetic ordering region but also below T_N like sample x=1.04 or x=1.00, which is seen as indication of coupling of the magnetic order and dielectric constant [47]. At all frequencies of the dielectric measurements the derivative of ε′(T) does not show any frequency dependency for the main peaks of two transitions at T_N and 69 K; hence these transitions are linked to athermal mechanisms of polarization. However the transition observed in ε´(T) at temperature T3max is neatly dependent on frequency, Figure 7-3.a.

The imaginary part of permittivity ε´´ of all measured samples shows a near Debye relation with a maximum of ε´´. The dependency of $T3_{max}$ on frequency, shown in Figure 7-3.b for sample $LuMn_{1.08}O_{3\pm\delta}$, signals the thermally activated nature of the dielectric relaxation mechanism of this low temperature anomaly of the dielectric behaviour. The shift of temperature of the peak with frequency in Figure 7-3.b can be traced from 18 K to 31 K corresponding to the frequencies of 50 kHz and 1 MHz, respectively. At frequencies below 50 kHz this peak becomes too faint to be distinguished from the noise of the measurements. For sample with x = 1.00, it was observed only for frequencies above 100 kHz. The temperature range (18-31 K) of this anomaly of the complex dielectric constant, $\varepsilon^*(T)$, of $LuMn_xO_{3\pm\delta}$ overlaps with the temperature of an analogous anomaly of both the real and imaginary components of $\varepsilon^*(T)$ centred at 23 K reported for the p-$Eu_{1-\xi}Lu_\xi MnO_3$ solid solution in the range $0 \leq \xi \leq 0.20$, this phase retaining the $RMnO_3$ perovskite crystalline structure until ξ reaches the limit ξ = 0.30 and converting to the hexagonal symmetry above this threshold [206,207].

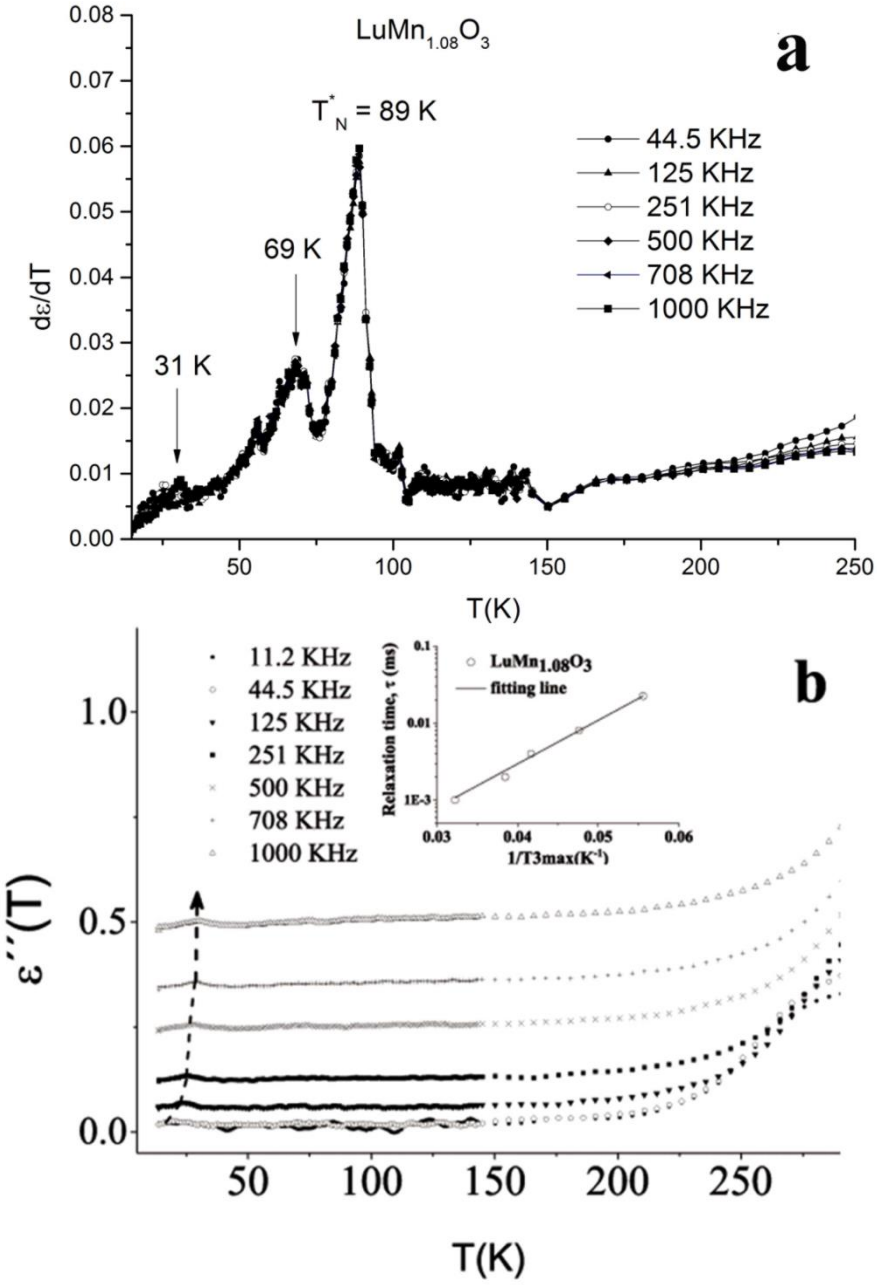

Figure 7-3. (a) Temperature derivative of the dielectric constant ε´(T) at different frequencies for the sample $LuMn_{1.08}O_{3\pm\delta}$ indicating frequency independent peaks at 89 K and 69 K and a frequency dependent transition around 31 K. (b) Imaginary part of the permittivity ε´´(T) of same sample $LuMn_{1.08}O_{3\pm\delta}$ exhibiting the frequency dependence of the transition temperature of the transition observed around 31 K, inset with the Arrhenius plot of the relaxation time τ of the same anomaly of the imaginary part of the permittivity [91].

The inset in Figure 7-3.b gives the Arrhenius plot of the relaxation time τ of this anomaly of the dielectric constant of sample $LuMn_{1.08}O_{3\pm\delta}$, a thermally activated mechanism where τ relaxation time is given by $\tau(T) = \tau_0 \exp[U/k_BT]$, U is the hopping energy, k_B the Boltzmann constant, $\tau = 1/f$, f being frequency of the dielectric measurement and $T = T3_{max}$ is the temperature at the maximum of ε´´. The increasing of the temperature of this maximum of ε´´ as the frequency rises to 1 MHz implies that faster switching of the dielectric dipoles demands higher thermal energy, the time dependent response of the dielectric dipoles existing inside the ferroelectric domains delaying the response to the applied a.c. electric field. The line in Figure 7-3.b represents the fit to Arrhenius law and yields the following values of the parameters of the dielectric relaxation: U = 12 meV and τ_0 = 12.5 ns. The present values reasonably match the corresponding values of the parameters of the polaron hopping mechanism of dielectric relaxation observed in the temperature range 75 – 150 K for $Sr_{0.97}(Ti_{0.80}Fe_{0.20})O_{3-\delta}$ sintered samples, with U = 60 meV and τ_0 = 30 ns [208] , as well as in the p-$Eu_{1-\xi}Lu_{\xi}MnO_3$ solid solution with $0.10 \leq \xi \leq 0.20$ in the temperature range 50 – 90 K, where U = 24 meV and $25 \leq \tau_0 \leq 55$ ns [207] . The low temperature behaviour of the $LuMn_xO_{3\pm\delta}$ samples ($x \geq 1$) and the values of τ_0 and U calculated accordingly to the equation of thermally activation of dielectric relaxation by polaron hoping [208,209], point to the presence of the polaron hopping as causes the frequency dependant anomaly in dielectric measurements, the effect becoming stronger as x increases.

7-1-2 Effect of annealing time on dielectric constant

The effect of increasing annealing time on properties such as elimination of porosity by sintering, grain growth or magnetic behaviour of off-stoichiometric samples confirmed that these as well other properties coupled to them could also be modified by extending the time of the high temperature processing step. The dielectric constant of h-$RMnO_3$ materials is coupled to the magnetic transitions [27]. The effect of sintering time on the

dielectric properties of the off-stoichiometric samples and magneto-dielectric coupling is investigated in this section. Figure 7-4.a gives the real part of the dielectric constant, ε´, as a function of T in the range 10-200 K, for selected samples of three compositions in the composition range under study, x=0.92, x=1.00 and x=1.04. All three samples were sintered for 5 days. The x=0.92 composition was included in this set of 5 days annealed samples because the lattice parameters of this sample of the XRD refinement yield the lowest value of χ^2, the sum of residuals, in Table 4-2 and hence it would be more reliable to say that the disordering inside lattice would play a smaller role here in comparison with the sample of same composition annealed only for 1 day. As the samples of 1 day annealing in Figure 7-1.a, all three samples in Figure 7-4.a clearly show the transition of the dielectric constant coupled to AFM ordering at temperatures very close to 90 K.

The first T derivative of ε´of x=1.00 and x=0.92 samples in Figure 7-4.b and c, respectively, retrieves values of T at the maximum of 88 K and 89 K, these values being very close to 90 K, almost coincident with the Neel ordering transition in magnetic measurements, Figure 5-9. As in Figure 7-4.a, a second transition below 90 K is also recorded here, being more prominent for the x=0.92 sample with the maximum of dε´/dT at 75 K, Figure 7-4.c, but still noticed in the x=1.04 sample as an ill-defined broad transition in the temperature range 70-78 K in Figure 7-4.a. Neither in the T derivative of ε´ nor in the imaginary part of permittivity, ε´´, could evidence of this second transition or anomaly below T_N be found in the x=1.00 sample. This second transition has no correspondence with any transition that could be detected in magnetic susceptibility measurements of the same samples in Chapter 5, Figure 5-9. A transition of spin ordering symmetry detected by optical second harmonic spectroscopy from $P\underline{6}_3\underline{c}m$ to the $P\underline{6}_3$ magnetic symmetry was early reported to occur at T≈60 K in $LuMnO_3$ [145]. The effect of spin reorientation in the antiferromagnetic structure below T_N was claimed to induce strong dielectric polarization variation under applied magnetic field in $HoMnO_3$, $ErMnO_3$ and $YMnO_3$ field [27]. This same reference confirmed that there are two transitions visible in dielectric constant below T_N, the corresponding transition temperatures changing with the magnitude of the applied magnetic field. One may expect

that transitions or anomalies of the dielectric constant below T_N in the present measurements have the same origin as in those h-$RMnO_3$ materials and are not necessarily seen in measurements of the magnetic susceptibility, although some of them appeared in the measurements of the magnetic moment once the applied magnetic field reached few thousand Oe [27]. The symmetrical presence of this second transition below T_N in the x=0.92 and x=1.04 samples could be interpreted as the effect of vacancy doping on the dielectric behavior of the crystalline lattice which may provoke distortion or perhaps provide regions (nanodomains or interfaces) of inhomogeneity in the structure and chemical composition which force the spin configurations of Mn^{3+} ions to change with temperature.

As in samples of one day annealing time in Figure 7-1 and Figure 7-3, the determination of ε with different frequencies confirmed that the anomaly of ε´associated to T_N and the second transition of the same property observed below T_N in the samples of longer annealing time, 5 days, in Figure 7-4. are athermal. In the same way as in samples of 1 day annealing, the anomaly ε´ observed at temperatures below 35 K in the x=0.92 sample of 5 day annealing in Figure 7-4.c is frequency dependent and thermally activated. The corresponding Arrhenius plot of the frequency as function of inverse of temperature at the local maximum of ε´´ in Figure 7-4.d reveals ranges with slightly different values of activation energy. The range of frequencies where the linear fitting on the data can be applied is limited to frequencies above 10 kHz. The same analysis of data from the x=1.00 and x=1.04 samples did not show any visible peak in this range of temperature below 35 K, neither in real part nor in the imaginary part of the permittivity. The fitting of the Arrhenius equation to the data in the high frequency range, in Figure 7-4.d, yields 18.6 meV for the activation energy, close to the corresponding value of 12 meV obtained for the relaxation time of ε´´ for Mn-rich samples of one day annealed in inset of Figure 7-3.b.

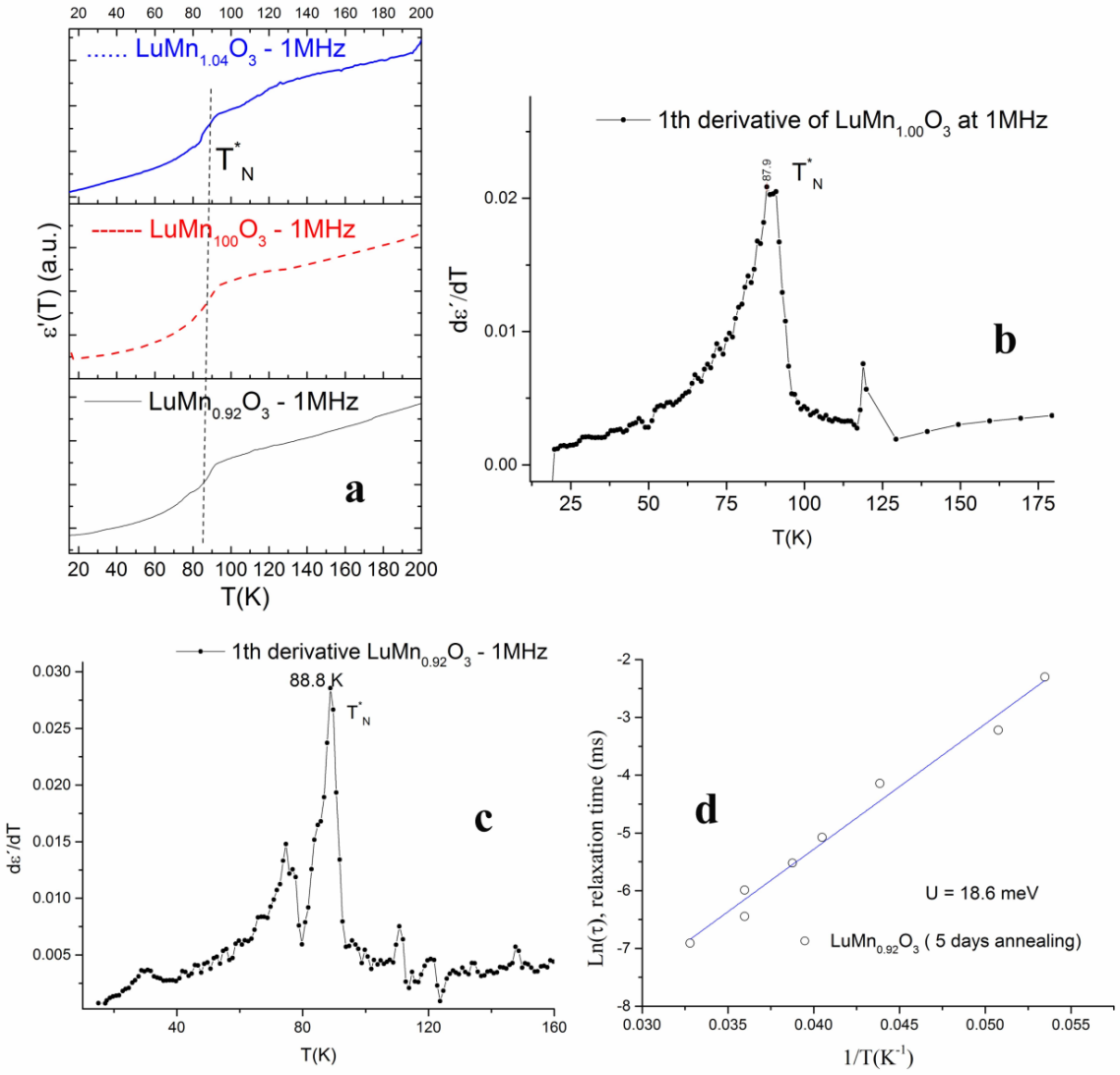

Figure 7-4. (a) The dielectric constant as a function of temperature for two compositions, x=0.92 and x=1.00 after 5 days annealing time, measured at 1 MHz frequency. (b) and (c) The first derivative of the dielectric constant for two compositions showing the Neel ordering transitions, another transition below 90 K and low temperature anomaly for x=0.92. (d) The thermal evolution of the dynamics of the anomaly at temperature range of 18 K to 30 K observed for x=0.92.

The lacking of the second transition below T_N in x=1.00 sample and of the low temperature peak in x=1.00 and x=1.04 samples of 5 day annealing may carry relevant information. From Rietveld refinement of XRD data in Table 4-1, Table 4-2 and Table 4-3

Chapter 4, it can be seen that the evolution of lattice parameters of samples with 1 day and 5 days annealing show large differences. Not just is the scatter in data of the longer annealing time lesser, but also the lattice parameters a-axis and cell volume come to a sort of stability (linear plateau) for x≥1.04. This value can be set as the stability limit of the $LuMn_xO_{3\pm\delta}$ solid solution [91]. The same could not be found for x<1 side with 5 days of annealing time. Only by duplicating the annealing time to 10 days, the equivalent plateau appeared for x<0.96. An analogous behaviour can be set from difference in the evolution of the residual χ^2 of the Rietveld refinement with annealing time in one side and another of the stoichiometry shift in the composition of the samples. As disorder inside the lattice cell affects the convergence of XRD Rietveld refinement such disorder is reduced when the annealing time is extended to five days, but more on the x>1 side. On the contrary, the Mn vacancy doped branch of the solid solution required even longer annealing times to get stability and properly ordered crystalline lattices. Within the limits of such inference the analysis of the dielectric constant would suggest that in Lu vacancy doped samples, a less disturbed crystalline lattice is shown up in the dielectric measurements with vanishing of the thermally activated peak of ε´´ below 35 K and fading away of the second transition below T_N for x=1.04. These two peaks would be essentially extrinsic. Ordering of ions in the crystalline structure of x=1 samples would be facilitated by the equal ratio of the Lu and Mn ions, the two extra transitions of ε´´ being absent in the corresponding results in Figure 7-1.a and Figure 7-4.a.

7-2 Piezoelectric response of off-stoichiometric ceramics

As state in Chapter 2, section 2-5, h-$RMnO_3$ oxides put interesting challenges in science as they show coupling of both AFM domains and FE domains [26, 27]. The AFM ordering transition dictates that such coupling only exists at low temperature below 90 K for $LuMnO_3$. But, potential application of these oxides could also be find above T_N, even at room temperature, because of the specific ferroelectric behaviour and intriguing

ferroelectric domain patterns they show. The nature of coupling of FE domains to structural defects was discussed in Chapter 2 and investigated in Chapter 6 by using TEM/STEM analysis and orienting the sample to specific zone axis, topological defects (APB/FE domain walls) having been observed. The advantage of TEM in looking at the atomic structure and structural distortions occurring on the domain walls and or other kinds of structural features becomes a constraint when looking for arrangement of the FE domains of large sizes, in the order of few microns, since at such scale it is hard to prepare from a bulk sample and later find such wide thin region of a particle transparent for electrons to be able to look at FE domains. The characterization of large size FE domains is possible via AFM/PFM techniques, but it needs very elaborated surface finishing being usually done only on single crystals after chemical etching of the surface [108]. The SEM study of grain growth as a function of composition and sintering time in section 4-3 of Chapter 4 confirms that the density of grain boundaries seen on sample surfaces is decreasing with annealing time to different extents dependent on x. Since XRD refinement shows change in lattice parameters, the same will happen in ferroelectric behaviour of the off-stoichiometric ceramics, because the displacement of the Lu ions in the unit cell is the main source of ferroelectric polarization [30,106,127]. The observation of ferroelectric domains on off-stoichiometric ceramics samples of the present study is reviewed in this section.

7-2-1 Preparing surfaces for AFM/PFM analysis

The viability of revealing the ferroelectric domains by the PFM technique depends strongly on both the quality of surface and the orientation of the particles. The particles with surfaces oriented to (110), (100) and (001) crystal directions may show vortex/anti-vortex clover leaf patterns under the PFM tip [49,79,108]. In the random distribution of crystal directions of bulk samples, Figure 4-20 and Figure 4-23, it will be rare to find grains on polished sections with due orientation and adequate quality of

surface finishing as needed for the PFM study. Due to porosity in samples of short annealing time and microcracking in samples of wider grain sizes, section 4-3 of Chapter 4, the mechanical polishing process produces coarse debris which fills in voids of the surface and once released repeatedly makes scratches across the surface being polished. Such scratches become easily seen in AFM images and affect the process of data acquisition in PFM mode. During the experiments one tried to land the PFM tip on flat, scratch free regions of the polished surface to eliminate ambiguity on interpreting the images. Polishing was done on diamond lapping papers with no use of polishing pastes because the loose abrasives will easy penetrate into pores or cracks of the surface. Quality of surface finishing was monitored during polishing with the optical microscope using polarized light illumination, the process being terminated when scratch free regions properly polished and containing a few particles of different polarization contrast were seen on the surface.

7-2-2 Off-stoichiometric effect on the ferroelectric domains

Figure 7-5 presents PFM images taken from flat regions of three selected samples, x=0.92, x=1.00 and x=1.04, 1 day annealing, to allow study of the ferroelectric domains with changes of x. The three images have different scales mainly because the composition with x≤1 has finer particle sizes and low relative density, section 4-3, Chapter 4. Therefore the mechanical polishing did not work so well to provide large area with low roughness in sample x=0.92 for the analysis. The opposite holds for samples with x=1.04 with larger grain size, less residual porosity and better finished surfaces. In Figure 7-5 the same grain size as in SEM images of Chapter 4, section 4-3 is observed for the ferroelectric domains. Changes in contrast across of the PFM image correspond to domains of different polarization, being better defined for the sample of Mn-rich side. The color is inverted in Figure 7-5.b for better clarity. Since in the crystalline structure of $LuMnO_3$ the electrical polarization is stronger along c-axis and restricted to this

orientation [33,131] where the displacement of the Lu ions could be seen more visible, this orientation must yield the maximum intensity of PFM contrast. Due to the prevailing orientation FE domain walls in the crystal, a sharp transition between FE domains of opposite polarization occurs in surfaces are oriented perpendicular to c-axis (a-c or b-c plane). Other orientations of the particle surfaces will produce different scales of the piezo response in a ceramic sample. For samples x=0.92 and x=1.04 the contrast in the colors from dark brown to bright does show the difference in orientations, including domains with Lu ions with upwards polarization, others with downwards polarization or inclined vectors of polarization.

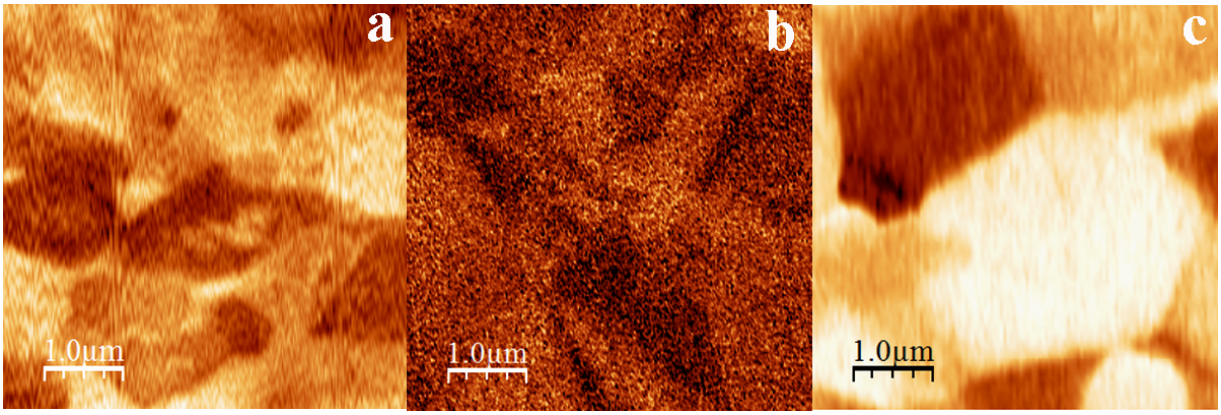

Figure 7-5. PFM images of different compositions, (a) x=0.92, (b) x=1.00 and (c) x=1.04 showing the ferroelectric domain in different sizes as the grain size of the compositions also changes by x.

Comparing the stoichiometric sample with x=1 to vacancy doped samples in Figure 7-5 shows a completely different pattern of polarization which may indicate that distortion of unit cells by vacancy doping in off-stoichiometric samples induced more intense electrical polarization. However, one should take into account that polarization strength can change just because of orientation of the crystalline grains in the region of the surface being analysed. Another important fact on the driving force of ferroelectricity in h-$RMnO_3$ is the re-hybridization of the Lu-O_{planar} bonds after lowering symmetry from

high symmetry PE phase to lower symmetry FE ferroelectric phase, which is being investigated for more than a decade [125,127,130,131,172,210], the evaluation of re-hybridization being left for later section 7-2-3.

Due to interference of disturbing interactions between PFM tip and sample surface from several sources the effective resolution of PFM amplitude mode in air is limited to 10 to 30 nm in most cases [211,212], the resolution limit for the PFM phase mode being one order of magnitude below this threshold. The contrast and resolution of the out-of-plane PFM phase image of the multiferroic hexagonal $YFeO_3$ thin films with 100 nm average grain size are superior to these features in corresponding out-of-plane PFM amplitude image. In such fine scale of grain sizes most nanograins hold just a single FE nanodomain [213]. With elimination of noise from electrostatic interferences near the tip or in circuitry, by avoiding large tip-surface forces in the contact and the appearance of condensate meniscus at the tip from humid environmental air the best of 10 nm resolution limit of PFM amplitude images can be attained in air with improved tip sensitivity and the use of tips of non-worn apex and small (20-50 nm) tip-radius of curvature [212,214]. FE nanodomains with irregular wavy contours and 100 nm average domain size of a single crystal of the PZN-PT (0.9 $PbMg_{1/3}Nb_{2/3}O_3$ - 0.1 $PbTiO_3$) relaxor became visible in the PFM image of the crystal surface [215]. Zooming by 15-20 times the image in Figure 7-5.b amidst the prevalent noise of the image reveals a pattern of maybe positive and negatively polarized areas of sizes ranging from 60 nm to 90 nm comparable to the nanodomain sizes of the PZN-PF relaxor. The liquid neck at surface-tip contact being one of the most disturbing causes of resolution loss in PFM, a further advance in resolution limit of out-of-plane PFM amplitude mode to 3 nm was achieved by immersion of sample-tip contact in suitable liquid media including distilled water [214].

7-2-4 Vortex patterns and domain switching

Figure 7-6 indicates different regions of $LuMn_{1.08}O_{3\pm\delta}$, 5 days annealed sample where PFM images were taken in the search for the right orientation of the ferroelectric axis for the observation of FE domains. In Figure 7-6.a and c the vortex patterns of the APB coupled to FE domains with up and down polarization is clearly seen, as it was discussed in section 2-5, Chapter 2.

The vortex/anti-vortex pattern does not show fully six-fold symmetrized domains, eventually due to slightly misorientation of the particles. As shown by the EBSD images in section 4-3, Chapter 4, neighbouring grains in a polycrystal may display almost the same orientation in two of the three Euler's angles, but not on the third one. Orientation change on neighbouring grains results in inhomogeneous contrast of piezoresponse of the ferroelectric domains. In Figure 7-6.b, the line profile drawn in Figure 7-6.a, shows 3 V difference between the bright regions (upward polarization) and the darker regions (downward polarization), with some fluctuations in order of hundred nanometers which could be from ferroelectric nanoscale FE domains, or noise. The images in Figure 7-6.c and the enlarged view in Figure 7-6.e taken from c are from other part of the same sample and show different ferroelectric patterns but not organized as 6-fold vortices with the corresponding topography. Figure 7-6.d gives the relief contrast image of the surface corresponding to PFM image aside in Figure 7-6.c. The importance of the low angle grain boundaries and grain boundaries in general can be understood as hindering the formation of stable or complete topological 6 fold vortices in ceramics with fine grain sizes.

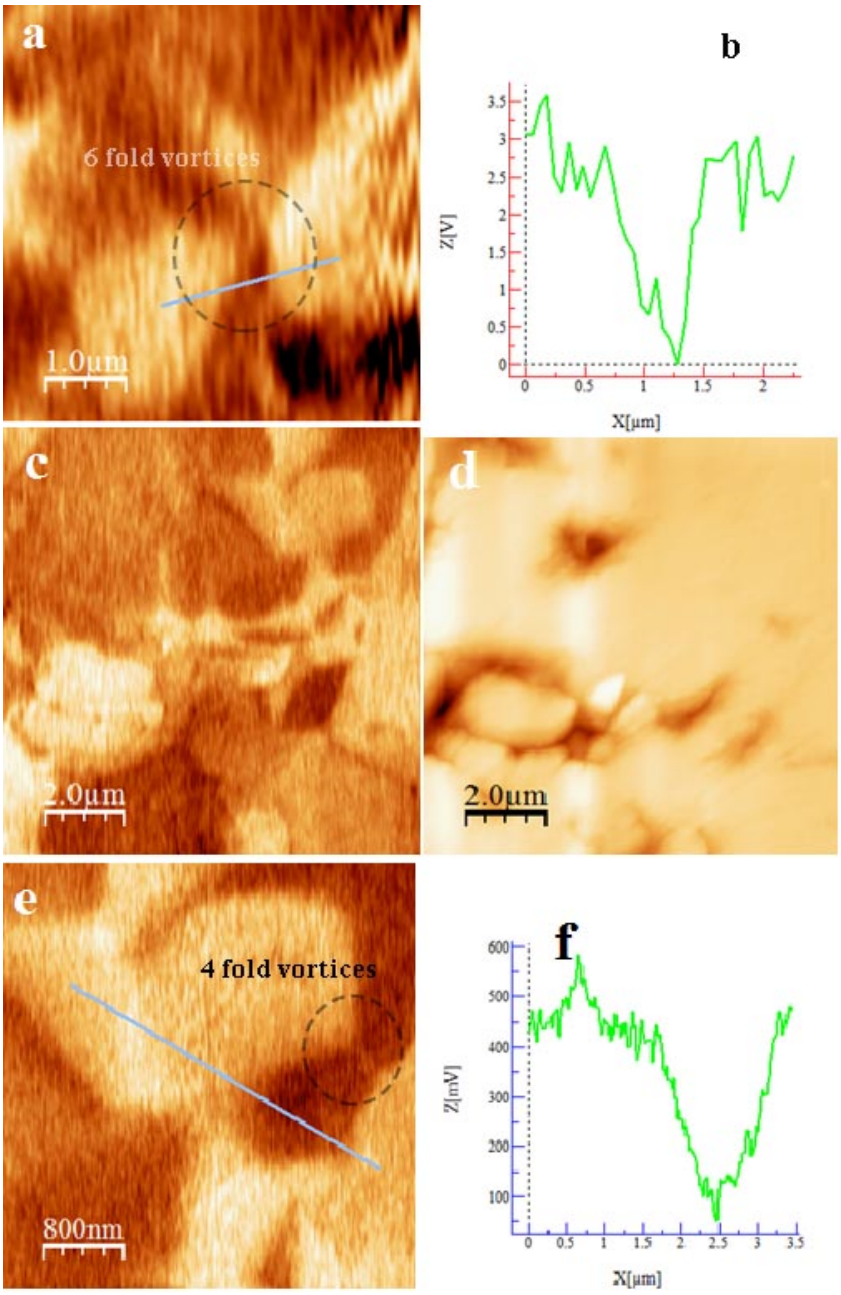

Figure 7-6. PFM images of sample with x= 1.08, 1 day annealed, of two different regions showing vortex pattern of 6 APB/FE domains or 4 APB/FE domains. (a) Image of 6 areas radiating of a common point in two alternating subsets of 3 upward polarized areas and 3 of downward polarization. (b) PFM signal intensity of line profile in (a). (c) PFM image of another part of the sample. (d) AFM image of surface of (c). (e) Enlarged view of the up, right part of (c) with 4-fold APB/FE vortex like pattern. (f) PFM signal intensity of line profile in e).

The effect of grain boundaries in distorting the lattice of two particles with very close zone axes is addressed in Figure 7-7.a and c showing the one on upper right oriented to (110) zone axis and the second low left with an orientation close to the given zone axis.

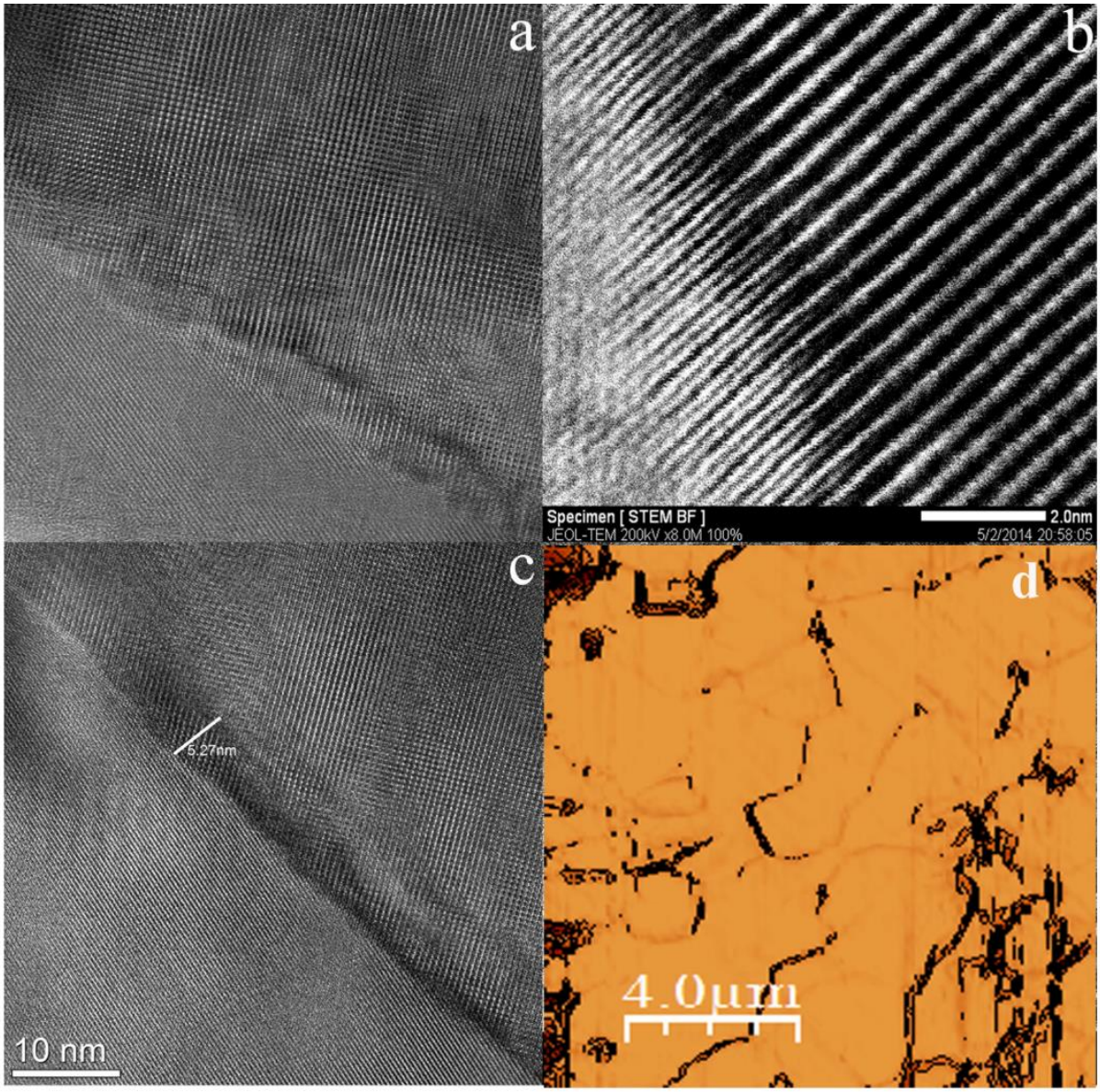

Figure 7-7. HRTEM images of x=1.04 orientated along (110) zone axis for right side particle across the boundary (a) and (c) and high magnification STEM image of the distorted lattices at boundary of two particles. (d) AFM image of the chemically etched surface of the same sample showing the effect of the grain boundaries.

Both HRTEM images and the BF-STEM image show in a clear way the distorted region along the grain boundary with a projection in image plane around 10 nm wide, which is small in scale of PFM images in Figure 7-5 and Figure 7-6 above. However, it contains inhomogeneity in composition, presents local lattice distortion (upper particle) and may affect the process of acquiring PFM images. Deeper understanding of the role of grain boundaries can be unravelled by chemical etching of the surfaces of the ceramics [216]. Figure 7-7.d shows the AFM image of chemically etched surface of the same sample where boundaries appear as dark (deep etched) or bright lines (light etched). The differences among these boundaries may correspond to different polarizations, however, it seems that etching process make the boundaries wider than the boundaries before etching.

7-2-5 Effect of sintering on ferroelectric domains

Figure 7-8 exhibits the effect of additional time of sintering on the ferroelectric domains of two selected compositions x=1.00 and x=1.04 for 5 days annealing time. Figure 7-8.b is the PFM response of the same area of the AFM image aside in Figure 7-8.a of sample $LuMnO_3$. The topology of FE domains in Figure 7-8.b displays 4-fold arrangements of APB/FE domains with larger sizes than the FE domains in the sample with identical composition of one day annealing time, Figure 7-5. Although the sample in Figure 7-5.b did not show contrasted and well defined FE domain patterns, after annealing for longer time the FE domains become clearly discriminated in Figure 7-8.b. However, topological 6-fold vortices are absent in this image. The PFM images in Figure 7-8.c and d display the FE domains of sample x=1.04, 5 day annealing time and include FE domains a few μm wide. The line profile of the PFM response of image d) also shown as Figure 7-8.e gives a large range for the PFM signal above 15 V in total, much more intense than the PFM response in samples of short annealing time, Figure 7-6.b and f. The topological 6-fold APB/FE domains were not found, too. The triple point where grain boundaries between

three particles met is seen in Figure 7-8.c with the characteristic local curvature of grain boundaries imposed by equilibrium of grain boundary surface tension forces along joining lines of three grain boundaries.

The large grain on the upper left of same image is split into 3 FE domains seeming to radiate from a point close to, or on the grain boundary. An analogous geometry of FE domains with one FE domain of near triangular shape between two other domains of opposite polarization, the three meeting together at point of a planar defect of $YMnO_{3-\delta}$ single crystal grown in Ar atmosphere is given in Figure 7-8.f, inset cut from original figure in ref.[162]. The planar defect eventually resulted from oxygen vacancy ordering and generated a set of flat FE domain walls quasi-straight aligned along it. Interaction of oxygen vacancies with FE domain walls of $YMnO_{3-\delta}$ created a domain structure of random shapes where round-closed ends coexist with straight FE domain walls [97,162]. The concentration of oxygen vacancies, aliovalent cation doping and cooling rate all contribute for changes of FE domain sizes of hexagonal $RMnO_3$ multiferroics [15,55,60,61,157,160]. FE domains with sizes close to the resolution limits of the PFM microscopy would be hard to characterize. Electrical poled by the applied fields the FE domains of $YMnO_{3-\delta}$ of random shapes also turn into parallel stripes as FE domain walls of topological vortices of stoichiometric hexagonal $RMnO_3$ crystals [157,162,203]. The better defined ferroelectric domains in Figure 7-8.b, c and d might result from improved homogeneity of the crystalline lattice in a wider scale than in the previous samples in Figure 7-5 and Figure 7-6. Longer annealing time resulted in larger grains which may support wider FE domains. One must underline that capturing the topological vortex pattern in PFM analysis of bulk ceramic $RMnO_3$ samples created unsolved difficulties.

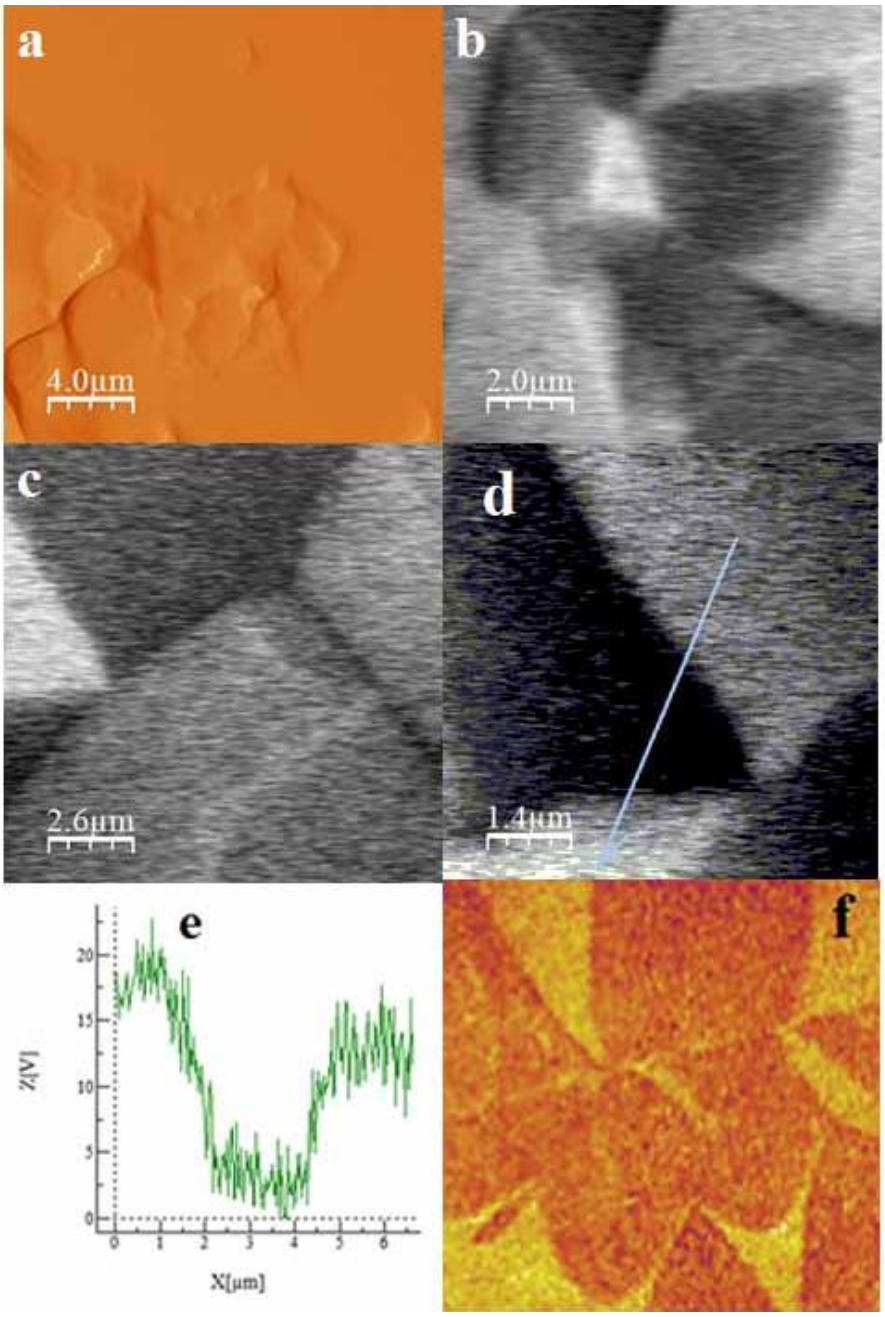

Figure 7-8. AFM topography and PFM images of x=1.00 and x=1.04, 5 day annealed samples. (a) AFM topography image of x=1.00 sample. (b) FEM image area in a. (c) PFM image of x=1.04 sample. d) Enlarged view of same area of a, with reversed polarization contrast. (e) Line profile of the FE domain transition as indicated in PFM image (d). (f) FE domains of $YMnO_{3-\delta}$ single crystal grown in Ar atmosphere [162].

Figure 7-9.a and b show respectively the PFM amplitude and phase images of sample x=1.04 annealed for 10 days. In the phase map of Figure 7-9.b the changing in phase contrast of successive FE domains in a total of six around the vortex alternating with upward polarization (brighter region in amplitude) and downward polarization (brown regions in the phase map) is more visible than in the corresponding amplitude map in Figure 7-9.a. The amplitude of the piezoresponse in Figure 7-9.a is faint for some of the areas however the phase shifts of the FE domains indicate that the six lines of clear contrast radiating from the vortex in the amplitude map correspond to antiphase FE domain walls separating each FE domain from the next one. The size of the clover leaf pattern captured in Figure 7-9.a and b is comparable to the one from single crystals of $LuMnO_3$ measured with PFM [60]. Inside each FE domain of the vortex/anti-vortex pattern in the amplitude map there are regions seemingly with different polarization orientation which may represent inhomogeneity inside the grains, or contamination of the surface. The investigation FE domains in other areas in the scale of few microns showed FE domains of different polarization amplitude and phase shift but not necessarily the full vortex/anti-vortex topology. Single polarization and phase of a FE domain was observed when going to smaller scale below 2 microns for similar sample of x=1.04 and there are FE domains with opposite polarizations (not shown here). The PFM amplitude and phase images in Figure 7-9.c and d of sample x=1.00 (after 5 days annealing) present similar patterns of FE domains as Figure 7-9.a and b. The size of vortex/anti-vortex pattern is 10 microns being smaller than the one observed for x=1.04 after 10 days annealing. As shown in Figure 4-16.a the grain size of sample x=1.04 of longer annealing time, 8 microns, is larger than the grain size of x=1.00 of shorter annealing time, 4 microns. In Figure 7-9.c, bright FE domains show upward polarization. Both amplitude and phase maps produce almost uniform distribution of the colors, accordingly to the polarization inside each FE domain. This may happen because the stoichiometric x=1.00 sample is less inhomogeneous in the region of analysis or because the area of analysis is small enough and clean from contamination or the topography of the surface does not interfere with the PFM analysis.

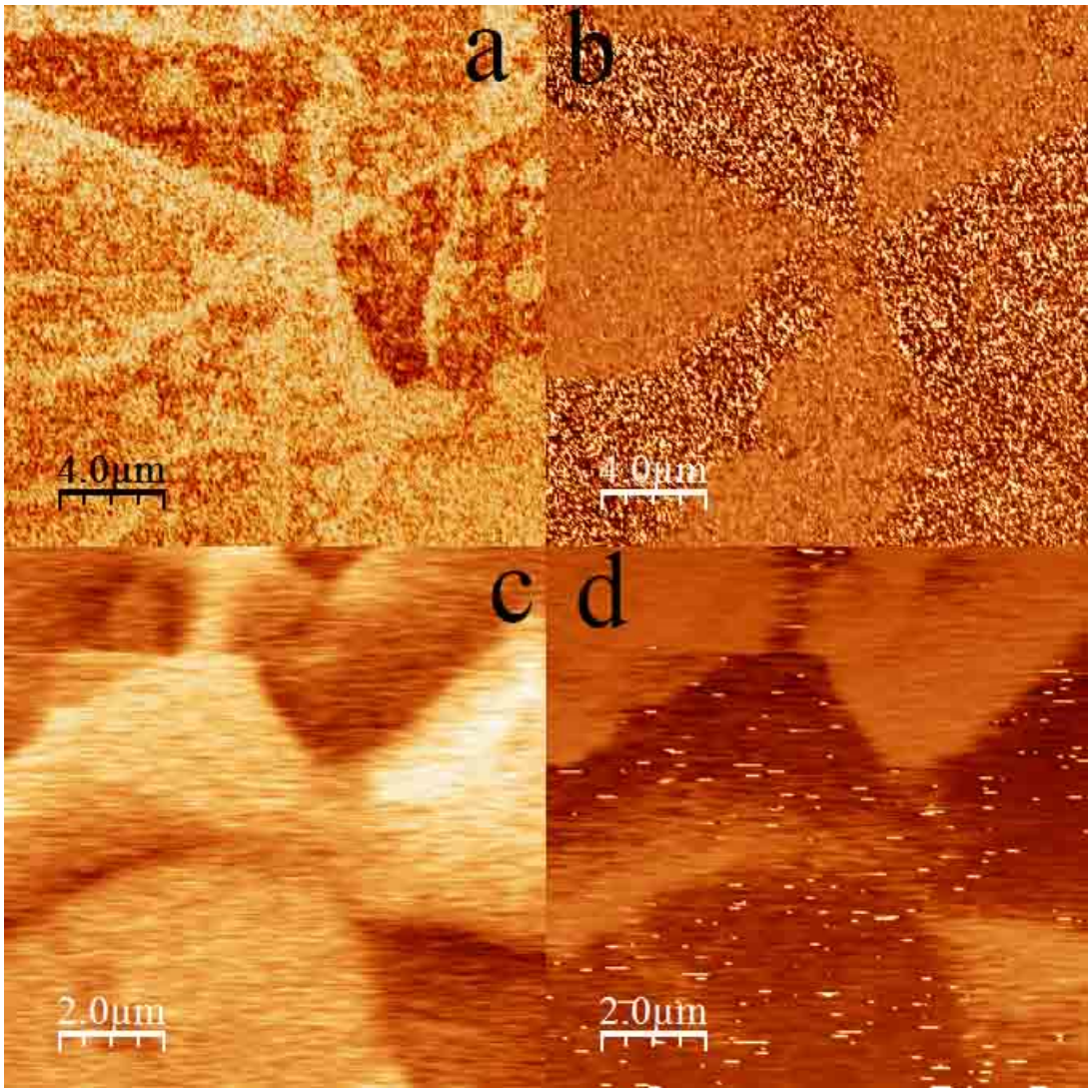

Figure 7-9. (a) Amplitude and (b) phase maps of a vortex/anti-vortex FE domains with the total size of around 16 microns of sample x=1.04 (10 days annealing), darker regions in (a) shows higher voltage than brighter regions. (c) and (d) present 10 micron size vortex/anti-vortex images of sample x=1.00 (annealed for 5 days) in amplitude and phase, respectively. In amplitude, the bright regions correspond to upward polarization.

Dark field (DF) images of three different areas of sample x=1.04, 1 day annealing time, in Figure 7-10 were taken along (110) zone axis with the objective of comparing the boundaries of the FE domain walls with other type of distortions also visible in TEM. The

topological 6-fold vortices are recognizable in the TEM images but only when scales of 100 nm to 200 nm are in use. The DF-STEM image in Figure 7-10.d gives the enlarged view of one of the topological defects seen in the TEM images. These topological vortices in DF-TEM images in Figure 7-10 are obviously of much smaller dimensions than the FE domains and APB/FE vortex patterns revealed by the contrast of the PFM images, Figure 7-5 and Figure 7-6 and Figure 7-8. Although the resolution of PFM equipment we use for analysis is not as high as to capture easily the 100 nm vortex patterns, in small scale the RMS of the surface plays important role. Also in nano-scale analysis of the TEM images, the effect of the dislocations on annihilation of the FE domains can be seen.

Discussed and shown in previous Chapter 6, FE domain with either up or down polarization in our TEM analysis could not be seen in large sizes even in the order of 0.5 micron. We assign this size limitation to the presence of defects and dislocations inside particles. In our PFM analysis, there is not such sensitivity to the nano-scale defects which prohibit extension of the FE domains. Each large FE domain with either up or down polarization may contain few small scale FE domains that cannot be observed in PFM images. At the nanoscale, partial edge dislocations alone, or associated in pairs and nanoinclusions become local topology breaking defects of FE domain structures in $RMnO_3$ lattices by decreasing or increasing in even numbers the ferroelectric domains with opposite polarization that can be seen radiating from a common point, the vortex-like center of broken topology [58,59]. Point defects such as oxygen vacancies and substitution of Mn by cations of different valence, namely the Ti^{4+}, generally break in a random way the topology of 6-fold vortices of FE domains of the hexagonal $RMnO_3$ lattices [97,160,162].

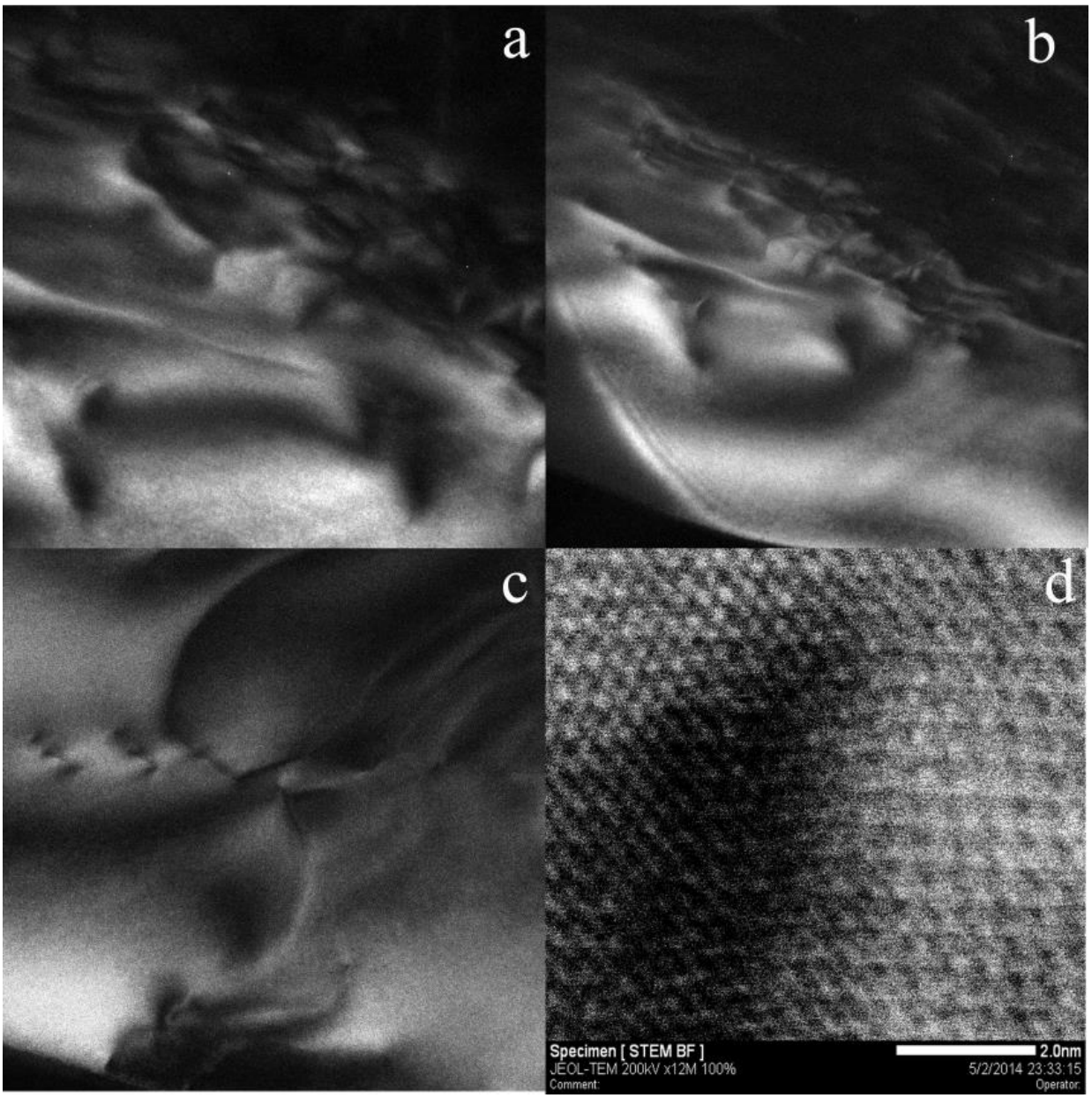

Figure 7-10. TEM-Dark Field images of sample $LuMn_{1.04}O_3$ after one day annealing by tilting sample slightly out of (110) zone axis. (a), (b) and (c) are showing topological domains by deferent excitation and different places of the particle. (d) STEM image of one of the defects.

7-2-3 Re-hybridization and DFT calculations

Since the beginning of the extensive research on ferroelectricity of the h-$RMnO_3$ materials when it was found out that the distortions in the unit cell promote the Lu ions to displace and induce electrical polarization in the unit cell, people paid attention to the asymmetric bonding of the Lu-O and Mn-O as the driving force of the changes of ferroelectric behaviour. Studying the atomic displacements of all ions inside the unit cell of $LuMnO_3$ could unravel that lowering symmetry from PE to FE phases would be accompanied by large off-centre movement of the Lu-O_{pl} ions which result in transferring of centrosymmetric positions to non-centrosymmetric positions in the final phase [33,128,130,172,217]. It was further understood that the main orbitals involved in asymmetric bonding of Lu^{3+}-O_{pl} are the $5dz^2$ (Lu)-$2p_z(O_{pl})$ [130]. The model of the so-called d°-ness claims that re-hybridization of the Mn(3d)-O(2p) and Y(4d)-O(2p) bonds for examples in $YMnO_3$ [131] occurs because of off-centre movements of the ions during PE/FE phase transition with the corresponding contributions to the large anomalies in Born effective charges (BEC).

Although, the re-hybridization of the Lu and O ions as the driving force of ferroelectricity has theoretical and experimental support, in opposite directions there are other authors which do not emphasize the importance of this kind of re-hybridization for the ferroelectricity of hexagonal $RMnO_3$ materials [127,218]. In fact, as the definition of BEC implies, the derivative of the polarization along direction the displacements of the Lu ions happens, along that same direction produces real BEC effective charges [218]. Therefore, what is usually discussed in favour of d°-ness model and PDOS of the relevant orbitals of R^{3+} and O_{pl} is the static charge occupancy, not real displacements. As already highlighted the covalent bonding and re-hybridization (chemical activity) may have minor roles on ferroelectricity of h-$RMnO_3$ oxides. Instead, the main contribution comes from the large off-centre displacements of the R^{3+} ions (R^{3+}- O_{pl} bonds), coupled to the rotation of the bipyramids during phase transformation [127,218]. Mn-O_{ap} tilting and R-

O_{pl} displacements cooperate together to create a stable energy structure with ferroelectricity driven from such distortion of the unit cell.

The partial Density of States (PDOS) of the orbitals of ions in the unit cell of $LuMnO_3$ is calculated via first-principles DFT approach using Full Potential Linearized Augment Plane Wave (FPLAPW) method implemented in Wien2K code [124]. A-type AFM arrangements of the Mn ions (z=0 spins up and z=0.5 spins down, or reverse) are assumed in the spin-polarized calculations in the FE phase [127]. The number of plane waves in the interstitial atomic spheres was limited to $K_{max} = 7.0/R_{MT}$ and 5×5×3 K-points were chosen. After getting convergence in the calculations by setting the convergence criteria to 0.0001 Ry and 0.0005 e for energy and charge respectively, the LDA+U approach was initialized which turns to be more appropriate in producing real band gap of the oxides, the same parameters and 0.44 Ry energy (6 eV) having been chosen [125].

Figure 7-11 presents the results of PDOS calculated with the DFT approach for the concerned orbitals of Lu ions (5d), oxygen planar and apical (both 2p) and Mn ions (3d) of $LuMnO_3$ for three selected compositions, one on each side of stoichiometric composition and x=1 composition. Back to the concept of re-hybridization of Lu(5d) – O(2p) orbitals, it is seen that overlapping of $5dz^2$(Lu) – $2p_z(O_{pl})$ is stronger for x=1.08 and x=0.92 compositions in close vicinity to the Fermi level (-0.5 eV), whereas in the partial PDOS of x=1.00 composition in Figure 7-11.b it is spreader towards lower energies (-1 eV).

In section 7-3 of this Chapter the DFT approach will be used to compare the polarization of the stoichiometric and off-stoichiometric compositions together and to investigate if the distortion of the $LuMnO_3$ lattice via vacancy doping may change electrical polarization, or not.

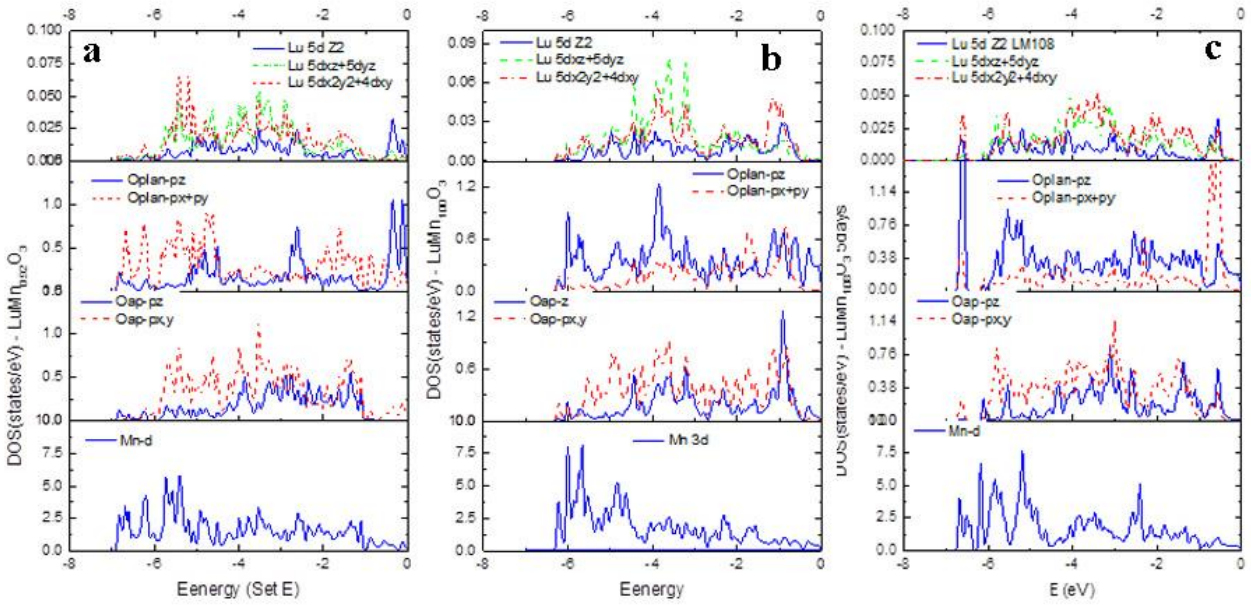

Figure 7-11. PDOS of three compsotions, (a) x=0.92, (b) x=1.00 and (c) x=1.08 for samples after 5 days annealing, calculated using LDA+U.

7-3 Mode analysis of $LuMn_xO_{3\pm\delta}$ lattices

7-3-1 Mode decomposition in h-$LuMnO_3$ materials

The results of PFM in previous section 7-2 show changes of PFM response of the ferroelectric domains with the shift in composition (x) of all samples of this study. Although ferroelectric domains are observed in stable phase $P6_3cm$ of $LuMnO_3$, ferroelectricity in this family of oxides is of improper type [219]. Symmetry group analysis of phase transition from the high symmetry, high temperature PE phase to the low symmetry, low temperature FE phase may bring further understanding to this matter. The Isotropy Suite software or Amplimode software available from Bilbao crystallographic server [220] were used here to perform the symmetry group analysis.

The later one is more suitable as it deals with both lattice parameters and atomic positions of centrosymmetric and distorted crystalline structures. The analysis of the mode decomposition of PE transition to FE of the present study is accompanied by unit cell tripling using Isotropy Suite software, as given in the following:

185 P6_3cm 1 GM1+ P1(1), 1 GM2- P1(1), 1 K1 P1(1), 1 K3 P1(1)

This operation shows all possible paths from the given PE (space group no. 194, P6_3/mmc) to the primary K_3 order parameter. The secondary order parameters are Γ1+, Γ2- (also shown as GM2-) and K_1. Detailed analysis of each decomposed mode is of great importance to trace the displacement of each orbit of the PE phase to the decomposed mode and their amplitudes. To do it, the PE unit cell of $YMnO_3$ was used as it is the only one available in the database [221]. Therefore, we first calculate all interested parameters for PE phase transition to FE phase of $YMnO_3$, and then the same methodology will be applied on $LuMn_xO_{3\pm\delta}$ samples. Annex E will provide details of the methodology and results of the mode decompositions for $YMnO_3$ unit cell.

The presence of ferroelectricity in an unstable K_3 mode was shown to exist because of the stable Γ_{2-} mode and coupling of these two modes together [10,106,130,219]. The K_3 distortion forces the stable Γ_{2-} mode to have its minimum energy shifted to a nonzero value of distortion of the unit cell (drawn from Landau Free energy expanded until 4^{th} order) [219]. That is why in this family of materials so-called improper ferroelectrics the antiferrodistortive structure coexists with ferroelectricity at room temperature.

The growing interest on interlocking of the ferroelectric behaviour and structural anti-phase domain walls have pushed researches to look for consequences of such interlocking on the properties of h-$RMnO_3$ materials as discussed in Chapter 2, section 2-5 [10,16,51,156]. It was calculated and later demonstrated that the degree of distortion of the unit cell in K_3 mode has direct effect on electrical polarization and net magnetization of Mn^{3+} and Fe^{3+} ions of h-$LuMnO_3$ and $LuFeO_3$ materials, respectively [10,219]. The importance of the mode analysis drove the present study to apply the

same analysis to the off-stoichiometric and nominally stoichiometric $LuMn_xO_{3\pm\delta}$ ceramics of 5 days and 10 days annealing. Program PSEUDO from Bilbao Crystallographic Server was used to retrieve the crystalline structure of the corresponding high temperature PE phase from conversion of the Rietveld refined FE crystal structure of the ceramics determined at room temperature [222]: only for the z-coordinate of Lu in PE phase the value of z=0 must be filled in instead of 0.5. Figure 7-12.a and b give the plots of mode amplitude Γ_{2-} ($P6_3mc$) and K_3 ($P6_3cm$), respectively, versus composition x of the $LuMn_xO_{3\pm\delta}$ samples.

For all compositions, the mode amplitude of K_3 is always higher than that for the Γ_{2-} mode. The K_3 mode amplitudes for 5 days and 10 days annealed samples show different trends. With increasing of annealing time and consequently more homogenous crystalline lattices according to XRD Rietveld refinement, Table 4-1, Table 4-2 and Table 4-3 in Chapter 4, a smoother trend would be expected for the mode amplitudes of samples annealed for longer times. In fact, in the $0.96\leq x\leq 1.04$ composition range both sintering times show changes of the amplitude mode when x passes the stoichiometric composition. Longer annealing time results in trendy behaviour of distortion of the lattice related to the K_3 mode upon the transition from PE to FE phases. This mode is mostly linked to tilting of MnO_5 bipyramids and buckling of the Lu planes, the corresponding calculated results being found in Figure 7-12.c and d, respectively. Figure 7-12.e and f display the change of tilt angles of planar and apical oxygen with respect to a-b plane and c-axis, respectively [35,106], and magnitude of tilting (angle of $Mn\text{-}O_{ap.}$ bond and c-axis, denoted as order parameter of the K_3 mode) [51], the first two angles representing polyhedral tilting angle following the change in K_3 mode with x for both annealing time. The buckling of the Lu ions has a smooth increase as x rises from 0.92 to 1.12. Such rising trend is much less pronounced on the amplitudes of either modes in Figure 7-12.a or b. Change of amplitudes may stress the stronger effect of the MnO_5 polyhedral tilting on the crystal structure more than displacement of the Lu ions. Some correlation on the change of buckling of Lu ions and tilting of the MnO_5 polyhedral can be found in the Figure 7-12.d and e, from the angle of O_{pl} with basal plane reminding

the concept of orbital re-hybridization of the Lu($5dz^2$) and ($2pz$)O_{pl} orbitals discussed earlier in section 7-2-5 of this chapter. Hence, such correlation may have some effects even if minor on the electrical polarization.

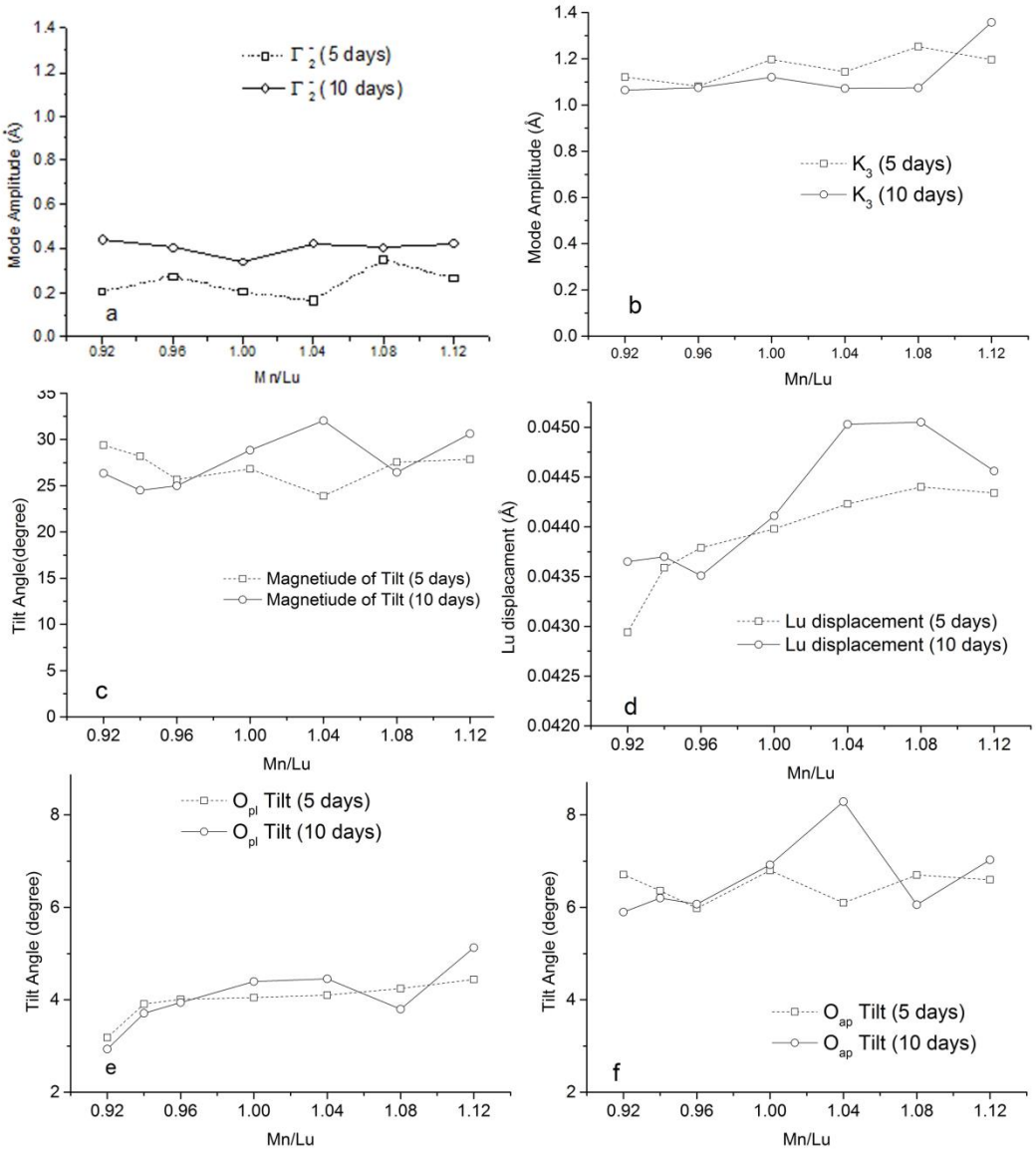

Figure 7-12. Results of mode analysis of $LuMn_xO_{3\pm\delta}$ ceramics, 5 days and 10 days annealing time: (a) and (b) mode amplitude of the distortion of Γ_{2-} and K_3 modes. (c) magnitude of the tile of the Mn-O_{ap} bond to z-axis [51], (d) displacement of the Lu ions in the unit cell, (e) and (f) are calculated tilt angles of the MnO_5 bipyramids [35,223].

To figure out better the reason behind the sudden jump of the K_3 mode amplitude for x=1.12 in Figure 7-12.b, if not just due to limit of error of the method, the change of O_1 and O_3 orbits for the Γ_2-and K_3 modes of both sets of samples are shown in Figure 7-13. As given by the values in Table E-3, the O_1 orbit in K_3 mode undergoes displacement in x, y coordinates whereas the displacement for O_3 orbit is along c-axis. Oxygen atomic position refinement may be accompanied by some inaccuracy in XRD Rietveld refinement. Orbits of O_1 and O_3 of K_3 mode in Figure 7-13.a and b indicate almost identical trends for both sets of samples. Linked to Lu displacement in Figure 7-12.d, Figure 7-13.b shows that both O_3 (planar oxygen) and Lu ions have the same shifts independent of the time of annealing. At limits of the range of x values the O_3 exhibits more accentuated change for both sets of samples; it is also the case for O_1 orbit (apical oxygen). The jump in K_3 mode amplitude for x=1.12 in Figure 7-12.b could be originated from oxygen displacements.

The Γ_{2-} mode of 5 days annealed samples in Figure 7-12.a shows a straight line for x in the range of 0.96 to 1.04, with deviation from straight line for x out of this range. Increased annealing time shows lesser fluctuation of the Γ_{2-} mode amplitude, with a minimum at stoichiometric composition. The evaluation of the mode amplitude for the O_1 and O_3 orbits of Γ_{2-} mode in Figure 7-13.c and d which undergo displacement along c-axis presents the almost identical trends for both annealing conditions. It is coherent with the fact that these two orbits of oxygen are not so significant for the amplitude of the ferroelectric mode.

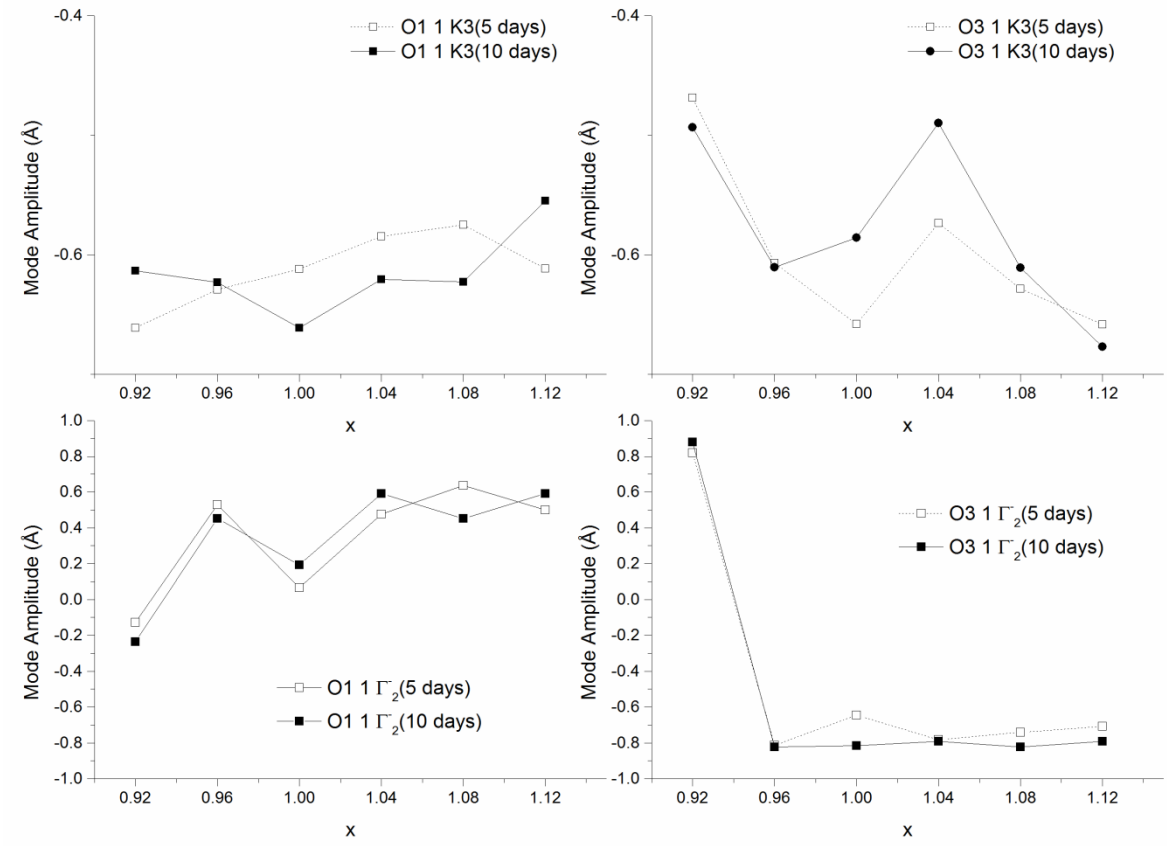

Figure 7-13. Behaviour of apical (O1) and planar (O3) oxygen of Γ_2- and K_3 modes versus selected compositions.

7-3-2 Ionic polarization of the off-stoichiometric unit cells

The results of the XRD Rietveld refinement are used to assess here the change of ionic polarization of $LuMn_xO_{3\pm\delta}$ with composition x and time of annealing. The ionic polarization, P_{ionic}, is calculated from the lattice parameters and atomic positions of all ions according to following equation of simple ionic model [106]:

$$P_{ionic} = \sum_i \frac{\Delta c_i Q_i m_i}{V} \qquad (7\text{-}1)$$

where V is the unit cell volume, Δc is the atomic displacement of each ion in relation to the PE phase, Q is charge in Coulomb (C, point charge model), and m is the multiplicity of the Wyckoff position of each ion, the index i running over all seven inequivalent ions of the unit cell as given in Table 2-2. Figure 7-14 compares the calculated ionic polarization P(μC/cm^2) for samples of both annealing conditions, 5 days and 10 days annealed.

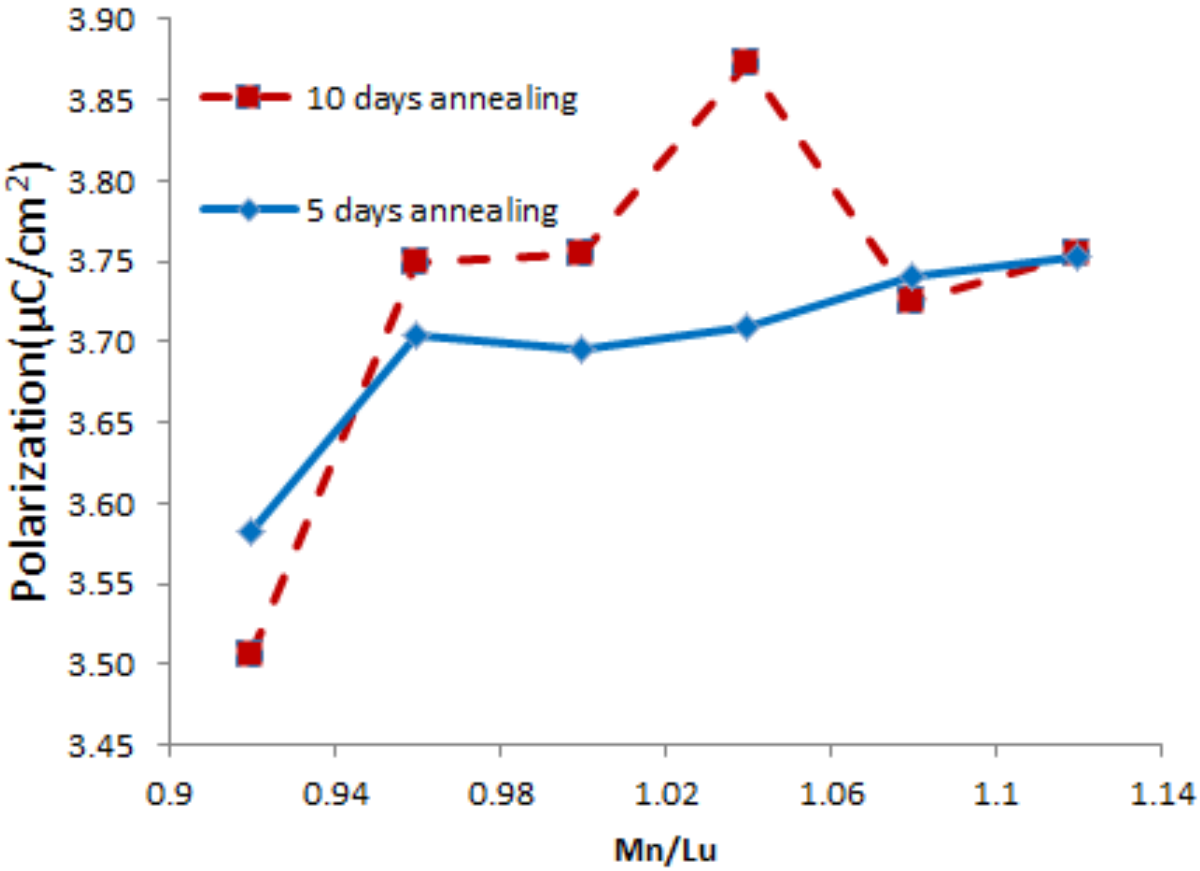

Figure 7-14.Ionic polarization of two sets of annealed samples, 5 days and 10 days, showing the effect of vacancy doping out of stoichiometric.

There is an apparent similarity in the dependence of P on x in Figure 7-14 and reported trends of the Lu displacement and of O_{ap} tilt angle in Figure 7-12.d and f, respectively. Vacancy doped samples in Figure 7-14 display a nearly flat plateau around the stoichiometric composition that evolves to a gentle slope towards high x values. But,

there is a remarkable deviation from such flat on the Lu-rich side for x≤0.96, perhaps revealing pronounced effect on ionic polarization, P, of the presence of high concentration of Mn vacancies at the low stability limit of the $LuMn_xO_{3\pm\delta}$ solid solution balanced by the creation of oxygen vacancies according to the simplified equation of effective charge neutrality, $2[V_O^{\cdot\cdot}] = 3[V_{Mn}^{'''}]$. The ionic polarization of $YMnO_3$ at room temperature calculated with the equation (7-1) given above is 4.2 μC/cm² [106]. The range of values of ionic polarization P of $LuMn_xO_{3\pm\delta}$ in Figure 7-14 are slightly lower but still close to the corresponding value of ionic polarization reported for $YMnO_3$. The value of total polarization $YMnO_3$ including both ionic and electronic components from DFT calculations is 5.5 μC/cm² [127]. The DFT result of polarization for $LuMnO_3$ when K_3 mode is in its maximum distortion (in fractional units, 1) was calculated to be around 8 μC/cm² [130], a slight higher value (P ≈ 10 μC/cm²) for $ErMnO_3$ having been determined by H. Das [10] in DFT calculations of the K_3 mode when it is in its maximum of distortion and the energy of the non-collinear magnetic state is at its minimum value.

7-3-3 Polarization from first principles calculations

The Berry Phase approach implemented in Wien2K code is used here to calculate both the ionic and electronic polarization of the ions in the unit cell and the total electrical polarization for three different values of composition, x [224]. Following the calculation of orbital re-hybridization, and in EELS spectroscopy done to evaluate the partial density of states of the ions in the unit cell in stoichiometric and off-stoichiometric samples, sections 6-4-1 and 7-2-5, the same calculated results were used to proceed with the Berry Phase approach in Wien2K code. In these calculations, the A-type AFM model [127] is used for Mn ions in the unit cell, and LDA+U with 6 eV for U potential was used to introduce the band gap. The result of the calculations for z-direction for selected 10 days annealed samples are given in Table 7-1, the values of mode amplitude K_3 in this table being the same as the ones plotted in Figure 7-12.b. The components of

polarization in other two directions in the basal plane are ignored in the present study as they are few orders of magnitude smaller than the polarization along c-axis [130].

Table 7-1. Berry Phase calculations of the three samples in stoichiometric and x=0.92 and x=1.08

x	K_3	Electronic polarization ($\mu C/cm^2$)	Ionic polarization ($\mu C/cm^2$)	Tot. Polarization($\mu C/cm^2$)
0.92	1.065	5.692	2.270	7.963
1.00	1.12	2.270	-5.071	-2.801
1.08	1.074	-3.662	-4.230	-7.892

The calculated results of Table 7-1 plotted and Figure 7-15 clearly show that the electronic polarization and hence the total electrical polarization too become larger in modulus when composition of the samples deviates from the stoichiometric x=1 value. On the contrary, the component of the ionic polarization at x=1.00 has larger modulus than for the composition on the two extremes of the studied range. The trend lines best-fitted to results in Figure 7-15 also suggest that the component of the ionic polarization P_i changed signal in the Lu-rich side and might have become very low at an intermediate nominal composition close to x≈0.95 while the component of the electronic polarization P_e which has a large positive value at x=0.92 remains positive at the stoichiometric composition x=1.00 and might have reversed its signal well inside the Mn-rich side of the solid solution at point of nominal composition close to x≈1.04. Since values of polarization with negative or positive signs denote measurable polarization in the direction along c-axis the change of signal of the total polarization P_t and crossing a null value at a composition slightly below stoichiometry (x≈0.99) may turn pertinent when comparing experimental studies of electrical polarization of the hexagonal $RMnO_3$ materials of nominal stoichiometric composition from different sources. At a first glance, these calculations in Table 7-1 would imply that the distortion on the lattice due to self-doping creating large concentration of vacancies can change ferroelectricity in the unit cell on both sides of the stoichiometric composition of the $LuMn_xO_{3\pm\delta}$ solid solution.

Results of calculated polarizations for off-stoichiometric sides of Lu or Mn vacancy doped samples in Table 7-1 and Figure 7-15 give values of total polarization of the order of magnitude of the values reported for the $LuMnO_3$ and $YMnO_3$ from DFT calculations [10,130]. Amplitude of Γ_{2-} mode of samples after 10 days annealing in Figure 7-12.a revealed a small decrease of mode amplitude at stoichiometric composition from x=1. The same scenario is present here in Figure 7-15 for the absolute values, or modulus of the component of electronic polarization and the modulus of total polarization, $|P_t|$, also seen in figure 3 of reference [10]. One may conclude that off-stoichiometry works on increasing the degree of distortion of the $LuMn_xO_{3\pm\delta}$ lattice in comparison to stoichiometric composition. Therefore, distortion in the unit cell driven by Lu or Mn vacancy doping would be a way to tune the polarization of the crystalline lattices of h-$RMnO_3$ materials.

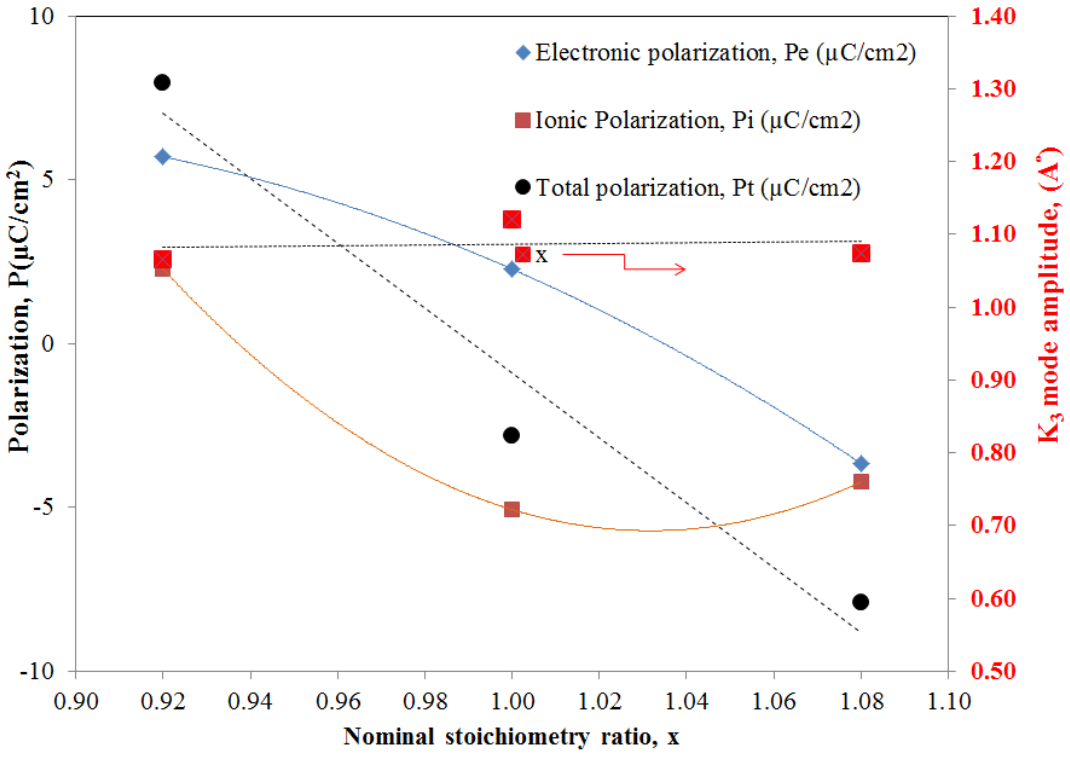

Figure 7-15. Berry phase polarization calculations for three selected samples x=0.92, 1.00 and 1.08 from sets of sample being annealed for 10 days vs. both K_3 mode amplitude (x-axis) and x-value for Mn/Lu ratio (right vertical axis).

The change of ionic polarization in Figure 7-15 with the maximum value at x=1.00, is in good agreement with ionic polarization in Figure 7-14 calculated with the simple ionic model from XRD Rietveld refinement. Both methods of calculation of P_i converge to the same trend and present maximum values of $|P_i|$ at stoichiometry of similar values: 5.1 μC/cm^2 for DFT calculations in Table 7-1 and 3.8 μC/cm^2 from simple ionic model of P_i in Figure 7-14. One should mention that in the calculations of the ionic polarization with the simple ionic model in Figure 7-14, the charge of each ion is considered as if the ion is in an isolated environment, meaning that the effective charge of each ion is 3+ for Mn and Lu ions and 2- for the O ions, regardless the lattice distortions or change in bond lengths.

7-3-4 Total changes of modes from DFT approach

In previous section 7-3-1 the amplitude of distortions for Γ_{2^-} and K_3 modes were characterized. The atomic positions of the displaced atoms from their PE Wyckoff positons in the unit cell determined with the Amplitude software and the corresponding unit cell of each of the modes are used calculate total energy of each mode for the given sample compositions. One aims he to gain some insight into the stability of samples of different composition.

The total energy per chemical formula calculated for each mode is shown in Figure 7-16.a for 10 day annealed samples. The same conditions as used in previous spin-polarized calculations in section 7-2-5 were adopted: A-type AFM configuration of Mn^{3+} moments, 6 eV energy for the U potential and LDA+U approach for 3d orbitals of Mn^{3+} ions, criteria for energy and charge convergence set as 0.00005 Ry and 0.0001 e, respectively. The PBE-GGA potential was used in calculations. The ranges of total energy calculated for K_3 and Γ_{2^-} modes have rather different magnitude, the values of total energy of the Γ_{2^-} being around 1/3 of the total energy of the K_3 mode. The energy values

for compositions on both sides of stoichiometry exhibits quite different trends, the Mn-rich side generally presenting more fluctuation in their energy values. The two sets of total energy on the Mn-rich side have the lower negative values close to x=1.08. The total energy does not show relevant difference of trends for both modes although Γ_{2-} mode includes the Mn displacement along c-axis and the K_3 mode does not. It conveys the idea that Mn ion positions and apical oxygen positions do not play significant role on the total energy. Compared to the calculated energy of the unit cells of 10 days annealed samples at room temperature in Figure 4-11.a, it implies that the general trend of Lu and Mn vacancy doped samples closely follows the trend of K_3 mode in Figure 7-16.a. Although the change in energy of both sides of stoichiometric composition is not the same, it may emphasize again that atomic displacement in Γ_{2-} mode along c-axis play significant role on stable structure of h-$RMnO_3$ lattices at room temperature. It is because the Γ_{2-} mode establishes before K_3 mode [106,219] that the results of the energy calculation both follow the same direction of change.

The corresponding results for the calculated magnetic moments of Mn^{3+} ions for the two modes are plotted in Figure 7-16.b. They follow almost the same trend for both calculated modes and sides of sample composition. In addition, calculated magnetic moments of room temperature unit cells of 10 days annealed samples in Figure 5-18 showed almost the same trend as seen in Figure 7-16.b. The values of magnetic moments in Figure 7-16.b would imply that K_3 would yield slightly higher magnetic moment than the Γ_{2-} mode, but seems that the displacements of the Mn ions in two modes cannot be critical to the calculated magnetic moments. However, off-stoichiometry in h-$LuMnO_3$ ceramics would result in change of AFM interactions in basal plane compared to the stoichiometric composition, first principle calculations in Figure 7-16.b showing the effect of off-stoichiometric on tuning the magnetic interactions of the magnetic ions in hexagonal $LuMnO_3$ material.

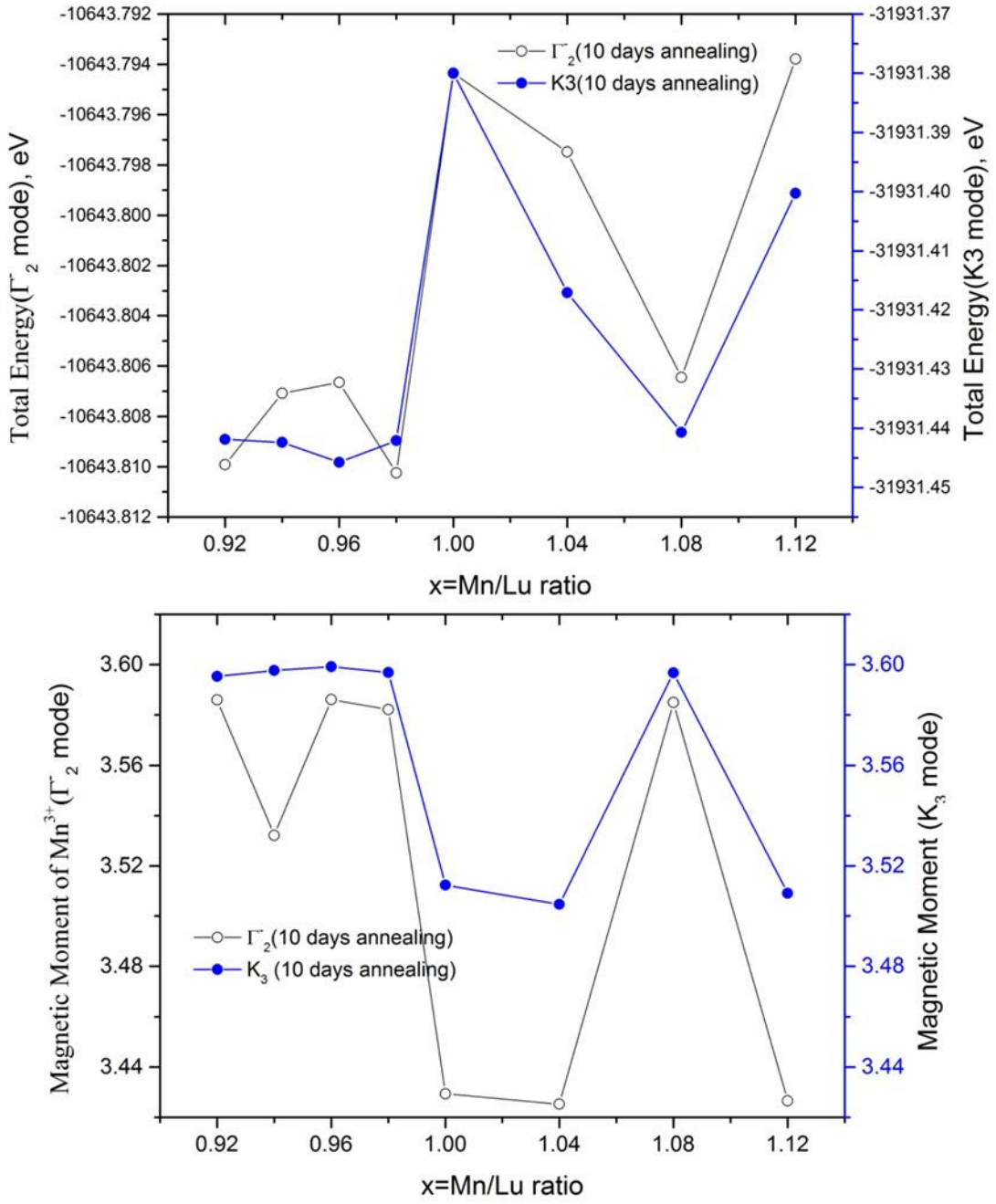

Figure 7-16. (a) Total energy of Γ_2- and K_3 modes calculated via DFT approach showing different behaviour on Lu-rich side whereas the Mn-rich side gives more fluctuation on the values. (b) Calculated magnetic moments of the Mn^{3+} ions in A-type AFM configuration for two different modes off-stoichiometric compositions.

It is also implicit in the calculated results in Figure 7-16.b that distortion of the unit cell as a whole like the bucking of MnO_5 bipyramids and displacement of Lu ions along c-axis played a more crucial role on final magnetic interactions of the Mn^{3+} ions in basal plane than the positioning of these ions in two different modes with different Wyckoff positions and displacements. Although Γ_{2-} mode is present well-above T_N, the present calculations may point towards the role of distortion in unit cell again in altering the magnetic moments with vacancy doping, rather than of simply modifying crystalline cell dimensions as determined by change lattice parameters. However, in all DFT calculations one just dealt with crystalline unit cells of the materials and assumed no internal interfaces or domain walls. Yet, both types of 2-dimensional crystal defects can result in significant changes of the multiferroic properties of the hexagonal $RMnO_3$ materials [10,16,48,79].

8. Conclusion and future work

The research completed during the PhD work combined both experimental and theoretical approaches to achieve the first comprehensive study on solid stability limit and non-stoichiometric effect on crystalline structure and multiferroic properties of the h-$LuMn_xO_{3\pm\delta}$ manganite ceramics.

XRD analysis with Rietveld refinement of lattice parameters of $LuMn_xO_{3\pm\delta}$ solid solution revealed shrinkage of both a-axis constant and of c-axis, this axis in lesser degree, and hence of the unit cell volume as the value of Mn/Lu ratio x increases. Lattice parameters still exhibit changes when the time of annealing increases from one day to five days and latter to ten days of isothermal annealing at 1300 °C. Having fluctuation of results in one day annealed samples, lattice constants and unit cell volume of five days annealing time already mark an upper limit of solid stability on the Mn-excess side at $x_H \approx 1.04$. Extending annealing time to 10 days sets the lower side of solid stability limit to $x_L \approx 0.94$. Values of c-axis constant always present more fluctuations in comparison to the a-axis constant.

The observed trend for faster grain growth in the microstructure of sintered samples with increasing values of x leads to grain sizes in samples with Mn excess that can even exceed 10 micron or even larger sizes after longer annealing time. Increasing the time of annealing from 24 hours to 240 hours at 1300 °C results in a monotonic increase of grain size of the h-$LuMn_xO_{3\pm\delta}$ ceramics given by an approximately parabolic dependence on time. The observed changes of the corresponding grain growth constant with x are consistent with the limits of stability of the h-$LuMn_xO_{3\pm\delta}$ solid solution established in XRD study. The anisotropy of the coefficient of thermal expansion of the hexagonal $LuMn_xO_{3\pm\delta}$ phase coupled to grain growth induces the appearance of micro-cracks in the

microstructure more frequently seen in the grain boundaries than as cleavage flaws inside the grains.

The secondary phase Lu_2O_3 can be detected in x<1.00 side in minor amounts which depend on sample composition x and annealing time. This secondary phase remains detectable in x=0.92 samples after 5 days and 10 days annealing in an amount approximately constant of 1.3% in weight fraction. For samples of Mn excess, x>1.00, traces of unreacted Mn_3O_4 are detected as a faint (103) peak in XRD spectra, particles of this impurity being clearly visible in SEM and TEM images. After 5 days or 10 days of annealing time, the presence of this secondary phase can be clearly seen in measurements of magnetization below 43 K and the change in magnetization being assigned to very small particles or planes of hausmannite left as atomic clusters or intergrowths in the particles of the main phase.

Once sample composition reached the extremes of the stability range of the h-$LuMn_xO_{3\pm\delta}$ phase in this study, the atomic structure of the lattices indicated disordering across the crystalline grains in a nano-scale, most probably driven by chemical gradients. The presence of nanodomains inside the crystalline particles produces internal interfaces, a characteristic of all samples. Basal plane images in [001] zone axis of the Mn trimers and Lu hexagons present distortions of the bipyramids inside nanodomains across the particles. Lattice images of h-$LuMn_xO_{3\pm\delta}$ ceramics along [110] zone axis show the displacement of the Lu ions which gives rise to ferroelectric domains. Image simulation done in this study and developed methods of interpretation of the lattice images taken along (110) or (100) orientations help in resolving the type of FE domains and type of domain walls found inside the crystalline grains of h-$LuMn_xO_{3\pm\delta}$. Probe corrected STEM microscopy clarified that presence of defects like stacking faults would result in locally distorted lattices, where missing of some atomic planes of a cation, and switching of the ferroelectric polarization direction can occur. Our extensive dark field studies of the nominal and off-stoichiometric compositions confirm presence of the extended line defects to few hundreds of nano-meters in most particles. Lattice images around defects

particularly seen along [110] zone axis confirm the interplay of the defects and Lu ions displacement resulting in phase shift of the FE domains or even switching the polarization direction upon entering the perturbed field around defects.

Confirming the geometrically magnetic frustrated structure of these materials, magnetic properties of self-doped h-$LuMn_xO_{3\pm\delta}$ manganite display the antiferromagnetic ordering AFM transition in all studied samples with Néel temperature T_N in the range 89-93 K, decreasing as x increases. Magnetic irreversible behaviour (ZFC-FC difference) appears in measurements of magnetization for all samples below T_N, being correlated with Mn/Lu ratio x of h-$LuMn_xO_{3\pm\delta}$ solid solution in the temperature range between Curie temperature of Mn_3O_4 $T_C \approx 43$ K and T_N of $LuMnO_3$ and to the residual fraction of Mn_3O_4 for T below 43 K. After subtraction of the magnetic signal of secondary phase from temperature dependant magnetization, calculated Curie-Weiss temperature of all samples present correlation to sample composition and annealing time. From the extreme of high x to the extreme of low x in all samples, Curie-Weiss temperature (TCW) becomes larger, -300 K average change of high x to low x sides was obtained. The frustration factor ($|T_{CW}|/T_N$) was calculated, and stays within the reported range of 6 (high x) and 9 (low x) for h-$RMnO_3$ materials of 5 and 10 days annealing.

Field dependent magnetization loops display magnetic hysteresis below Neel ordering transition which become wider along the magnetic field and magnetization axes at lower temperatures when the magnetic moment of the secondary phase Mn_3O_4 also contributes to total magnetic signal. Above 43 K the limit of temperature for ferrimagnetic ordering transition of Mn_3O_4, the observed coercive field and magnetic remanence both increase in their values with increasing of the x ratio. The magnetic exchange bias has been observed in the magnetic hysteresis loops of the h-$LuMn_xO_{3\pm\delta}$ ceramics even for samples with $x \leq 1.00$. Supported by the microscopy images of the secondary phase and internal interfaces, one can hypothetically admit that the additional magnetic component right below T_N may have the origin in magnetic distortion at internal interfaces of the nano-structural domains. Also, shifts in chemical composition

across a crystalline grain would provoke changes in the magnetic features just in parts of its volume when one would expect the magnetic behaviour of either the R-site or Mn-site vacancy doped composition. Using local electron probe of EELS in TEM to look for different oxidation states of Mn ions, no clear deviation from 3+ valence of the Mn ions could be found inside the crystalline grains on both sides of the stoichiometry range of sample composition.

Magneto-electric coupling was characterized in selected samples of self-doped h-$LuMn_xO_{3\pm\delta}$ ceramics by measuring the frequency and temperature dependent complex dielectric constant. The clear change in the complex dielectric constant was observed for all tested samples at T_N. Combined with measurements of magnetization, these measurements confirm the presence of athermal magneto-electric coupling in off-stoichiometric ceramics as well as in stoichiometric h-$LuMnO_3$ at T_N. A second athermal transition in the dielectric constant was observed at temperatures around 69 K. At low temperatures below 35 K an additional thermally activated transition in the dielectric constant was observed which closely matches the anomalies of transitions displayed in parallel by magnetization. The activation energy of this transition was calculated in the range of 10 meV to 20 meV in the range of values of activation energy of the polaron hopping mechanism reported in the bibliography for several dielectrics in the this temperature range. The presence of nano-structural domains and their interfaces frequently observed in TEM images might be associated with the observed anomalies in magnetic and dielectric susceptibility below T_N.

Images of piezo-force microscopy (PFM) of ferroelectric domains display enlargement of their dimensional scales linked to grain size which increases with time of annealing and the value of Mn/Lu cation ratio x. The vortex/anti-vortex patterns captured in PFM images of samples of long annealing time reveal the total size of cloverleaf pattern up to 20 microns, comparable to the size of the same patterns in single crystals of h-$RMnO_3$ materials. Observable in PFM images, the effect of the grain boundaries and internal interfaces on FE domain formation was explored in these ceramics samples, giving rise

to sub-micron FE domain inside large scale, few microns FE domains. Linked to our TEM observation Lu displacement in the lattices in sub-micron ranges, both TEM and PFM images unravel the role of interfaces or chemical inhomogeneities inside a particle on growing FE domains. The large sizes of the FE domains and vortex/anti-vortex patterns in sintered ceramics of current study confirms further understanding of the dependency of FE domain size and density on heating process and cooling rate.

In the DFT modelling study of the present thesis the hypothesis of orbital re-hybridization of Lu ($5dz^2$)-($2p_z$) O_{pl} bonds did not exactly explain the experimental results either in PFM images or of the calculated polarization based on crystal structure data. The EELS spectra of oxygen K-edge in stoichiometric and off-stoichiometric samples showed the appearance of the oxygen pre-peak besides of peaks assignable to oxygen K-edge. Although the EELS resolution in absence of an energy monochromator in TEM is lower than in EXAFS or in Cs-corrected TEM/STEM, using available EXAFS data and preforming density functional calculations in this study one did find out that the pre-peak of oxygen edge effectively corresponds to Mn (3d)-(2p)O bonding. More patent in the pre-edge of oxygen, the EELS study suggests that the orbital arrangements of the Mn-O and Lu-O bonds are sensitive to local change in the lattice as seen in the intensity of the corresponding peaks of EELS spectra. Local sensitivity of the atomic bindings restrain the hypothesis of the orbital hybridization driven ferroelectricity to nano-scale regions, explain its weakness on giving a thorough picture of ferroelectricity from DFT calculations of the unit cells without counting the lattice defects. The calculated polarization from DFT shows the effect of non-stoichiometry on the change of electrical polarization and suggests that vacancy doping will enhance electrical polarization of the h-$RMnO_3$ ceramics for both sites of cation vacancies.

Using data of unit cells of self-doped h-$LuMn_xO_{3\pm\delta}$ ceramics extracted from XRD Rietveld refinement the total energy, band gap and magnetic moments of Mn^{3+} ions were calculated via DFT implemented in Wien2K code. Symmetry mode analysis also guided this study in getting detailed information of K_3 and Γ_{2-} modes upon PE phase transition

and gave the possibility to conduct DFT calculations for the unit cells of each mode. Both sets of calculations assume only unit cell changes induced by vacancy doping and leaded to the conclusion that tilting of MnO_5 polyhedron and buckling of Lu planes would be of greater importance on the calculated properties than displacement of the specific ions like Mn or changes in dimensions of lattice parameters.

Unsolved issues and future work:

The role of oxygen vacancies in the lattices of the off-stoichiometric h-$RMnO_3$ multiferroics could not be appropriately ascertained within the limits of this research. The indication of experimental results that Mn ion retains the valence state of $Mn3^+$ in self-doped h-$LuMn_xO_{3\pm\delta}$ when $x\neq1.00$ points to the presence of positively charged $V_O^{\bullet\bullet}$ oxygen vacancies compensating the effectively negative charge of either $V_{Mn}^{'''}$ or $V_{Lu}^{'''}$ vacancies in the electric charge neutrality condition of point defects in the defect chemistry of the crystals. Applying diffraction techniques did not show indication of oxygen vacancies in large, discernible scale. However, due to the low amount of vacancy doping allowed by narrow stability limits of the $LuMn_xO_{3\pm\delta}$ solid solution in equilibrium with the point defects, one might expect that oxygen vacancies if not exactly randomly distributed at room temperature must be organized very local and in low concentration which demands precise local probes of electrons which are not yet available in the electron microscopy laboratory that supported this research.

Observation of new vortex/anti-vortex patterns in $Y_xLu_{1-x}MnO_3$ is a strong motivation for the study of co-doped R-site materials and self-doped hexagonal manganites to disclose the effect of shifts in chemical composition on topological defects. Literature reviewing of doped lattices of h-$RMnO_3$ family has shown that doping of R-site via two or three different rare-earth ions as already done for $Y_xLu_{1-x}MnO_3$ may offer new insights into the changes of lattice constants and magnetic or ferroelectric properties. It would be worthy if research around vacancy-doped lattices can be extended to other systems of the same

family especially $YMnO_3$ and $ScMnO_3$ oxides, to have a more complete set of vacancy modified lattice parameters. The change in ionic radii of Lu, Y and Sc and also the different T_N values would be interesting matter of further research to get deeper insight on the role of ionic radii of rare-earth ions in changing multiferroic properties when associated to vacancies in the lattice.

Although it is viable to study temperature dependant lattices of off-stoichiometric crystals of the h-$RMn_xO_{3\pm\delta}$ solid solutions using XRD as done here, the lacking of sensitivity of the XRD technique to oxygen occupancy and positions would demand refining the analysis with neutron diffraction. In such continuation of this research neutron diffraction must include scanning the range of temperature from near zero Kelvin to T_N and then to room temperature, in order to investigate the magneto-elastic coupling at T_N, effective magnetic moment of Mn^{3+} ions and probable spin reorientation below T_N. High temperature phase transition is another matter to be investigate by diffraction techniques because any effort to enhance ferroelectricity of these materials is entangled to higher temperature phases.

It is our project to perform further studies with self-doped $LuMn_xO_{3\pm\delta}$ ceramics in order to investigate with the means of probe corrected STEM microscopy the local shifts in electronic structure and Mn oxidation states on the domain walls where symmetry breaking induces new physical relationships and modified chemical environments for the elements. Combined to First-principles modelling of such interfaces, the objective of the extension of the work would be the effect of non-negligible concentrations of Mn or Lu vacancies on these interfaces, crystal field and oxidation state of the Mn ions within the scale of few unit cells the width of interfaces.

Extending this research on self-doping of h-$RMnO_3$ multiferroics to other families of hexagonal rare-earth oxides like $RFeO_3$ will be useful for their potential applications as they have magnetic ordering transitions at higher temperatures than h-$RMnO_3$ family. The research on $RFeO_3$ oxides is progressing fast. Our methodology on studying

concerned multiferroic properties in current PhD thesis would be of use in similar studies.

Annexes

A. Low temperature XRD of sample $LuMn_{0.98}O_{3\pm\delta}$

Magneto-electric coupling and magneto-elastic coupling both entail changes in magnetic, dielectric and lattice properties once the h-$RMnO_3$ oxide crosses T_N [30,37]. Investigation of the lattice parameters upon cooling the sample under study to T_N and below would provide information on the possible different degrees of change of the unit cell when vacancies are introduced by self-doping. Results in this annex are from the only sample tested in a trial test as by the time this only experiment was done the intended more systematic experiments of low temperature XRD had to be stopped due to damage on the X-Ray tube of the diffractometer.

Figure A-1 shows the unit cell parameters from Rietveld refinement of the XRD patterns of x=0.98 sample measured at 89 K, 95 K, 200 K and 300 K, the first temperature coinciding with T_N. Although the number of points is sparse, the a-axis, c-axis and cell volume display the general trend of change of lattice parameters with temperature as found in results of e.g. Lee et al [37]. The a-axis and cell volume expand as temperature rises, whereas the c-axis presents shrinkage in the low temperature range from T_N to approximately 200 K and expands at higher temperatures.

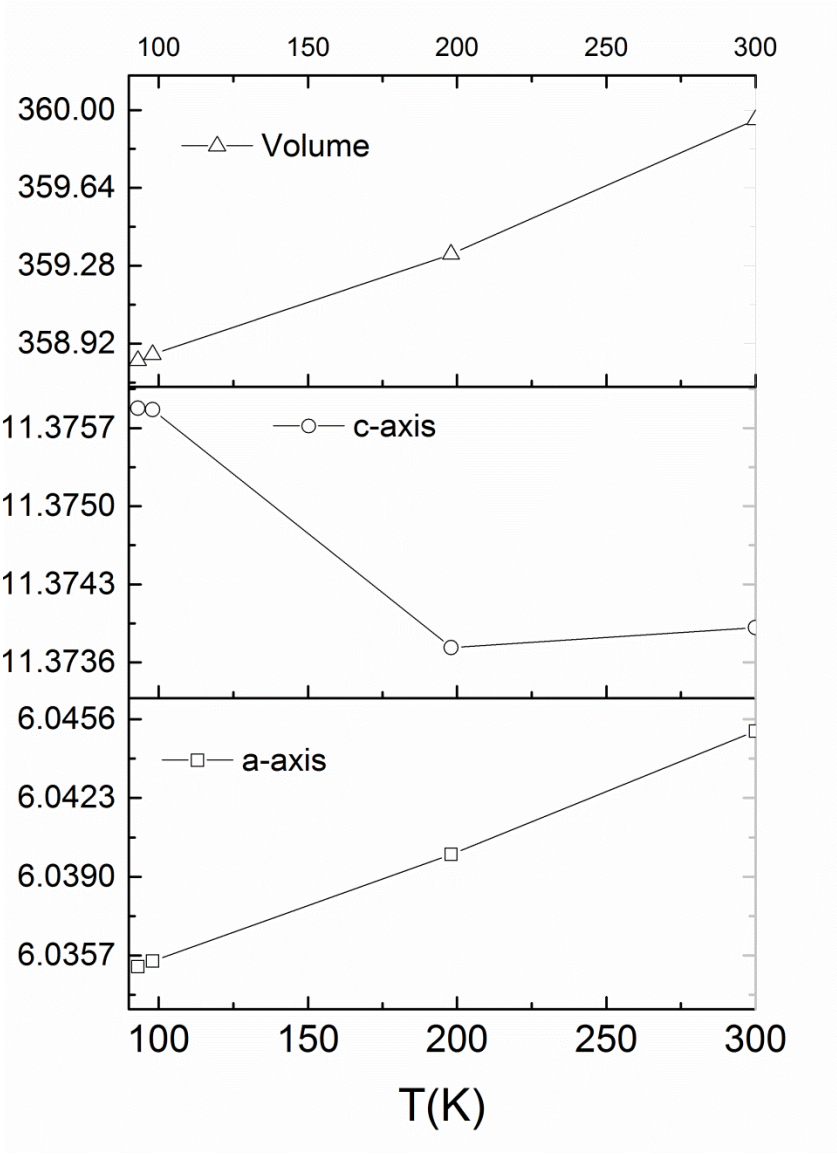

Figure A-1. Lattice parameters of the $LuMn_{0.98}O_{3\pm\delta}$ after one day annealing as a function of temperature.

B. EBSD analysis of an inclusion of hausmannite

Main results of EBSD analysis of the samples of this study were presented in chapter 4. In this annex a feature of the microstructure of sample of x=1.08 after one day annealing in a thin section prepared for TEM analysis is characterized by EBSD. Particles of the secondary phases Lu_2O_3 and Mn_3O_4 were found close together separated by a few grains of the main phase. The Lu_2O_3 inclusions are single crystalline grains of small size, around 1 to 2 μm. The hausmannite inclusion is of much wider size, roughly 7 μm and consists of several crystalline grains. In some areas of the EBSD phase and orientation maps the quality of phase matching is poor (larger density of zero-solutions associated mostly to roughness and damage of the surface). At the border of the hausmannite inclusion near the contact with the surrounding matrix of the main phase in Figure B-1 there is one of these areas with the dark contrast of zero-solutions. Besides the effect of relief which can hardly be seen there in Figure B-1.a, the local density of zero-solution might be an indication of the thick interface with the matrix or intermediary phase originated by changes in concentrations of Lu and Mn as was shown in Figure 4-18, and it cannot be identified with known phases in the phase diagram of Lu_2O_3-Mn_aO_b oxide system [109].

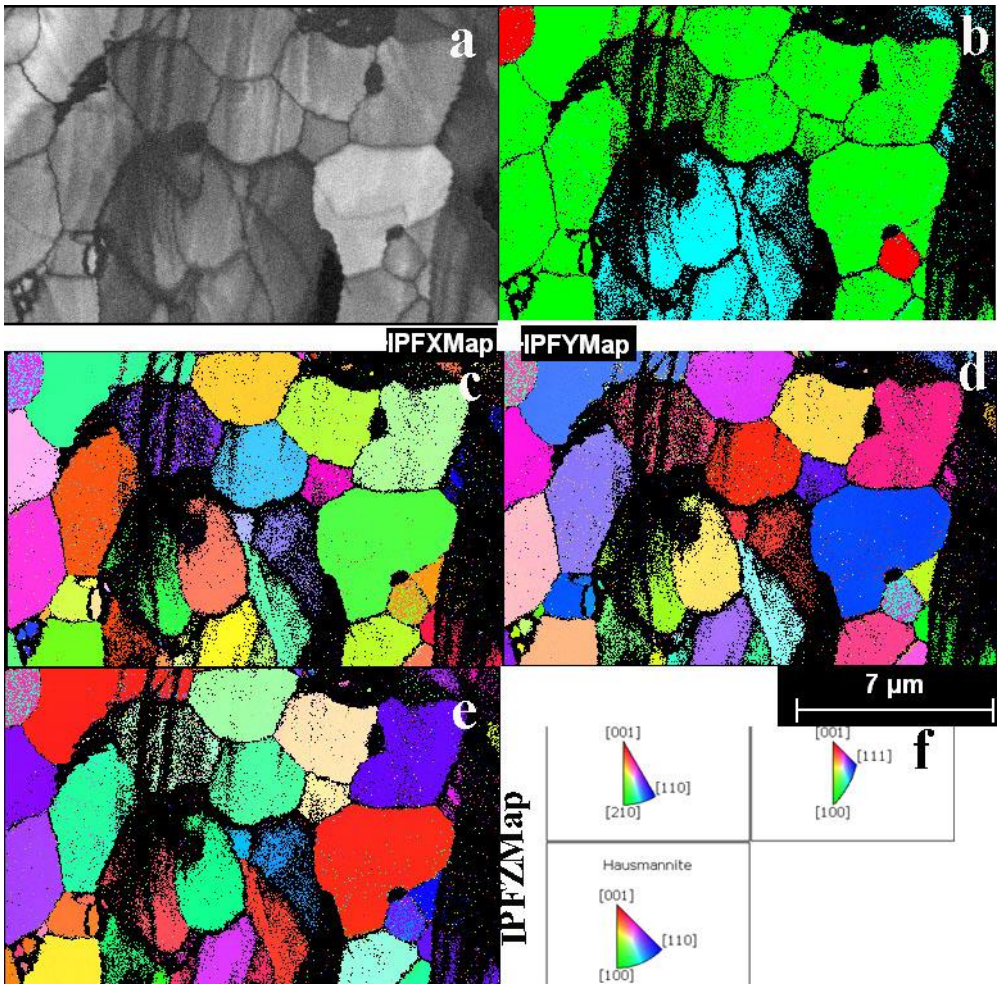

Figure B-1. EBSD analysis of the sample $LuMn_{1.08}O_{3\pm\delta}$, (a) pattern quality map, (b) phase map (red: Lu_2O_3, blue: Mn_3O_4 and green:$LuMnO_3$), (c) to e show different componenet of the Euler´s angles and (f) the color code of the orientaions.

C. Parameters of the magnetic susceptibility in the paramagnetic region

C-1 Background magnetization in temperature dependent magnetic measurements

Figure C-1 represents the zero field cooled (ZFC) magnetic moments as a function of temperature measured under 100 Oe applied field of all samples with one day annealing time. The enlarged scale of the magnetization axis allows better observation of the intensity of paramagnetic moment with the background of the different samples. For measuring magnetic properties of the powders, they were encapsulated in plastic vials, wrapped in Kapton foil and put inside a plastic straw. Figure C-1 gives in (a) the raw data of magnetic moments as measured and the same magnetization, after background subtraction using equation (C-1) in (b). The insverse of the magnetic susceptibility in the paramagnetic region above T_N would be expected to follow the Curie-Weiss law equation (C-1), and be linearly correlated to temperature. A shown later, this is not the case for most samples. In this section of Annex C one tries to evaluate the contribute of different sources for the deviation of $1/\chi$ from the linear Curie-Weiss law.

Since background can affect the offset of the linear Curie-Weiss law, as a first approach, background subtraction is tested and the effect of magnetic background will be given in tables C-1 to C-3 below.

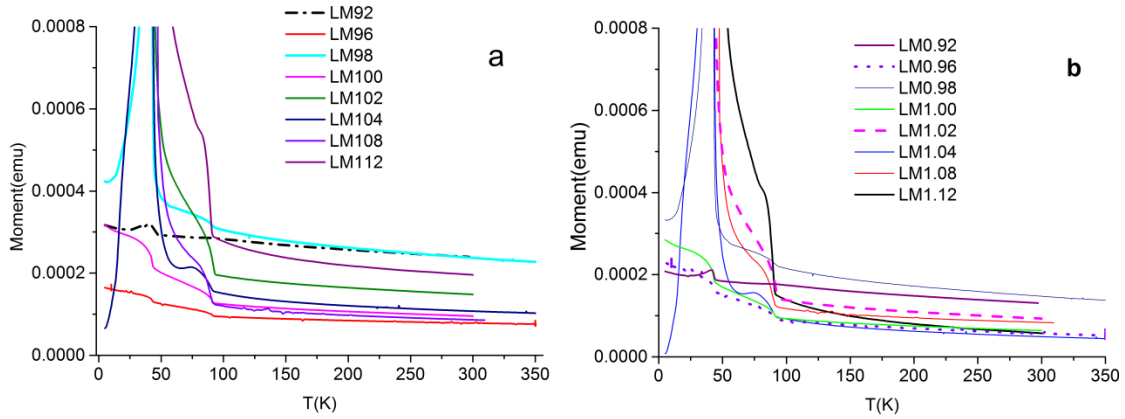

Figure C-1. ZFC magnetization under 100 Oe applied magnetic field of the samples of one day annealing time (a) magnetization (raw data) as measured for samples with different masses. (b) Magnetization of the same measurements and samples of (a) after subtracting background as is described in the text.

In this starting approach, a three parameters fitting function is used as given by equation (C-1) which is Curie-Weiss law with the additional term χ_0 which represents the background magnetization:

$$\chi\left(\frac{emu}{gr.Oe}\right) = \chi_0 + \frac{c}{T - T_{CW}} \qquad \text{(C-1)}$$

here, χ_0, C the Curie constant and T_{CW} the Curie-Weiss temperature are three adjustable parameters. Fitting is done with the least-square algorithm embedded in Origin Pro 9.0 package. Table C-1 and Figure C-2 summarize the results of the fitting taking this approach. It was found that the results of the fitting are very dependent on the range of temperature considered for the fitting. Accounting for extension to temperatures above T_N of any magnetic contribution which may change the linear behaviour of the Curie-Weiss law in paramagnetic region [34], the temperature range for the fittings was restricted to temperatures from 150 K to the upper end of temperature of the magnetization measurements, which means that the fitting is launched more than 50 K above the AFM transition temperature.

Table C-1. Fitting of three parameters Curie-Weiss like approach equation C-1 to the magnetic susceptibility of samples of one day annealing time. The subscript of zero (columns 3 to 5) denotes the initial values of the variables for starting of the least-square fitting, χ_0 in column 9 represents the magnetic background determined by the fitting

x	range	$T_{CW,0}$	$\chi_{0,initial}$	C_0	T_{CW}(K)	χ_0(emu/g.Oe)	C(emu.K/g.Oe)	R square
0.92	150-300 K	1.5	4.41E-05	0.0020	-563.5	2.1E-05	0.0243	0.99995
0.96	150-350 K	2.0	1.48E-05	0.0008	-336.5	1.0E-05	0.0048	0.99947
0.98	150-350 K	1.5	1.11E-05	0.0007	-445.9	4.5E-06	0.0067	0.99961
1	150-300 K	1.6	1.19E-05	0.0008	-442.5	4.0E-06	0.0077	0.99994
1.02	150-300 K	1.5	1.18E-05	0.0000	-489.9	4.0E-06	0.0080	0.99993
1.04	150-350 K	1.7	1.03E-05	0.0008	-202.7	6.8E-06	0.0031	0.99633
1.08	150-310 K	2.0	1.23E-05	0.0009	-334.4	5.5E-06	0.0063	0.99403
1.12	150-300 K	0.9	1.32E-05	0.0009	-60.1	1.2E-05	0.0015	0.99952

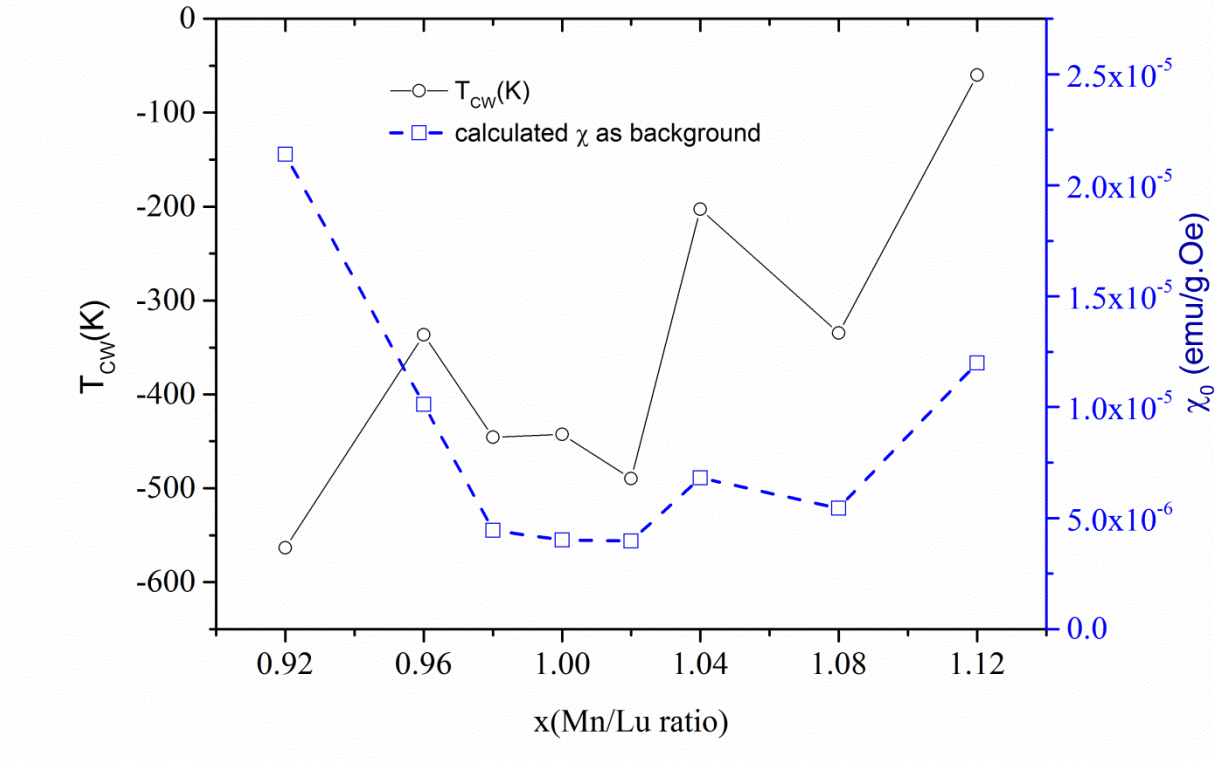

Figure C-2. Dependence of results of the T_{cw} and χ_0 (background) on sample composition after fitting using the equation C-1 in the temperature range from 150 K up to at least 300 K or above.

C-2 Background correction with fixed value for all samples

In this approach the value of χ_0 calculated for sample x=0.96, which does not show secondary phase of Mn_3O_4 in XRD pattern and has a low amount of the diamagnetic Lu_2O_3 secondary phase is used to fix the value of χ_0 constant $\chi_0 = 4.67947 \times 10^{-5} emu$ for all samples (we do this exercise on raw data of magnetic measurements). The fitting with two free parameters, C and T_{CW}, is refined (equation C-2), data are calculated and plotted in Figure C-3. The constant value for χ_0 is calculated from magnetic signal of x=0.96 as it shows linear behaviour of inverse susceptibility in the temperature range above 175 K. Therefore, to apply this constant value for other samples, we shifted the starting range of temperature for fitting to 175 K, the corresponding values of the calculated parameters being given on Table C-1 (note that here fitting was done on raw data with unit of emu).

$$\chi(emu) = \chi_0(4.67947 \times 10^{-5}) + \frac{C}{T - T_{CW}} \qquad \text{(C-2)}$$

Table C-2.Results of the 2 parameters fitting, considering constant background from sample x=0.96.

Mn/Lu	Range of Fitting	T_{CW} (K)	χ_0(emu)	C(emu.K)
0.92	175-300 K	-847.2	4.68E-05	0.220
0.96	175-350 K	-325.3	4.68E-05	0.020
0.98	175-350 K	-561.3	4.68E-05	0.164
1	175-300 K	-257.7	4.68E-05	0.027
1.02	175-300 K	-416.6	4.68E-05	0.073
1.04	175-350 K	-251.8	4.68E-05	0.033
1.08	175-310 K	-164.4	4.68E-05	0.018
1.12	175-300 K	-397.5	4.68E-05	0.103

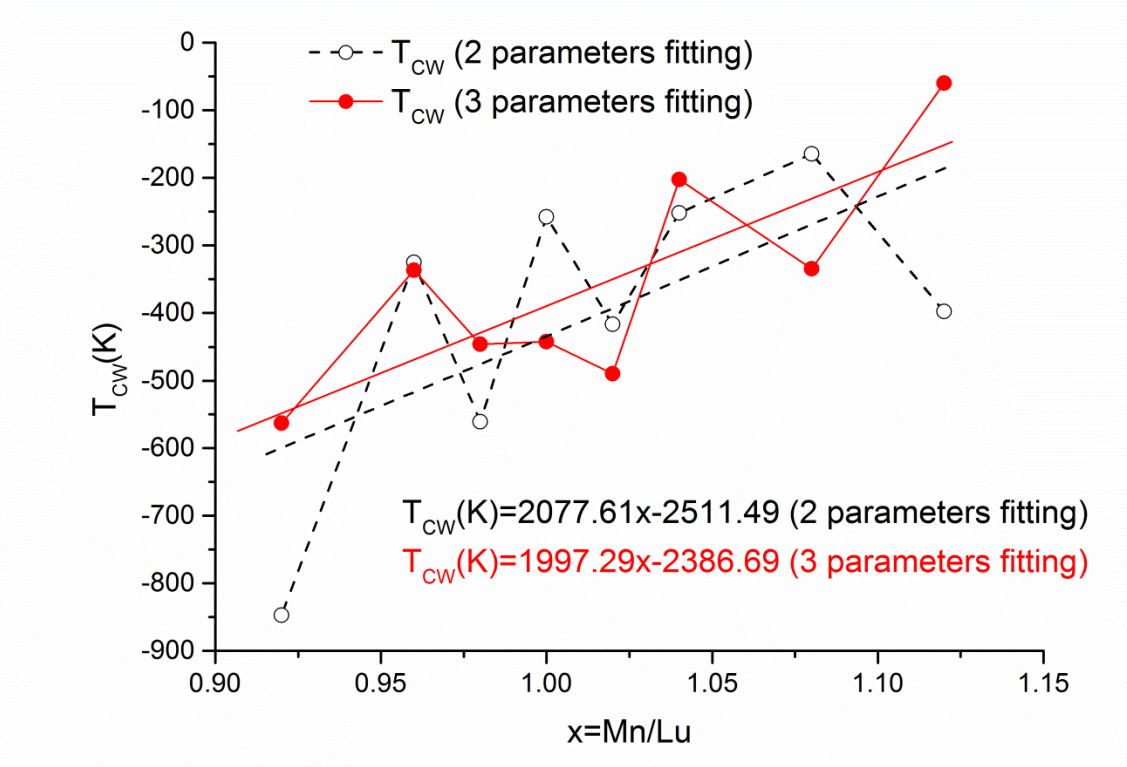

Figure C-3. Comparing the Curie-Weiss temperature T_{CW} obtained from fitting for two different approaches were used on Table C-1 and Table C-2. The linear fitting of the data in figure is shown for both sets of the data.

C-3 Estimation of the contribution of hausmannite secondary phase

Since the behaviour of ferrimagnetic hausmannite even above the its Curie temperature (around 43 K) in the paramagnetic region results in a non-linear term for the reverse of the magnetic susceptibility, the Curie-Weiss law of the magnetic susceptibility of samples with residuals of hausmannite is no longer valid, at least in range of temperature below 200 K [143]. To assess the trends of calculated values of Curie-Weiss temperature and effective magnetic moments of samples with hausmannite as a secondary phase, in a first trial simulated values of magnetic susceptibility in the paramagnetic region are generated with Curie-Weiss law of the magnetic susceptibility of a pure $LuMnO_3$ sample

(-880 K for T_{CW}) and combined with Lotgering function of the magnetic susceptibility of hausmanite (different values, Table 5-1), given in equation (5-3) of main text with zero background. Table C-3 gives three series of results for different approaches tested to retrieve back the parameters of equation. χ_0 is the magnetic signal from background. Since in equation (5-5) there are more than three parameters for fitting, the choice of initial values and parameters which should be relaxed or not in the fitting affects the output results. The analysis showed that if the background susceptibility χ_0 is left relaxed (as a variable of the fitting), there will be important divergence of the values of calculated parameters from those used in equation (5-3). Therefore, the results of data fitting in Table C-3 are reported with background susceptibility χ_0 values fixed and constant. Values of background magnetization χ_0 when different from zero were estimated by the initial guess of values from fitting. Then to continue the iteration, we chose the background variable to be fixed. The values of $(1\text{-}f_m)$ shown as 0.90 are due to the bound applied to restrict the amount of secondary phase between $0.00 < f_m < 0.10$, and when fitting diverges to values beyond this limit, it creates 0.90. Overall assessment of the results in Table C-3 may draw the conclusion that relaxing $(1\text{-}f_m)$ in these fittings can generate values which may not be realistic. As XRD would clearly show less than 5% in weight fraction of magnetic secondary phase, if such large amounts did not show up in XRD pattern, then the large amounts of secondary phase obtained in the sample would represent overestimation of the real value and divergence of the fitting algorithm.

Finally in the fitting method we came up with a solution where values of $(1\text{-}f_m)$ should be extracted from XRD analysis, as often done, and background susceptibility set at a constant value, normally 1% of the raw data of total susceptibility in the paramagnetic region. Without these of assumptions the fitting would give unrealistic values of the parameters of equation (5-5) definitively for samples with no indication of hausmannite in the XRD spectra. Table C-4 gives the results of fitting using equation (5-5) assuming 1% magnetic background (χ_0) and the amount of Mn_3O_4 secondary phase determined from XRD Rietveld refinement.

Table C-3. Lotgering function combined with Curie-Weiss law and constant magnetic background were used to calculate the Curie constant C and Curie-Weiss temperature T_{CW} as adjustable parameters in the fitting.

Mn/Lu	χ_0(emu/gr.oe)	T_{CW}(K)	C(emu.K/g.Oe)	1-f_m	Adj. R-Square	comment
sample name	***Fixed***	***Relaxed***	***Relaxed***	***Fixed***		
1.12	4.00E-06	-455.3	0.01095	0.95	0.99707	constant background, and fixed values for secondary phase.
1.08	0.00	-168.5	0.00375	0.97	0.99974	
1.04	6.09E-06	-254.7	0.00436	0.97	0.99985	
1.02	4.70E-06	-421.4	0.00739	0.99	0.99995	
1	7.24E-06	-252.6	0.00419	0.999	0.99951	
0.98	2.68E-06	-571.7	0.00953	0.998	0.99929	
0.96	1.05E-05	-312.2	0.00435	0.995	0.99953	
0.92	9.70E-06	-862.5	0.04644	0.999	0.9999	
	Fixed	***Relaxed***	***Relaxed***	***Relaxed***		
1.12	4.00E-06	-457.9	0.01142	0.9	0.99714	
1.08	9.00E-06	-170.2	0.00372	1	0.99975	
1.04	6.09E-06	-251.9	0.00449	0.9	0.99986	
1.02	4.70E-06	-420.9	0.00734	1	0.99995	
1	7.24E-06	-253.0	0.00417	1	0.99463	
0.98	2.68E-06	-585.6	0.01032	0.9	0.99933	
0.96	1.05E-05	-312.4	0.00435	1	0.99953	
0.92	9.70E-06	-861.7	0.04636	1	0.9999	
	Fixed	***Relaxed***	***Relaxed***	***Relaxed***		
1.12	0	-645.2	0.01842	0.9	0.9961	
1.08	0	-578.2	0.01604	0.9	0.9982	
1.04	0	-640.5	0.01408	0.9	0.9915	
1.02	0	-716.4	0.0163	0.9	0.99977	
1	0	-678.3	0.0156	0.9	0.99981	
0.98	0	-790.5	0.01596	0.9	0.9991	
0.96	0	-1067.3	0.02407	1	0.99591	
0.92	0	-1132.5	0.07825	0.9	0.99982	

Table C-5 and Table C-6 summarizes the calculated parameters of the fitting for selected samples with longer sintering time to be compared to the results of Table C-4 of one day annealing time. In this section of Annex C we have just shown the method taken to calculate parameters of the magnetic properties in the paramagnetic region. Discussion of the results of calculated Curie-Weiss temperature and corresponding calculated frustration factor were included in the main text of Chapter 5, section 5-3-3.

Table C-4. Parameters of the Curie-Weiss law with 1% constant background (χ_0) which is subtracted from the experimental data of χ of samples from 1 day annealing time to be used in fitting model of the equation (5-5). Relaxing the weight fraction of hausmannite phase in the least-square fitting results in unrealistic values for secondary phase, which is detectable easily in XRD pattern. Fixing the weight fraction of secondary phase to the values extracted from Rietveld refinement of the XRD patterns can be more stable approach among all approaches have been tested.

Mn/Lu	χ_0(emu/g.oe)	T_{CW}(K)	Curie Constant (emu.K/g.Oe)	1-f_m	Adj. R-Square
Fitting	Fixed	Relaxed	Relaxed	Relaxed	
1.12	1% raw data	-928.9	0.0169	0.9	0.99822
1.08	1% raw data	-805.9	0.01385	0.9	0.99995
1.04	1% raw data	-1065.9	0.01254	0.9	0.99976
1.02	1% raw data	-804.3	0.01471	0.96585	0.99997
1	1% raw data	-747.9	0.01396	0.96776	0.99996
0.98	1% raw data	-957.4	0.01462	0.95681	0.99934
0.96	1% raw data	-1879.8	0.03201	0.93084	0.99982
0.92	1% raw data	-1085.2	0.06795	1	0.99929

Table C-5. Results of applying developed methodology (Table C-4) to calculate magnetic parameters after subtracting secondary phase contribution for samples of 5 days and 10 days annealing time. Notice that for x=1.12 compositions the amount of secondary phase was considered higher than in other compositions.

samples with one day annealing time at 1300°C						
	χ_0(emu/gr.oe)	T_{CW}(K)	C(emu.K/g.Oe)	1-f_m	chi square	range of fitting
Fitting	Fixed	Relaxed	Relaxed	Fixed	after fitting	
1.12	1.96256E-5	-605	0.01515	0.974	0.99334	150 K-350 K
1.08	1.83208E-5	-588.4	0.01413	0.98	0.9994	150 K-350 K
1.04	1.46916E-5	-651.7	0.01233	0.977	0.99845	175 K-350 K
1.02	1.6113E-5	-721.5	0.01427	0.982	0.99976	150 K-350 K
1	1.60747E-5	-661.5	0.01366	0.99	0.99974	150 K-350 K
0.98	1.43228E-5	-770	0.01396	0.99	0.99898	150 K-350 K
0.96	1.79633E-5	-1078	0.02395	0.998	0.99776	150 K-350 K
0.92	5.24922E-5	-1082	0.06894	0.998	0.99952	150 K-350 K
samples with 5 days annealing time at 1300°C						
Fitting	Fixed	Relaxed	Relaxed	Fixed	after fitting	
1.12	1.9E-05	-628.5	0.01579	0.99	0.99493	150 K-350 K
1.08	1.6E-05	-537.7	0.01262	0.99	0.99662	150 K-350 K
1.04	1.6E-05	-611.8	0.01338	0.99	0.99789	150 K-350 K
1	1.2E-05	-661.7	0.00997	0.995	0.9984	150 K-350 K
0.96	1.9E-5	-819.4	0.01996	0.998	0.99855	125 K-350 K
0.92	1.3E-05	-827.3	0.01413	0.995	0.99991	150 K-350 K
samples with 10 days annealing time at 1300°C						
Fitting	Fixed	Relaxed	Relaxed	Fixed	after fitting	
1.12	1.9E-05	-543.6	0.01416	0.99	0.99685	175 K-350 K
1.08	1.7E-05	-528.4	0.01248	0.99	0.99879	150 K-350 K
1.04	1.8E-05	-559.7	0.01434	0.99	0.99606	150 K-350 K
1	1.6E-05	-616.1	0.01369	0.995	0.99853	150 K-350 K
0.98	1.3E-05	-683.3	0.01167	0.995	0.99902	150 K-350 K
0.96	1.6E-05	-825.2	0.01705	0.995	0.99915	150 K-350 K
0.92	1.2E-05	-720.8	0.01169	0.995	0.99976	150 K-350 K

Table C-6. Values of frustration factor f and magnetic moments calculated from the data of T_{CW} and C of previous table. T_N values are calculated from the first derivative of the transitions in FC magnetic susceptibility data observed at values of temperature around 90 K.

	samples with 1 day annealing time				
	T_N	T_{CW}(K)	f ($\|T_{CW}\|$/TN)	Magnetic Moment(μB)	range of fitting
1.12	89.5	-605	6.8	1.8	150 K-350 K
1.08	89.98	-588.4	6.5	3.6	150 K-350 K
1.04	89.7	-651.7	7.3	2.5	175 K-350 K
1.02	91.69	-721.5	7.9	4.1	150 K-350 K
1	90.9	-661.5	7.3	4.0	150 K-350 K
0.98	91.7	-770	8.4	3.7	150 K-350 K
0.96	91.1	-1078	11.8	3.5	150 K-350 K
0.92	94.5	-1082	11.4	7.3	150 K-350 K
	samples with 5 days annealing time				
1.12	88.9	-628.5	7.0	5.9	150 K-350 K
1.08	90.22	-537.7	6.0	5.2	150 K-350 K
1.04	90.44	-611.8	6.8	5.4	150 K-350 K
1	90.94	-661.7	7.3	4.6	150 K-350 K
0.96	90.5	-819.4	9.1	6.5	125 K-350 K
0.92	92.351	-827.3	9.0	5.4	150 K-350 K
	samples with 10 days annealing time				
1.12	88.97	-543.6	6.1	5.6	150 K-350 K
1.08	88.72	-528.4	6.0	5.2	150 K-350 K
1.04	88.84	-559.7	6.3	5.5	150 K-350 K
1	89.45	-616.1	6.9	5.4	150 K-350 K
0.98	90.5	-683.3	7.6	5.0	150 K-350 K
0.96	90.47	-825.2	9.1	6.0	150 K-350 K
0.92	90.6	-720.8	8.0	4.9	150 K-350 K

D. Analysis of field dependant M(T)

As for the analysis of M/H of the $LuMn_{1.04}O_{3\pm\delta}$ sample in Figure 5-16, section 5-3-5, three temperatures were chosen for the analysis of the effect of magnetic field: 80 K, where anomaly of ZFC magnetization below T_N appears (81 K in the analysis of ZFC magnetization in Figure 5-17.b), 55 K where the values of ZFC field normalized magnetization, M/H, for a large span of different magnetic fields are constant, and 40 K below the Curie temperature of hausmannite. The analysis was done for three selected samples of 5 days annealing time with composition x=0.96, x=1.00 and x=1.04. The calculated values of the constant, exponent and correlation coefficient of the empirical equation given by the power relation on $M \propto H^{\eta}$ are given in Table D-1.

Figure D-1 shows that M has a non-linear dependence of magnetic field at 80 K given by values of the exponent $0.8<\eta<0.96$ definitively below one. The decrease of this exponent η with sample composition is nearly linear on x, the non-linearity of the dependence of M on H being accentuated in Mn-rich side of the $LuMn_xO_{3\pm\delta}$ solid solution. As displayed in Figure D-1, the exponent η for ZFC magnetization at 55 K is very close to the unity for the all three samples of different composition, and as already shown for $LuMn_{1.04}O_{3\pm\delta}$ sample in the corresponding power law plot in Figure 5-17.b, ZFC magnetization in the intermediate temperature range 45-65 K is directly proportional to the magnetic field. The values of exponent η for FC magnetization at the same temperature of 55 K show linearity on composition ratio x and a larger deviation from linearity of the dependence of M on H which becomes more prominent in the Mn-rich side towards the x=1.04 composition. Below the Curie temperature of hausmannite, the dependence of magnetization M on H at 40 K has values of the exponent η around ½ in the x=1.04 sample, for both FC and ZFC conditions. On the Lu-rich side of $LuMn_xO_{3\pm\delta}$ solid solution values of η for x=0.96 at 40 K still stay close to one, indicating simple proportionality

between M and H while for x=1.00 sample values of η remain above 0.7, both samples showing the presence of much lower amounts of residual hausmannite in comparison to x=1.04 sample, last line of Table 4-2.

Table D-1. Values of exponent, η and a constant of power law (Constant.H^{η}, where H holds for magnetic field) from fitting with their respective R^2 (quality of fitting) for 3 samples of 5 days annealing.

		ZFC measurement			FC measurement		
		Constant	η	R^2	Constant	η	R^2
40 K	1.04	0.0078	0.526	0.933	0.2821	0.371	0.9685
40 K	1	12.458	0.836	0.9977	355.88	0.714	0.9977
40 K	0.96	3.062	0.954	1	4.8513	0.905	0.9996
55 K	1.04	4.00E-05	0.968	0.9995	0.0024	0.776	0.9984
55 K	1	4.1791	0.94	0.9998	93.499	0.846	0.9985
55 K	0.96	2.513	0.967	1	3.7071	0.930	0.9997
80 K	1.04	8.00E-05	0.868	0.9998	0.001	0.846	0.9986
80 K	1	3.7585	0.936	0.9993	51.628	0.868	0.9993
80 K	0.96	2.6761	0.964	1	2.9772	0.949	0.9999

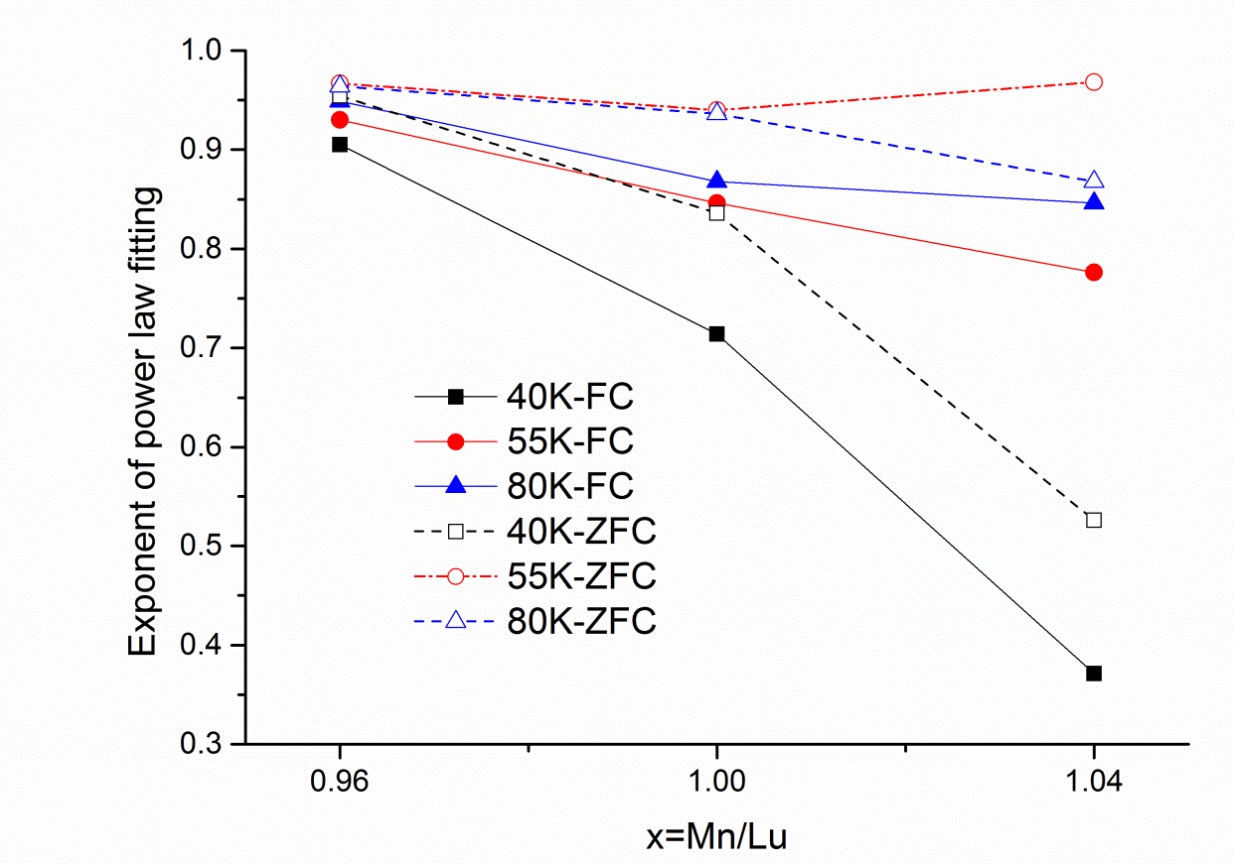

Figure D-1. Exponent of power law obtained by fitting a power law curve on the data of field dependent magnetization measured at different magnetic fields at 40 K, 55 K and 80 K for x=1.04, x=1.00 and x=0.96, both FC and ZFC conditions.

E. Mode decomposition of $YMnO_3$

To perform mode decomposition, we need to have the structural file of the high temperature, high symmetry PE phase of the $YMnO_3$ compound. Given below is the available data for $YMnO_3$ from the literature [225]. Amplimode program available from Bilbao Crystallographic Server was used [220,225].

194
3.61 3.61 11.39 90.00 90.00 120.00
4

Y	1	2a	0.000000	0.000000	0.000000
Mn	1	2c	0.333333	0.666670	0.250000
O	1	4f	0.333333	0.666670	0.087000
O	3	2b	0.000000	0.000000	0.250000

The transformation matrix which connects the PE phase to decomposed modes is:

$$\begin{pmatrix} 2 & 1 & 0 \\ -1 & 1 & 0 \\ 0 & 0 & 1 \end{pmatrix} \begin{pmatrix} a \\ a \\ c \end{pmatrix} = \begin{pmatrix} a' \\ b' \\ c' \end{pmatrix}$$

with the origin shifted of (0,0, 0.24700) as suggested by the Amplimode program. Table E-1.a gives the four expected modes after phase transition allowed by the rules of group symmetry analysis. The second table, Table E-1.b lists the atoms which are displaced during phase transition and the result of the corresponding destination mode. Amplitude of the modes confirms that K_3 mode is the primary mode as it has higher amplitude, giving also rise to tripling of the unit cell after phase transition.

Table E-1. Amplitude of the different decomposed modes (a) and the orbits (atoms) (b) involved in displacement during phase transition for each mode in hexagonal $LuMnO_3$ lattices

a						b		
K-vector	Irrep	Direction	Isotropy Subgroup	Dimension	Amplitude (Å)	Atoms	WP	Modes
(0,0,0)	GM1+	(a)	P6_3/mmc (194)	1	0.0057	O1	4*f*	GM1+(1) GM2-(1) K1(1) **K3(1)**
(0,0,0)	GM2-	(a)	P6_3mc (186)	4	0.1539	Mn1	2*c*	GM2-(1) K1(1)
(1/3,1/3,0)	K1	(a,0)	P6_3/mcm (193)	2	0.0166	O3	2*b*	GM2-(1) **K3(1)**
(1/3,1/3,0)	K3	(a,0)	P6_3cm (185)	3	0.5380	Y1	2*a*	GM2-(1) **K3(1)**

Table E-2. Atomic displacement of the 4 ions in PE phase to 7 different Wyckoff positions. u_x, u_y and u_z are given in relative units. |u| is the absolute distance given in Å.

WP		Atom	Atomic Displacements			
			u_x	u_y	u_z	|u|
2a	(0,0,z)	Y1	0.0000	0.0000	-0.0195	0.2221
4b	(1/3,2/3,z)	Y1_2	0.0000	0.0000	0.0213	0.2426
6c	(x,0,z)	Mn1	0.0000	0.0019	-0.0030	0.0361
6c	(x,0,z)	O1	0.0000	0.0254	-0.0028	0.1618
6c	(x,0,z)	O1_2	-0.0250	-0.0250	-0.0033	0.1610
2a	(0,0,z)	O3	0.0000	0.0000	-0.0248	0.2825
4b	(1/3,2/3,z)	O3_2	0.0000	0.0000	0.0156	0.1777

Details of the displacement of the ions after phase transition are given in Table E-2. The GM1+ (Γ_{1+}) mode has the smallest amplitude. This mode involves the change in z coordinate of apical oxygen (strain of lattice). GM2-(Γ_{2-}) is accompanied by displacement of z-coordinates of all ions resulting in a polar phase. K_1 and K_3 modes give rise to expansion of the PE unit cell by $\sqrt{3}$ a $\times$ $\sqrt{3}$ b $\times$ 1 (a=b, so tripling the unit cell) with the same K vector (1/3,1/3,0) as can be found in equilibrium structure of h-$RMnO_3$ oxides at room temperature. K_1 allows O_{ap}-Mn-O_{ap} axis to be displaced in the basal plane where O

is assigned to the apical oxygen. K_3 mode is in fact the stable $P6_3cm$ mode (antiferrodistortive) leading to tilt of the MnO_5 bipyramids and antiparallel displacements of the Y ions [106,219].

K-vector: Γ = (0,0,0)

Irrep: Γ_{1+} Direction: (a) Isotropy Subgroup: 194 P6_3/mmc D6h-4

Irrep: Γ_{2-} Direction: (a) Isotropy Subgroup: 186 P6_3mc C6v-4

K = (1/3,1/3,0) Irrep: K1 Direction: (a,0) Isotropy Subgroup: 193 P6_3/mcm D6h-3

Irrep: K_3 Direction: (a,0) Isotropy Subgroup: 185 P6_3cm C6v-3

Table E-3. Atomic displacement of the PE Wyckoff positions of the ions in the unit cell and their splitting in respective irreducible representations.

Irrep.	**Γ_{1+}**			**Γ_{2-}**			**K_1**			**K_3**		
Atom	δx	δy	δz	δx	δy	δz	δx	δy	δz	δx	δy	δz
Y1	0.0000	0.0000	0.0000	0.0000	0.0000	0.0283	0.0000	0.0000	0.0000	0.0000	0.0000	-0.0292
Y1_2	0.0000	0.0000	0.0000	0.0000	0.0000	0.0283	0.0000	0.0000	0.0000	0.0000	0.0000	0.0146
Mn1	0.0000	0.0000	0.0000	0.0000	0.0000	-0.0118	0.0000	0.0648	0.0000	0.0000	0.0000	0.0000
O1	0.0000	0.0000	0.0253	0.0000	0.0000	-0.0120	0.0000	0.0058	0.0000	0.0000	0.0270	0.0000
O1_2	0.0000	0.0000	-0.0253	0.0000	0.0000	-0.0120	0.0058	0.0058	0.0000	-0.0270	-0.0270	0.0000
O3	0.0000	0.0000	0.0000	0.0000	0.0000	0.0075	0.0000	0.0000	0.0000	0.0000	0.0000	-0.0289
O3_2	0.0000	0.0000	0.0000	0.0000	0.0000	0.0075	0.0000	0.0000	0.0000	0.0000	0.0000	0.0145

The orbit splitting of the modes with larger amplitude of distortion for Γ_{2-} and K_3 from the table above show the change of unit cell when the mode is either K_3 or Γ_{2-} mode. In

Γ_{2-} mode, Table E-3 indicates that the atomic displacements from PE to Γ_{2-} occur only along c-axis, the polarization direction, confirming that polarization of the lattice comes from this mode. On the contrary, the undergoing atomic displacements when K_3 mode is the primary mode includes the z-direction shifts for the rare-earth ion and planar oxygen, the shift in apical oxygen occurring in the basal plane. Mn ions do not show any displacement in this mode. The calculated energy of all modes, particularly K_3 and Γ_{2-}, confirmed that with exception of the K_3 mode, the other modes are stable when their energies are plotted versus the corresponding degree of distortion from zero amplitude [219].

F. Papers published in journals or conference proceedings

1- C. O. Amorim, F. Figueiras,J. S. Amaral, P. Mirzadeh Vaghefi, P. B.Tavares, M. R. Correia, *A. Baghizadeh*, E. Alves, J. Rocha, and V. S.Amaral, "*Peculiar Magnetoelectric Coupling in BaTiO3:Fe113ppm Nanoscopic Segregations*", accepted for publication in ACS Applied Materials & Interfaces, 2015

2- A. Baghizadeh, J. M. Vieira, J. S. Amara, M.P. Graça, M. R. Soares, D. A. Mota, V. S. Amaral, "*Crystal structure, magnetic and dielectric behavior of h-$LuMn_xO_{3\pm\delta}$ ceramics ($0.95 \le x \le 1.04$)*", Journal of Magnetism and Magnetic Materials 395(2015)303–311.

3- J. M. Vieira, A. Baghizadeh, J. S. Amaral, J. N. Gonçalves, B. A. Almeida, M-G. Willinger, V. S. Amaral, *Assessing Segregation Effects on Multiferroic Properties of Antiferromagnetic-Weak Ferromagnetic Coupled Systems by Analytical HRTEM*, 4th joint congress of Portuguese and Spanish microscopy societies, 9-11 Sep.2015, Porto University, Porto (Oral Presentation). MFS2015 Book of Abstracts (2015) 49-50. *Submitted to Microscopy & Microanalysis*.

4. A. Baghizadeh, J. M. Vieira, J.S.Amaral, M. Graça, J N Gonçalves, P.Mirzadeh, M.Willinger, V. S. Amaral, *Magnetic properties and Magnetoelectric coupling of vacancy doped hexagonal $LuMn_xO_{3\pm\delta}$ ceramics*, 20th International Conference on Magnetism 2015, 5-10 July 2015, Barcelona, Spain. (Poster)

5- .Mohseni, *A. Baghizadeh* , M. Pereira, N.Fortunato, J. S. Amaral, A. C. Lourenço, J. M. Vieira, *Alnico thin films with improved saturation magnetization and coercivity*, 20th International Conference on Magnetism 2015, 5-10 July 2015, Barcelona, Spain. (Poster).

6- J. N. Gonçalves, V. S. Amaral, J. G. Correia, A. Stroppa, A. S. Fenta, *A. Baghizadeh*, S. Picozzi, "*Local probing of multiferroics: First-principles study of hyperfine parameters in $YMnO_3$ and YMn_2O_5*", EPJ Web of Conferences, 75(2014) 09002

7-. A.Baghizadeh, P. Mirzadeh Vaghefi, M. Willinger, M.P.F.Graça, V. S. Amaral, J.M.Vieira, "*Electrical Polarization and Microstructure of Self-doped* $LuMn_xO_{3\pm\delta}$ *(0.94≤x≤1.04) Ceramics",* ELECTROCERAMICS XIV, Bucharest, Romania, 16 -20 June, 2014.

8- P. Mirzadeh Vaghefi, A. Baghizadeh, A. M. Viana, M. J. Pereira, Marc G. Willinger, A. A. C. S. Lourenço, "structural and magnetic properties of RF-sputtered perovskite oxide BaMnO3 thin films on Si", 13th European Vacuum Conference, Aveiro University, Aveiro, Portugal (September, 2014).

9- *"Self-doped $Lu_xMn_{1-x}O_3$ Structural Analysis and Electronic Structure",* Presentation at the *Electron Microscopy Seminar* of the Department of Inorganic Chemistry in Fritz Haber Institute, Berlin, Germany**,** November 12, 2013. (Oral presentation)

10- A.Baghizadeh, J.M.Vieira, M.G.Willinger, V.S.Amaral, "*Structural and compositional studies of the self-doped $LuMn_{1-x}O_3$ solid solution*", European Microbeam Analysis Society (EMAS), May 12-16, 2013, Porto, Portugal. (Oral presentation and poster)

11- "*Magnetic and Dielectric Coupling of the Multiferroic $RMnO_3$ Compounds",* Presentation at the Budapet Neutron Centre in KFKI, Budapest, Hungary, June 2013. *(Oral Presentation and Poster)*

12- A.Baghizadeh, J.M.Vieira, M.G.Willinger, V.S.Amaral, J. N. Gonçalves, F.Figueiras, "*EELS study of multiferroic $Lu_{2-x}Mn_xO_3$ compounds*", IX CICECO Meeting, May 18-19, 2013, Aveiro University, Portugal.

13- A. Baghizadeh, J. M. Vieira , M-G. Willinger, J. N. Gonçalves, M.Ferro, V. S. Amaral, *Effect of Self-doping on the Nanostructure of the Non-stoichiometric $LuMn_xO_{3\pm\delta}$ Ceramics*, to be submitted.

References

[1] B. Lorenz, Hexagonal Manganites — ($RMnO_3$): Class (I) Multiferroics with Strong Coupling of Magnetism and Ferroelectricity, 2013 (2013).

[2] W. Eerenstein, N.D. Mathur, J.F. Scott, Multiferroic and magnetoelectric materials, Nature. 442 (2006) 759–765. doi:10.1038/nature05023.

[3] M. Fiebig, Revival of the magnetoelectric effect, J. Phys. D. Appl. Phys. 38 (2005) R123–R152. doi:10.1088/0022-3727/38/8/R01.

[4] C. Sang-wook, M. Mostovoy, Multiferroics : a magnetic twist for ferroelectricity, Nat. Mater. 6 (2007) 13.

[5] R. Ramesh, N.A. Spaldin, Multiferroics: progress and prospects in thin films, Nat. Mater. 6 (2007) 21–29. doi:10.1038/nmat1805.

[6] G. Lawes, G. Srinivasan, Introduction to magnetoelectric coupling and multiferroic films, J. Phys. D. Appl. Phys. 44 (2011) 243001. doi:10.1088/0022-3727/44/24/243001.

[7] E. Dagotto, Y. Tokura, Strongly Correlated Electronic Materials: Present and Future, MRS Bull. 33 (2011) 1037–1045. doi:10.1557/mrs2008.223.

[8] E. Dagotto, Open Questions in CMR Manganites, Relevance of Clustered States, and Analogies with other Compounds, (2003) 15. http://arxiv.org/abs/cond-mat/0302550

[9] M. Fiebig, T. Lottermoser, D. Frohlich, A. V Goltsev, R. V Pisarev, Observation of coupled magnetic and electric domains, Nature. 419 (2002) 818–820. doi:10.1038/nature01077.

[10] H. Das, A.L. Wysocki, Y. Geng, W. Wu, C.J. Fennie, Bulk magnetoelectricity in the hexagonal manganites and ferrites, Nat. Commun. 5 (2014) 1–11. doi:10.1038/ncomms3998.

[11] A. Brinkman, M. Huijben, M. van Zalk, J. Huijben, U. Zeitler, J.C. Maan, W.G. van der Wiel, G. Rijnders, D.H.A. Blank, H. Hilgenkamp, Magnetic effects at the interface between non-magnetic oxides., Nat. Mater. 6 (2007) 493–6. doi:10.1038/nmat1931.

[12] C. Cen, S. Thiel, G. Hammerl, C.W. Schneider, K.E. Andersen, C.S. Hellberg, J. Mannhart, J. Levy, Nanoscale control of an interfacial metal-insulator transition at room temperature., Nat. Mater. 7 (2008) 298–302. doi:10.1038/nmat2136.

[13] Z. Yan, D. Meier, J. Schaab, R. Ramesh, E. Samulon, E. Bourret, Growth of high-quality hexagonal $ErMnO_3$ single crystals by the pressurized floating-zone method, J. Cryst. Growth. 409 (2015) 75–79. doi:10.1016/j.jcrysgro.2014.10.006.

[14] S.-Z. Lin, X. Wang, Y. Kamiya, G.-W. Chern, F. Fan, D. Fan, B. Casas, Y. Liu, V. Kiryukhin, W.H. Zurek, C.D. Batista, S.-W. Cheong, Topological defects as relics of emergent continuous symmetry and Higgs condensation of disorder in ferroelectrics, Nat. Phys. 10 (2014) 970–977. doi:10.1038/nphys3142.

[15] M. Lilienblum, T. Lottermoser, S. Manz, S.M. Selbach, A. Cano, M. Fiebig, Ferroelectricity in the multiferroic hexagonal manganites, Nat. Phys. 11 (2015) 1070-1073. doi:10.1038/nphys3468.

[16] S. Artyukhin, K.T. Delaney, N. a Spaldin, M. Mostovoy, Landau theory of topological defects in multiferroic hexagonal manganites, Nat. Mater. 13 (2014) 42–49. doi:10.1038/nmat3786.

[17] L. Jeuvrey, O. Pena, A. Moure, C. Moure, Synthesis and magnetic properties of hexagonal $Y(Mn,Cu)O_3$ multiferroic materials, J. Magn. Magn. Mater. 324 (2012) 717–722. doi:10.1016/j.jmmm.2011.09.002.

[18] I. Gelard, N. Jehanathan, H. Roussel, S. Gariglio, O.I. Lebedev, G. Van Tendeloo, C. Dubourdieu, Off-Stoichiometry Effects on the Crystalline and Defect Structure of Hexagonal Manganite $REMnO_3$ Films (RE = V, Er, Dy), Chem. Mater. 23 (2011) 1232–1238. doi:10.1021/cm1029358.

[19] W.R. Chen, F.C. Zhang, J. Miao, B. Xu, L.X. Cao, X.G. Qiu, B.R. Zhao, Magnetic properties of the

self-doped yttrium manganites $YMn_{1+x}O_3$, J. Physics-Condensed Matter. 17 (2005) 8029–8036. doi:10.1088/0953-8984/17/50/020.

[20] M.B. Salamon, M. Jaime, The physics of manganites: Structure and transport, Rev. Mod. Phys. 73 (2001) 583–628. doi:10.1103/RevModPhys.73.583.

[21] B. Dabrowski, S. Kolesnik, A. Baszczuk, O. Chmaissem, T. Maxwell, J. Mais, Structural, transport, and magnetic properties of $RMnO_3$ perovskites (R = La, Pr, Nd, Sm, Eu-153, Dy), J. Solid State Chem. 178 (2005) 629–637. doi:10.1016/j.jssc.2004.12.006.

[22] A. Oleaga, A. Salazar, D. Prabhakaran, J.G. Cheng, J.S. Zhou, Critical behavior of the paramagnetic to antiferromagnetic transition in orthorhombic and hexagonal phases of $RMnO_3$ (R = Sm, Tb, Dy, Ho, Er, Tm, Yb, Lu, Y), Phys. Rev. B. 85 (2012) 184425. doi:10.1103/PhysRevB.85.184425.

[23] T. Kordel, C. Wehrenfennig, D. Meier, T. Lottermoser, M. Fiebig, I. Gelard, C. Dubourdieu, J.W. Kim, L. Schultz, K. Doerr, Nanodomains in multiferroic hexagonal $RMnO_3$ films (R = Y,Dy,Ho,Er), Phys. Rev. B. 80 (2009) 045409–8. doi:10.1103/PhysRevB.80.045409.

[24] A.A. Bosak, C. Dubourdieu, J.P. Senateur, O.Y. Gorbenko, A.R. Kaul, Hexagonal rare earth (R=Eu-Dy) manganites: XRD study of epitaxially stabilized films, Cryst. Eng. 5 (2002) 355–364. doi:10.1016/s1463-0184(02)00047-3.

[25] B.B. Van Aken, T.T.M. Palstra, Influence of magnetic on ferroelectric ordering in $LuMnO_3$, Phys. Rev. B. 69 (2004) 134113. doi:10.1103/PhysRevB.69.134113.

[26] I. Munawar, S.H. Curnoe, Theory of magnetic phases of hexagonal rare earth manganites, J. Physics-Condensed Matter. 18 (2006) 9575–9583. doi:10.1088/0953-8984/18/42/004.

[27] B. Lorenz, Hexagonal Manganites—($RMnO_3$): Class (I) Multiferroics with Strong Coupling of Magnetism and Ferroelectricity, ISRN Condens. Matter Phys. 2013 (2013) 43. doi:10.1155/2013/497073.

[28] J.A. Alonso, M.J. Martínez-Lope, M.T. Casais, M.T. Fernández-Díaz, Evolution of the Jahn-Teller distortion of MnO_6 octahedra in $RMnO_3$ perovskites (R = Pr, Nd, Dy, Tb, Ho, Er, Y): a neutron diffraction study., Inorg. Chem. 39 (2000) 917–23. http://www.ncbi.nlm.nih.gov/pubmed/12526369 (accessed March 9, 2015).

[29] B.B. van Aken, A. Meetsma, T.T.M. Palstra, Hexagonal $LuMnO_3$ revisited, Acta Crystallogr. Sect. E-Structure Reports Online. 57 (2001) I101–I103. doi:10.1107/s1600536801015896.

[30] T. Katsufuji, M. Masaki, A. Machida, M. Moritomo, K. Kato, E. Nishibori, M. Takata, M. Sakata, K. Ohoyama, K. Kitazawa, H. Takagi, Crystal structure and magnetic properties of hexagonal $RMnO_3$ (R=Y, Lu, and Sc) and the effect of doping, Phys. Rev. B. 66 (2002) 134434. doi:10.1103/PhysRevB.66.134434.

[31] I. V. Solovyev, M. V. Valentyuk, V. V. Mazurenko, Magnetic structure of hexagonal $YMnO_3$ and $LuMnO_3$ from a microscopic point of view, Phys. Rev. B. 86 (2012) 054407. doi:10.1103/PhysRevB.86.054407.

[32] X. Fabreges, S. Petit, I. Mirebeau, S. Pailhes, L. Pinsard, A. Forget, M.T. Fernandez-Diaz, F. Porcher, Spin-Lattice Coupling, Frustration, and Magnetic Order in Multiferroic $RMnO_3$, Phys. Rev. Lett. 103 (2009) 067204. doi:10.1103/PhysRevLett.103.067204.

[33] S.-J. Ahn, J. Kim, N. Shin, Y.-M. Koo, The covalent bonding interaction in the ferroelectric $LuMnO_3$, J. Appl. Phys. 110 (2011) 084112. doi:10.1063/1.3655986.

[34] J.G. Park, S. Lee, M. Kang, K.-H. Jang, C. Lee, S. V Streltsov, V. V Mazurenko, M. V Valentyuk, J.E. Medvedeva, T. Kamiyama, J.G. Park, Doping dependence of spin-lattice coupling and two-dimensional ordering in multiferroic hexagonal $Y_{1-x}Lu_xMnO_3$ ($0 \leq x \leq 1$), Phys. Rev. B. 82 (2010) 054428. doi:10.1103/PhysRevB.82.054428.

[35] T. Katsufuji, S. Mori, M. Masaki, Y. Moritomo, N. Yamamoto, H. Takagi, Dielectric and magnetic anomalies and spin frustration in hexagonal $RMnO_3$ (R = Y, Yb, and Lu), Phys. Rev. B. 64 (2001) 104419. doi:10.1103/PhysRevB.64.104419.

[36] D.G. Tomuta, S. Ramakrishnan, G.J. Nieuwenhuys, J.A. Mydosh1, The magnetic susceptibility, specific heat and dielectric constant of hexagonal $YMnO_3$, $LuMnO_3$ and $ScMnO_3$, J. Phys. Condens. MATTER. 13 (2001) 4543–4552. 10.1088/0953-8984/13/20/315.

[37] S. Lee, A. Pirogov, M. Kang, K.-H. Jang, M. Yonemura, T. Kamiyama, S.W. Cheong, F. Gozzo, N. Shin, H. Kimura, Y. Noda, J.G. Park, Giant magneto-elastic coupling in multiferroic hexagonal manganites, Nature. 451 (2008) 805–809. doi:10.1038/nature06507.

[38] J.G. Lin, Y.S. Chen, T.C. Han, Correlation of magnetic ordering and electric polarization in multiferroic $LuMn_{1-x}Fe_xO_3$ ($0 \leq x \leq 0.2$), J. Appl. Phys. 107 (2010) 09D902. doi:10.1063/1.3360355.

[39] W.A. Harrison, Elementary electronic structure, World Scientific Singapore, 2004.

[40] J.-S. Zhou, J. Goodenough, J. Gallardo-Amores, E. Morán, M. Alario-Franco, R. Caudillo, Hexagonal versus perovskite phase of manganite $RMnO_3$ (R=Y,Ho,Er,Tm,Yb,Lu), Phys. Rev. B. 74 (2006) 014422. doi:10.1103/PhysRevB.74.014422.

[41] T. Lonkai, D. Tomuta, U. Amann, J. Ihringer, R. Hendrikx, D. Többens, J. Mydosh, Development of the high-temperature phase of hexagonal manganites, Phys. Rev. B. 69 (2004) 134108. doi:10.1103/PhysRevB.69.134108.

[42] S. Lee, A. Pirogov, J.H. Han, J.G. Park, A. Hoshikawa, T. Kamiyama, Direct observation of a coupling between spin, lattice and electric dipole moment in multiferroic $YMnO_3$, Phys. Rev. B. 71 (2005) 180413(R). doi:10.1103/PhysRevB.71.180413.

[43] M. Poirier, F. Laliberté, L. Pinsard-Gaudart, A. Revcolevschi, Magnetoelastic coupling in hexagonal multiferroic $YMnO_3$ using ultrasound measurements, Phys. Rev. B. 76 (2007) 174426. doi:10.1103/PhysRevB.76.174426.

[44] C. dela Cruz, F. Yen, B. Lorenz, Y. Wang, Y. Sun, M. Gospodinov, C. Chu, Strong spin-lattice coupling in multiferroic $HoMnO_3$: Thermal expansion anomalies and pressure effect, Phys. Rev. B. 71 (2005) 060407. doi:10.1103/PhysRevB.71.060407.

[45] S. Yano, D. Louca, S. Chi, M. Matsuda, Intertwining of Frustration with Magneto-Elastic Coupling in the Multiferroic $LuMnO_3$, J. Phys. Soc. Japan. 024601 (2013) 2–5. http://dx.doi.org/10.7566/JPSJ.83.024601.

[46] A.R. Akbashev, V. V Roddatis, A.L. Vasiliev, S. Lopatin, V.A. Amelichev, A.R. Kaul, Reconstruction of the polar interface between hexagonal $LuFeO_3$ and intergrown Fe_3O_4 nanolayers., Sci. Rep. 2 (2012) 672. doi:10.1038/srep00672.

[47] Z.J. Huang, Y. Cao, Y.Y. Sun, Y.Y. Xue, C.W. Chu, Coupling between the ferroelectric and antiferromagnetic orders in Y MnO_3, Phys. Rev. B. 56 (1997) 2623–2626. doi:10.1103/PhysRevB.56.2623.

[48] A. V Goltsev, R. V Pisarev, T. Lottermoser, M. Fiebig, Structure and interaction of antiferromagnetic domain walls in hexagonal $YMnO_3$, Phys. Rev. Lett. 90 (2003) 177204–1. doi:10.1103/PhysRevLett.90.177204.

[49] T. Choi, Y. Horibe, H.T. Yi, Y.J. Choi, W. Wu, S.-W.W. Cheong, Insulating interlocked ferroelectric and structural antiphase domain walls in multiferroic $YMnO_3$, Nat. Mater. 9 (2010) 253–258. doi:10.1038/nmat2632.

[50] Y. Geng, N. Lee, Y.J. Choi, S.-W.W. Cheong, W. Wu, Collective Magnetism at Multiferroic Vortex Domain Walls, Nano Lett. 12 (2012) 6055–6059. doi:10.1021/nl301432z.

[51] Y. Kumagai, N.A. Spaldin, Structural domain walls in polar hexagonal manganites, Nat. Commun. 4 (2013) 1. doi:10.1038/ncomms2545.

[52] T. Matsumoto, R. Ishikawa, T. Tohei, H. Kimura, Q. Yao, H. Zhao, X. Wang, D. Chen, Z. Cheng, N. Shibata, Y. Ikuhara, Multivariate Statistical Characterization of Charged and Uncharged Domain Walls in Multiferroic Hexagonal $YMnO_3$ Single Crystal Visualized by a Spherical Aberration-Corrected STEM, Nano Lett. 13 (2013) 4594–4601. doi:10.1021/nl402158c.

[53] D. Meier, M. Lilienblum, P. Becker, L. Bohaty, N. a. A. Spaldin, R. Ramesh, M. Fiebig, L. Bohatý, N. a. A. Spaldin, R. Ramesh, M. Fiebig, Translation domains in multiferroics, Phase Transitions. 86 (2013) 33–52. doi:10.1080/01411594.2012.696116.

[54] Q.H. Zhang, L.J. Wang, X.K. Wei, R.C. Yu, L. Gu, A. Hirata, M.W. Chen, C.Q. Jin, Y. Yao, Y.G. Wang, X.F. Duan, Direct observation of interlocked domain walls in hexagonal $RMnO_3$ (R=Tm, Lu), Phys. Rev. B. 85 (2012) 020102. doi:10.1103/PhysRevB.85.020102.

[55] S.M. Griffin, M. Lilienblum, K.T. Delaney, Y. Kumagai, M. Fiebig, N. a. Spaldin, Scaling Behavior and Beyond Equilibrium in the Hexagonal Manganites, Phys. Rev. X. 2 (2012) 041022. doi:10.1103/PhysRevX.2.041022.

[56] X. Wang, M. Mostovoy, M.G. Han, Y. Horibe, T. Aoki, Y. Zhu, S.-W. Cheong, Unfolding of Vortices into Topological Stripes in a Multiferroic Material, Phys. Rev. Lett. 112 (2014) 247601. doi:10.1103/PhysRevLett.112.247601.

[57] F.-T. Huang, X. Wang, S.M. Griffin, Y. Kumagai, O. Gindele, M.-W. Chu, Y. Horibe, N.A. Spaldin, S.-W. Cheong, Duality of Topological Defects in Hexagonal Manganites, Phys. Rev. Lett. 113 (2014) 267602. doi:10.1103/PhysRevLett.113.267602.

[58] Q.-H. Zhang, G.-T. Tan, L. Gu, Y. Yao, C.-Q. Jin, Y.-G. Wang, X.-F. Duan, R.-C. Yu, Topology breaking of the vortex in multiferroic $Y_{0.67}Lu_{0.33}MnO_3$, Appl. Phys. Lett. 105 (2014) 012902. doi:10.1063/1.4887057.

[59] L. Tian, Y. Wang, B. Ge, X. Zhang, Z. Zhang, Direct observation of interlocked domain walls and topological four-state vortex-like domain patterns in multiferroic $YMnO_3$ single crystal, Appl. Phys. Lett. 106 (2015) 112903. doi:10.1063/1.4915259.

[60] X. Wang, F.-T. Huang, R. Hu, F. Fan, S.-W. Cheong, Self-poling with oxygen off-stoichiometry in ferroelectric hexagonal manganites, APL Mater. 3 (2015) 041505. doi:10.1063/1.4908159.

[61] M.H. Harunsani, J. Li, Y.B. Qin, H.T. Tian, J.Q. Li, H.X. Yang, R.I. Walton, Spontaneous formation of circular and vortex ferroelectric domain structure in hexagonal $YMnO_3$ and $YMn_{0.9}Fe_{0.1}O_3$ prepared by low temperature solution synthesis, Appl. Phys. Lett. 107 (2015) 062905. doi:10.1063/1.4928565.

[62] M. Bieringer, J.E. Greedan, Magnetic structure and spin reorientation transition in $ScMnO_3$, J. Solid State Chem. 143 (1999) 132–139. doi:10.1006/jssc.1998.8127.

[63] W.R. Chen, F.C. Zhang, J. Miao, B. Xu, X.L. Dong, L.X. Cao, X.G. Qiu, B.R. Zhao, P.C. Dai, Re-entrant spin glass behavior in Mn-rich $YMnO_3$, Appl. Phys. Lett. 87 (2005) 042508. doi:10.1063/1.1991980.

[64] S.Y. Jang, D. Lee, J.-H. Lee, T.W. Noh, Y. Jo, M.-H. Jung, J.-S. Chung, Oxygen vacancy induced re-entrant spin glass behavior in multiferroic $ErMnO_3$ thin films, Appl. Phys. Lett. 93 (2008) 162507. doi:10.1063/1.3006325.

[65] M. Kumar, R.J. Choudhary, D.M. Phase, Metastable magnetic state and exchange bias training effect in Mn-rich $YMnO_3$ thin films, J. Phys. D. Appl. Phys. 48 (2015) 125003. doi:10.1088/0022-3727/48/12/125003.

[66] I. Iliescu, M. Boudard, L. Rapenne, O. Chaix-Pluchery, H. Roussel, H. Roussel, MOCVD selective growth of orthorhombic or hexagonal $YMnO_3$ phase on Si(100) substrate, Appl. Surf. Sci. 306 (2014) 27–32. doi:10.1016/j.apsusc.2014.01.090.

[67] A. Ghosh, J.R. Sahu, S.V. Bhat, C.N.R. Rao, A Raman study of multiferroic $LuMnO_3$, Solid State Sci. 11 (2009) 1639–1642. doi:10.1016/j.solidstatesciences.2009.06.002.

[68] C. Zhang, J. Su, X. Wang, F. Huang, J. Zhang, Y. Liu, L. Zhang, K. Min, Z. Wang, X. Lu, F. Yan, J. Zhu, Study on magnetic and dielectric properties of $YMnO_3$ ceramics, J. Alloys Compd. 509 (2011) 7738–7741. doi:10.1016/j.jallcom.2011.04.128.

[69] A.A. Belik, Origin of magnetization reversal and exchange bias phenomena in solid solutions of $BiFeO_3$-$BiMnO_3$: intrinsic or extrinsic?, Inorg. Chem. 52 (2013) 2015–21. doi:10.1021/ic302384j.

[70] Y.J. Yoo, Y.P. Lee, J.S. Park, J.H. Kang, J. Kim, B.W. Lee, M.S. Seo, Spin-glass behavior of Cr-doped $YMnO_3$ compounds, J. Appl. Phys. 112 (2012) 013903. doi:10.1063/1.4731631.

[71] K. Singh, M.-B. Lepetit, C. Simon, N. Bellido, S. Pailhes, J. Varignon, A. De Muer, Analysis of the multiferroicity in the hexagonal manganite $YMnO_3$, J. Physics-Condensed Matter. 25 (2013) 416002. doi:10.1088/0953-8984/25/41/416002.

[72] C.T. Wu, B.N.Lin, H.C.Ku, Y.Y.Hsu, Variation of triangular antiferromagnetic order in ferroelectromagnetic $Sc_{1-x}Lu_xMnO_3$ manganites, Chinese J. Phys. 41 (2003) 652–661.

[73] Y. Romaguera-Barcelay, J.A. Moreira, a. Almeida, J.P. de la Cruz, Structural and electrical properties of $LuMnO_3$ thin film prepared by chemical solution method, Thin Solid Films. 520 (2012) 1734–1739. doi:10.1016/j.tsf.2011.08.044.

[74] S. Pailhes, X. Fabreges, L.P. Regnault, L. Pinsard-Godart, I. Mirebeau, F. Moussa, M. Hennion, S. Petit, Hybrid Goldstone modes in multiferroic $YMnO_3$ studied by polarized inelastic neutron scattering, Phys. Rev. B. 79 (2009) 134409. doi:10.1103/PhysRevB.79.134409.

[75] K. Yoshii, H. Abe, Magnetic properties of $LnMnO_3$ (Ln=Ho, Er,Tm,Yb, and Lu), J. Solid State Chem. 165 (2002) 131–135. doi:10.1006/jssc.2001.9514.

[76] A. Munoz, J.A. Alonso, M.J. Martinez-Lope, M.T. Casais, J.L. Martinez, M.T. Fernandez-Diaz, R. Mno, Y. Mno, A. Munoz, J.A. Alonso, M.J. Martinez-Lope, M.T. Casais, J.L. Martinez, M.T. Fernandez-Diaz, Magnetic structure of hexagonal $RMnO_3$ (R = Y, Sc): Thermal evolution from neutron powder diffraction data, Phys. Rev. B. 62 (2000) 9498–9510. doi:10.1103/PhysRevB.62.9498.

[77] R. Das, A. Jaiswal, S. Adyanthaya, P. Poddar, Origin of Magnetic Anomalies below the Neel Temperature in Nanocrystalline $LuMnO_3$, J. Phys. Chem. C. 114 (2010) 12104–12109.

doi:10.1021/jp103037r.

[78] S. Namdeo, S.S. Rao, S.D. Kaushik, V. Siruguri, A.M. Awasthi, Disorder-driven spin-reorientation in multiferroic h-$YMn_{1-x}Fe_xO_3$, J. Appl. Phys. 116 (2014) 024105. doi:10.1063/1.4887809.

[79] Y. Geng, H. Das, A.L. Wysocki, X. Wang, S.-W. Cheong, M. Mostovoy, C.J. Fennie, W. Wu, Direct visualization of magnetoelectric domains., Nat. Mater. 13 (2014) 163–7. doi:10.1038/nmat3813.

[80] T. Lottermoser, M. Fiebig, Magnetoelectric behavior of domain walls in multiferroic $HoMnO_3$, Phys. Rev. B. 70 (2004) 220407. doi:10.1103/PhysRevB.70.220407.

[81] V. Skumryev, V. Laukhin, I. Fina, X. Martí, F. Sánchez, M. Gospodinov, J. Fontcuberta, Magnetization Reversal by Electric-Field Decoupling of Magnetic and Ferroelectric Domain Walls in Multiferroic-Based Heterostructures, Phys. Rev. Lett. 106 (2011) 057206. doi:10.1103/PhysRevLett.106.057206.

[82] H.W. Zheng, Y.F. Liu, W.Y. Zhang, S.J. Liu, H.R. Zhang, K.F. Wang, Spin-glassy behavior and exchange bias effect of hexagonal $YMnO_3$ nanoparticles fabricated by hydrothermal process, J. Appl. Phys. 107 (2010) 053901. doi:10.1063/1.3296323.

[83] J.M. Patete, J. Han, A.L. Tiano, H. Liu, M.-G. Han, J.W. Simonson, Y. Li, A.C. Santulli, M.C. Aronson, A.I. Frenkel, Y. Zhu, S.S. Wong, Observation of Ferroelectricity and Structure-Dependent Magnetic Behavior in Novel One-Dimensional Motifs of Pure, Crystalline Yttrium Manganese Oxides, J. Phys. Chem. C. 118 (2014) 21695–21705. doi:10.1021/jp5068582.

[84] T.C. Han, M.R. Tsai, C.Y. Wei, Size effect on magnetic properties of hexagonal $HoMnO_3$ nanoparticles, J. Appl. Phys. 109 (2011) 07B517. doi:10.1063/1.3556945.

[85] T.-C. Han, W.-L. Hsu, W.-D. Lee, Grain size-dependent magnetic and electric properties in nanosized $YMnO_3$ multiferroic ceramics, Nanoscale Res. Lett. 6 (2011) 201. doi:10.1186/1556-276x-6-201.

[86] K. Bergum, H. Okamoto, H. Fjellvåg, T. Grande, M.-A. Einarsrud, S.M. Selbach, Synthesis, structure and magnetic properties of nanocrystalline $YMnO_3$., Dalton Trans. 40 (2011) 7583–9. doi:10.1039/c1dt10536a.

[87] E. Hanamura, Y. Tanabe, Phase transitions and second-harmonics of ferroelectric and antiferromagnetic $RMnO_3$, Phase Transitions. 79 (2006) 957–971. doi:10.1080/01411590601067169.

[88] D. Lee, J.-H. Lee, P. Murugavel, S.Y. Jang, T.W. Noh, Y. Jo, M.-H. Jung, Y.-D. Ko, J.-S. Chung, Epitaxial stabilization of artificial hexagonal $GdMnO_3$ thin films and their magnetic properties, Appl. Phys. Lett. 90 (2007) 182504. doi:10.1063/1.2735546.

[89] N. Jehanathan, O. Lebedev, I. Gelard, C. Dubourdieu, G. Van Tendeloo, Structure and defect characterization of multiferroic $ReMnO_3$ films and multilayers by TEM, Nanotechnology. 21 (2010) 075705–11. doi:10.1088/0957-4484/21/7/075705.

[90] A.A. Belik, Negative Exchange Bias in Polycrystalline Hexagonal $ScMnO_3$, $InMnO_3$, $YMnO_3$, 4H -$SrMnO_3$, and 6H-$SrMnO_3$ and Perovskite $YMnO_3$: Effects of Impurities, J. Phys. Soc. Japan. 83 (2014) 074703. doi:10.7566/JPSJ.83.074703.

[91] A. Baghizadeh, J.. Vieira, J.S. Amaral, M.P. Graça, M.R. Soares, D.A. Mota, V.S. Amaral, Crystal structure, magnetic and dielectric behavior of h-$LuMn_xO_{3\pm\delta}$ ceramics ($0.95\leq x\leq 1.04$), J. Magn. Magn. Mater. 395 (2015) 303–311. doi:10.1016/j.jmmm.2015.07.082.

[92] R. Tackett, G. Lawes, B.C. Melot, M. Grossman, E.S. Toberer, R. Seshadri, Magnetodielectric coupling in Mn_3O_4, Phys. Rev. B. 76 (2007) 024409. doi:10.1103/PhysRevB.76.024409.

[93] O.M. Fedorova, Y. V Golikov, Homogeneity ranges for yttrium and holmium manganites $Ln_{(2-x)}$ $Mn_{(x)}O_{(3\pm\delta)}$ (Ln = Y, Ho) in air, Russ. J. Appl. Chem. 84 (2011) 512–514. doi:10.1134/s1070427211030323.

[94] L.B. Vedmid', V.F. Balakirev, a. M. Yankin, Y. V. Golikov, O.M. Fedorova, Effect of Oxygen Pressure on Phase Equilibria in the Lu–Mn–O System, Glas. Phys. Chem. 30 (2004) 345–348. doi:10.1023/B:GPAC.0000038708.77042.9f.

[95] V.F. Balakirev, A.M. Yankin, O.M. Fedorova, L.B. Vedmid, Y. V Golikov, Phase Diagrams for Systems Formed by Manganese and Rare Earth Metal Oxides, Russ. J. Inorg. Chem. 55 (2010) 1774–1778. doi:10.1134/s0036023610110148.

[96] A.J. Overton, J.L. Best, I. Saratovsky, M.A. Hayward, Influence of Topotactic Reduction on the Structure and Magnetism of the Multiferroic $YMnO_3$, Chem. Mater. 21 (2009) 4940–4948. doi:10.1021/cm9021276.

[97] D.P. Chen, Y. Du, X.L. Wang, Z.X. Cheng, S.X. Dou, Z.W. Lin, J.G. Zhu, B. Xu, Oxygen-vacancy effect on structural, magnetic, and ferroelectric properties in multiferroic $YMnO_3$ single crystals, J. Appl. Phys. 111 (2012) 07D913. doi:10.1063/1.3676000.

[98] J.S. White, M. Bator, Y. Hu, H. Luetkens, J. Stahn, S. Capelli, S. Das, M. Doebeli, T. Lippert, V.K. Malik, J. Martynczuk, A. Wokaun, M. Kenzelmann, C. Niedermayer, C.W. Schneider, Strain-Induced Ferromagnetism in Antiferromagnetic $LuMnO_3$ Thin Films, Phys. Rev. Lett. 111 (2013) 037201. doi:10.1103/PhysRevLett.111.037201.

[99] S. Farokhipoor, C. Magén, S. Venkatesan, J. Íñiguez, C.J.M. Daumont, D. Rubi, E. Snoeck, M. Mostovoy, C. de Graaf, A. Müller, M. Döblinger, C. Scheu, B. Noheda, Artificial chemical and magnetic structure at the domain walls of an epitaxial oxide, Nature. 515 (2014) 379–383. doi:10.1038/nature13918.

[100] F. Wang, Y.Q. Zhang, W. Liu, X.K. Ning, Y. Bai, Z.M. Dai, S. Ma, X.G. Zhao, S.K. Li, Z.D. Zhang, Abnormal magnetic ordering and ferromagnetism in perovskite $ScMnO_3$ film, Appl. Phys. Lett. 106 (2015) 232906. doi:10.1063/1.4922727.

[101] O.M. Fedorova, Y. V. Golikov, Region of homogeneity for $Lu_{2-x}Mn_xO_{3\pm\delta}$ solid solution in air, Russ. J. Phys. Chem. A. 85 (2011) 2241–2243. doi:10.1134/S0036024411120089.

[102] O.M. Fedorova, V.F. Balakirev, Y. V Golikov, Composition Ranges of $Ln_{(2-x)}Mn_{(x)}O_{(3\pm\delta)}$ (Ln = Y, Ho, Er) Solid Solutions between 900 and 1400 degrees C in Air, Inorg. Mater. 47 (2011) 192–195. doi:10.1134/s0020168511020051.

[103] O.M. Fedorova, V.F. Balakirev, Y. V Golikov, Homogeneity regions of yttrium and ytterbium manganites in air, Russ. J. Inorg. Chem. 56 (2011) 173–175. doi:10.1134/s0036023611020070.

[104] L.B. Vedmid', a. M. Yankin, O.M. Fedorova, V.F. Balakirev, Evolution of phase equilibrium states in the Y-Mn-O system in the thermal dissociation of the compound YMn_2O_5, Russ. J. Inorg. Chem. 59 (2014) 519–523. doi:10.1134/S0036023614050180.

[105] M.C. Sekhar, N.V. Prasad, Dielectric, Impedance, Magnetic and Magnetoelectric Measurements on $YMnO_3$, Ferroelectrics. 345 (2006) 45–57. doi:10.1080/00150190601020966.

[106] A.S. Gibbs, K.S. Knight, P. Lightfoot, High-temperature phase transitions of hexagonal

$YMnO_3$, Phys. Rev. B. 83 (2011) 094111. doi:10.1103/PhysRevB.83.094111.

[107] B.A. Almeida, M.C. Ferro, A. Ravanan, P.M.F. Grave, H.-Y. Wu, M.-X. Gao, Y. Pan, F.J. Oliveira, A.B. Lopes, J.M. Vieira, Study of multi-carbide B 4 C-SiC/(Al, Si) reaction infiltrated composites by SEM with EBSD, IOP Conf. Ser. Mater. Sci. Eng. 55 (2014) 012001.

doi:10.1088/1757-899X/55/1/012001.

[108] M. Lilienblum, E. Soergel, M. Fiebig, Manipulation of ferroelectric vortex domains in hexagonal manganites, J. Appl. Phys. 110 (2011) 052007. doi:10.1063/1.3623777.

[109] O.M. Fedorova, Y. V Golikov, Region of Homogeneity for $Lu_{2-x}Mn_xO_{3\pm\delta}$ Solid Solution in Air, Russ. J. Phys. Chem. A. 85 (2011) 2241–2243. doi:10.1134/s0036024411120089.

[110] G. Dezanneau, a Sin, H. Roussel, M. Audier, H. Vincent, Magnetic properties related to structure and complete composition analyses of nanocrystalline $La_{1-x}Mn_{1-y}O_3$ powders, J. Solid State Chem. 173 (2003) 216–226. doi:10.1016/S0022-4596(03)00027-6.

[111] H.N. Lee, Y.T. Kim, Y.K. Park, Memory window of highly c-axis oriented ferroelectric $YMnO_3$ thin films, Appl. Phys. Lett. 74 (1999) 3887. doi:10.1063/1.124213.

[112] J. Magesh, P. Murugavel, R.V.K. Mangalam, K. Singh, C. Simon, W. Prellier, Role of rare earth on the Mn3+ spin reorientation in multiferroic $Ho_{1-x}Lu_xMnO_3$, J. Appl. Phys. 114 (2013) 094102. doi:10.1063/1.4819969.

[113] N. Jiang, X. Zhang, Atomistic simulation of Mn-site substitution in multiferroic h-$YMnO_3$., J. Physics. Condens. Matter. 24 (2012) 235402. doi:10.1088/0953-8984/24/23/235402.

[114] C. Zhang, X. Zhang, Y. Sun, S. Liu, Atomistic simulation of Y-site substitution in multiferroic h-$YMnO_3$, Phys. Rev. B. 83 (2011) 054104. doi:10.1103/PhysRevB.83.054104.

[115] K. Uusi-Esko, J. Malm, N. Imamura, H. Yamauchi, M. Karppinen, Characterization of $RMnO_3$ (R=Sc, Y, Dy-Lu): High-pressure synthesized metastable perovskites and their hexagonal precursor phases, Mater. Chem. Phys. 112 (2008) 1029–1034. doi:10.1016/j.matchemphys.2008.07.009.

[116] I.E. Graboy, A.A. Bosak, O.Y. Gorbenko, A.R. Kaul, C. Dubourdieu, J. Se, HREM Study of Epitaxially Stabilized Hexagonal Rare Earth Manganites, Chem.Mater. 2 (2003) 2632–2637. doi:10.1021/cm021315b.

[117] M.C. Lin, Y.S. Chen, T.C. Han, J.G. Lin, C.H. Chen, Origin of R-Dependent Dielectric Anomalies in $RMnO_3$ with R=Y, Ho, Er, Tm, Yb and Lu, Ferroelectrics. 380 (2009) 38–47. doi:10.1080/00150190902872834.

[118] S.D. Kaushik, A.K. Singh, V. Siruguri, S. Patnaik, A.B. Garg, R. Mittal, R. Mukhopadhyay, Effect of Dy doping in frustrated multiferroic h-Y MnO_3, in: SOLID STATE PHYSICS, Proc. 55TH DAE SOLID STATE Phys. Symp. 2010, AIP Publishing, 2011: pp. 1283–1284. doi:10.1063/1.3606336.

[119] M. Sekhar, S. Lee, G. Choi, C. Lee, J.-G. Park, Doping effects of hexagonal manganites $Er_{1-x}Y_xMnO_3$ with triangular spin structure, Phys. Rev. B. 72 (2005) 014402. doi:10.1103/PhysRevB.72.014402.

[120] M. El Amrani, V. Ta Phuoc, M.R. Ammar, M. Zaghrioui, F. Gervais, Structural modifications of disordered $YMn_{1-x}In_xO_3$ solid solutions evidenced by infrared and Raman spectroscopies, Solid State Sci. 14 (2012) 1315–1320. doi:10.1016/j.solidstatesciences.2012.06.013.

[121] S. Malo, a. Maignan, Co-substitution at the Mn-site in $YMnO_3$: Structural stability and physical properties, Mater. Res. Bull. 47 (2012) 974–979. doi:10.1016/j.materresbull.2012.01.015.

[122] U. Adem, A.A. Nugroho, A. Meetsma, T.T.M. Palstra, Ferroelectric displacements in multiferroic Y (Mn , Ga)O_3, Phys. Rev. B. 75 (2007) 014108. doi:10.1103/PhysRevB.75.014108.

[123] A.E. Smith, H. Mizoguchi, K. Delaney, N.A. Spaldin, A.W. Sleight, M.A. Subramanian, Mn^{3+} in trigonal bipyramidal coordination: a new blue chromophore., J. Am. Chem. Soc. 131 (2009) 17084–6. doi:10.1021/ja9080666.

[124] P. Blaha, K. Schwarz, G.K.H. Madsen, K. Kvasnicka, J. Luitz, Wien2K, An Augmented Plane Waves+Local Orbital Program for Calculating Crystal Properties, (2001).

[125] J E Medvedeva, V I Anisimov, M A Korotin, O N Mryasov, A J Freeman, The effect of Coulomb correlation and magnetic ordering on the electronic structure of two hexagonal phases of ferroelectromagnetic $YMnO_3$, J. Phys. Condens. Matter. 12 (2000) 4947. doi:http://dx.doi.org/10.1088/0953-8984/12/23/304.

[126] W. Choi, D. Kim, S. Seo, S. Moon, D. Lee, J. Lee, H. Lee, D.-Y. Cho, Y. Lee, P. Murugavel, J. Yu, T. Noh, Electronic structures of hexagonal $RMnO_3$ (R=Gd, Tb, Dy, and Ho) thin films: Optical spectroscopy and first-principles calculations, Phys. Rev. B. 77 (2008) 045137. doi:10.1103/PhysRevB.77.045137.

[127] B.B. Van Aken, T.T.M. Palstra, A. Filippetti, N. a Spaldin, The origin of ferroelectricity in magnetoelectric $YMnO_3$., Nat. Mater. 3 (2004) 164–70. doi:10.1038/nmat1080.

[128] A.M. Sousa, W.S. Coutinho, A.F. Lima, M. V Lalic, Structural, bonding, and electronic properties of the hexagonal ferroelectric and paraelectric phases of $LuMnO_3$ compound: A density functional theory study., J. Chem. Phys. 142 (2015) 074703. doi:10.1063/1.4907787.

[129] C. Zhong, Q. Jiang, H. Zhang, X. Jiang, Effect of spin frustration and spin-orbit coupling on the ferroelectric polarization in multiferroic $YMnO_3$, Appl. Phys. Lett. 94 (2009) 224107. doi:10.1063/1.3151912.

[130] S. Song, J.-H. Lee, H.M. Jang, Mode coupling between nonpolar and polar phonons as the origin of improper ferroelectricity in hexagonal $LuMnO_3$, J. Mater. Chem. C. 2 (2014) 4126. doi:10.1039/c4tc00182f.

[131] D.-Y. Cho, J.-Y. Kim, B.-G. Park, K.-J. Rho, J.-H. Park, H.-J. Noh, B.J. Kim, S.-J. Oh, H.-M. Park, J.-S. Ahn, H. Ishibashi, S.-W. Cheong, J. Lee, P. Murugavel, T. Noh, a. Tanaka, T. Jo, Ferroelectricity Driven by Y d^0-ness with Rehybridization in $YMnO_3$, Phys. Rev. Lett. 98 (2007) 217601. doi:10.1103/PhysRevLett.98.217601.

[132] T.-C. Han, J.-W. Chen, Y.-H. Liu, Y.-M. Hu, Grain size effect on magnetic and electric properties of $LuMnO_3$ nanocrystalline materials, J. Appl. Phys. 113 (2013) 17B507. doi:10.1063/1.4794977.

[133] J.E. Burke, J.H. Rosolowski, Treatise on Solid State Chemistry, Springer US, Boston, MA, 1976. doi:10.1007/978-1-4684-8082-5.

[134] Y. Ohya, Z. Nakagawa, Measurement of crack volume due to thermal expansion anisotropy in aluminium titanate ceramics, J. Mater. Sci. 31 (1996) 1555–1559. doi:10.1007/BF00357864.

[135] T.P. Hoepfner, E.D. Case, An estimate of the critical grain size for microcracks induced in

hydroxyapatite by thermal expansion anisotropy, Mater. Lett. 58 (2004) 489–492. doi:10.1016/S0167-577X(03)00531-7.

[136] M. Pezzotta, Z.L. Zhang, M. Jensen, T. Grande, M.-A. Einarsrud, Cohesive zone modeling of grain boundary microcracking induced by thermal anisotropy in titanium diboride ceramics, Comput. Mater. Sci. 43 (2008) 440–449. doi:10.1016/j.commatsci.2007.12.011.

[137] G. Lescano, F.M. Figueiredo, F.M.B. Marques, J. Schmidt, Synthesis and electrical conductivity of $Y_{1-x}Mn_{1-y}O_3$, J. Eur. Ceram. Soc. 21 (2001) 2037–2040. doi:10.1016/S0955-2219(01)00111-X

[138] C. Moure, J.F. Fernandez, M. Villegas, P. Duran, Non-Ohmic Behaviour and Switching Phenomena in $YMnO_3$-Based Ceramic Materials, J. Eur. Ceram. Soc. 19 (1999) 131–137. doi:10.1016/S0955-2219(98)00180-0.

[139] C. Moure, M. Villegas, J.F. Fernandez, J. Tartaj, P. Duran, Phase transition and electrical conductivity in the system $YMnO_3$-$CaMnO_3$, J. Mater. Sci. 34 (n.d.) 2565–2568. doi:10.1023/A:1004692430582.

[140] Y. Ma, Y.J. Wu, X.M. Chen, J.P. Cheng, Y.Q. Lin, In situ synthesis of multiferroic $YMnO_3$ ceramics by SPS and their characterization, Ceram. Int. 35 (2009) 3051–3055. doi:10.1016/j.ceramint.2009.04.018.

[141] M. Tomczyk, A.M. Senos, P.M. Vilarinho, I.M. Reaney, Origin of microcracking in $YMnO_3$ ceramics, Scr. Mater. 66 (2012) 288–291. doi:10.1016/j.scriptamat.2011.11.014.

[142] S.-H. Liu, J.-C.-A. Huang, X. Qi, W.-J. Lin, Y.-J. Siao, C.-R. Lin, J.-M. Chen, M.-T. Tang, Y.-H. Lee, J.-C. Lee, Structural transformation and charge transfer induced ferroelectricity and magnetism in annealed $YMnO_3$, AIP Adv. 1 (2011) 032173. doi:10.1063/1.3647519.

[143] G. Srinivasan, M. Seehra, Magnetic properties of Mn_3O_4 and a solution of the canted-spin problem, Phys. Rev. B. 28 (1983) 1–7. doi:10.1103/PhysRevB.28.1.

[144] P.A. Sharma, J.S. Ahn, N. Hur, S. Park, S.B. Kim, S. Lee, J.G. Park, S. Guha, S.W. Cheong, Thermal conductivity of geometrically frustrated, ferroelectric $YMnO_3$: Extraordinary spin-phonon interactions, Phys. Rev. Lett. 93 (2004) 177202–1. doi:10.1103/PhysRevLett.93.177202.

[145] M. Fiebig, D. Frohlich, K. Kohn, S. Leute, T. Lottermoser, V. V Pavlov, R. V Pisarev, Determination of the magnetic symmetry of hexagonal manganites by second harmonic generation, Phys. Rev. Lett. 84 (2000) 5620–5623. doi:10.1103/PhysRevLett.84.5620.

[146] J.G. Lin, Y.S. Chen, T.C. Han, Correlation of magnetic ordering and electric polarization in multiferroic $LuMn_{1-x}Fe_xO_3$ ($0 \leq x \leq 0.2$), J. Appl. Phys. 107 (2010) 09D902. doi:10.1063/1.3360355.

[147] Charles Kittle, Introduction to Solid State Physics, Edition 7t, John Wiley and Sons, Inc, 1995.

[148] J. Nogués, D. Lederman, T.J. Moran, I.K. Schuller, Positive Exchange Bias in Fe F 2 -Fe Bilayers, Phys. Rev. Lett. 76 (1996) 4624–4627. doi:10.1103/PhysRevLett.76.4624.

[149] N. Kumar Swamy, N. Pavan Kumar, P.V. Reddy, M. Gupta, S.S. Samatham, D. Venkateshwarulu, V. Ganesan, V. Malik, B.K. Das, Specific heat and magnetocaloric effect studies in multiferroic $YMnO_3$, J. Therm. Anal. Calorim. 119 (2014) 1191–1198. doi:10.1007/s10973-014-4223-3.

[150] S. Chauhan, S. Kumar Srivastava, R. Chandra, Zero-field cooled exchange bias in hexagonal $YMnO_3$ nanoparticles, Appl. Phys. Lett. 103 (2013) 042416. doi:10.1063/1.4816725.

[151] A.A. Belik, Fresh Look at the Mystery of Magnetization Reversal in YVO_3, Inorg. Chem. 52 (2013) 8529–8539. doi:10.1021/ic401042x.

[152] F. Hong, Z. Cheng, J. Wang, X. Wang, S. Dou, Positive and negative exchange bias effects in the simple perovskite manganite $NdMnO_3$, Appl. Phys. Lett. 101 (2012) 102411. doi:10.1063/1.4751990.

[153] T. Sato, S. Lee, T. Katsufuji, M. Masaki, S. Park, J. Copley, H. Takagi, Unconventional spin fluctuations in the hexagonal antiferromagnet $YMnO_3$, Phys. Rev. B. 68 (2003) 014432. doi:10.1103/PhysRevB.68.014432.

[154] C. Zhong, Z. Dong, C. Li, J. Zhao, Spin frustration and spin–lattice coupling in multiferroic hexagonal $HoMnO_3$ investigated by the first principles, J. Magn. Magn. Mater. 360 (2014) 6–9. doi:10.1016/j.jmmm.2014.01.060.

[155] A. Paul, P. Sharma, U. V. Waghmare, Spin-orbit interaction, spin-phonon coupling, and

anisotropy in the giant magnetoelastic effect in $YMnO_3$, Phys. Rev. B. 92 (2015) 054106. doi:10.1103/PhysRevB.92.054106.

[156] B. Mettout, P. Tolédano, M. Lilienblum, M. Fiebig, Combinatorial model for the ferroelectric domain-network formation in hexagonal manganites, Phys. Rev. B. 89 (2014) 024103. doi:10.1103/PhysRevB.89.024103.

[157] S.C. Chae, N. Lee, Y. Horibe, M. Tanimura, S. Mori, B. Gao, S. Carr, S.-W. Cheong, Direct Observation of the Proliferation of Ferroelectric Loop Domains and Vortex-Antivortex Pairs, Phys. Rev. Lett. 108 (2012) 167603. doi:10.1103/PhysRevLett.108.167603.

[158] A. Cano, Hidden order in hexagonal $RMnO_3$ multiferroics (R= Dy-Lu,In,Y and Sc), Phys. Rev. B. 89 (2014) 214107. doi:10.1103/PhysRevB.89.214107.

[159] S. Mori, J. Tokunaga, Y. Horibe, T. Asada, Y. Koyama, T. Katsufuji, Doping Effect on Ferroelectric Microstructure in $YMn_{1-x}Ti_xO_3$, Ferroelectrics. 348 (2007) 170–176. doi:10.1080/00150190701196393.

[160] S. Mori, K. Kurushima, H. Kamo, Y. Ishii, F.-T. Huang, Y. Horibe, T. Kastufuji, S.-W. Cheong, Ferroelectric and Structural Antiphase Domain and Domain Wall Structures in $Y(Mn,Ti)O_3$, Ferroelectrics. 462 (2014) 50–54. doi:10.1080/00150193.2014.890855.

[161] M.-G. Han, Y. Zhu, L. Wu, T. Aoki, V. Volkov, X. Wang, S.C. Chae, Y.S. Oh, S.-W. Cheong, Ferroelectric Switching Dynamics of Topological Vortex Domains in a Hexagonal Manganite, Adv. Mater. 25 (2013) 2415–2421. doi:10.1002/adma.201204766.

[162] Y. Du, X. Wang, D. Chen, Y. Yu, W. Hao, Z. Cheng, S.X. Dou, Manipulation of domain wall mobility by oxygen vacancy ordering in multiferroic $YMnO_3$., Phys. Chem. Chem. Phys. 15 (2013) 20010–5. doi:10.1039/c3cp52892h.

[163] J.H. Choi, J.Y. Lee, Y.T. Kim, Formation of Y_2O_3 interface layer in a $YMnO_3$/Si ferroelectric gate structure, Appl. Phys. Lett. 77 (2000) 4028. doi:10.1063/1.1332101.

[164] X. Martí, F. Sánchez, D. Hrabovsky, J. Fontcuberta, V. Laukhin, V. Skumryev, M.V. García-Cuenca, C. Ferrater, M. Varela, U. Lüders, J.F. Bobo, S. Estradé, J. Arbiol, F. Peiró, Epitaxial growth of biferroic $YMnO_3$(0001) on platinum electrodes, J. Cryst. Growth. 299 (2007) 288–294. doi:10.1016/j.jcrysgro.2006.11.272.

[165] H. Wu, J. Yuan, T. Peng, Y. Pan, T. Han, K. Shen, B.R. Zhao, C. Liu, Control of the epitaxial orientation and reduction of the interface leakage current in $YMnO_3$ /GaN heterostructures, J. Phys. D. Appl. Phys. 42 (2009) 185302. doi:10.1088/0022-3727/42/18/185302.

[166] K. Asokan, C.L. Dong, C.W. Bao, H.M. Tsai, J.W. Chiou, C.L. Chang, W.F. Pong, P. Duran, C. Moure, O. Peña, Comparison of electronic structures of orthorhombic and hexagonal manganites studied by X-ray absorption spectroscopy, Solid State Commun. 134 (2005) 821–826. doi:10.1016/j.ssc.2005.03.030.

[167] Q. Zhang, S. Guo, B. Ge, P. Chen, Y. Yao, L. Wang, L. Gu, Y. Wang, X. Duan, C. Jin, B. Liu, R. Yu, A New Ferroelectric Phase of $YMnO_3$ Induced by Oxygen- Vacancy Ordering, J. Am. Ceram. Soc. 97 (2013) 1264–1268. doi:10.1111/jace.12747.

[168] K. Asokan, Y.S. Chen, C.W. Pao, H.M. Tsai, C.W.O. Lee, C.H. Lin, H.C. Hsueh, D.C. Ling, W.F. Pong, J.W. Chiou, M.-H. Tsai, O. Peña, C. Moure, Effect of Co, Ni, and Cu substitution on the electronic structure of hexagonal $YMnO_3$ studied by x-ray absorption spectroscopy, Appl. Phys. Lett. 95 (2009) 131901. doi:10.1063/1.3224905.

[169] K.H. Wu, I.C. Gou, C.W. Luo, T.M. Uen, J.-Y. Lin, J.Y. Juang, C.K. Chen, J.M. Lee, J.M. Chen, Anisotropic electronic structure in single crystalline orthorhombic $TbMnO_3$ thin films, Thin Solid Films. 518 (2010) 2275–2279. doi:10.1016/j.tsf.2009.09.089.

[170] K.H. Wu, I.C. Gou, C.W. Luo, T.M. Uen, J.-Y. Lin, J.Y. Juang, T. Kobayashi, C.K. Chen, J.M. Lee, J.M. Chen, Polarization-dependent x-ray absorption spectroscopy of hexagonal and orthorhombic $TbMnO_3$ thin films, J. Phys. Conf. Ser. 200 (2010) 012227. doi:10.1088/1742-6596/200/1/012227.

[171] J.-S. Kang, S. Han, J.-G. Park, S. Wi, S. Lee, G. Kim, H. Song, H. Shin, W. Jo, B. Min, Photoemission and x-ray absorption of the electronic structure of multiferroic $RMnO_3$ (R=Y,Er), Phys. Rev. B. 71 (2005) 092405. doi:10.1103/PhysRevB.71.092405.

[172] J. Kim, K.C. Cho, Y.M. Koo, K.P. Hong, N. Shin, Y–O hybridization in the ferroelectric transition of $YMnO_3$, Appl. Phys. Lett. 95 (2009) 132901. doi:10.1063/1.3233943.

[173] K. Asokan, J.C. Jan, K.V.R. Rao, J.W. Chiou, H.M. Tsai, S. Mookerjee, W.F. Pong, M.-H. Tsai, R. Kumar, S. Husain, J.P. Srivastava, Electron- and hole-doping effects on the electronic

structure of manganite studied by x-ray absorption spectroscopy, J. Phys. Condens. Matter. 16 (2004) 3791–3799. doi:10.1088/0953-8984/16/21/027.

[174] S. Nishida, S. Kobayashi, A. Kumamoto, H. Ikeno, T. Mizoguchi, I. Tanaka, Y. Ikuhara, T. Yamamoto, Effect of local coordination of Mn on Mn-$L_{2,3}$ edge electron energy loss spectrum, J. Appl. Phys. 114 (2013) 054906. doi:10.1063/1.4817425.

[175] H. Tan, J. Verbeeck, A. Abakumov, G. Van Tendeloo, Oxidation state and chemical shift investigation in transition metal oxides by EELS, Ultramicroscopy. 116 (2012) 24–33. doi:10.1016/j.ultramic.2012.03.002.

[176] M. Varela, M.P. Oxley, W. Luo, J. Tao, M. Watanabe, A.R. Lupini, S.T. Pantelides, S.J. Pennycook, Atomic-resolution imaging of oxidation states in manganites, Phys. Rev. B. 79 (2009) 085117. doi:10.1103/PhysRevB.79.085117.

[177] H.K. Schmid, W. Mader, Oxidation states of Mn and Fe in various compound oxide systems., Micron. 37 (2006) 426–32. doi:10.1016/j.micron.2005.12.004.

[178] D. Pearson, C. Ahn, B. Fultz, White lines and d-electron occupancies for the 3d and 4d transition metals, Phys. Rev. B. 47 (1993) 8471–8478. doi:10.1103/PhysRevB.47.8471.

[179] T. Riedl, T. Gemming, K. Wetzig, Extraction of EELS white-line intensities of manganese compounds: methods, accuracy, and valence sensitivity., Ultramicroscopy. 106 (2006) 284–91. doi:10.1016/j.ultramic.2005.09.002.

[180] L.A.J. Garvie, A.J. Craven, High-resolution parallel electron energy-loss spectroscopy of Mn $L_{2,3}$-edges in inorganic manganese compounds, Phys. Chem. Miner. 21 (1994). doi:10.1007/BF00202132.

[181] G. Zampieri, F. Prado, A. Caneiro, J. Briático, M. Causa, M. Tovar, B. Alascio, M. Abbate, E. Morikawa, Electronic structure of $CaMnO_x$ with $2.66 \leq x \leq 3.00$ studied with photoemission and x-ray-absorption spectroscopy, Phys. Rev. B. 58 (1998) 3755–3761. doi:10.1103/PhysRevB.58.3755.

[182] Q. Zhang, S. Guo, B. Ge, P. Chen, Y. Yao, L. Wang, L. Gu, Y. Wang, X. Duan, C. Jin, B. Liu, R. Yu, A New Ferroelectric Phase of $YMnO_3$ Induced by Oxygen-Vacancy Ordering, J. Am. Ceram. Soc. 97 (2013) 1264–1268. doi:10.1111/jace.12747.

[183] A. Torres-Pardo, A. Gloter, P. Zubko, N. Jecklin, C. Lichtensteiger, C. Colliex, J.-M. Triscone, O. Stéphan, Spectroscopic mapping of local structural distortions in ferroelectric $PbTiO_3/SrTiO_3$ superlattices at the unit-cell scale, Phys. Rev. B. 84 (2011) 220102. doi:10.1103/PhysRevB.84.220102.

[184] M. Haruta, K. Kurashima, T. Nagai, H. Komatsu, Y. Shimakawa, H. Kurata, K. Kimoto, Visualization of hybridization states with atomic resolution using electron energy loss spectroscopy mapping, Appl. Phys. Lett. 100 (2012) 4. doi:10.1063/1.4704558.

[185] M. Haruta, H. Kurata, K. Matsumoto, S. Inoue, Y. Shimakawa, S. Isoda, Local electronic structure analysis for brownmillerite $Ca(Sr)FeO_{2.5}$ using site-resolved energy-loss near-edge structures, J. Appl. Phys. 110 (2011) 8. doi:10.1063/1.3610526.

[186] S. Kobayashi, Y. Tokuda, T. Mizoguchi, N. Shibata, Y. Sato, Y. Ikuhara, T. Yamamoto, Quantitative analyses of oxidation states for cubic $SrMnO_3$ and orthorhombic $SrMnO_{2.5}$ with electron energy loss spectroscopy, J. Appl. Phys. 108 (2010) 124903. doi:10.1063/1.3520655.

[187] D. Qian, B. Xu, M. Chi, Y.S. Meng, Uncovering the roles of oxygen vacancies in cation migration in lithium excess layered oxides., Phys. Chem. Chem. Phys. 16 (2014) 14665–8. doi:10.1039/c4cp01799d.

[188] S. Remsen, B. Dabrowski, Synthesis and Oxygen Storage Capacities of Hexagonal $Dy_{1x}Y_xMnO_{3+\delta}$, Chem. Mater. 23 (2011) 3818–3827. doi:10.1021/cm2006956.

[189] A. Travlos, N. Boukos, G. Apostolopoulos, A. Dimoulas, Oxygen vacancy ordering in epitaxial layers of yttrium oxide on Si (001), Appl. Phys. Lett. 82 (2003) 4053. doi:10.1063/1.1581985.

[190] F. Pailloux, M. Jublot, R. Gaboriaud, M. Jaouen, F. Paumier, D. Imhoff, Interfacial phases in epitaxial growth of Y_2O_3 on MgO studied via combining electron energy-loss spectroscopy and real-space self-consistent full multiple scattering calculations, Phys. Rev. B. 72 (2005) 125425. doi:10.1103/PhysRevB.72.125425.

[191] Q.H. Zhang, X. Shen, Y. Yao, Y.G. Wang, C.Q. Jin, R.C. Yu, Oxygen vacancy ordering and its mobility in $YMnO_3$, J. Alloys Compd. 648 (2015) 253–257. doi:10.1016/j.jallcom.2015.07.032.

[192] H. Kurata, C. Colliex, Electron-energy-loss core-edge structures in manganese oxides, Phys. Rev. B. 48 (1993) 2102–2108. doi:10.1103/PhysRevB.48.2102.

[193] P.-T. Chen, C.-M. Tseng, T.-Y. Yung, M.-W. Chu, C.-H. Chen, M. Hayashi, First-principle calculations analysis of ELNES splitting for Mn_3O_4 spinels related to atomic local symmetry., Ultramicroscopy. 140 (2014) 51–6. doi:10.1016/j.ultramic.2014.02.002.

[194] L. Wang, Y.G. Shi, Z. Chen, Y.B. Qin, H.F. Tian, C. Ma, H.X. Yang, A.A. Belik, Synthesis, structural and physical properties of $ScMn_2O_4$, Solid State Commun. 153 (2013) 71–75. doi:10.1016/j.ssc.2012.10.017.

[195] P.A. van Aken, B. Liebscher, Quantification of ferrous/ferric ratios in minerals: new evaluation schemes of Fe L_{23} electron energy-loss near-edge spectra, Phys. Chem. Miner. 29 (2002) 188–200. doi:10.1007/s00269-001-0222-6.

[196] I. Dzyaloshinsky, A thermodynamic theory of "weak" ferromagnetism of antiferromagnetics, J. Phys. Chem. Solids. 4 (1958) 241–255. doi:10.1016/0022-3697(58)90076-3.

[197] T. Moriya, Anisotropic Superexchange Interaction and Weak Ferromagnetism, Phys. Rev. 120 (1960) 91–98. doi:10.1103/PhysRev.120.91.

[198] J.-H. Lee, P. Murugavel, H. Ryu, D. Lee, J.Y. Jo, J.W. Kim, H.J. Kim, K.H. Kim, Y. Jo, M.-H. Jung, Y.H. Oh, Y.-W. Kim, J.-G. Yoon, J.-S. Chung, T.W. Noh, Epitaxial Stabilization of a New Multiferroic Hexagonal Phase of $TbMnO_3$ Thin Films, Adv. Mater. 18 (2006) 3125–3129. doi:10.1002/adma.200601621.

[199] A.E. Berkowitz, G.F. Rodriguez, J.I. Hong, K. An, T. Hyeon, N. Agarwal, D.J. Smith, E.E. Fullerton, Monodispersed MnO nanoparticles with epitaxial Mn_3O_4 shells, J. Phys. D. Appl. Phys. 41 (2008) 134007. doi:10.1088/0022-3727/41/13/134007.

[200] D.L. Cortie, A.G. Biternas, R.W. Chantrell, X.L. Wang, F. Klose, Microscopic model for exchange bias from grain-boundary disorder in a ferromagnet/antiferromagnet thin film with a nanocrystalline microstructure, Appl. Phys. Lett. 105 (2014) 032402. doi:10.1063/1.4890580.

[201] J.A. Moyer, R. Misra, J.A. Mundy, C.M. Brooks, J.T. Heron, D.A. Muller, D.G. Schlom, P. Schiffer, Intrinsic magnetic properties of hexagonal $LuFeO_3$ and the effects of

nonstoichiometry, APL Mater. 2 (2014) 012106. doi:10.1063/1.4861795.

[202] S. AMELINCKX, Structural aspects of stacking faults and fault propagations in the fine structure of dislocations, J. Phys. Colloq. 35 (1974) C7–1–C7–33. doi:10.1051/jphyscol:1974701.

[203] S.C. Chae, Y. Horibe, D.Y. Jeong, S. Rodan, N. Lee, S.-W. Cheong, Self-organization, condensation, and annihilation of topological vortices and antivortices in a multiferroic., Proc. Natl. Acad. Sci. U. S. A. 107 (2010) 21366–70. doi:10.1073/pnas.1011380107.

[204] Y. Du, X.L. Wang, D.P. Chen, S.X. Dou, Z.X. Cheng, M. Higgins, G. Wallace, J.Y. Wang, Domain wall conductivity in oxygen deficient multiferroic $YMnO_3$ single crystals, Appl. Phys. Lett. 99 (2011) 252107. doi:10.1063/1.3671393.

[205] N. Hur, I.K. Jeong, M.F. Hundley, S.B. Kim, S.W. Cheong, Giant magnetoelectric effect in multiferroic $HoMnO_3$ with a high ferroelectric transition temperature, Phys. Rev. B. 79 (2009) 134120–4. doi:10.1103/PhysRevB.79.134120.

[206] D.A. Mota, Y. Romaguera Barcelay, P.B. Tavares, M.R. Chaves, A. Almeida, J. Oliveira, W.S. Ferreira, J. Agostinho Moreira, Competing exchanges and spin-phonon coupling in $Eu_{1-x}R_xMnO_3$(R=Y, Lu), J. Phys. Condens. Matter. 25 (2013) 235602(7pp).

[207] J. Oliveira, J.A. Moreira, A. Almeida, M.R. Chaves, J.M.M. da Silva, J.B. Oliveira, M.A. Sá, P.B. Tavares, R. Ranjith, W. Prellier, Phase diagram of the orthorhombic, lightly lutetium doped $EuMnO_3$ magnetoelectric system, Phys. Rev. B. 84 (2011) 94414. http://link.aps.org/doi/10.1103/PhysRevB.84.094414.

[208] C. Ang, J.R. Jurado, Z. Yu, M.T. Colomer, J.R. Frade, J.L. Baptista, Variable-range-hopping conduction and dielectric relaxation in disordered $Sr_{0.97}(Ti_{1-x}Fe_x)O_{3-\delta}$, Phys. Rev. B. 57 (1998) 11858–11861. doi:10.1103/PhysRevB.57.11858.

[209] S. Komine, E. Iguchi, Dielectric properties in $LaFe_{0.5}Ga_{0.5}O_3$, J. Phys. Chem. Solids. 68 (2007) 1504–1507. doi:10.1016/j.jpcs.2007.03.024.

[210] S.C. Abrahams, Ferroelectricity and structure in the $YMnO_3$ family, Acta Crystallogr. Sect. B Struct. Sci. 57 (2001) 485–490. doi:10.1107/S0108768101009399.

[211] S. Kalinin, A. Borisevich, S. Jesse, B. Rodriguez, A. Morozovska, E. Eliseev, S. Pennycook,

Spatial Resolution, Information Limit, and Contrast Transfer in Piezoresponce Force Microscopy, Microsc. Microanal. 13 (2007) 1594–1595. doi:10.1017/S143192760707763X.

[212] S. V Kalinin, A.N. Morozovska, L.Q. Chen, B.J. Rodriguez, Local polarization dynamics in ferroelectric materials, Reports Prog. Phys. 73 (2010) 056502. doi:10.1088/0034-4885/73/5/056502.

[213] R.-L. Zhang, C.-L. Chen, Y.-J. Zhang, H. Xing, X.-L. Dong, K.-X. Jin, Ferroelectricity in hexagonal $YFeO_3$ film at room temperature, Chinese Phys. B. 24 (2015) 017701. doi:10.1088/1674-1056/24/1/017701.

[214] B.J. Rodriguez, S. Jesse, A.P. Baddorf, S. V. Kalinin, High Resolution Electromechanical Imaging of Ferroelectric Materials in a Liquid Environment by Piezoresponse Force Microscopy, Phys. Rev. Lett. 96 (2006) 237602. doi:10.1103/PhysRevLett.96.237602.

[215] V. V. Shvartsman, A.L. Kholkin, Evolution of nanodomains in $0.9PbMg_{1/3}Nb_{2/3}O_3$-$0.1PbTiO_3$ single crystals, J. Appl. Phys. 101 (2007) 064108. doi:10.1063/1.2713084.

[216] S. Chae, Y. Horibe, D. Jeong, N. Lee, K. Iida, M. Tanimura, S.-W. Cheong, Evolution of the Domain Topology in a Ferroelectric, Phys. Rev. Lett. 110 (2013) 167601. doi:10.1103/PhysRevLett.110.167601.

[217] R.E. Cohen, Origin of ferroelectricity in perovskite oxides, Nature. 358 (1992) 136–138. doi:10.1038/358136a0.

[218] Y. Kumagai, A.A. Belik, M. Lilienblum, N. Leo, M. Fiebig, N.A. Spaldin, Observation of persistent centrosymmetricity in the hexagonal manganite family, Phys. Rev. B. 85 (2012) 174422. doi:10.1103/PhysRevB.85.174422.

[219] C.J. Fennie, K.M. Rabe, Ferroelectric transition in $YMnO_3$from first principles, Phys. Rev. B. 72 (2005) 100103. doi:10.1103/PhysRevB.72.100103.

[220] J.M. Perez-Mato, D. Orobengoa, M.I. Aroyo, Mode crystallography of distorted structures., Acta Crystallogr. A. 66 (2010) 558–90. doi:10.1107/S0108767310016247.

[221] B.B. Van Aken, A. Meetsma, T.T.M. Palstra, Hexagonal $YMnO_3$, Acta Crystallogr. Sect. C Cryst. Struct. Commun. 57 (2001) 230–232. doi:10.1107/S0108270100015663.

[222] C. Capillas, E.S. Tasci, G. de la Flor, D. Orobengoa, J.M. Perez-Mato, M.I. Aroyo, A new computer tool at the Bilbao Crystallographic Server to detect and characterize pseudosymmetry, Zeitschrift Für Krist. 226 (2011) 186–196. doi:10.1524/zkri.2011.1321.

[223] B. Van Aken, J.-W. Bos, R. de Groot, T. Palstra, Asymmetry of electron and hole doping in YMnO3, Phys. Rev. B. 63 (2001) 125127. doi:10.1103/PhysRevB.63.125127.

[224] S.J. Ahmed, J. Kivinen, B. Zaporzan, L. Curiel, S. Pichardo, O. Rubel, BerryPI: A software for studying polarization of crystalline solids with WIEN2k density functional all-electron package, Comput. Phys. Commun. 184 (2013) 647–651. doi:10.1016/j.cpc.2012.10.028.

[225] D. Orobengoa, C. Capillas, M.I. Aroyo, J.M. Perez-Mato, AMPLIMODES : symmetry-mode analysis on the Bilbao Crystallographic Server, J. Appl. Crystallogr. 42 (2009) 820–833. doi:10.1107/S0021889809028064.